UNIVERSITÀ DEGLI STUDI FIRENZE
DAGRI DIPARTIMENTO DI SCIENZE E TECNOLOGIE AGRARIE, ALIMENTARI, AMBIENTALI E FORESTALI

Consiglio Nazionale delle Ricerche
CNR - Istituto per la BioEconomia

IUFRO
Interconnecting Forests, Science and People

WITH THE CONTRIBUTION OF FONDAZIONE CR FIRENZE

IWMS26

14.15 APRIL 2025 - FLORENCE

MEETING PROCEEDINGS

SPONSORED BY

TERMOLEGNO
TIMBER DRYING KILNS SINCE 1994

acimall
ITALIAN WOODWORKING TECHNOLOGY ASSOCIATION

FLA FEDERLEGNOARREDO

IMALPALAB
UP-CYCLE RESEARCH CENTER

incomac
Future Drying Systems

WDE WOOD DRYING ENGINEERING
MASPELL

SUNDAY 13TH APRIL 2025

18.30-20:00 **Welcome cocktail**
Crudi e Bollicine - Via Faenza, 4/A, 50123 Florence

MONDAY 14TH APRIL 2025 Aula Magna

08:30 Registration and welcome coffee

09:00 Greetings from the University of Florence and the International advisory board
Giacomo Goli and Gary Schajer

09:15 Welcome from IUFRO
Julie Cool and Louis Denaud

09:25 Memorial for Ryszard Szymani

09:40 **Keynote 1** ***Chair Giacomo Goli***

09:40 k1 Forest resources in Europe and the role of Italy for a forest based bio-economy
Davide Pettenella

10:00 k2 Circular economy for wood
Stefano Saviola

10:20 k3 The woodworking machinery international market
Dario Corbetta

10:40-11:15 Coffee break and poster discussion

11:20 **Session 1 CUTTING MECHANICS** ***Chair Christian Gottlöber***

11:20 S1.2 Calibration and sensitivity analysis of a bonded particle model for the simulation of chip ejection from wood cutting tools
Julius Hausmann, Christian Gottlöber

11:35 S1.3 Impact of sandpaper and machining settings on triboelectric charges in wood sanding
Lena Maria Leiter, Julie Cool

11:50 S1.4 Analysis of tool-workpiece interaction in peripheral planing of Douglas Fir using jointed hydro-clamped tools
Christian Kortüm

12:10 **Session 2 CUTTING FORCE AND POWER** ***Chair Julie Cool***

12:10 S2.1 Chip formation research using high speed filming, cutting force measurements and computed tomography scanning – a first approach
Magnus Fredriksson, Frank Schleicher, Fredrik Larsson, Jörgen Kajberg, Yunbo Huang, Mikael Svensson

12:25 S2.2 Friction forces between cutting edge flanks and machined wood due to Scots pine wood elasticity
Daniel Chuchala, Yunbo Huang, Kazimierz Orlowski, Mikael Svensson, Magnus Fredriksson

IWMS26 14.15 APRIL 2025 - FLORENCE

12:40 S2.3 Cutting force predictions in orthogonal cutting by a foam model
Gerhard Sinn, Andreas Schütz, Helga Lichtenegger, Kazimierz Orlowski, Daniel Chuchala

12:55-13:50 Lunch and poster discussion

13:55 **Keynote 2** *Chair Michela Zanetti*

13:55 k4 Use of millimeter waves for non-destructive quality analysis during the production stages of fiber-based panels
Massimo Bergonzini, Riccardo Centi, Giuseppe Amico

14:15 k5 Tracking and learning: AI cross training between scanners in sawmills
Enrico Ursella

14:40 **Session 3 NEW TOOLS AND MACHINES** *Chair Louis Denaud*

14:40 S3.1 Wood-based materials for machine components such as machine enclosures
Matthias Schneider, Thomas Stehle, André Jaquemod, Hans-Christian Moehring

14:55 S3.2 Cutting area observation coupled with dynamically compensated cutting forces to characterize the chip formation in wood peeling
Hugo Curial, Louis Denaud, Joffrey Viguier, Bertrand Marcon, Fabrice Verjat

15:10 S3.3 Exclusive finishing with DMC laser technology
Marco Venturini

15:30 **Session 4 CHIPLESS MANUFACTURING PROCESSES** *Chair Tadashi Ohtani*

15:30 S4.1 Thermally Modified Wood (TMW) with TermoVuoto method
Alessio Lucarelli, Umberto Pagnozzi

15:45 S4.2 Water repellency of wood surfaces by high-speed friction processing
Tadashi Ohtani, Ryuichi IIDA, Doppo Matsubara

16:15 **CLOSE DAY 1**

17:00 In-seminar tour
Meeting at 16.45 in front of the Basilica della Santissima Annunziata in Piazza della SS. Annunziata, 50122, Florence

20:00 CONFERENCE BANQUET
Appointment with Scaramuzzi Team Hostess at 19:45 in front of T2 Tram Stop "MORGAGNI-UNIVERSITA"
VENUE BANQUET- Associazione Progetto Villa Lorenzi,
Via Pietro Grocco, 31, 50139, Florence

08:30 Arrival

08:45 **Session 5 SENSORS AND QUALITY** *Chair Gerhard Sinn*

08:45 S5.1 Advances in robotic sanding of wooden parts
Alfredo Aguilera, Ricardo Alzugaray, Pablo Sanhueza, Eduardo Diez, Fabián Iglesias

09:00 S5.2 Deep learning approaches for the automation of lathe check detection in wood veneers
Caroline Marc, Bertrand Marcon, Louis Denaud, Stéphane Girardon

09:15 S5.3 Systematic and comprehesive quality specification and verfication for furniture industry - DIN 919, DIN 68100, VDI 3414, VDI 3415
Frieder Scholz, Adrian Riegel, Christian Kortüm

09:30 S5.4 Evaluation of the capability of poly-articulated robots for wood machining and identification of parameters correlated with surface quality in robotic wood machining
Linda Nasri, Rémi Curti, Pierre Larricq , Florent Eyma

09:45 S5.5 Influence of pinewood moisture swelling and shrinkage on robotic montage susceptibility
Maciej Sydor, Anna Jasińska, Wojciech Turbański

10:00 S5.6 Simulation of internal defect detection in logs scanned with a tilted X-ray imager
Jakub Sandak, Piotr Taube, Daniel Chuchala, Kazimierz Orlowski

10:15 S5.7 Embedded sensors in wood cutting tools State of Art and future developments
Abdou Djouadi

10:30-11:05 Coffee break

11:10 **Session 5 SENSORS AND QUALITY (continuation)** *Chair Gerhard Sinn*

11:10 S5.8 Optimization of knots assessment using laser scattering for predicting beech mechanical properties
Michela Nocetti, Giovanni Aminti, Martin Bacher, Nicola Conforto, Michele Brunetti

11:25 S.5.9 EDGE-o-SCOPE System for real-time assessment of laminated particleboard edge quality
Bartosz Pałubicki, Grzegorz Kowaluk, Martino Negri, Jakub Sandak

11:45 **Lecture and Keynote SESSION** *Chair Paola Mazzanti*

11:45 **Lecture**
Critical Speed Design of Circular Saws ***Gary Schajer***

12:15 **Keynote 6**
Driving Digital Servitization Forward ***Alessandra Benedetti***

12:40-13:25 Lunch

13:30 **Session 6 PROCESS OPTIMIZATION** *Chair Alfredo Aguilera*

13:30 S6.1 Efficient timber construction production: process integration and cyber-physical systems for batch size one manufacturing
Stefan Andreas Böhm, Daniel Schulz, Sebastian Bitzan, Lucas Heider, Lars Jonas, Fabian Riß

13:45	S6.2	Autoencoder-based anomaly detection in wood machining for quality assurance and process monitoring ***André Jaquemod, Kamil Güzel, Hans-Christian Moehring***
14:00	S6.3	Attempts at controlling the size of Japanese cedar chip by adjusting cutting conditions of a disc chipper ***Yosuke Matsuda, Yukari Matsumura, Takashi Yanagida, Kiyohiko Fujimoto***
14:15	S6.4	Steam softening for solid wood bending, focussing on dry, kiln dried or pre-bend lumber ***Otto Eggert***
14:30	S6.5	High volume semi automatized on-site production of sustainable refugee shelters ***Adrian Riegel***
14:45	S6.6	Effect of tool wear and wood species on surface quality and finger-joint performance ***Julie Cool, Shiqing Li, William Nkeuwa***
15:00	S6.7	How digital printing technology can optimize the wood-based element finishing process ***Lorenzo Melloni***
15:15	S6.8	A case study on acoustic anomaly detection for a wood planing machine dataset ***Anthony Deschênes, Rémi Georges, Cem Subakan, Michael Morin***
15:30-16:05		Coffee break
16:10		**Session 7 ENVIRONMENTAL AND MARKET ISSUES** ***Chair Daniel Chuchala***
16:10	S7.1	Assessing the impact of machining processes on industrial wood packaging: an LCA-based approach ***Giulia Cortina, Giacomo Goli, Viola Arena, Lisa Bernacchi, Massimo Delogu***
16:25	S7.2	Influence of wood chip moisture content on the environmental impact of a biomass boiler of a sawmill drying plant in Veneto ***Annalisa Magnabosco, Martina Boschiero, Michela Zanetti***
16:40	S7.3	Wood traceability along the whole value chain: exaggeration or obligation ***Gianni Picchi, Antonio Ruano, Simon Stegel, Jana Hmeljak, Bengt Sörvik, Mari Selkimäki, Heli Kymäläinen, Blas Mola, Enrico Ursella, Gennaro Azzollini, Johan Ekenstedt, Garret Mullooly, Alejandro Poveda, Silvia Melegari, Ryszard Sandak, Cuauhtli Campos Mijangos, Jakub Sandak***
17:00		Closing remarks and prizes ***Giacomo Goli and Gary Schajer***
17:15		END of the scientific part of the conference

The conference will continue with a post seminar tour on April 16 and 17 only for the one who booked in advance.
Departure on 16th April 2025 at 7:40 from Piazzale Montelungo, 50129, Florence.
Return to the same place on 17th April 2025 at dinner time.

POSTERS

P1	Shear cutting in fiber direction of several wood species ***Marcus Herzberg, Christian Korn, Mathias Stirn, Christian Gottlöber, Julius Hausmann, Julius Hausmann***
P2	Effect of sawing and drying processes on bow and crook of dimension lumber from large-diameter sugi (Cryptomeria japonica) logs ***Yukari Matsumura, Yosuke Matsuda, Kana Yamashita, Erina Kojima, Hideo Kato, Hirofumi Ido, Yuji Ikami***
P3	Modern feed systems for optimizing cross-cut saws ***Kazimierz Orlowski, Wojciech Blacharski, Daniel Chuchala, Przemyslaw Dudek, Jakub Sandak, Gerhard Sinn***
P4	Effects of the lubricant in high-speed friction processing ***Ryuichi IIDA, Tadashi Ohtani***
P5	Influence of pre-treatments on the machining processes of softwood and hardwood and evaluation of surface roughness ***Paola Cetera, Jarno Bontadi, Mario Marra, Martino Negri***
P6	Effect of wood properties on warp of lumber sawn from large-diameter sugi (Cryptomeria japonica) logs ***Kana Yamashita , Yukari Matsumura , Yosuke Matsuda, Miyuki Matsuo-Ueda, Masato Yoshida, Hiroyuki Yamamoto***
P7	Effect of Wood Surface Brushing on Delamination Resistance of Glue-Laminated Timber ***Drago Pregl, Tomaž Petrun, Ambrož Ahec, Edit Földvári-Nagy , Ryszard Sandak, Andreja Kutnar, Jakub Sandak***
P8	Early wood quality assessment for a better use of the forest resource. The DigiMedFor project ***Michela Nocetti, Giovanni Aminti, Michele Brunetti, Giovanni Fontani, Simo Kivimaki, Timo Rouvinen, Luigi Saulino***

Meeting Proceedings of the 26th International Wood Machining Seminar

14-15 April 2025
Firenze

EDITORS

Francesco Buonamici, Giacomo Goli, Jakub Sandak, Gary Schajer, Michela Zanetti

INTERNATIONAL ADVISORY BOARD

Prof. Gary Schajer - Canada (Chair)
Dr. Magnus Fredriksson - Sweden
Dr. Kiyohiko Fujimoto - Japan
Dr. Christian Gottlöber - Germany
Prof. Christian Kortuem - Germany
Prof. Nobuaki Hattori - Japan
Prof. Roger Hernandez - Canada
Dr. Kohji Murata - Japan
Prof. Kazimierz Orlowski - Poland
Prof. Jega Ratnasingam - Malaysia
Dr. Jakub Sandak - Slovenia
Dr. Darrell Wong - Canada

ORGANISING COMMITTEE

Prof. Giacomo Goli, Firenze University, DAGRI, Italy – Chair
Dr. Franco Bulian – CATAS, Italy
Dr. Francesco Buonamici – Firenze University, DIEF, Italy
Dr. Jarno Bontadi, CNR IBE, Italy
Dr. Michele Brunetti, CNR IBE, Italy
Prof. Gianni Campatelli, Firenze University, DIEF, Italy
Ing. Dario Corbetta – ACIMALL, Italy
Prof. Massimo Delogu - Firenze University, DIEF, Italy
Prof. Rocco Furferi - Firenze University, DIEF, Italy
Dr. Paola Mazzanti, Firenze University, DAGRI, Italy
Prof. Andrea Laschi. Palermo University, SAAF, Italy
Dr. Martino Negri, CNR IBE, Italy
Dr. Jakub Sandak, InnoRenew CoE, Slovenia
Prof. Michela Zanetti, Padova University, TESAF, Italy

These Proceedings of the
26th International Wood Machining Seminar
are dedicated to the memory of

Dr. Ryszard Szymani

21 August 1939 – 4 September 2024

It is with great sadness that we announce the passing of Dr. Ryszard Szymani, a major pillar of the wood machining research community. His many contributions to the International Wood Machining Seminars go back almost to the start and he served as Director for the Seventh Seminar in 1982, and as Chair and Host of the 15th Seminar in 2001. He had attended and spoken at almost every meeting, most recently as the keynote speaker at the 24th Seminar in 2019.

Ryszard Szymani was born in Poland and earned a Masters degree in Wood Technology at the College of Agriculture in Poznan. In a daring exploit he escaped across the then closed border, eventually making his way to North America, where he earned a further Masters degree at UBC in Canada and a PhD at UC Berkeley in California. He went on to be an Assistant Professor at Oregon State University, a Project Leader at the UC Forest Products Lab and a Research Scientist at the California Cedar Products Company. In parallel with this work, he established the Wood Machining Institute in 1984, within which he organized the highly successful SawTech and ScanTech series of conferences. He was also the Technical Program Chair for the first seven of the International Conferences on Scanning Technology and Process Optimization in the Wood Products Industry, and over the years he gave almost 30 two-day industrial Workshops on Design, Operation and Maintenance of Saws and Knives. His work at the Wood Machining Institute, notably the 35-year run of the bimonthly newsletter *Wood Machining News*, together with the over 80 technical papers on wood machining and related subjects that he wrote, created a major technical resource for the entire wood machining research community.

Above all, Ryszard Szymani was a kind, generous and sincere man, and the IWMS community deeply mourns his passing. We have all been enlarged by our association with him.

Gary Schajer
Chair, IWMS International Advisory Committee

Welcome to IWMS-26
from the IWMS International Advisory Committee

On behalf of the IWMS International Advisory Committee, it is my pleasure to welcome you to the 26th International Wood Machining Seminar. I hope that you will have a memorable and productive time. The International Wood Machining Seminars have a long history dating back to 1963, and during that time have become the pre-eminent forum to present and discuss the latest research and advances in wood processing technology. Most significantly, they have also become a central place to meet and interact with other researchers from around the world, a big fraction of whom are long-time attendees. The resulting close social atmosphere is a distinguishing characteristic of the Seminars, one of which we are particularly proud and work hard to maintain. Our meeting this year is in Florence, a city world-famous for its rich cultural history and beauty, we are very excited to be able to meet within such a spectacular environment. A great thank you to Professor Goli and his colleagues at DAGRI for hosting the meeting and for making such wonderful arrangements for us.

I wish you every success at IWMS-26. Welcome!

Gary S. Schajer
Chair, IWMS International Advisory Committee

Welcome to IWMS-26
from the IWMS Organizing Committee

The 26th International Wood Machining Seminar, being held in Florence this year, will bring together over 70 participants from more than 10 countries, demonstrating the vitality of the sector. A total of 38 contributions will be presented during the conference, divided into 6 keynotes, 1 lecture and 31 orals. 9 posters will also be exhibited and discussed during coffee breaks and lunches. The interest in the conference and the topics discussed is also demonstrated by the strong response from the industrial sector, whom both the Organising Committee and the International Advisory Board would like to thank for their fundamental contribution to the organisation of the conference. This book of proceedings is published in electronic format prior to the conference, without undergoing a peer review process, to provide participants with a guide to follow during the sessions. This book will be followed, for those authors who wish to confirm their contribution, by a peer-reviewed volume to be published in the Springer Proceedings in Materials series which will be indexed by Scopus. This will give authors the opportunity to have their work recognised in terms of bibliometric indexes, as well as giving the sector a better understanding of the impact of the conference on the scientific world. Each author is strongly encouraged to participate with a final paper in the Scopus-indexed proceedings.

We hope that you will enjoy the programme, which is full of very interesting presentations, as well as your stay in Florence, and we wish you a fruitful scientific exchange.

On behalf of the organising committee.

Giacomo Goli
Chair, IWMS Organizing Committee

Giacomo Goli

Index – Day 1

Introductive Session

Session 1

Session 2

Keynote Session

Session 3

Session 4

Index - Day 2

Session 5

Lecture and Keynote Session

Session 6

Session 7

Index – Posters

Acoustic anomaly detection for industrial planers: A case study

Anthony Deschênes[1, 5, 6][0000-0002-6670-6837], Rémi Georges[2,5][0000-0003-1226-7469], Cem Subakan[1, 3, 6][0000-0002-7593-6589] and Michael Morin[4, 5][0000-0002-1008-4303]

[1] Department of Computer Science and Software Engineering, Université Laval, QC, Canada
[2] Department of Wood and Forest Sciences, Université Laval, QC, Canada
[3] Department of Computer Science and Software Engineering, Concordia University, QC, Canada
[4] Department of Operations and Decision Systems, Université Laval, QC, Canada
[5] FORAC Research Consortium, QC, Canada
[6] Mila-Quebec AI Institute, QC, Canada

Abstract. The shortage of skilled labor is a growing issue facing the Canadian wood products industry. This shortage has led to a deterioration in equipment operational control and an increase in unexpected equipment breakdowns, driving up costs for companies already operating in a highly competitive market. While experienced operators are often able to identify defects or malfunctions, less experienced operators may not be able to do so as easily. One way to support less experienced operators is through acoustic monitoring. In this research project, we propose a new framework that uses microphones and deep learning models to automatically detect defects and anomalies and raise flags to assist operators. As a case study, this framework is tested on a new dataset containing the operational sounds of an industrial planer. The dataset contains labeled normal and anomalous operating sounds from real operations in a lumber planing mill. The results show that the proposed framework detects anomalous operational sounds. Using fine-tuning techniques and models from previous work, our algorithms flag most of the different anomalies. As such, our proposed approach has the potential to gain the trust of expert operators who can understand its output, but also, after further improvements, can help new operators understand the reason for the alarms raised. This approach is a step towards automating wood processing equipment and providing decision support for machine operators.

Keywords: Anomaly Detection, Deep Learning, Wood Planing, Convolutional Neural Networks, Transformer

Efficient Timber Construction: Application of Cyber-Physical Systems for Batch Size One Manufacturing

Stefan Andreas Böhm[1,3,*] , Daniel Schulz[1,2,*] , Sebastian Bitzan[3,*] , Lucas Heider[3] , Lars Jonas[3], and Fabian Riß[1]

[1] Rosenheim Technical University of Applied Sciences, Hochschulstr. 1, 83024 Rosenheim, Germany
[2] innFactory GmbH, Luitpoldstr. 9, 83022 Rosenheim, Germany
[3] holzbau.tech GmbH, Fr¨uhlingstraße 32a, 83022 Rosenheim, Germany * Equal Contributors

Abstract. The construction industry faces significant challenges, including labor shortages and the demand for sustainable, efficient building methods. Prefabrication in timber construction offers a solution, but many companies struggle with integrating more advanced and efficient technologies into their workflows. This study presents a cyberphysical system for batch size one timber element production, integrating robotics, artificial intelligence, and digital twin technology. A sixaxis articulated robot performs vertical wall panel cladding, leveraging AI-driven CAD analysis for optimized gripping positions and process reliability. The system employs deep learning-based feature recognition for enhanced process reliability and a Unity-simulated digital robot twin for precise path planning. A custom gripper and automated material supply ensure high position precision of the production materials. Combining AI, robotics, and Industry 5.0 principles enhances efficiency and sustainability in timber construction, addressing key industry challenges and paving the way for fully integrated, intelligent manufacturing workflows.

Keywords: Keywords: Wood Construction, Robotics, Process Optimization, Deep Learning, Graph Neural Networks

1 Introduction

Our society is currently facing unprecedented challenges that demand urgent and comprehensive solutions. Among these, climate change remains one of the most pressing issues. Addressing climate change requires sustainable innovations across all sectors [1]. One such sector is the construction industry, which faces the dual challenge of reducing its environmental impact while meeting the growing demand for affordable housing. This issue is particularly critical for lower- and middle-income groups, who struggle to find cost-effective living spaces, especially in high-density metropolitan areas [2]. At the same time, the construction sector is experiencing a severe shortage of skilled workers, mirroring challenges faced by many other industrial fields. As a result, conventional methods are becoming increasingly insufficient to meet housing demands. Companies increasingly integrate robotics into their operations to bridge this gap. These technologies do not simply compensate for workforce shortages – they offer transformative potential by enabling more precise, cost-effective, and scalable construction processes. Streamlining production and improving efficiency pave the way for a more sustainable, resilient, and automated construction industry [3]. However, actual progress requires more than mere automation; it demands a holistic rethinking of the construction process. Robots and humans each possess unique strengths, and an optimal system should leverage both in complementary ways. A promising approach to this is upright element fabrication, as introduced by Karatza et al. [4]. This methodology employs six-axis articulated robots (6AARs) for the sheathing of wall elements, where robots perform pick-and-place operations and directly attach panels to upright wall structures. Such tasks are physically demanding and ergonomically unsuitable for human workers but can be efficiently executed by 6AARs equipped with advanced end effectors. A key advantage of this method is its ability to facilitate simultaneous work on both sides of the wall, thereby significantly accelerating the production of multilayer timber construction walls. However, as construction processes become more complex, conventional automation solutions are no longer sufficient. Instead, cyber-physical systems (CPS) are required to seamlessly integrate digital workflows, real-world execution, and expert knowledge following the principle of Industry 5.0, which emphasizes human-centered, resilient, and sustainable manufacturing [5]. This work presents a prototype robotic application that holistically integrates key technological components: an optimized placement and gripping concept, AI-driven CAD analysis for enhanced process reliability, and a digital twin for path planning. By interconnecting these elements, the system moves beyond isolated automation and towards a more adaptive and intelligent construction workflow. The remainder of this work is structured as follows: Section 3.1 details the material supply and the robot gripping mechanism. In Section 3.2, a novel CAD analysis approach is introduced to identify suboptimal gripping points, thereby improving process reliability. Section 3.3 presents an intuitive path-planning method that leverages a digital twin for simulated robotic motion planning. Finally, the work concludes in Section 4, summarizing key findings and outlining future research directions.

2 Related Work

Intelligent robotic systems must incorporate the necessary expert knowledge to successfully execute complex tasks, which include environment analysis and position estimation. Particularly for the planking process, a comprehensive understanding of the wooden boards to be processed is required to ensure high accuracy. In addition to conventional camera-based methods widely used in practice, approaches from the literature include those based on the analysis of CAD Data.

These have the advantage that, with precise processing, the 3D models exactly correspond to the actual object and thus meet high standards. With the flexibility gained through adaptive algorithms, recent methods have mainly focused on various forms of deep learning.

For example, FeatureNet [6] successfully identifies features in 3D models in STL format by decomposing a model into so-called voxels, which are threedimensional structures that are subsequently processed with a three-dimensional convolutional neural network (CNN). A similar method, multiple sectional view net (MSVNet) [7], also based on CNNs, processes two-dimensional side views of a CAD model to classify the features contained within, determine their positions, and transfer them to the overall object. The most promising methods, however, take it a step further by analyzing CAD models with exceptionally high detail by considering all available data points and faces in the model and modeling them as a graph for processing by a graph neural network (GNN). Hierarchical CADNet [8] and attributed adjacency graph net (AAGNet) [9] follow this approach and achieve better performance than FeatureNet or MSVNet through the precise segmentation of features.

A commonality among the methods mentioned, however, is the use of synthetic data [6–9]. The otherwise labor-intensive annotation process is already performed during data generation, making the creation of a real dataset with the thousands of necessary 3D models for training practically impossible.

Besides data analysis, another key area of expertise in robotics is path planning, which heavily depends on factors like the handled material, environment, and type of robot used. As a result, reinforcement learning has gained traction in robotic control. For instance, Josifovski et al. [10] presented a robotic application where a pick-and-place task was trained in simulation using two sequential machine learning agents – one for translational movement and another for rotational control. This trained model was transferred to a real robot, making the process more efficient and autonomous.

However, even with advanced machine learning, individual CAD analysis and path planning remain only partially effective for complex tasks like wood construction assembly. Managing this complexity requires holistic approaches that integrate design and manufacturing. Building information modeling (BIM) is a key factor, a digital process for creating and managing detailed 3D building models that integrate design, construction, and operational data. Current research explores BIM and automation through two key approaches: a Designto-Manufacturing (DtM) framework [11] and BIM-supported robotic simulation for automated construction [12]. Both build on BIM to enhance designto-manufacturing interoperability but differ in methodology and technological implementation.

The DtM framework integrates BIM, computation design, robotic manufacturing, and off-site construction, enabling continuous feedback between design and production. In contrast, [12] optimize robotic assembly through a six-phase simulation strategy, particularly for timber structures. While DtM embeds manufacturing programming into the design process, [12] focus on virtual optimization. Both approaches vary in practical applications: DtM is applied in robotic 3D printing for concrete and modular timber processing using Revit, Grasshopper 3D, and Speckle Systems. Wong Chong et al. employ Webots for simulation, B-Prolog for modeling, and IKPy for kinematics, prioritizing virtual workflow optimization over direct manufacturing control [12].

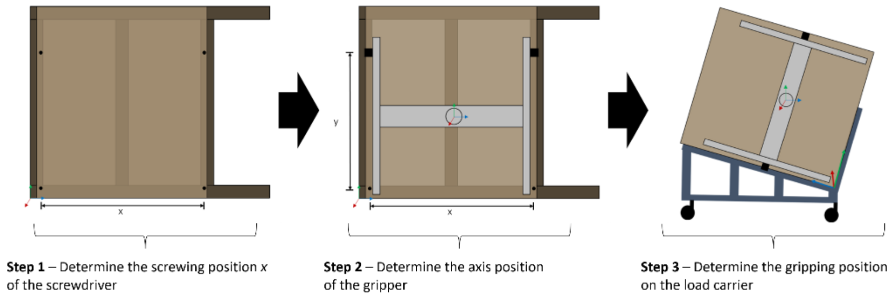

Fig. 1. Gripper alignment on wooden boards and transmission of placement to load carrier. Own representation.

3 Methodology

Building on the fundamental concepts of [4], [12], [11] this work presents a threepart holistic concept for robot-assisted wall paneling: An autonomous material supply system with mechanical centering of panel materials, an AI-based CAD analysis approach for validating the robot's pick positions, and an intuitive path planning methodology based on the Unity game engine, enabling IoT communication with the robot.

3.1 Hardware Setup

This research focuses on establishing a seamless process chain by leveraging existing technical solutions and introducing strategic innovations to integrate the 6AARs into production efficiently and reliably. The primary objective is to develop a user-friendly, low-threshold batch-size-one production system. The workflow and required hardware have been clearly defined and implemented in a prototypical demonstrator at Rosenheim Technical University of Applied Sciences. A specialized load carrier and a custom gripper were developed to handle wooden panels. The panel material, pre-cut in an earlier processing step, is placed onto the load carrier. The load carrier also secures the loaded wooden panels through an inclined support surface, which uses gravity to hold the panel materials at a central point. Afterward, the load carrier is transported by an autonomous guided vehicle (AGV) to a designated position within the robot cell. The robot uses the custom-built gripper to attach the panels to a standing timber frame wall.

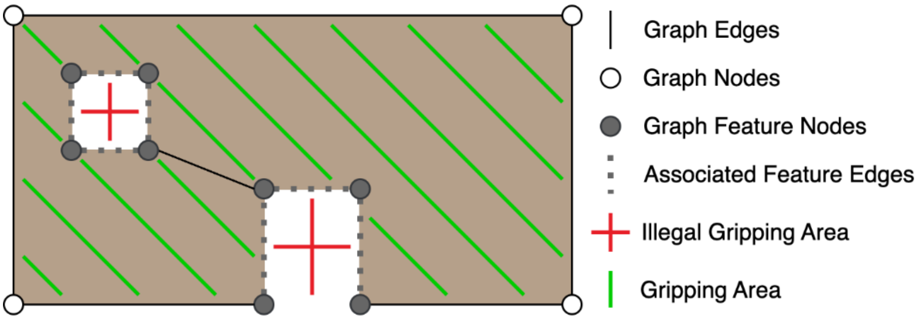

Fig. 2. Simplified result of the 3D model analysis procedure. Nodes (vertices) and edges in an STL file are classified into features, then segmented, and finally, the gripping area is derived. Own representation.

The gripper was designed to grasp plates from 300 mm × 150 mm to 1250 mm × 2000 mm, or up to 3800 mm in actual operation, and attach them to a vertically standing wall. The gripper axes can move in the X-direction depending on the width of the plates to be gripped. Along these axes, screwing units move in the X-direction. This allows the plates to be screwed onto the framing of the wall. The gripper concept consists of three key steps, as illustrated in Figure 1. First, screw positions are determined based on the stud locations where fasteners will be placed. Since the screw units are fixed to the suction bars along the X-axis, their spacing directly corresponds to the spacing of the suction bars. Additionally, the screw units can move along the Y-axis, enabling complete fastening of the panels without repositioning the gripper. In the final step, the gripper's precise gripping position on the load carrier is determined, ensuring optimal alignment of the suction bars for accurate handling. A programmable logic controller (PLC) performs all calculations for this process and ensures the robot's safe operation. The PLC continuously synchronizes with digital twin control systems, optimizing and automating the production chain for increased efficiency and reliability.

3.2 Data preparation

A feature recognition system ensures that the calculated gripping positions on the PLC do not intersect with potential voids in the wooden panels to enhance process reliability. The presented process includes an individual check of the panel materials' CAD data. These data are then compared with the machine data from the preceding processes for validation.

For that, we adapt the state-of-the-art by utilizing deep learning-based methods and present a methodology that enables the creation of a compact, essential description of the wooden boards used in the process by classifying each node in a 3D model of a board into well-defined features. The foundation of this approach is the dynamic graph CNN (DGCNN) [13], a GNN designed to capture relationships between the vertices in CAD data, which delivers more accurate results due to node-level classification compared to image-based processing in MSVNet or voxel-based processing in FeatureNet. The classified points of the 3D model are subsequently merged into segments based on the edges defined in the model to derive both potentially faulty and correct gripper positions as depicted in Figure 2. Our method allows decision-making within seconds to keep the cycle time low for productive operation. Depending on the application, it is evaluated for accuracy using real CAD data.

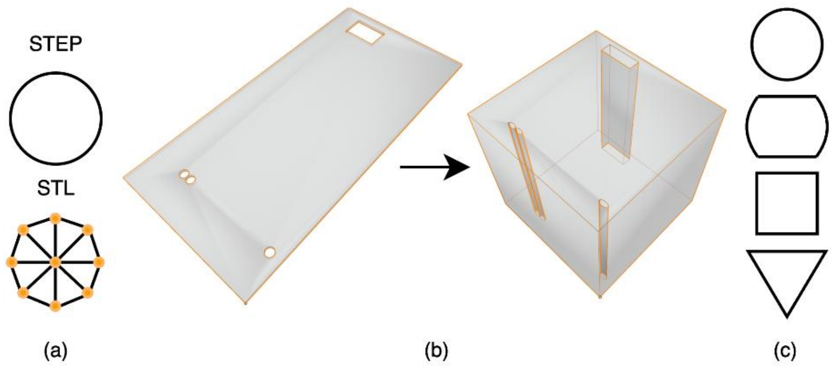

Fig. 3. Simplified surface in a STEP file and its graph representation in a converted STL file (a), normalization process applied to a wooden board (b) and excerpt of basic shapes used for dataset generation (c). Own representation.

The STEP file format, which contains complex surface information such as roundings, interfaces the timber construction software for designing components and the analysis method. While other methods utilize this surface information through elaborate preprocessing for segmentation [8, 9], our approach is based on the classification of vertices in a 3D model, necessitating conversion to a different file format. STL is beneficial in this context, as it can serve directly as input for GNNs without an elaborate modeling process since 3D models in this format are defined solely as vertices with linear relationships to each other, as shown in Figure 3 (a). Accuracy losses in the conversion process can be neglected, as they are too small in relation to the gripper size to affect position determination. In addition to the conversion to the STL file format, scaling is also performed as a normalization operation to an arbitrary but uniform value range of 10 × 10 × 10 mm to facilitate learning the contained features for objects of different sizes. This reversible step allows detected features to be transferred back to the board's original state. After this operation, the scaled wooden boards resemble a cubic shape. Figure 3 (b) depicts this normalization process for a usual wooden board.

In addition to preprocessing CAD data for productive use, training data is required for a GNN to learn features. In the case of node classification, each vertice must be assigned a class, which is very labor-intensive for accurate, complex 3D models without automation. Furthermore, several thousand 3D models are needed for training to ensure generalization to unseen models in productive use, which is practically impossible to achieve given potentially changing requirements in operation. Additionally, datasets like [6] are not diverse enough for our application, so we decided to develop a unique generator for synthetic CAD data that cannot be distinguished from real data in simple wooden boards with cutouts. The starting point for the data generator is the open-source software Blender and its Python programming interface for execution without human interaction, with which thousands of 3D models in STL format can be created and annotated within a few hours. The basis for generating each synthetic model is a cube with dimensions of 10 × 10 × 10 mm, to which random boolean operations for subtracting features and simulating drilling and milling operations are applied on various sides and positions. The points created by subtraction are automatically captured and assigned to the features, serving as ground truth for the subsequent learning process. The features serve as input to the data generator in the form of 3D models in STL format, can be extruded from simple shapes, shown in Figure 3 (c), and are defined according to the application, offering more flexible use cases for different production processes. Finally, our dataset generator also supports intersecting features, simulating more complex cutouts in wooden construction.

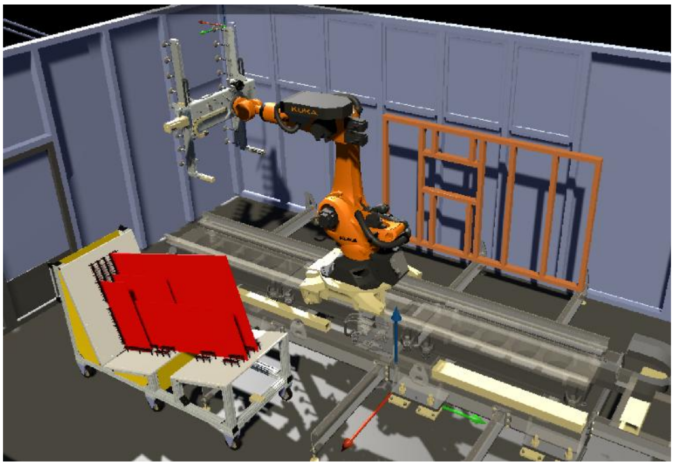

Fig. 4. Virtual environment based on a digital twin, including the robot on a linear axis, the custom load carrier equipped with wooden boards, and the target frame for the sheathing process. Own representation.

3.3 Cyber-physical Manufacturing process

In a preliminary BIM process, all necessary machine data is generated for the Pick & Place application in the sheathing process. The available CAD wall data is revalidated using the CAD analysis framework to ensure additional process stability as described in Section 3.2. The BIM data, including process information such as cutting and sorting instructions for the required panel materials, is converted and provided in a standardized JSON file created during the preliminary BIM process.

The necessary sheathing process information is imported from this JSON file into a digital twin of the real robot. The JSON file contains information about each wooden panel, such as its dimensions and Pick & Place information. This data foundation enables the calculation of gripper and screw positioning in the digital twin, allowing for quick and flexible adaptation to different panel formats. The digital twin depicted in Figure 4 processes the described data and was created using the Unity game engine. Unity allows for developing a highly accurate 3D digital replica of the robot. This digital environment is essential for simulating the path-planning process, which later serves as the controller for the robot's control system.

The control system is managed through Unity's realvirtual.io plugin [14], which utilizes inverse kinematics for robot path planning. An OPC UA interface between the robot controller and Unity ensures that all robot-relevant parameters are correctly transmitted and processed. Motion data from Unity is sent via OPC UA to the programmable logic controller, which controls the gripper motors, robot axes, and the robot's movement along the linear axis. Simultaneously, the PLC transmits the current position values back to Unity.

Communication with the KUKA controller is handled via EtherCAT, ensuring precise synchronization between the digital twin and the physical system. The sheathing process consists of several steps: first, a panel is picked up from the load carrier, then transported by the robot to its designated wall position, where it is fastened at the predefined screw points.

4 Conclusion

BIM-based manufacturing processes are beneficial in a circular economy, as they provide the best opportunity to plan dismantling and repurposing processes systematically. Given current technological trends, CAD data such as STEP, STL, or wood-construction-specific IFC files are expected to remain readable even in 100 years, ensuring long-term accessibility of information regarding the original construction of buildings. This knowledge will be essential for efficient deconstruction and resource recovery. A BIM-to-Machine approach, as outlined in the state of research, represents the most desirable long-term solution because it follows precisely the CAD introduction. The approach presented here, which combines CAD/CAM and digital twin technology, is both future-proof and readily implementable due to its low technical barriers. Moreover, integrating AI-based methods already offers significant advantages in quality assurance, further enhancing the efficiency and reliability of these processes.

Acknowledgement. This work was funded by the Bavarian State Ministry of Economic Affairs, Regional Development, and Energy as part of the Bavarian Joint Funding Program (BayVFP).

References

1. Niu, Y., Rasi, K., Hughes, M., Halme, M., Fink, G.A.: Prolonging life cycles of construction materials and combating climate change by cascading: The case of reusing timber in Finland. In: Elsevier, Resources, Conservation and Recycling, Volume 170 (2021).
2. Colomb, C., Gallent, N.: Post-COVID-19 mobilities and the housing crisis in European urban and rural destinations. Policy challenges and research agenda. In: Planning Practice & Research, Volume 37, Taylor & Francis (2022).
3. Xiao, B., Chen C., Xianfei Y.: Recent advancements of robotics in construction. In: Automation in Construction, Volume 144, 104591 (2022).

4. Karatza, N.: Development of a compact flexible manufacturing cell for producing timber frame elements. In: Proceedings of the 24th International Wood Machining Seminar (2019).
5. Breque, M., De Nul, L., Petridis, A.: Industry 5.0: towards a sustainable, humancentric and resilient European industry. In: Luxembourg, LU: European Commission, Directorate-General for Research and Innovation (2021).
6. Zhang, Z., Jaiswal, P., Rai, R.: FeatureNet: Machining feature recognition based on 3D Convolution Neural Network. In: Computer-Aided Design, pp. 12-22, Volume 101 (2018).
7. Shi, P., Qi, Q., Qin, Y., Scott, P.J., Jiang, X.: A novel learning-based feature recognition method using multiple sectional view representation. In: Journal of Intelligent Manufacturing, pp. 1291-1309, Volume 31 (2020).
8. Colligan, A.R., Robinson, T.T., Nolan, D.C., Hua, Y., Cao, W.: Hierarchical CADNet: Learning from B-Reps for Machining Feature Recognition. In: Computer-Aided Design, Volume 147, 103226 (2022).
9. Wu, H., Lei, R., Peng, Y., Gao, L.: AAGNet: A graph neural network towards multi-task machining feature recognition. In: Robotics and Computer-Integrated Manufacturing, Volume 86, 102661 (2024).
10. Josifovski, J., Auddy, S., Malmir, M., Piater, J., Knoll, A., Navarro-Guerrero, N.: Continual Domain Randomization. arXiv preprint, arXiv:2403.12193 (2024).
11. Anane, W., Iordanova, I., Ouellet-Plamondon, C.: BIM-driven computational design for robotic manufacturing in off-site construction: an integrated Design-toManufacturing (DtM) approach. In: Automation in Construction, Volume 150, 104782 (2023).
12. Chong, O. W., Zhang, J., Voyles, R. M., Min, B. C.: BIM-based simulation of construction robotics in the assembly process of wood frames. In: Automation in Construction, Volume 137, 104194 (2022).
13. Wang, Y., Sun, Y., Liu, Z., Sarma, S., Bronstein, M.M. Solomon, J.M.: Dynamic Graph CNN for Learning on Point Clouds. In: ACM Transactions on Graphics, pp. 1-12, Volume 146 (2019).
14. Liu, Y., Wang, X., Yang, K., Pan, Y., Wang, Q.: Architecture and Implementation of High-Fidelity Digital Twins for Industrial Robots. In: International Conference on Frontiers of Robotics and Software Engineering, pp. 207-214, (2023).

Shear cutting in fiber direction of several wood species

Marcus Herzberg [1[0009-0006-6881-6147]], Christian Gottlöber[2[0000-0002-6570-4151]], Christian Korn[2], Mathias Stirn[2] and Julius Hausmann[2] [[0000-0002-1355-012X]]

1 Holzpflasterwerk Böhrigen GmbH, 09661 Striegistal, Germany,
m.herzberg@holzpflaster-boehrigen.de
2 Dresden University of Technology, Institute of Natural Materials Technology, Professorship of Wood Technology and Fibre Materials Technology, 01062 Dresden, Germany,
mathias.stirn@tu-dresden.de

Abstract. Compared to the established, widely used and almost fully optimized cutting processes in woodworking, chipless cutting in the grain direction by means of punching could offer several advantages. Therefore, a new chipless cutting process in the grain direction of wood is part of a current research project at the Institute of Natural Materials Technology of Dresden University of Technology. The process development should make it possible to produce a large-format work-piece contour reproducibly, in perfect quality and suitable for the material for the use as wooden flooring.

The paper describes basically experimental tests of chipless shear cutting of native wood in fiber direction. The tests involved several indigenous wood species in different moisture contents, different widths and thicknesses. In order to determine optimal processing parameters, the cutting angle, cutting edge position and cutting speed are varied. The primary evaluation criterions for grading the quality of the shear cutting process is an exact contour fidelity and a suitable edge quality for a homogeneous surface and a uniform appearance as a wooden floor. In addition to the visual evaluation, classic force-displacement diagrams were recorded and discussed. Apart from that large deviation of the fiber course as well as wood defects as large knots and resin inclusions lead to inadequate cutting quality.

Keywords: Shear cutting, cutting angle, wooden flooring.

1 Introduction

Solid wood floor coverings are robust, timeless and suitable for many interior design applications. This also applies to so-called wood planks, in which the fiber direction is oriented vertically and the cross-section (R-T level of the wood) serves as a running surface. This achieves greater compressive strength and creates a lively appearance due to the view of the end grain or the cross-section of the wood structure. Compared to floor coverings made of petrochemical materials or which are given their appearance using digital printing processes, floor coverings made of wood paving can only be individualized for customers to a limited extent. In addition, the ability to offer large-format cross-sections or block geometries is limited by the technical wood drying process, as very large cross-sections can only be dried very slowly and are correspondingly costly and energy-intensive. These two research questions of individualization of block geometry through process development and development of a drying process are being addressed as part of a publicly funded project between the company of Holzpflasterwerk Böhrigen GmbH and the Dresden University of Technology. This article essentially describes the process development of a chipless cutting process for the exemplary production of a block geometry suitable for parquetry. The chosen process approach is based on the fiber-parallel cutting of unformatted wood slices to a finished final contour in a single process step.

2 Process approach

The overall objective of establishing a new drying process for wooden discs and carrying out their formatting in the subsequent production process makes it necessary to replace the conventional separation processes, for example by milling long squared timbers, with new ones. Accordingly, the approach of chipless cutting in the fiber direction was chosen, as all other processes would be too complicated for the handling of individual wood slices. The comparatively low process forces are a significant advantage, as the low inherent rigidity of the thin wooden slices means that no transverse forces can occur in the radial or tangential direction. In contrast to the established milling and sawing methods used in wood paving production, chipless cutting [1] uses wedge-shaped tool blades that "wedge" into the material to be processed, inducing deformations and material stresses that ultimately lead to material breakage or cracking and complete the cutting process with virtually no chip waste [2]. Among the existing sub-applications of chipless cutting, knife cutting against a rigid base or into the solid material is of particular interest and importance in the application of formatting wood paving discussed here.

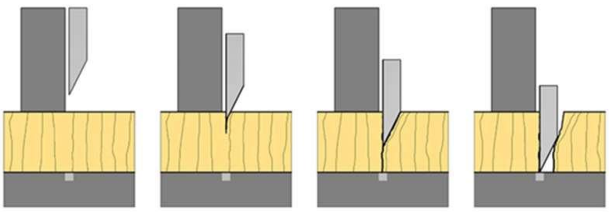

Fig. 1. Phase sections for knife-cutting in main cutting direction B according to Kivimaa [3].

When cutting with a pressure or wedge cut (see Fig. 1), a compressive stress is built up in front of the cutting edge in the cutting direction. As a result of the resulting evasive movement of the material, there is an increasing elongation of the material transverse to the compressive stress. At the wedge flanks of the cutting part (usually asymmetrical wedge design, see Fig. 1), a bending stress is also induced in the material of the workpiece as a result of this and, if the material strength is exceeded, this ultimately leads to cracking and crack propagation in the cutting direction. Depending on the workpiece material and the selected cutting direction, a pre-splitting resulting from the anatomy of the workpiece material is superimposed with the crack propagation in front of the cutting edge (main cutting direction B according to Kivimaa [3]), which follows the fiber direction. This can lead to quality restrictions on the cut surface. Compressionrelated damage to the fiber structure may also occur due to the described softening movement of the workpiece material as a result of the resulting stress. [2]

The basics of the mechanics of knife cutting are shown using the example of cutting veneer stacks by Csanady and Magoss in [4]. The cutting force Fc in the cutting direction and the cutting normal force FcN perpendicular to it (Eq. 1 and 2) act on the cutting wedge during the cutting action in the assumed working plane [5], which depend on the cutting forces to be applied in the pre-splitting direction and the pressure (normal) forces and resulting friction forces on the cutting part caused by the wedge displacement.

$$F_c = 2 * \rho * b * \sigma_c + \frac{E * h_i^2}{2 * H}(\tan\beta + \mu) \tag{1}$$

$$F_{cN} = \frac{E * h_i^2}{2 * H}(1 - \mu * \tan\beta) \tag{2}$$

In it, ρ is the radius of curvature of the cutting edge, b is the length of the engaging cutting edge, σ_c is the compressive strength in the cutting direction of the wood, E is the modulus of elasticity of the wood, hi is the deformation of the wood when the cutting edge enters, H is the thickness of the workpiece or the cutting path, β is the wedge angle of the cutting part and μ is the coefficient of friction between the cutting material and the wood.

The ratios for knife-cutting in pressure- or wedge-cutting can only be used in the case shown here for main cutting direction B for engagement ratios with large residual wood widths. For smaller residual wood widths, this dimension can also be understood as chip thickness. In this case, the ratios correspond more to the chip removal with geometrically defined cutting edges (see Fig. 1; [6]).

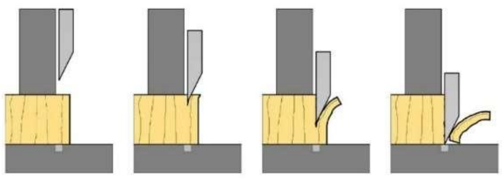

Fig. 2. Phase sections during chip removal with geometrically defined cutting edge in main cutting direction B according to Kivimaa [3].

Here, the cutting edge splits the wood in front of the cutting edge in the direction of the grain after a short compressive stress, whereby the rake face of the cutting edge then bends the resulting chip against the chip root until the permissible bending stress (bending strength) in the chip is exceeded and it is literally broken. Depending on the chip thickness and the direction of the pre-splitting (into the chip or into the resulting ideal cutting surface) as well as when the bent chip breaks, different qualities of the cut surfaceare possible. In contrast to knife-cutting in pressure- or wedge-cutting, the chip is only released shortly before the cutting part exits the workpiece.

Sitkei et al. [4, 7, 8] describe the basic mechanics of cutting in main cutting direction B. The chip is deformed on the cutting wedge surface with a certain radius. Using the equilibrium of the bending moments, it is possible to establish calculation equations forthe cutting force F_c and the cutting normal force F_{cN} (Eq. 3-5).

$$F_c = \left[2 * \rho * \sigma_c + \frac{\tan\delta'}{f(\mu,\delta)} * \frac{E}{50} * \left(\frac{h}{R}\right)^2 * h\right] * b \tag{3}$$

$$F_{cN} = \frac{1}{f(\mu,\delta)} * \frac{E}{50} * b * \left(\frac{h}{R}\right)^2 * h \tag{4}$$

$$\text{with } f(\mu,\delta) = \sin\delta * (1 - \mu * \tan\delta) + \left(\sin\delta - \frac{x_0}{R}\right) * \tan\delta * (\tan\delta + \mu) \tag{5}$$

In it, ρ is the rounding radius of the cutting edge, σc is the compressive strength in the cutting direction of the wood, δ is the cutting angle of the cutting part, μ is the coefficient of friction of the active pairing of cutting material and wood, E is the modulus of elasticity of the wood, h is the chip thickness, R is the bending radius of the chip, b is the length of the engaging cutting edge and x0 is the pre-split length. The cutting force and also the cutting surface quality can be positively influenced by using the so-called drawing cut (tool inclination angle λS > 0°).

3 Constructive Development

In order to develop a practicable process for the industrial production of wood paving, the process is first verified on a laboratory scale. For this purpose, an apparatus was developed and built that can be integrated into a universal testing machine to determine reaction and cutting forces and to assess the fracture and separation behavior (Fig. 3).

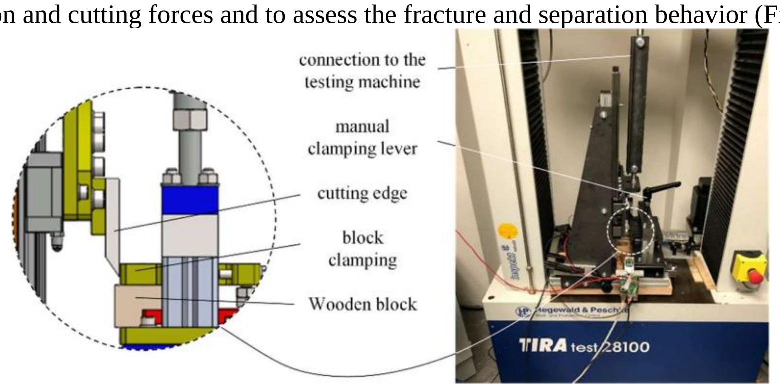

Fig. 3. Experimental apparatus: CAD model section (left) and real setup at the Institute of Natural Materials Technology of Dresden University of Technology (right).

The residual wood width has a decisive influence on the fracture mechanics when a cutting edge penetrates almost parallel to the fiber. Depending on the wood species and material properties as well as the tool geometry, arrangement and infeed, a transition from pressure and wedge cutting with large residual wood widths to chipping with small residual wood widths could be achieved. The aim of the design development is to harmonize the shape and movement of the workpiece in such a way that the cutting process, which ultimately determines the shape and geometry, is carried out as chipping with a geometrically defined cutting edge. Favorable values for the cutting angle of the cutting part δ, the cutting angle and the feed rate were determined from the evaluation of the partial factorial test plan with five realizations per factor stage, depending on the type of wood.

Fig. 4 illustrates on the one hand the different modes of material failure depending on the type of wood, the chip corner and the cutting geometry and on the other hand the resulting cutting force curves and performance requirements for the drive train of an apparatus for the production of wood paving. Furthermore, it was shown that the separating edges visible in the figure on the right had no influence on the reproducibility of the fracture behavior and that targeted crack control is not possible as hoped. Rather, the fiber orientation determines the shear and fracture behavior depending on the wood species. In summary, the fiber orientation is a very critical parameter for the resulting cut surface when shearing and cutting the test specimen.

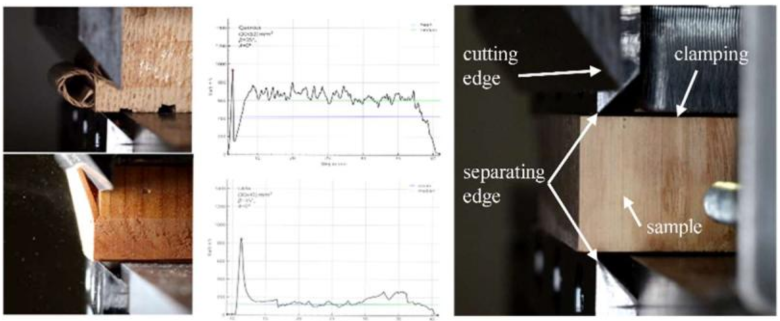

Fig. 4. Test results – example: chip development (left), force curves (center) and detail of sample clamping (right).

Observing, describing and finally explaining the chip formation is crucial for the design of the cutting process. The forming chip is deflected from the cutting plane by the translationally moved cutting wedge. The bending of the lengthening chip leads to a periodic buckling near the tip of the cutting edge without the chip being cut through. A continuous chip is formed over the entire cutting path (Fig. 4; top left). The cutting forces fluctuate over the cutting path. It can be observed how the forces increase up to the point at which a chip bends, then fall and increase again (Fig. 4; top center). In the cutting tests carried out, a fundamentally different chip formation was observed between the oak as a hardwood and the two softwoods investigated. The buckling lengths or the periodal duration at which buckling of the chip occurs was greater in the softwoods larch and spruce than in the oak. The anatomical structure of hardwoods and softwoods is seen as the cause here. The cells of the wood tissue of softwoods are generally significantly longer than those of hardwoods. Similarly, significantly different chip formation was observed at the different cutting speeds of 250 mm/min and 500 mm/min. A low cutting speed had a positive effect on the cut surface formed. It is assumed that the relaxation of stresses in the chip at low feed speeds reduces the uncontrolled splitting of the wood in front of the cutting edge.

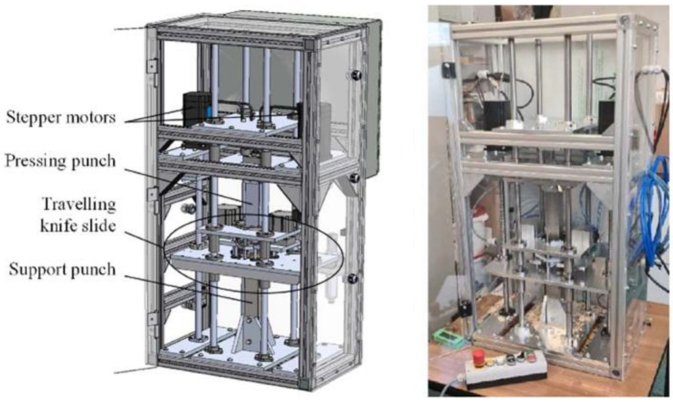

Fig. 5. Wood punching machine: CAD model (left) and real structure at the Institute of Natural Materials Technology of Dresden University of Technology (right).

A concept with multi-stage separation was developed in order to allow the highest possible inclined fiber content in an industrial process for wood paving production. Separation concepts with dynamic force application were rejected due to the unfavorable, fiber orientation-dependent fracture behavior. The developed device enables the semi-automatic production of hexagonal wood paving blocks. The machine concept provides for the simultaneous cutting of all cut edges by the feed of specifically arranged blades (Fig. 5). For the hexagonal shape, 6 blades are moved synchronously through the blank in multiple stages. Alternatively, serial processing is also possible with either a stationary workpiece and successively plunging blades or with a reversing cutting edge and respective alignment of the workpiece to the cutting line. The selected concept promises to enable low angle and length tolerances for the finished block with high output at comparatively low mechanical engineering costs.

The hexagonal cross-section is established as a wood paving shape and offers the advantage in process development that the radial and tangential proportions differ for the 6 cut surfaces, allowing the influence of the cutting direction in the individual samples to be analyzed and evaluated. In principle, the ‘travelling knife carriage’ assembly can also be modified for other cross-section geometries such as rectangles (Fig. 6). The knife carriage is driven by two NEMA 34 stepper motors with 12 Nm holding torque in closed-loop operation. With the transmission ratio of the ball screws, a feed force of approx. 12 kN is realized. The extrapolation of the required feed forces exceeds this value for knife infeeds without tool inclination. To reduce the maximum force, a tool inclination angle of $\lambda S = 10°$ is provided for the first knife stage. The wood paving block is to be preformatted in this stage. To ensure the feasibility of overlapping blades at the corners of the hexagon, a tool inclination angle of at least $\lambda S = -28°$ must be provided from the second blade stage onwards when using standard molding knives with a height of 25 mm and for hexagon spanner widths of 80 mm. The preliminary tests showed that an angle of inclination of λS =-35° significantly reduces the maximum forces for both large and small residual wood widths.

The multi-stage arrangement of parting planes enables the transition from pressure or wedge cutting with hardly predictable crack propagation in front of the cutting edge to machining with a geometrically defined cutting edge and thus a reproducible cutting plane with low shape tolerances.

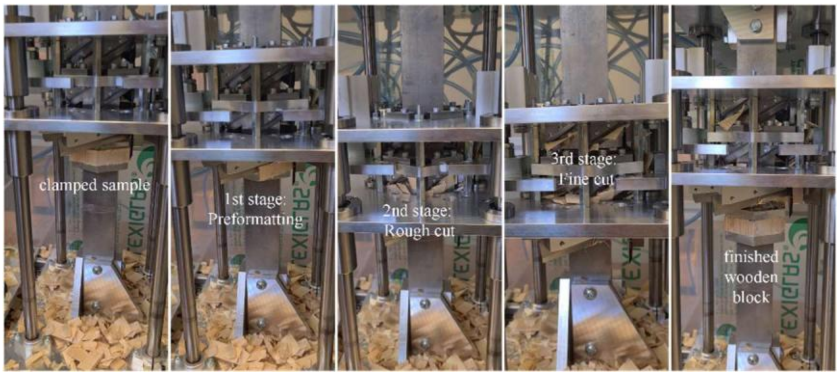

Fig. 6. Development of fracture behavior and chip characteristics over the progress of the process.

Proof of the application of the innovative separation process and thus for the production of wood paving blocks was provided as an example for softwoods (spruce, larch, Weymouth pine) and hardwoods (European oak). Depending on the type of wood and the requirements for output, tool life and required tolerances, it may be advantageous to expand to four cutting stages. A wedge angle of 25° has proven to be suitable for the first stage of preformatting. For rough and fine cutting, larger wedge angles of approx. 40° are favorable for reproducible and smooth cut surfaces.

4 Results and Discussion

The geometric quality requirements for wood paving are essentially described in [9]. Achievable accuracies are ± 1 mm in the longitudinal and transverse direction, which implies a maximum joint width of 2 mm. Geometries suitable for parquet flooring for use in flooring areas must ensure that the joint width between the individual elements is as uniform as possible. In contrast to laying classic rectangular wood flooring in an English bond, the dimensions and angles of the selected hexagonal geometry have a particular influence on the overall visual impression. As there is currently no adequate test standard for this, an optical evaluation was carried out as part of the project, which is intended to outline the practical application by measuring and simulated composition of the test samples produced.

The selected hexagonal pattern geometry is described by the side lengths and the internal angles. A conventional flatbed scanner was used to create raster graphics of both end grain surfaces with a resolution of 600 dpi, which corresponds to an image scale of 42 μm/pixel. The raw images were binarized using an adaptive thresholding method. The contours of each block geometry were then approximated using a polygon approximation (OpenCV). With this method, the detected corner points of the paving blocks are often imprecise due to small breakouts or protruding fibers. Therefore, the recognized polygon segments (side contours) were approximated by a straight line and the method of least squares was used for the adjustment calculation. In this way, the influence of breakouts and protruding fibers could be reduced. If the corner points of the hexagon are known, the side lengths and internal angles can be determined by calculation (Fig. 7; left).

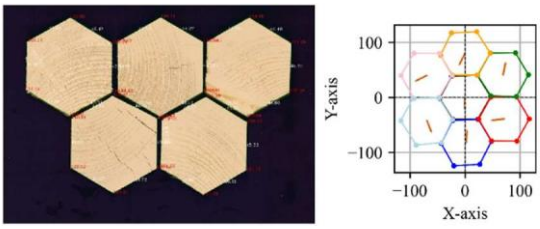

Fig. 7. Raw image of spruce blocks using a flatbed scanner and superimposed contours and measurement results of the evaluation (left) and 'flower-shaped' arrangement of hexagonal wooden blocks in an optimized, simulated arrangement without overlaps (unit of the axis values = millimeters (right))

In addition, the simulated 'flower-shaped' arrangement was used to determine an expected average joint width and end joint width (Fig. 7; right). The end joint areas in particular pose a visual problem here. When the pattern blocks are laid randomly, around 15 % of the joints have an end width greater than 1.5 mm. These joint widths are nevertheless within the geometric limits described in the standards, which could also be shown in the further analyses. Strategies for reducing the joint end widths must therefore be considered for practical application. These can be identified from both the design and process side.

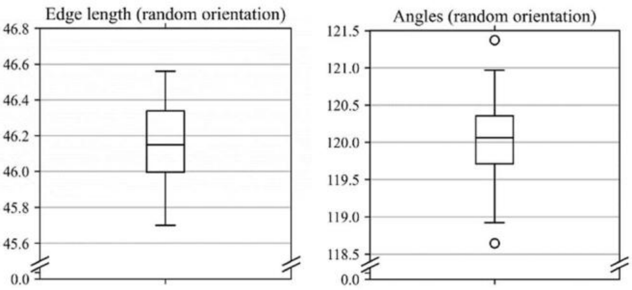

Fig. 8. Boxplot of all measured side lengths with Mean = 46.2 mm; Std = 0.5 mm (left) and inner angle with Mean = 120.0°; Std = 1.1° (right), sample size n = 120 in each case.

The hexagonal test specimens were manufactured with a target spanner width of 80 mm. This results in side lengths of approx. 46.19 mm and internal angles of 120°. The actual side lengths and internal angles were determined on 20 wood paving blocks made of spruce. Fig. 8 shows the measured side lengths and angles as box plots. The mean values are close to the ideal geometry values, which is to be expected with a closed contour, as the deviations from the mean value must cancel each other out. The distributions are almost symmetrical and are represented by normal distributions within the simulation.

5 Conclusions

As part of the project, two new processes were developed with which the conventional manufacturing process for wood paving could be significantly changed. The subprocess step described here for producing the final contour offers extensive potential for industrial implementation. The process approach and the processing quality of the sample blocks is determined by the width of the protrusion between the raw material and the final contour as well as the chip thickness. It was possible to produce parquetable blocks with sufficient accuracy. A particular challenge is the formation of a closed contour, whereby the grain direction significantly influences the quality depending on the type of wood.

References

1. DIN 8588: Manufacturing Processes Severing – Classification, Subdivision, Terms and Definitions. German standard, Beuth, Berlin (2013).
2. Kivimaa, E.: Cutting Force in Wood-Working. Dissertation, Finland's Institute of Technology, Helsinki (1950).
3. Gottlöber, C.: Cutting and Disintegration of Wood and Wood-Based Materials. In:
4. Niemz, P., Teischinger, A., Sandberg, D. (eds) Springer Handbook of Wood Science and Technology. Springer Handbooks, Springer, Cham. https://doi.org/10.1007/978-3-030-81315-4_12 (2023).
5. Csanády, E., Magoss, E.: Mechanics of Wood Machining. Springer, Cham, https://doi.org/10.1007/978-3-030-51481-5 (2020).
6. ISO 3002/1: Basic quantities in cutting and grinding – Part 1: Geometry of the active part of cutting tools — General terms, reference systems, tool and working angles, chip breakers. International standard, ISO (1982).
7. DIN 8589-0: Manufacturing processes chip removal – Part 0: General – Classification, subdivision, terms and definitions. German standard, Beuth, Berlin (2003).
8. Sitkei, G.: Fortschritte in der Theorie des Spanens von Holz. holztechnologie 24(2), 67–70 (1983).
9. Sitkei, G., Horvath, M., Gyuracz, S., Dery, J., Csanady, E. Jr.: Theorie des Spanens von Holz – Mitteilungen vom Lehrstuhl für Holzbearbeitung, Acta Facultatis Lignensis, Universität Sopron (1990).
10. DIN 68702: Wood paving. German standard, Beuth, Berlin (2017).

Chip Formation Research Using High Speed Filming, Cutting Force Measurements and Computed Tomography Scanning – a First Approach

Magnus Fredriksson[1*] [0000-0002-9182-4536], Frank Schleicher2 [0009-0001-2829-2792], Fredrik Larsson[1] [0000-0001-5280-0710], Jörgen Kajberg[1] [0000-0001-5218-396X], Yunbo Huang[1] [0000-0002-3286-2292], and Mikael Svensson[3]

*Corresponding author
[1] Luleå University of Technology, Forskargatan 1, 93187 Skellefteå, Sweden
magnus.1.fredriksson@ltu.se, fredrik.larsson@ltu.se, jorgen.kajberg@ltu.se, yunbo.huang@ltu.se
[2] RISE Research Institutes of Sweden, Laboratorgränd 2C, 93177 Skellefteå, Sweden
frank.schleicher@ri.se
[3] LSAB Sverige AB, Svinöhed 415, 77673 Långshyttan, Sweden
mikael.svensson@lsab.se

Abstract. In 2018, 4.8 million m^3 of forest material was turned to sawdust in Swedish sawmills. The difference in value-added between sawdust and main products, i.e., planks and boards, is large, while products made from sawn timber generally have a longer lifespan compared to those made from sawdust. This results in carbon storage for a longer period, contributing to climate benefits, while solid wood can be reused, whereas sawdust is usually burned. The largest loss in value-added is generated by the cutting tools that break down the logs, and thinner tools can reduce the amount of short-lived products and allow for a greater proportion of long-lived products.

Thinner cutting tools reduce the amount of chips produced but results in a sensitive process that is more easily affected by disturbances, such as those caused by chip formation and handling. To develop technical solutions, a better understanding of what happens in the cutting process and with the chips generated is needed, and therefore, new equipment is required to measure quantities that describe the cutting process and chip formation in the same conditions as in today's sawmill machines.

A preliminary study has been conducted where two measurement technologies for short-time events have been examined: High-speed filming technology and cutting force measurements using piezoelectric load cells. Together with computed tomography scanning of the work piece, a laboratory infrastructure is being constructed where we foresee possibilities to increase understanding of chip formation mechanisms, test new tool designs and increase collaboration with sawmills and the wood industry.

Keywords: Cutting mechanics, Imaging, Machining, Material properties, X-ray

1 Introduction

The wood industry is crucial for producing a wide range of products, including lumber, plywood, and engineered wood products. However, optimizing the log sawing process remains a persistent challenge, particularly in relation to chip formation during cutting. Chip formation plays a key role in determining the quality of the final wood product [1, 2, 3], the efficiency of the sawmill [4], and the amount of waste produced. Despite advances in technology, the intricate dynamics of chip generation, including the effects of cutting speed, tool geometry, and material properties, remain insufficiently understood.

This research aims to address this gap by focusing on chip formation during log sawing using high-speed filming. The primary aim is to provide real-time in-sights into the chip formation process, enabling a deeper understanding of how different cutting conditions influence chip morphology and ejection. By closely examining the behavior of wood fibers during cutting, the study seeks to develop more effective and optimized sawing methods that improve operational efficiency, reduce material waste, and enhance the quality of the final product.

The process of chip formation in wood sawing has been explored in previous research but much of this work has been based on theoretical models or low-speed observation methods [5]. While factors such as cutting speed, tool geometry, and feed rate have been extensively studied in relation to their influence on chip quality, the detailed real-time dynamics remain largely unexplored. Previous studies have highlighted the importance of controlling cutting conditions to minimize undesirable phenomena such as excessive dust, uneven chip formation, and tool wear, which can compromise the overall efficiency of the sawing process. Similar equipment to what we propose here has been used to analyze chip formation for milling cutter tools [6]. High-speed filming of chip formation when sawing wood was presented by Ekevad et al. in 2012 [7].

The objective of the first part of our method development has been to construct a laboratory equipment capable of combining high-speed filming, real time force measurements, and à priori computed tomography (CT) scanning of the wood material, to enable simultaneous studies of cutting forces and chip formation and ejection, together with detailed local material properties, tool data, and cutting data. This first part is limited to method and equipment development together with initial feasibility tests of high-speed filming and cutting force measurements on a limited material.

2 Experimental Setup, Method, and Material

The laboratory setup consists of a CNC routing machine (Hyundai-Wia F500 Plus) with three work axes and adjustable cutting parameters, including feed rate, cutting speed, and cutting depth. A high-speed camera (Vision Research - Phantom v2512) was positioned to capture detailed footage of the cutting process, with a specific focus on chip formation and ejection. The camera can capture 25 700 frames per second at 1280×800 resolution, and up to a million frames per second at lower resolution (256×32). The first version of the setup is presented in Fig. 1.

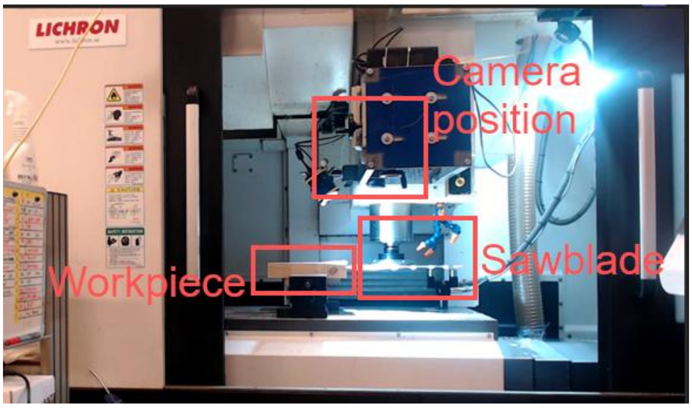

Fig. 1. Experimental setup with high-speed camera but with a simple workpiece holder, not yet including the force measurement plate.

A sawblade with a single tooth was attached to a custom holder on the spindle of the machine, Fig. 2.

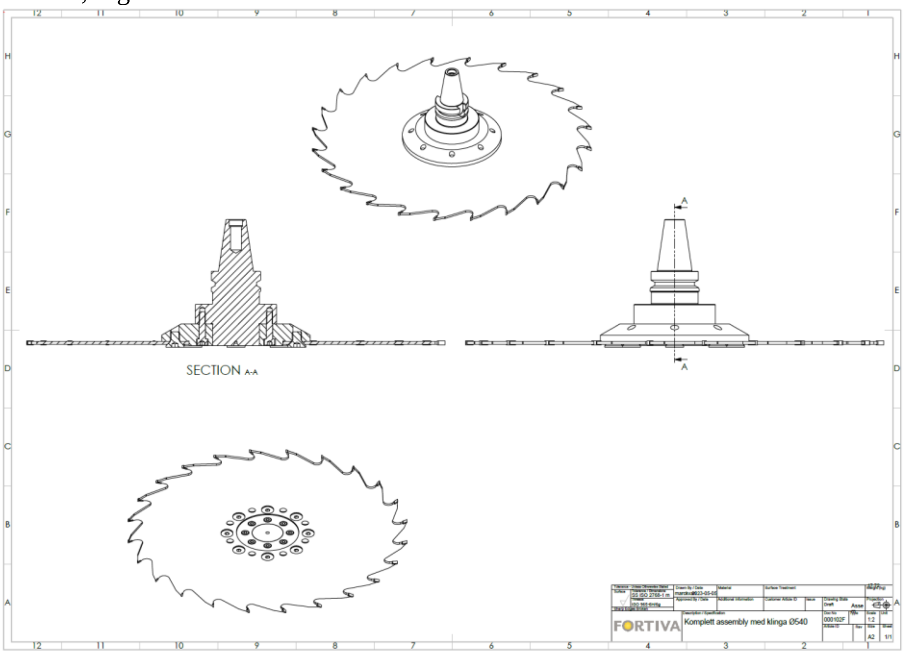

Fig. 2. Custom made tool holder for sawblade, manufactured by LSAB Sweden.

Furthermore, a force measurement plate with piezoelectric sensors (Kistler Multi-component Dynamometer, Type 9129AA) was used to mount the workpiece using custom made brackets and screws (Fig. 3). This setup allows continuous force measurements in three orthogonal directions (marked with *x*, *y* and *z* in Fig. 3) while machining the workpiece and filming the chip formation at the same time, for different cutting directions.

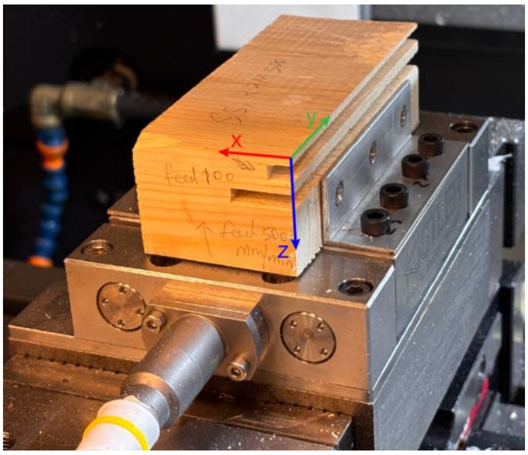

Fig. 3. Force measurement plate (below the wooden workpiece, with cable attached) fixed to the machine table and the workpiece is in turn fixed using steel brackets and screws.

The high-speed filming was performed by cutting in an open cut parallel to the top side of the workpiece, thus allowing filming of the process from above. In these tests, no force measurement was made. In total, eight pieces of dried Scots pine (*Pinus Sylvestris* L.) from northern Sweden were cut: six were up milled (feed opposite to direction of rotation) and two were down milled (feed with the direction of rotation). The cut was 60 mm wide across the feed direction, and the cut was made at a width of approximately 5 mm to ensure an open cut given the tool width of 5.5 mm. Filming was done using different resolutions (from 256×128 to 1024×400) and fps rates (60431–381818) to test the capabilities of the camera. The spatial area being filmed was 125×62 mm.

Tool and cutting data for the high-speed filming tests are presented in Table 1.

Table 1. Tool and cutting data for the high-speed filming experiments.

Quantity	Amount	Unit
Sawblade diameter	540	mm
Number of teeth	1	-
Tool width	5.5	mm
Cutting width	5	mm
Rake angle	25	degrees
Cutting speed	49.5	m/s
Feed speed	2700	mm/min
Average uncut chip thickness	0.485	mm

The force measurements were done in a separate experiment without filming, to test the feasibility of the force measurement plate. A feed speed of 100 mm/min and an rpm of 500 was used, which is lower than for the high-speed filming. The sampling frequency was 15 kHz, which resulted in approximately 0.9 mm between force measurement points. In this case, the cuts were also made somewhat differently, in close cuts instead of open cuts. The same sawblade as in the high-speed filming experiments was used. The feeding was in this case done in the *x* direction in Fig. 3, meaning that cutting was mainly done in the *y* direction. The center of the sawblade was approximately aligned with the center of the workpiece.

3 Results

Cropped still images from the high-speed filming of one of the specimens, at different positions in up milling, are presented in Fig. 4. There is a distinct difference in chip shape when cutting along the grain compared to cutting across the grain. Initial cracking and chip breakage can be seen.

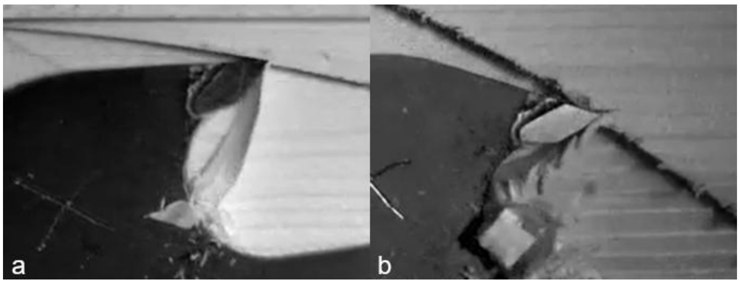

Fig. 4. Cutting the same specimen, but at different angles in relation to the general fiber direction, *a* being near tangential to the fibers and *b* showing cutting closer to a 45° angle. The spatial resolution is about 0.1 mm per pixel.

A more zoomed out image of one of the down milling specimens at higher resolution shows that it is feasible to trace individual chip particles in each frame (Fig. 5).

Fig. 5. A zoomed-out view of down milling where the chip trajectory into and inside the gullet can be seen. Individual particles can be traced in consecutive picture frames (not shown here). The spatial resolution is about 0.1 mm per pixel.

Force measurements from a single cut using the Kistler measurement plate are presented in Fig. 6. As can be seen, the force component in the *y* direction had the same sign throughout the cut, and the highest absolute value – mostly consisting of the main cutting force. The force component in the *x* direction changes sign at a point approximately in the middle of the cut. This is consistent with *x* being the feed direction and the center of the circular sawblade being aligned with the center of the work piece, so the cutting changes from down milling to up milling. The force component in the *z* direction represents side forces.

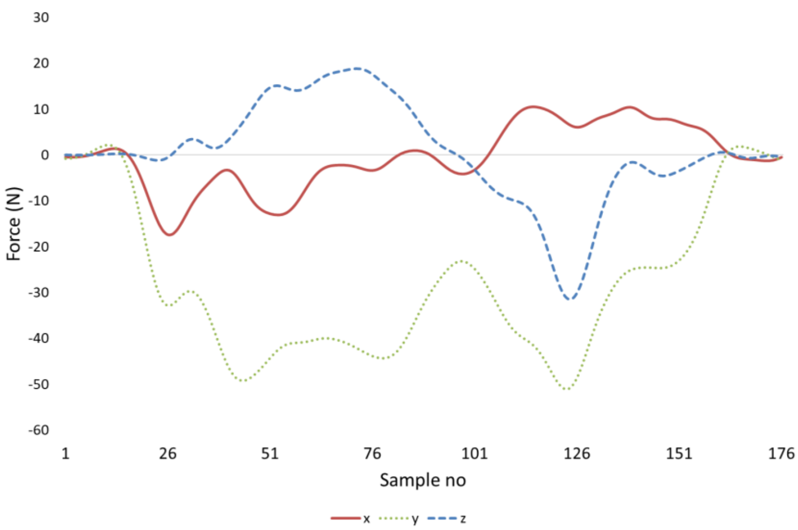

Fig. 6. Force measurements from a single cut using the force measurement plate. See Fig. 3 for definition of coordinates *x*, *y*, *z*.

4 Discussion

The experimental setup offers potentially significant insights into the dynamics of chip formation, contributing to a better understanding of how different cutting parameters influence the efficiency and precision of the sawing process. High-speed footage allows us to observe subtle details, such as the deformation of wood fibers at the cutting edge, the initial breakage of the wood surface, and the expulsion of chips from the saw blade. The chips can be traced in physical space as they are ejected.

From the high-speed footage together with force measurements, we hope to be able to identify specific factors that contribute to optimal chip formation, including the ideal cutting speed for different wood species, the effect of tool geometry on chip shape and size, and the relationship between feed rate, blade geometry, and chip ejection direction. These findings are essential for improving sawmill operations, as optimizing chip formation can lead to reduced waste, improved material recovery, and enhanced product quality.

In particular, understanding the interaction between tool geometry and wood properties will help in designing more effective saw blades that minimize waste and undesirable phenomena, such as excessive chipping, breakage, or uneven cutting forces. Additionally, the study can inform the development of automated systems that adjust cutting parameters in real time to ensure optimal chip formation during continuous sawing operations. This can be added to other optimization targets such as value recovery, product quality, energy consumption etc. in a multi objective sawing optimization.

Since a versatile CNC machine is used, it is possible to study chip formation using other types of tools and in other cutting conditions, both in sawmill applications and wood manufacturing applications.

Another potential use for the laboratory setup is to invite industry and tool manufacturers to test prototypes or investigate the effect of various settings and geometries on their machining processes.

4.1 Future work

To capture the effect of material properties, workpieces will be CT scanned before renewed cutting experiments, and density information will be used both in itself and to determine knot locations, fiber directions, and annual ring directions.

To capture a wide range of cutting conditions, experiments are planned to be conducted using different wood species and conditions, as variations in material properties (e.g., density, grain orientation, and moisture content) are expected to influence chip formation dynamics. The wood species will include mostly softwoods but also possibly hardwoods, representing a range of common materials used in the Swedish and European industry. The footage is to be analyzed frame by frame to identify patterns in chip formation, such as size, shape, and direction of ejection.

Key parameters to be investigated include:

- Cutting speed
- Feed rate
- Blade geometry
- Wood species

- Local density
- Local fiber directions
- Temperature of workpiece (e.g. sub-zero conditions)
- Moisture content of workpiece
- Cutting forces

By observing chip formation under varying conditions, the study aims to establish correlations between these factors and the resulting chip morphology. In this way prediction models for chip size, shape and trajectory can be made taking many interacting factors into account.

It is therefore necessary to spatially align the force measurements with the high-speed filming and CT data, to ensure that the correct local data (density, fiber directions, cutting forces etc.) is connected to the chip formation seen in the images. To some extent this has already been done in Huang et al. [8], but aligning the high-speed images with the other data is still work in progress.

5 Conclusion

This study presents an initial approach to investigating chip formation in wood sawing using high-speed filming, cutting force measurements, and eventually also computed tomography scanning. The developed laboratory setup enables simultaneous analysis of cutting dynamics, chip morphology, and associated forces, providing new insights into the sawing process. The preliminary results highlight significant differences in chip formation depending on cutting direction, confirming previous knowledge, but reveal the potential for optimizing sawing operations through improved tool design and cutting parameter selection.

High-speed footage demonstrates the complexity of chip formation, including fiber deformation, initial breakage, and ejection dynamics. The force measurements validate the feasibility of capturing real-time cutting forces under controlled conditions, paving the way for future studies aimed at refining cutting models and optimizing tool geometries. Furthermore, the ability to spatially align cutting forces with high-speed imaging and CT-scanned material data represents a significant future advancement in understanding the interplay between material properties and machining outcomes.

Future work will extend the study by incorporating a broader range of wood species and cutting conditions, integrating density and fiber direction data from CT scans, and refining predictive models for chip morphology, building on previous theoretical and practical work. These advancements will contribute to the development of more efficient, precise, and sustainable sawing methods, ultimately reducing waste and improving material recovery in the wood processing industry.

Acknowledgements. The authors would like to thank LSAB Sweden for their kind support with manufacturing tools and tool holders, as well as the partners of the CT WOOD research program and the Norrlandsnavet center for business development, for lending financial support for the development of the laboratory infrastructure.

References

1. Csanády, E., Magoss, E., Tolvaj, L.: Quality of machined wood surfaces (Vol. 183). Cham: Springer (2015).
2. Koc, K.H., Erdinler, E.S., Hazir, E., Öztürk, E.: Effect of CNC application parameters on wooden surface quality. Measurement 107, 12–18 (2017).
3. Gurau, L., Irle, M.: Surface roughness evaluation methods for wood products: A review. Current forestry reports 3, 119–131 (2017).
4. Nasir, V., Cool, J.: A review on wood machining: characterization, optimization, and monitoring of the sawing process. Wood Material Science & Engineering 15(1), 1–16 (2020).
5. Zhu, Z., Buck, D., Ekevad, M., Marklund, B., Guo, X., Cao, P., Zhu, N.: Cutting forces and chip formation revisited based on orthogonal cutting of Scots pine. Holzforschung 73(2), 131–138 (2019).
6. Pfeiffer, R., Collet, R., Denaud, L.E., Fromentin, G.: Analysis of chip formation mechanisms and modelling of slabber process. Wood Science and Technology 49, 41–58 (2015).
7. Ekevad, M., Marklund, B., Gren, P.: Wood-chip formation in circular saw blades studied by high-speed photography. Wood Material Science & Engineering 7(3), 115–119 (2012).
8. Huang, Y., Chuchala, D., Buck, D., Orlowski, K.A., Fredriksson, M., Svensson, M.: Analysis of the relationship between cutting forces and local structural properties of Scots pine wood aided by computed tomography. The International Journal of Advanced Manufacturing Technology 135(9), 4975–4987 (2024).

Cutting force predictions in orthogonal cutting by a foam model

Gerhard Sinn[1], Andreas Schütz[1], Daniel Chuchała[2], Kazimierz Orłowski[2] and Helga Lichtenegger[1]

[1] Inst. of Physics and Materials Science, BOKU University, Austria
[2] Faculty of Mechanical Engineering and Ship Technology, Gdansk University of Technology, Poland
gerhard.sinn@boku.ac.at

Abstract. Wood cutting can be described as an interaction between a tool and a material causing complex local deformations. This material response to loading takes place at a scale where the size of the involved process is in the range of the cell wall dimension, which makes it difficult to be described analytically, therefore, often semi-empirical or statistical models are used for modeling the process and derive cutting forces and power for the design of machines, tools and processes. Nevertheless, analytical models have the advantage of granting deeper insight into processes and interactions, where statistical or machine learning models might fail. One of these models, originally developed for metal cutting, combines fracture mechanics with strengths of materials and provided insight into the general functionality between uncut chip thickness and force per width and it is based on the material parameters strength and fracture energy combined with cutting geometry. Several publications show the suitability of this approach to the wood cutting process. Nonetheless, both material parameters require additional, specialized experiments and effort. Statistical models alternatively show strong correlation of cutting forces with density. Motivation for this work was to combine these ideas and predict strength and fracture energy by their related density using a foam model, and therefore, reduce the cutting equation to minimum set of parameters and generalize it at the same time for the prediction of cutting forces in a range of densities. Besides the theoretical work, experiments on several wood species in orthogonal cutting conditions parallel to wood grain and perpendicular were performed and showed sufficient agreement with the new scaling law.

Keywords: wood cutting, cutting model, foam.

1 Introduction

The cutting of wood accounts for a large part of wood processing technology. The first processing step is often chain-sawing and takes part already at the forest site followed by several other segmentation processes like debarking, band-sawing, circular-sawing, planing, milling, turning and even sanding to summarize some of them. All these processes were often improved by an evolutionary process of technological development.

From a scientific point of view cutting might be reduced to a process called tool-workpiece-interaction. In this kind of analysis, the material is assumed to be the stationary part, and the tool is the moving part. To describe this process several theories were developed and experiments conceived. Some of them were classified and summarized in Krenke et al. [1-3]. Among them are very simple and widely used models like that from Ettelt [4] and statistically sophisticated ones like the model of Axelsson et al. [5] or from Porankiewicz [6, 7]. The first model mentioned uses only a single parameter, the specific cutting force, the second requires 9 and the last two require 27 parameters or 21 respectively.

In this paper we will focus on the discussion of a cutting model developed by Atkins [8-10] using a classical modeling approach. In this model, chip formation is described by shearing in front of the tool, see also Franz [11] and Koch [12] on chips formation and classification by shear. The cutting model can be applied to the wood cutting process and describes a technological important, because stable cutting process where chips are produced by shear. For isotropic materials like metals, whereof the model was originally derived, it involves only four parameters, two material properties, one interaction parameter and one parameter from the geometry of cutting. The material parameters are the rigid-plastic shear yield strength τ and the specific work of surface creation R (called alternatively fracture toughness by Atkins [9], which in general has a different meaning in materials science). The interaction parameter is given by the friction coefficient μ between the separated chip and the tools rake face. The fourth parameter is the rake angle α. The shear angle, measured between cutting direction and chip shear plane, is not a constant but a response of the system.

What is still missing in the cutting model is the full implementation of wood anisotropy. Nevertheless, some attempts were made to consider the work of surface creation and yield strength in directions other than the main material axis [13, 14], e.g. influence of moisture and dynamic response to loading. Nevertheless, the model was enhanced and applied successfully to different cutting processes, like gang-sawing and circular sawing [13]. Here the study is interested in an orthogonal cutting process along the grain on different wood species and also try to reduce the parameters fracture energy and shear strength to a function of density, which would simplify cutting force predictions. To do this, wood will be described as a foam or cellular solid [15, 16], which limits our analysis to low density softwoods. The modified theoretical model will then be applied to cutting experiments performed on four soft-wood species of low density in two cutting directions.

2 Materials and Methods

2.1 Materials

Four softwood species were chosen for the experimental part of this work: Western Redcedar (Thuja plicata), Norway spruce (Picea abies), European larch (Larix decidua), and Scots pine (Pinus sylvestris). Their densities and average moisture contents are summarized in Table 1

Table 1. Densities of wood species

Wood species	raw density ρ, (kg/m³)	Oven dry density ρ_{od}, (kg/m³)	Moisture content $u \approx \frac{\rho}{\rho_{od}} - 1$, (%)
Thuja plicata	361 ± 11	346 ± 10	5,2
Picea abies	459 ± 14	444 ± 13	3,4
Pinus sylvestris	519 ± 16	496 ± 15	4,6
Larix decidua	675 ± 20	641 ± 19	5,3

2.2 Cutting experiments

Cutting experiments were performed in two directions, longitudinal 90°-0° and tangential 0°-90° on a sledge microtome at slow speed (v_c = 0.11m/s) under orthogonal cutting conditions with a tungsten carbide tool with protruding cutting edge. Cutting direction was classified according to the definition in McKenzie [17]: the first angle provides the orientation of the main cutting edge with respect to the grain orientation and the second angle provides the direction of the cutting velocity vector with respect of the grain orientation (see fig. 1a).

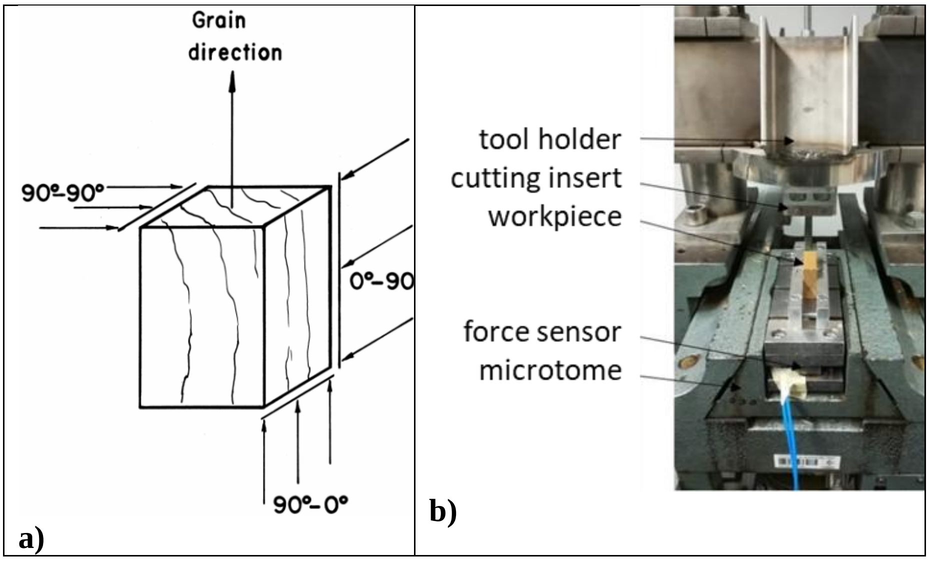

Fig. 1. a) Main cutting directions specified with respect to the grain orientation (from [17]), b) Experimental setup

Cutting forces were measured on specimens mounted on a force plate equipped with two 3d piezoelectric force sensors, model 260A01, from PCB Piezotronic Inc. While the tool is fixed, the specimen is moving with the force plate during cutting, see fig. 1b.

The rake angle was $\alpha = 20°$

2.3 Cutting model

The original cutting model from Atkins describes the cutting force composed of contributions from friction on the rake face, shear deformations in the shear plane, and specific work of surface creation. After some mathematical transformations the cutting force $\boldsymbol{F_c}$ can be rewritten in the form of equation 1 as a function of the uncut chip thickness $\boldsymbol{h_0}$ and the parameters shear strength $\boldsymbol{\tau}$, specific fracture energy $\boldsymbol{R}$, and the friction angle $\boldsymbol{\beta}$, which is calculated from friction coefficient $\boldsymbol{\mu}$ as $\mu = \tan\beta$. from the contact of the tool with the chip on the rake faces. $\boldsymbol{\gamma}$ is the strain along the shear plane and given in equation 3.

$$\frac{F_c}{w} = \frac{1}{Q}\left(\tau_y\,\gamma\,h_0 + R\right) \tag{1}$$

$$Q = \left[1 - \frac{(\sin\beta\sin\phi)}{\cos(\beta-\alpha)\cos(\phi-\alpha)}\right] \tag{2}$$

$$\gamma = \frac{\cos\alpha}{\cos(\phi-\alpha)\sin\phi} \tag{3}$$

The shear angle $\boldsymbol{\Phi}$ is a result of the cutting process and theoretically the result of minimum work assumption applied to equation 1. The shear angle is governed by the parameter $Z = \frac{R}{\tau_y h_0}$ [8].

For numerical analysis, the friction coefficient was assumed to be 0.6 and therefore the friction angle is β = 0.54. As first approximation in the linear range the shear angle can be approximated from the analysis of Merchant [18] as $\Phi = \frac{\pi}{4} - \frac{1}{2}(\beta - \alpha) = 0.69$ and Q = 0.65 resulting in a shear strain of γ = 1.57.

2.4 Cellular material or foam model

The following considerations are based on a treatise of Gibson and Ashby [15] on cellular solids. The most important parameter to describe cellular solids is the relative density, the density of the porous material normalized by the density of the material forming the cells. Kellog and Wangaard [19] provided a range of cell wall densities between ρ_s =1517 – 1529 kg/m³ for American *Pinus* and *Picea* species. The average will be used in the calculations. According to Gibson and Ashby [15] the description of a foam as cellular material works fine up to a relative density of 0.3 corresponding to a wood oven dry density of 457 kg/m³.

Table 2 Approximate equations for wood crushing strength in terms of density. Axial crushing strength: $\sigma_{ys} = 350MPa$ (table adopted from [15])

Property	Tangential	Radial	Axial
Crushing strength	$\frac{\sigma_T^*}{\sigma_{ys}} = 0.14\left(\frac{\rho^*}{\rho_s}\right)^2$	$\frac{\sigma_R^*}{\sigma_{ys}} = 0.20\left(\frac{\rho^*}{\rho_s}\right)^2$	$\frac{\sigma_A^*}{\sigma_{ys}} = 0.34\left(\frac{\rho^*}{\rho_s}\right)$

The relationships between the strength of wood and their densities are taken from table 10.5 in [15] and summarized in table 1.

For an arbitrary loading direction between axial and tangential direction, the Hankinson formula [20, 21] is used for predicting the strength, see equation 4. Analog equation is derived for the RT-direction.

$$\sigma_\Phi = \frac{\sigma_T \sigma_A}{\sigma_A \sin^2\Phi + \sigma_T \cos^2\Phi} = \sigma_{ys} \frac{0.14\left(\frac{\rho^*}{\rho_S}\right)^2}{\sin^2\Phi + 0.41\cdot\left(\frac{\rho^*}{\rho_S}\right)\cos^2\Phi} \tag{4}$$

Since the specific surface energy $\boldsymbol{R}$ is related to the energy release rate $\boldsymbol{G} = \frac{\boldsymbol{K_{IC}^2}}{\boldsymbol{E}}$ we can correlate the specific surface energy to the density. Following the arguments of Gibson and Ashby [15] fracture can occur in peeling or breaking mode. Since a sharp cutting tool defines the separation path, breaking mode of fracture should be dominant separation process. Therefore, it follows that

$$G_{cutting} \approx G_c^b\left(\frac{\rho^*}{\rho_S}\right) = 1650\left(\frac{\rho^*}{\rho_S}\right)\frac{J}{m^2} \tag{5}$$

The constant 1650 J/m² is determined from Ashby et al. [22] by the transition of peeling mode, separation of cells at the middle lamella, to breaking mode of cell walls. The transition takes place around a relative density of 0.2.

For cutting wood along the grain, it is important to summarize that the relative surface energy should scale with the density of wood, while the strength should be proportional to the square of density. This hypothesis will be checked in the following.

3 Results and discussion

3.1 0°-90° cutting

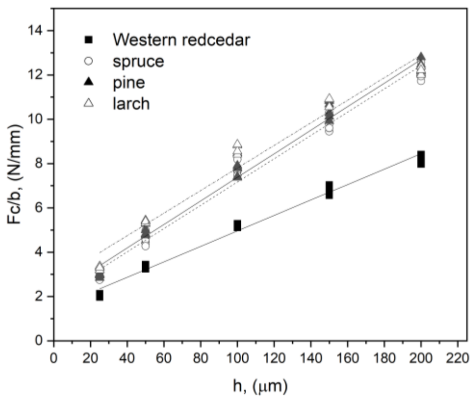

Fig. 2. Normalized *cutting forces as a function of uncut chip thickness in the 0°-90° direction*

In fig. 2 the normalized cutting force is shown as a function of the uncut chip thickness. High linearity with correlation coefficients above 0.96 were found for all four species investigated.

Taking a closer look at the influence of density on the intercept, a linear correlation of the intercept with the density was found as predicted by the cellular solid model (see fig. 3a). For the relative density of 0.2 corresponding to an absolute density of 305 kg/m³ the cellular model predicts a specific surface energy of 330 J/m², whereas the extrapolation of the experimental data to the relative density of 0.2 gives a value of R = (845 J/m²·Q) = 549 J/m², which is around 1.7-times the prediction of the model, Nevertheless the linear dependency of R from the density is represented very well from the approach. The higher experimental value of R compared to the modelled value might be attributed to the complex breaking behavior of cell wall, e.g. to turning out of microfibrils [22].

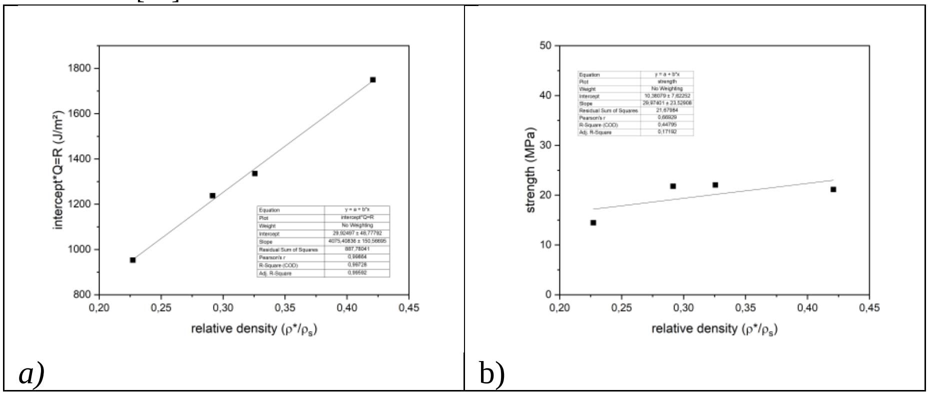

Fig. 3. a) Surface energy R in the 0°-90° direction, b) Wood strength from cutting in the 0°-90° direction

The linear correlation of wood strength (fig.3b) to density is low and statistically not significant (0.05 level). If equation 4 is linearized within the relative densities (0.23 – 0.43) we get equation 6. The function is linear increasing with relative density:

$$\sigma_{\Phi=0.69} = -9 + 61.3 \cdot \left(\frac{\rho^*}{\rho_s}\right) \qquad (6)$$

The resulting range is from 5.3 MPa to 15.11 MPa, which is lower than the experimental range, which nevertheless shows high uncertainty.

3.2 90°-0° cutting

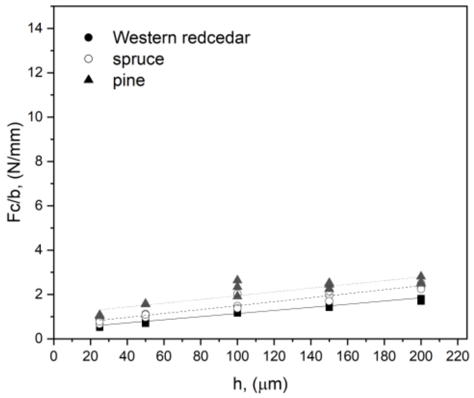

Fig. 4. Normalized cutting forces as a function of uncut chip thickness in the 90°-0° direction

Normalized cutting forces were lower by a factor of approx. 3 in the 90°-0° direction. Within the experimental range of uncut chip thickness, good linearity was observed. Nevertheless, at higher cutting depths and densities, large sample damage was observed and led to the exclusion of larch from the further analysis.

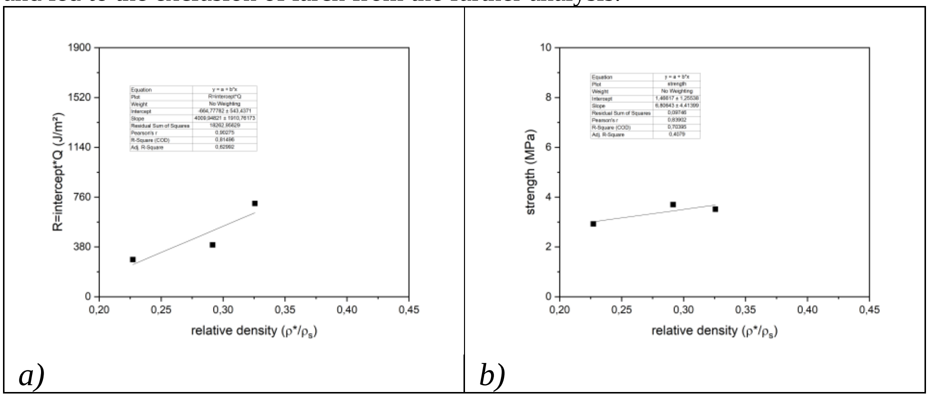

Fig. 5. a) Surface energy R in the 0°-90° direction, b) Wood strength from cutting in the 0°-90° direction

It can be seen in figure 5a that the surface energies R are much lower than those from the cutting direction analyzed first. Wood fibers are now arranged parallel to the cutting edge and can be easily separated. This observed, different behavior is not covered by the foam model since it is unable to distinguish between the two directions for R, when the sample is rotated in the working plane. In both cases the fibers are broken, and the resulting surface is the same. An indication of the observed differences behind it, might give the exclusion of larch from analysis, where severe surface damage was observed.

If separation took place at the weaker cell middle lamella in peeling mode the toughness values are expected to be lower [22] and the resulting surfaces rougher. For the peeling mode of the cell wall, Ashby et al. propose a value of G = 300 J/m², which is closer to the measured data.

Lower values were also observed for wood strength, see figure 5b, which are lower than 4 MPa. Model strength is approximately independent of orientation in the RT direction since the radial and tangential strength are very similar and scale with the square of the relative density. Linear approximation to the experimental range and adaptation to RT shear gives equation 7.

$$\sigma_{\Phi=0.69} = -6 + 37.2 \cdot \left(\frac{\rho^*}{\rho_s}\right) \tag{7}$$

The modelled range of strengths are within 2.68 MPa and 10.11 MPa and are close to the experimental values.

4 Conclusions

The cellular foam model can predict cutting forces for low density softwoods within certain limits. While the linearity of specific fracture energy R is well represented, the dependency of strength from density could not be finally judged. More samples of different densities would be necessary for analysis. Nevertheless, there are other factors which might influence the results, like anatomy or tool sharpness. Also, moisture content is not considered from the foam model and might weaken the strength.

References

1. Krenke, T., et al., Internationaler Stand zur Schnittkraftuntersuchung bei Holz - Teil 3. Holztechnologie, 2015. **56**(2): p. 43--50.
2. Krenke, T., S. Frybort, and U. Müller, Internationaler Stand zur Schnittkraftuntersuchung bei Holz - Teil 1. Holztechnologie, 2014. **55**(4): p. 39--45.
3. Krenke, T., A. Martinez-Conde Lopez, and U. Müller, Internationaler Stand zur Schnittkraftuntersuchung bei Holz - Teil 2. Holztechnologie, 2015. **56**: p. 35-44.
4. Ettelt, B. and H.-J. Gittel, Sägen, Fräsen, Hobeln, Bohren - Die Spanung von Holz und ihre Werkzeuge. 3. ed. 2004, Leinfelden-Echterdingen: DRW-Verlag.
5. Axelsson, B.O.M., Å.S. Lundberg, and J.A. Grönlund, Studies of the main cutting force at and near a cutting edge. Holz als Roh- und Werkstoff, 1993. **51**(1): p. 43-48.
6. Porankiewicz, B., et al., Main and normal cutting forces by machining wood of Pinus sylvestris. BioResources, 2011. **6**(4): p. 3687-3713.
7. Porankiewicz, B., et al., Modelling Cutting Forces using the Moduli of Elasticity in Oak Peripheral Milling. BioResources, 2021. **16**(1): p. 1424--1437.
8. Atkins, A.G., Modelling metal cutting using modem ductile fracture mechanics: quantitative explanations for some longstanding problems. International Journal of Mechanical Sciences, 2003. **45**(2): p. 373-396.
9. Atkins, A.G., Toughness and cutting: a new way of simultaneously determining ductile fracture toughness and strength. Engineering Fracture Mechanics, 2005. **72**(6): p. 849-860.
10. Atkins, T., The Science and Engineering of Cutting. 2009.

11. Franz, N.C., An analysis of the wood-cutting process, in Univ. Mich. 1958: Ann Arbor. p. 152.
12. Woodson, G.E. and P. Koch, Tool Forces and Chip Formation In Orthogonal Cutting Of Loblolly Pine. 1970, U.S. Department of Agriculture Forest Service Research Paper SO-52. p. 1-25.
13. Orlowski, K.A., et al., Application of fracture mechanics for energetic effects predictions while wood sawing. Wood Science and Technology, 2013. **47**(5): p. 949-963.
14. Orlowski, K.A., et al., Estimation of fracture toughness and shear yield stress of orthotropic materials in cutting with rotating tools. Engineering Fracture Mechanics, 2017. **178**: p. 433-444.
15. Gibson, L.J. and M.F. Ashby, Cellular Solids. 2014.
16. Gibson, L.J., Biomechanics of cellular solids. J Biomech, 2005. **38**(3): p. 377-99.
17. McKenzie, W.M., Fundamental analysis of the wood cutting process, in DEpartment of Wood Technology. 1961, University of Michigan: Michigan. p. 151.
18. Merchant, M.E., Mechanics of the Metal Cutting Process. I. Orthogonal Cutting and a Type 2 Chip. Journal of Applied Physics, 1945. **16**(5): p. 267-275.
19. Kellogg, R.M. and F.F. Wangaard, <1352-Article Text-1352-1-10-20141206-1.pdf>. Wood and Fiber Science, 1969. **3**: p. 180-204.
20. Kim, K.Y., A note on the Hankinso formula. Wood and Fiber Science, 1986. **1812**: p. 345-348.
21. Division., U.S.A.A.S.E., Investigation of crushing strength of spruce at varying angles of grain, in Air Service information circular (Aviation) ; v. 3, no. 259; McCook Field report ; Serial no. 1570. 1921: Washington, D.C.
22. Ashby, M.F., et al., The fracture and toughness of woods. Proceedings of the Royal Society of London. A. Mathematical and Physical Sciences, 1997. **398**(1815): p. 261-280.

Advances in robotic sanding of wooden parts

Fabián Iglesias[1[0000-0003-1012-8254]], Alfredo Aguilera[2], Ricardo Alzugaray[1[0009-0003-5247-4208]], Pablo Sanhueza[1] and Eduardo Diez[1[0000-0001-8456-7212]]

[1] Department of Mechanical Engineering, Universidad de La Frontera, Temuco, Chile.
[2] Instituto de Bosques y Sociedad, Universidad Austral de Chile, Valdivia, Chile.
aguilera@uach.cl, eduardo.diez@ufrontera.cl

Abstract. This work presents advances in the development of an intelligent robotic sanding system for wooden parts manufacturing, focusing on online monitoring of abrasive condition and inspecting surface quality using computer vision techniques. A sanding module equipped with an acoustic emission sensor was implemented to evaluate two abrasive conditions: abrasive loading and wear. The feasibility of using acoustic emission signals to predict sandpaper condition and optimize its replacement strategy was demonstrated. On the other hand, an inspection system based on machine vision algorithms, calibrated through confocal microscopy measurements, was developed to estimate surface roughness parameters. Additionally, the study investigates the relationship between the surface roughness and wettability of robot-sanded parts, which directly affects subsequent finishing processes such as coating, painting, and adhesive bonding. A deeper understanding of this relationship enables to achieve optimal surface characteristics for different manufacturing requirements. The results reported in this work contribute to the development of autonomous sanding cells capable of making decisions based on sensors and data processing techniques in advanced manufacturing environments.

Keywords: Robotic sanding cell, acoustic emission monitoring, surface roughness assessment, computer vision inspection, wood surface wettability.

1 Introduction

Sanding is a fundamental step in the manufacturing process of wooden parts to obtain products with a high-quality surface finish. This operation improves the appearance and texture of the parts and directly influences the performance of protective coatings [1], which add value to the product by extending its service life. Proper surface preparation by sanding is essential to ensure the adhesion of coatings [2] and to reduce defects that could compromise product quality. However, traditional sanding operations on complex parts rely heavily on subjective factors related to the operator's experience and perception of quality, which develops through their senses, increasing the variability of inspection time and product quality.

In recent decades, the increasing demand for automation in industrial processes has driven the development of robotic solutions for sanding [3]. These technologies enable robots to perform tasks with high precision and consistency, especially under repetitive conditions. Robotic systems equipped with end-tools can control critical parameters such as sanding force and tool trajectories [4], improving finish quality and reducing scrap rates. However, achieving full automation of the process remains challenging, particularly in monitoring abrasive conditions and assessing the surface quality of the finished product.

The condition of the abrasive plays a crucial role in the sanding process [5], as wear and loading directly affect process efficiency and the quality of the treated surface. The influence of grit size, sanding pressure, and cutting time on the material removal rate and acoustic emission has been previously investigated [6], showing that the progressive wear of the abrasive grains and saturation with dust reduce the cutting efficiency and limit sanding performance [7]. Although various technologies have been developed to monitor wear and loading [8], including machine vision systems, optical sensors and acoustic emission techniques, most research have focused on belt-based processes rather than rotating tools, leaving a knowledge gap that deserves to be investigated for the development of new industrial applications.

On the other hand, surface roughness, a direct result of the sanding process [9], is a critical parameter affecting the key properties of the final product, such as wettability [10]. Roughness determines the interaction of the wood surface with coatings and adhesives, influencing finish quality and product functionality. Numerous studies have explored methods for measuring surface roughness using image analysis techniques and machine learning algorithms [11]. These methods include the application of a grey-level co-occurrence matrix (GLCM) to extract textural features and train predictive models based on neural networks. However, the non-linear relationship between roughness on wettability [12] has not yet been fully understood, highlighting the need for further research in this field.

In addition, research has highlighted the influence of various factors on surface roughness and wettability, including abrasive grit size, surface heat treatment and ambient conditions. These findings have shown that the surface properties of wood and wood-based products are highly dependent on the characteristics of the material being processed and the parameters of the sanding operation. Therefore, modelling and optimising sanding operations require a holistic approach that accounts for the inherent complexity of these materials and the physical interaction between the abrasive and the surface.

In this context, this paper reports advancements in robotic sanding technology, focusing on two key aspects: online monitoring of abrasive condition, specifically grain wear and abrasive loading, surface roughness inspection through machine vision techniques. In addition, this study explores the relationship between surface roughness and wettability of wood, providing a scientific basis for improving the efficiency and predictability of the sanding process in industrial applications.

2 Robotic sanding system

In recent years, interest in the robotisation of industrial processes has grown considerably, and the high-value-added wood manufacturing sector has been no exception. Industrial robots, mainly used in handling and palletising tasks, are increasingly integrated into processes with higher level of complexity by means of advanced sensorisation techniques or even in processes that require direct interaction with operators through collaborative robotics. Today's robotics technology enables to develop operations involving complex movements, such as sanding parts with curved geometries, improving product quality with more uniform production rates while minimizing operator exposure to repetitive and hazardous tasks. However, although a large number of terminal tool-type sanding solutions are available on the market, their implementation only replaces the manipulation capabilities of the operator, providing much lower levels of autonomy and flexibility than manual sanding, where the operator not only controls the sanding tool but also makes critical decisions for the process, such as assessing the condition of the abrasive and inspecting the surface quality of the part being sanded.

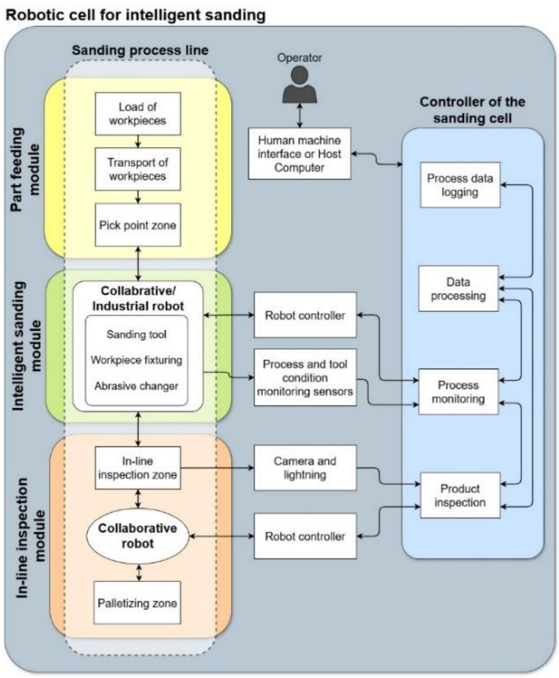

Fig. 1. Schematic of the intelligent sanding cell.

This work presents advancements in the development of intelligent robotic sanding systems designed to improve the level of autonomy of robots in the finishing operations of wood and wood-based product manufacturing. To this end, a robotic sanding cell is being developed, consisting of two modules interacting with an industrial controller to conduct sanding and inspection operations autonomously (Figure 1). The first module, called intelligent sanding, consists of a collaborative robot equipped with a custom-designed sanding tool. The tool is driven by a servomotor, which enables precise control of the sanding speed and online monitoring of the motor current consumption. This measurement indicates the level of mechanical solicitation on the tool and is transmitted to the cell controller to evaluate the performance of the process. For example, sanding harder woods or using coarser grits increases the tool solicitation. The intelligent sanding module includes an acoustic emission sensor close to the sanding area, allowing the controller to monitor the abrasive condition in real time and determine its suitability for further processing. In addition, the cell has an intelligent inspection module equipped with a camera that assess the surface condition of parts using machine vision techniques. This module gives the cell the ability to objectively estimate the surface quality by quantifying the roughness of the part and identifying wood attributes such as knots, cracks or sanding marks, which can be reprocessed by the cell if necessary.

3 Tool condition monitoring

The intelligent sanding module monitors the evolution of the abrasive condition to determine the optimal point for replacement or reconditioning. Unlike conventional systems, which rely on cutting time or the operator experience, the system proposed in this work allows the robot to automatically estimate the condition of the sanding element by measuring and analysing indirect process variables, which provides insights on the development of the operation.

For this purpose, amplitude parameters extracted from the acoustic emission signal are monitored, as this magnitude has proven to be a descriptor variable in machining processes due to its sensitivity to phenomena related to the interaction between the abrasive element and the surface being processed.

Abrasive degradation is a progressive phenomenon that depends on the operating conditions of the process, mainly on the sanding pressure, feed rate and tool rotation speed, as well as on the properties of both the abrasive and the work material. Since sandpaper can degrade through various mechanisms, this work analyses two of its main failure modes: abrasive wear and loading, the latter caused by the accumulation of sanding dust particles between the grains.

3.1 Acoustic emission measurement chain

Regarding the measurement chain, the acoustic emission is measured with a Kistler 8152C piezoelectric transducer and a Kistler 5125C conditioning unit. This system provides an analogue output signal extending over the frequency range from 50 to 400 kHz. The transducer is rigidly mounted to the fixture that holds the workpiece, ensuring a direct transmission path between the transducer and the excitation source.

Data acquisition is performed by an NI PXIe-1062Q platform equipped with the NI PXI-6132 card, a dedicated device for measuring high-frequency signals. This system operates at a sampling rate of 2 MHz, which allows accurate recording of the acoustic emission signal.

In addition, the mass of specimens is recorded at regular intervals during the sanding process to evaluate the effectiveness of the abrasive using the material removal rate.

3.2 Abrasive condition estimation results

To validate the monitoring system, an experiment was designed to analyse the acoustic emission response during the sanding of solid oak (*Nothofagus obliqua*) panels under varying wear and loading conditions. The operating conditions in both tests are identical, with a sanding disc rotation speed of 3000 min^{-1}, a feed rate of 10 mm/s and a normal sanding force of 10 N. Regarding sanding grit, P150 sandpaper is used for the saturation tests and P220 sandpaper for the wear tests.

The results shown in Figure 2(A) indicate that the acoustic emission is sensitive to changes in the loading of the abrasive element. As dust particles accumulate on the abrasive surface, the acoustic emission activity decreases due to the reduction of the active cutting profile, caused by the clogging of the dust evacuation channels. This trend is verified by the material removal rate measurements presented in Figure 2(B) and by visual inspection of the abrasive element in both fresh and clogged conditions, as shown in Figure 2(C). Therefore, this characteristic can be used as a criterion to determine the optimal time for reconditioning the abrasive element, and extending its service life.

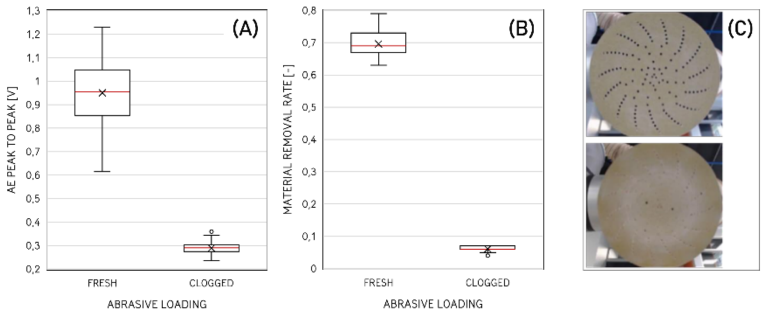

Fig. 2. Comparison of the abrasive response as a function of the loading condition: (A) acoustic emission, (B) material removal rate and (C) visual inspection of the sandpaper in both fresh and clogged state.

On the other hand, Figure 3(A) shows the evolution of the acoustic emission for three states of wear of the abrasive element: fresh, partially worn and severe wear. In the fresh condition, the abrasive exhibits high acoustic emission activity due to a high material removal rate, which is attributed to well-defined grain edges and heterogeneity in the grain amplitude profile. As the abrasive elements settle, the acoustic emission activity decreases but increases significantly in the final phase of severe wear. This behaviour may be associated with changes in the acoustic emission excitation mechanism, where friction gradually becomes the dominant phenomenon, replacing the cutting action. To corroborate these results, scanning electron microscopy (SEM) images of the abrasive disc were analysed, presented in Figure 3(B) and 3(C) for the fresh and severe wear states of the sandpaper.

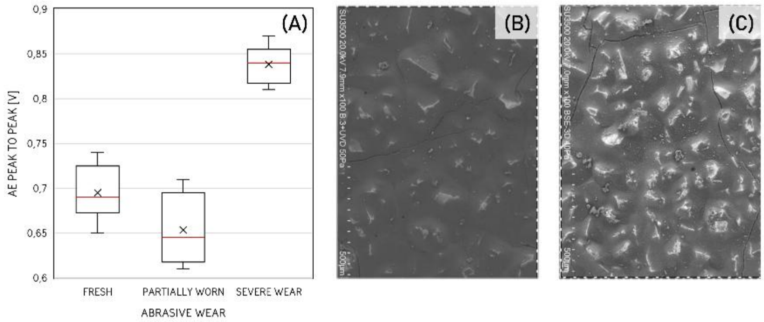

Fig. 3. Comparison of the abrasive response as a function of wear level: (A) acoustic emission, (B) SEM image of fresh sandpaper and (C) SEM image of sandpaper with severe wear. SEM images were captured at 100X magnification.

4 Product inspection

The second advancement in robotic sanding of wooden parts involves the automation of product inspection as part of the cell's inspection module. A system has been developed that uses an artificial vision algorithm to estimate the roughness of the parts, calibrated and validated against conventional roughness measurements obtained by contact profilometry and confocal microscopy. Additionally, the wettability of the parts was evaluated by measuring the contact angle using a goniometer.

4.1 Roughness measurement

Two conventional laboratory methods were used to measure the surface roughness of a sanded piece of medium-density fibreboard (MDF): a roughness profilometer and a confocal microscope. The Mitutoyo SJ-310 roughness profilometer, with a 5 µm radius stylus, was used to obtain the roughness profile and calculate the corresponding parameters according to ISO 21920-2 (2021). The processing of the profile and the roughness parameters were calculated in MATLAB. A Zeiss LSM 700 confocal microscope, equipped with an Epiplan-Apochromat 10x/0.4 DIC M27 C objective and a 405 nm laser light fluorescence contrast system, was also used to generate high-resolution images (10240 × 512 px, equivalent to 12.80 mm × 640.17 µm). Layer separation was set to 1 µm, and image processing was performed with Zen Black 2012 software, complemented by Mountains ConfoMap Premium for roughness parameter calculation.

4.2 Inspection system

The inspection system integrates machine vision tools to assess the quality of the sanded parts. In the cell environment, the intelligent sanding module provides information on the development of the process through online monitoring of the solicitations on the tool. The analysis of these solicitations is then used to define critical areas for inspection, where the surface analysis is then carried out using artificial vision to detect defects and estimate roughness.

The developed inspection system includes the following components: KAISER Reprostativ RSX 5512 reproducer, a Genie Nano M4020 camera with 8 mm Computar V0828-MPY2 optics and Effilux LED illumination with low incidence angle diffuser plate. Images captured in greyscale are processed by an algorithm that estimates roughness parameters according to ISO 21920-2. This is done by extracting grey-level co-occurrence matrix (GLCM) features from images previously treated with edge detection masks. A model relates the feature that best correlates with the roughness parameters, explicitly adjusted for each material and illumination condition. During calibration, conventional measurements are used, and once this stage is completed, the model can be implemented. The roughness estimation was initially evaluated on MDF, obtaining high correlations [13]. Subsequently, it was validated on Chilean oak wood a semi-industrial workshop, where the algorithm was adjusted to specific industrial conditions.

4.3 Measuring wettability

For wettability tests, distilled water was applied with a 1 ml syringe with a 25 gauge needle (external diameter: 0.53 mm) mounted on a Krüss DSA25B. The droplets were deposited in the middle part of each specimen, with five replicates per sample. Data acquisition began upon contact of the droplet with the surface, recording three readings per second for up to 15 seconds.

4.4 Product inspection results

After applying the calibration algorithm, a model for roughness estimation in MDF parts was obtained, using the energy of the grey-level co-occurrence matrix processed by the Roberts edge detection algorithm as the main feature (see Figure 4A).

Regarding wettability, the contact angle showed a non-linear behaviour in relation to the surface roughness parameter S_{a}, which is described by a logarithmic model. Sanding with finer grits increases wettability, as evidenced by a decrease in the contact angle (see Figure 4B).

In tests with solid wood, carried out on oak (*Nothofagus obliqua*) and pine (*Pinus radiata*), a higher uncertainty in the model was observed compared to the results obtained with MDF. This is attributed to the inherent variability of wood and the presence of structural features such as knots and cracks, which affect the model and require pre-processing for removal. Another critical factor was the variability in illumination depending on the capture area of the photograph.

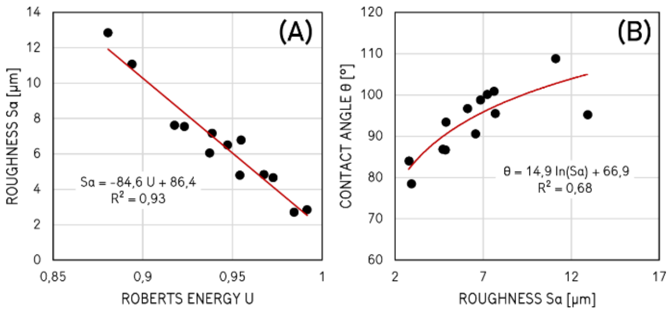

Fig. 4. (A) Roughness estimation model for MDF parts based on image analysis. (B) Contact angle behaviour as a function of surface roughness.

5 Conclusions

This work addressed the development of two new enabling technologies for intelligent robotic sanding of wooden parts, in which a robot can perform the sanding process autonomously. Advances are reported in online monitoring of the abrasive condition through analysing acoustic emission signals and inspection of product surface roughness using machine vision techniques.

In abrasive condition monitoring, the influence of two typical failure mechanisms, abrasive loading and grain wear, on the material removal rate and the acoustic emission produced by the operation were evaluated. The results confirmed the feasibility of using acoustic emissions from the sanding process to monitor the abrasive condition. In the case of abrasive loading, it was observed that this condition reduces the amplitude of the acoustic emissions, attributed to a shorter active edge length of the grains caused by dust clogging. On the other hand, grain wear also correlated with the acoustic emission level due to changes in the sanding regime. At severe levels of grain wear, a significant increase in acoustic emission was observed compared to the activity in the early stages of wear. This increase was associated with higher levels of friction and the loss of the abrasive capacity of the sandpaper. These results confirm the suitability of acoustic emission for predicting the condition of the abrasive in robotic rotary sanding.

In product inspection, surface roughness estimation was performed using machine vision. An algorithm was developed that enhances greyscale images using Roberts edge detection, followed by the calculation of features from the grey-level co-occurrence matrix. A high correlation was obtained between the roughness measurements made with the confocal microscope and the energy uniformity feature, allowing the estimation of a linear model. Furthermore, it was observed that the wettability of the MDF parts increases as finer grits are used, which is reflected in a reduction of the contact angle as the roughness parameter S_a decreases with non-linear behaviour.

In the future, the implementation of these advances in a final product capable of taking actions based on the techniques presented in this article, and validated in a relevant industrial environment, will be considered.

Acknowledgements The authors would like to thank the Agencia Nacional de Investigación y Desarrollo (Chile) for funding this research through the FONDEF

IT21i0069 and FONDEF VIU22P0027 projects. The authors also express their gratitude to the project partners: Universidad Politécnica de Madrid (Spain), Maderas Nativas Woodnic SpA (Chile) and Robotec SA (Chile), for their participation in the development of these projects.

References

1. Luo, B., Zhang, J., Bao, X., Liu, H., Li, L.: The effect of granularity on surface roughness and contact angle in wood sanding process. Meas. J. Int. Meas. Confed. 165, (2020). https://doi.org/10.1016/j.measurement.2020.108133.
2. Ugulino, B., Hernández, R.E.: Analysis of sanding parameters on surface properties and coating performance of red oak wood. Wood Mater. Sci. Eng. 13, 64–72 (2018). https://doi.org/10.1080/17480272.2016.1266511.
3. Diez Cifuentes, E., Alzugaray Franz, R., Padilla Bernedo, A., Leal Muñoz, E., Madaf Poblete, M.: Robotized workstation for intelligent sanding processes of wooden workpieces. DYNA. 98, 362–368 (2023). https://doi.org/10.6036/10873.
4. Wen, Y., Pagilla, P.: A 3D path following control scheme for robot manipulators. IFAC-PapersOnLine. 53, 9968–9973 (2020). https://doi.org/10.1016/j.ifacol.2020.12.2713.
5. Ratnasingam, J., Reid, H.F., Perkins, M.C.: The productivity imperatives in coated abrasives - Application in furniture manufacturing. Holz als Roh - und Werkst. 57, 117–120 (1999). https://doi.org/10.1007/s001070050026.
6. Matsumoto, H., Murase, Y.: Acoustic Emission Characteristics in Wood Sanding Amplitude distribution of acoustic emission in disc sanding process. J. Fac. Agric. Kyushu Univ. 43, 257–268 (1998). https://doi.org/10.5109/24270.
7. Saloni, D.E., Lemaster, R.L., Jackson, S.D.: Process monitoring evaluation and implementation for the wood abrasive machining process. Sensors (Switzerland). 10, 10401–10412 (2010). https://doi.org/10.3390/s101110401.
8. Du, Y., Tian, B., Zhang, J., Li, L., Liu, H., Luo, B.: Sanding performance and failure progress of precision-shaped abrasive belt during sanding MDF. Eur. J. Wood Wood Prod. (2023). https://doi.org/10.1007/s00107-023-02013-7.
9. Tan, P.L., Sharif, S., Sudin, I.: Roughness models for sanded wood surfaces. Wood Sci. Technol. 46, 129–142 (2012). https://doi.org/10.1007/s00226-010-0382-y.
10. Hernández, R.E., Cool, J.: Evaluation of three surfacing methods on paper birch wood in relation to water- and solvent-borne coating performance. Wood Fiber Sci. 40, 459–469 (2008).
11. Ma, J., Li, G., Zhan, Q., Wu, D., Wei, X., Wang, X., Zhao, Q., Zuo, J.: Surface roughness detection based on image analysis. In: ACM International Conference Proceeding Series. pp. 196–200. Association for Computing Machinery (2021). https://doi.org/10.1145/3478905.3478945.
12. Papp, E.A., Csiha, C.: Contact angle as function of surface roughness of different wood species. Surfaces and Interfaces. 8, 54–59 (2017). https://doi.org/10.1016/j.surfin.2017.04.009.
13. Iglesias, F., Aguilera, A., Padilla, A., Vizan, A., Diez, E.: Application of computer vision techniques to estimate surface roughness on wood-based sanded workpieces. Measurement. 224, 113917 (2024). https://doi.org/10.1016/J.MEASUREMENT.2023.113917.

Autoencoder-Based Anomaly Detection in Wood Machining for Quality Control and Process Monitoring

André Jaquemod[1], Kamil Güzel[1] and Hans-Christian Möhring[1]

[1] Institute for Machine Tools, Holzgartenstraße 17, 70174 Stuttgart, Germany
andre.jaquemod@ifw.uni-stuttgart.de

Abstract. Machine learning is increasingly revolutionizing machining, particularly in the fields of quality control and process optimization. Autoencoder techniques show great promise for detecting voids and material anomalies, which are critical for enhancing manufacturing efficiency by reducing or identifying scrap parts. Moreover, machine learning lays the groundwork for automated process control in wood machining, as natural wood variability often complicates anomaly detection. This study introduces an analogy experiment using defined holes in quasi-homogeneous MDF to address these challenges. Acceleration and force data collected during milling were used to train an autoencoder to identify undisturbed paths, thus establishing a baseline for anomaly detection. Testing the model with datasets containing drilled holes demonstrated its capability to detect anomalies. This study highlights the autoencoder's effectiveness not only in identifying artificial defects but also in detecting natural wood anomalies, such as fibre misalignments. Yet, it also demonstrated that the selection of signals is of paramount importance. Nevertheless, the findings underscore machine learning's potential for improving quality control in wood machining. By enabling accurate and efficient anomaly detection, this research work can pave the way for adaptive, intelligent process management, including multisensory solutions and the integration of measurement systems at the spindle for more complex machining paths.

Keywords: Wood Machining, Machine Learning, Autoencoder, Process Monitoring

1 Introduction

In the wood machining industry, there is a growing demand for improved part quality and performance at lower costs. Therefore, advanced methods for material classification and the modelling of workpiece properties are required to improve process monitoring and adaptive process control. Due to improved sensory and control data acquisition and the increasing use of artificial intelligence in the context of manufacturing [1], self-optimizing manufacturing systems are gradually becoming possible [2]. Especially with regard to the specific properties, diversity and complexity of natural wood, wood-based materials and wood composites, it showed that these enabling technologies are needed to realise intelligent wood machining [3]. In this context, various sensor technologies and machine learning approaches have been used to investigate and optimize the machining process. These include structure-borne acoustic emission (AE) sensors that detect vibrations within the workpiece and microphones that pick up airborne sound (AS) travelling through the air. Furthermore, acceleration sensors, dynamometers and power meters have often been used to monitor the machining process. AE sensors with a resonant frequency of 175 kHz have been applied to monitor tool wear in wood machining. Moreover, carbide-tipped tools and sawblades were analysed by means of ultrasonic AE [4]. A feed-forward neural network was employed to investigate the link between tool health and airborne sound (AS) in the 20 Hz to 20 kHz range with a classification accuracy varying between 78% for softwood and 97% for hardwood, depending on the wood species [5]. [6] used a microphone to measure AS up to 100 kHz for a tool wear analysis, based on AS energy ratios between consecutive teeth. Surface roughness has been widely studied in relation to AS. [7] examined the effect of tool geometry on AS (4-100 kHz) and surface roughness during wood drilling, finding a Pearson correlation coefficient between 0.76 and 0.99. The sound pressure level (SPL) has also been used for roughness predictions. For example, [8] achieved a 0.98 Pearson correlation when modelling surface roughness by means of wood milling sound. In [9] found out that AE correlated with surface roughness in milling, with R^2 values of 0.59 for a two-knife milling head and 0.66 for a four-knife head. Other studies on AE in wood machining were carried out by [10], [11] and [12]. Multisensor systems have been explored to enhance process monitoring [3,13,14]. Advanced analysis techniques, including dimensionality reduction and AI, have been applied as well. [15] used an AE sensor alongside other sensors to monitor sawing, training an artificial neural network with fuzzy logic to predict process quality. [16] studied a multisensor system for wood milling, linking AS loudness to feed speed and chip dimensions. Electric current was also analysed as a response variable based on chip thickness and feed speed.

The machine learning classification achieved 96.6% accuracy in distinguishing machined materials for autonomous machining control [17]. A novel AS microphone based on laser interferometers [18] was used to study wood machining. In [19] presented a sensor fusion approach that integrates data from acoustic emissions, airborne sound, and power consumption during the milling of solid wood and wood-based composites. The approach achieved accurate material classifications and modelled workpiece characteristics such as surface roughness and density, reaching a classification accuracy of 92.16% and regression models for surface roughness and density with R^2 values between 0.79 and 0.98. [20] introduced an analysis framework for monitoring wood milling, using an optical microphone and a machine learning classification model based on Linear Discriminant Analysis to distinguish between wood species. A machine learning approach with regression models was developed for predicting the properties of wood products during milling [21]. [22] investigated the combination of Singular Spectrum Analysis (SSA) and machine learning methods to improve not only the accuracy of predicting surface roughness and sample density but also the classification of cutting speeds and wood species. The current state of the art shows that monitoring wood machining is still a challenge. This is partly due to the multifaceted nature of wood as a material to be machined. The aims of the present study were to develop a method for detecting anomalies with an autoencoder and a proactive approach, already used to detect anomalies in metals.

2 Experimental setup and methods

2.1 Method for analogy testing

In order to address the challenges of acquiring extensive datasets for detecting anomalies in different materials, we adopted a proactive approach used in a previous study [23]. Rather than relying on natural defects in the specimen and measuring them, the study incorporated artificial inhomogeneities into homogeneous samples, thereby ensuring controlled and reproducible testing conditions. This method and its adaptation is shown in Fig 1. The inhomogeneous and fibrous nature of wood with its varying densities, grain patterns, and imperfections makes it nearly impossible to achieve true homogeneity. As an alternative, MDF (medium-density fibreboard) was used due to its uniform composition, offering a reliable substitute for natural wood. Drill holes with diameters of 1–2 mm were deliberately produced with programmed machining processes to generate consistent defects. Homogeneous undrilled MDF was utilised as a reference material for comparative analyses. This methodological approach yielded precise defect locations, facilitated data labelling, and enhanced the reliability of datasets for machine learning applications.

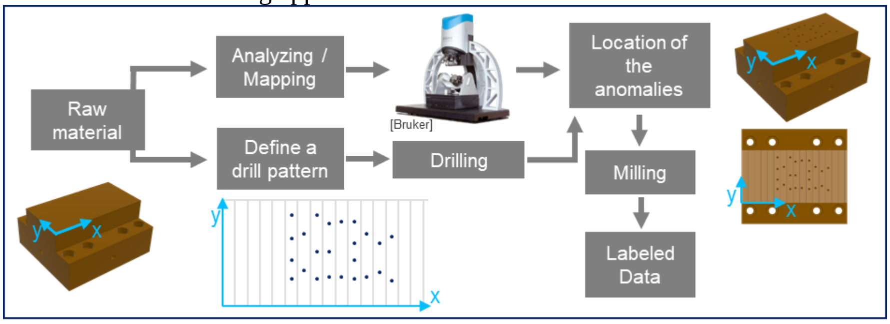

Fig. 1. Methodological approach for generating data to detect voids

2.2 Data acquisition and measurement setup

To capture and subsequently compare different measurements of the workpiece, the test specimen was equipped with two distinct sensors. As illustrated in Figure 2, the sample body was securely mounted on a force measurement platform (Kistler 9129AA), which recorded the process forces (FSpec) during machining. Additionally, an acceleration sensor was fixed to the specimen with wax to gather vibration signals (ACCSpec). The data acquisition cards (Type 9230 and 9223), provided by National Instruments, ensured the capture of high-quality data. The measurements were recorded at a sampling rate of 10 kHz, which facilitated a detailed analysis of the dynamic process characteristics. Then grooves were milled into the specimen using a 6 mm, two-tooth finishing cutter by Leuco. Here, a 6 mm width of cut (a_e) and a 5 mm depth of cut (a_p) were produced at a cutting speed of 7.54 m/s (24.000 rpm) and a feed rate of 0,15 mm per tooth. Each milling path generated 0.45 seconds of measurement time, producing 4000 acceleration and force data samples. All milling experiments were conducted with a Holzher Promaster 7017 CNC machining centre.

Fifteen grooves were milled for each mounted specimen. To assess the algorithms in the context of solid wood, the experiment was repeated with samples made of spruce. The spruce boards were cut in the direction of the grain. To facilitate the transfer of a prepared sample to a naturally-grown one, the detection of branches was necessary. To mitigate the impact of tool wear, a new tool was utilised for each test specimen.

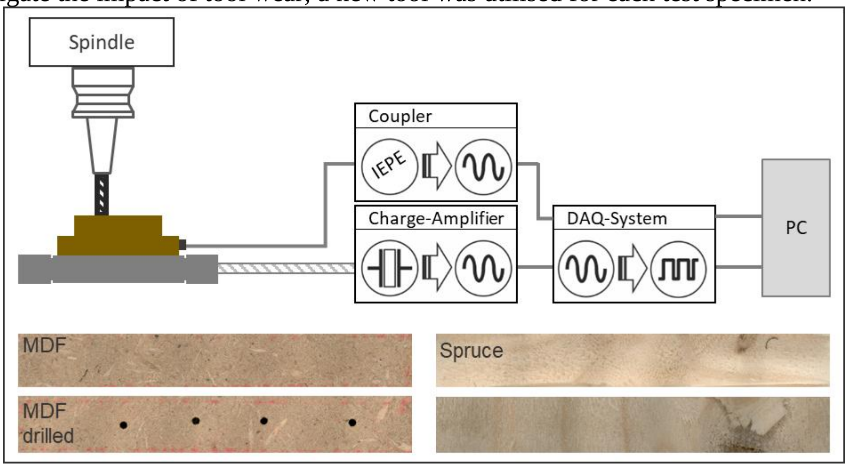

Fig. 2. Experimental setup and measuring technology

2.3 Machine learning

The acquired data had to be initially processed for training purposes, which involved removing the periods of idleness and tool entry/exit regions. Subsequently, the data was normalized and the mean value was shifted to align it to a Y-intercept of zero. Each milling path was sliced into small datasets of 50 points. When the position of the drill holes was known, the data can be labelled. In order to accommodate material variations and the influences of wear or other anomalies, these factors were intentionally varied. Algorithm training was implemented using randomly assembled data from experiments conducted on different test days.

Autoencoders were trained using Python frameworks, focusing on one distinct architecture: dense autoencoders. The advantage of dense autoencoders was their fully connected layers to capture global patterns in the data.

The autoencoder model's hyperparameters were optimized using manual grid search, which systematically explored a range of 400 predefined parameter combinations. For each combination, the model was trained and validated on scaled and sequenced time-series data. The mean absolute error (MAE) of the reconstruction loss in the validation set served as the evaluation metric. The best configuration, yielding the lowest validation loss, was found to be as follows: hidden layer size = 64, activation function = Relu, learning rate = 0.01, batch size = 128, and number of epochs = 75. This configuration was subsequently used for the final model training and testing.

3 Results

The presented graphs demonstrate the effectiveness of the autoencoder-based anomaly detection method in identifying deliberately introduced anomalies in a milling dataset. Four drill holes were deliberately introduced in the set of acceleration data (x-axis) shown in Fig 3.

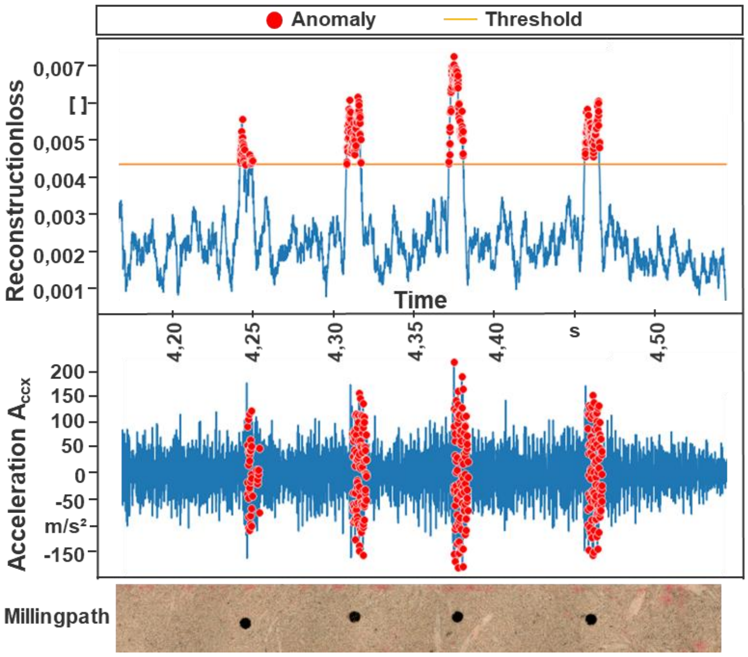

Fig. 3. Reconstruction loss of the acceleration in X-direction for the milling path of the drilled specimen

The reconstruction loss measured the deviation of the original input sequence from the reconstructed sequence predicted by the autoencoder. Peaks in the reconstruction loss corresponded to regions where the model struggled to accurately reproduce the input signal, indicating potential anomalies. In the case of the used acceleration data, the reconstruction loss was lower than 0.003 for normal data. The plot highlighted peaks in four areas with values of 0.004 to 0.007. These peaks, exceeding the predefined threshold of 95% (orange line), indicated areas where the model struggled to accurately reconstruct the input signal. In the raw signal plot (below), the red markers signified anomalies identified by the model.

A comparison with the positions of the drilled holes (Fig. 3 milling path) showed that they agreed with the locations where anomalies were artificially introduced.

The clear distinction between normal and anomalous patterns confirmed that the autoencoder accurately detected deliberate disruptions in the signal. These results validated the autoencoder's capability to reliably identify anomalies in time series of milling data, demonstrating its potential for a real-time monitoring of operations and an early fault detection.

However, when other sensor signals were analysed, it became evident how strongly the signal type affected the effectiveness of the anomaly detection.

Regarding the acceleration data from the z-axis in Fig. 4, the base noise of the reconstruction loss ranged between 0.004 and 0.010. The range was wider than before, but peaks were still observed. However, instead of the four expected peaks (corresponding to the drill holes), there were over 10 peaks above the threshold.

This demonstrates that anomaly detection is not always reliable and highlights the critical dependence on the alignment of the sensor's axis with the direction of the expected anomalies. Signals with minimal response to disruptions are inherently less suited to a precise anomaly identification, emphasizing the importance of carefully selecting and analysing data from appropriate sensor directions for a reliable detection.

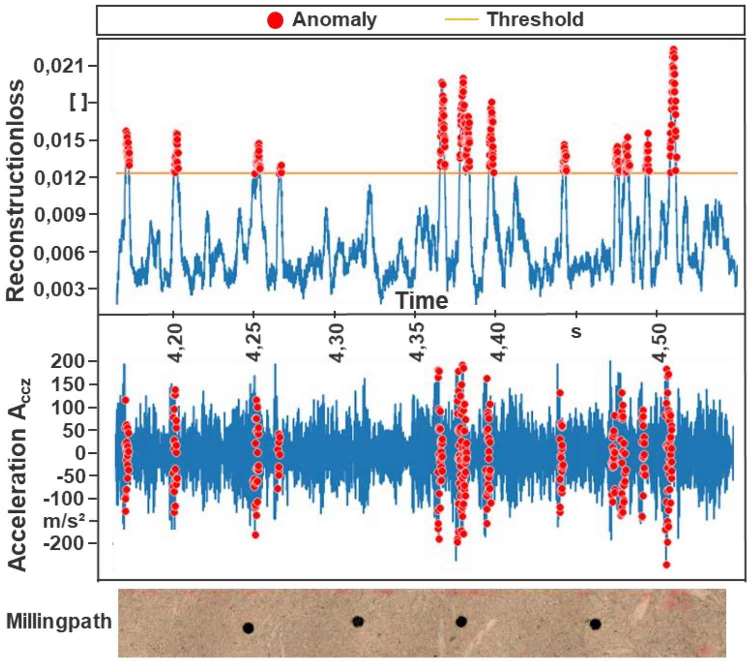

Fig. 4. Reconstruction loss of the acceleration in Z-direction for the milling path of the drilled specimen

When examining force data (Fig. 5), particularly of the x-component, it was observed that the agreement was similarly great as for the acceleration signal in the x-direction. Figure 5 illustrates the reconstruction loss and the raw force signal, confirming an accurate anomaly detection at the drilled holes. The agreement between the detected anomalies and the drill holes was comparable to that of the acceleration signal. The basic reconstruction loss was, however, higher compared with the loss for the acceleration. It ranged from 0.0045 to 0.0085. In addition, the peak values were different. This became particularly evident when examining the ratio of noise to peak values. For the force data, the ratio was 0.73, whereas it was 0.43 for the acceleration data. This clearly demonstrated that detecting anomalies in acceleration signals is easier, as the difference between the normal range and the anomalies is significantly more pronounced.

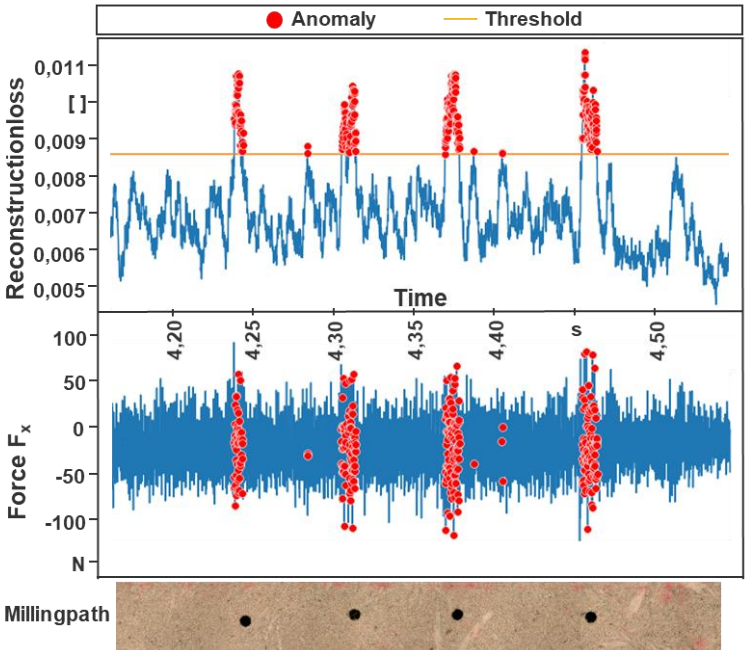

Fig. 5. Reconstruction loss of the force in X-direction for the milling path of the drilled specimen

When analysing the milling data of a spruce specimen containing a knot, it became evident that an anomaly was detected at the location of the knot. However, as Fig. 6 shows, the area in front of the knot was also marked as anomalous. Notably, the reconstruction loss began to rise significantly at 4.37 seconds and reached its maximum value of 0.025 even before the knot. Consequently, the signal in this region was identified as anomalous despite the absence of a discernible spike in the raw signal. Superimposed on the data, the subsequent examination of the milling path revealed deviations in the fibre orientation from its "normal" travel. These deviations indicated a shift in the fibre structure, which, even though not immediately apparent, contributed to the model's identification of anomalies.

This example demonstrates that anomalies can be detected not only in controlled experiments with artificially drilled holes but also in natural features such as spiral grain deviations and significant changes in fibre orientation. These findings highlight the model's capability to identify both predefined and naturally occurring material irregularities, underscoring its potential for broader applications to detect defects in wood machining.

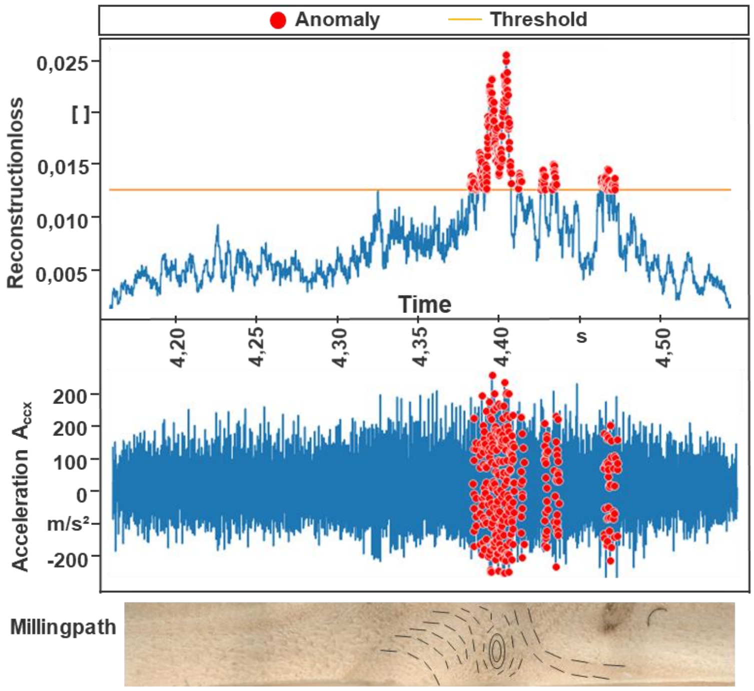

Fig. 6. Reconstruction loss of the acceleration in X-direction for the milling path of the spruce specimen

4 Summary and outlook

This paper presents a method for successfully detecting anomalies in milling processes, both in artificially produced irregularities in quasi-homogeneous MDF material and in natural anomalies in spruce specimens. While anomalies in MDF were represented by pre-drilled holes, the anomalies in spruce boards included not only visible knots but also deviations in fibre orientation, demonstrating the ability of the model to detect more complex, less obvious structural irregularities in natural materials.

The results highlight the critical role of signal selection in anomaly detection. Acceleration signals proved to be particularly effective due to their greater reconstruction loss differences, enabling a clearer differentiation between normal and anomalous data. Additionally, significant variations were observed within signal types, such as between spatial directions (e.g. X and Z), emphasizing the need for directional analysis.

Future work will focus on integrating data from multiple sensor types to develop a multisensory solution, aimed at detecting anomalies along complex tool paths, which resemble real-world machining scenarios more closely. The exploration of measurement systems at the spindle is also supposed to enhance the detection accuracy and broaden the application possibilities.

References

1. Gao R. X., Krüger, J., Merklein, M., Möhring, H.-C., Vancza, J. (2024) Artificial intelligence in manufacturing: State of the art, perspectives, and future directions. CIRP Annals 73:2. https://doi.org/10.1016/j.cirp.2024.04.101
2. Möhring H.-C., Wiederkehr, P., Erkorkmaz, K., Kakinuma, Y. (2020) Self-optimizing machining systems. CIRP Annals 69:2. https://doi.org/10.1016/j.cirp.2020.05.007
3. Möhring, H. C., Eschelbacher, S., Güzel, K., Kimmelmann, C., Schneider, M., Zizelmann, C., Häusler, A. and Menze, C. (2019) En route to intelligent wood machining-current situation and future prespectives. Journal of Machine Engineering, 19(4), 5–26. DOI:10.5604/01.3001.0013.6227
4. Lemaster, R. L. and J. Schultz. 2016. The use of acousto-ultrasonics to determine the quality of the brazing of carbide-tipped cutting tools. Wood Mat. Sci. Eng. 11(3):164 – 16 https://doi.org/10.1080/17480272.2016.1146798
5. Zafar, T., K. Kamal, Z. Sheikh, S. Mathavan, A. Jehanghir, and U. Ali. 2015. Tool health monitoring for wood milling process using airborn acoustic emission. In: Proceedings of the 2015 IEEE International Conference on Automation Science and Engineering (CASE), August 24–28, 2015, Gothenburg, Sweden; Institute of Electrical and Electronics Engineers (IEEE), New York.
6. Zhu, N., C. Tanaka, and T. Ohtani. 2002. Automatic detection of damaged bandsaw teeth during sawing. Holz Roh Werkst. 60(3):197– 201. https://doi.org/10.1007/s00107-002-0291-3
7. Cyra, G., C. Tanaka, M. Yoshinobu, and Y. Nishino. 1998. Effects of helical angle of router bit on acoustic emission. J. Wood Sci. 44(3):169-176. https://doi.org/10.1007/BF00521959
8. Iskra, P. and C. Tanaka. 2005b. The influence of wood fiber direction, feed rate, and cutting width on sound intensity during routing. Holz Roh Werkst. 63(3):167–172. https://doi.org/10.1007/s00107-004-0541-7
9. Aguilera, A., M. Vega, and P.-J. Me´ausoone. 2006. Effects of grain angle on the amplitudes of acoustic emission and surface roughness in wood machining. Wood Sci. Technol. 41(4):373 – 381. https://doi.org/10.1007/s00226-006-0117-2
10. Aguilera, A. 2010. Surface roughness evaluation in medium density fibreboard rip sawing. Eur. J. Wood Wood Prod. 69(3):489–493. https://doi.org/10.1007/s00107-010-0481-3
11. Aguilera, A. and J. L. Barros. 2010. Sound pressure as a tool in the assessment of the surface roughness on medium density fibreboard rip sawing process. Maderas Cienc, Tecnol. 12(3). https://doi.org/10.4067/s0718-221x2010000300001
12. Murase, Y., K. Matsumoto, and T. Ohuchi. 2008. Acoustic emission and cutting resistance in cutting of solid wood, MDF and particleboard. J. Fac. Agric. Kyushu Univ. 53(2):485–490. https://doi.org/10.5109/12862
13. Aguilera, A. and J. L. Barros. 2011. Surface roughness assessment on medium density fibreboard rip sawing using acoustic signals. Eur. J. Wood Wood Prod. 70(1–3):369– 372. https://doi.org/10.1007/s00107-011-0528-0
14. Nasir, V., J. Cool, and F. Sassani. 2019. Intelligent machining monitoring using sound signal processed with the wavelet method and a self-organizing neural network. IEEE Robot. Autom. Lett. 4(4):3449–3456. https://doi.org/10.1109/lra.2019.2926666
15. Nasir, V., S. Dibaji, K. Alaswad, and J. Cool. 2021. Tool wear monitoring by ensemble learning and sensor fusion using power, sound, vibration, and AE signals. Manuf. Lett. 30:32 – 38. https://doi.org/10.1016/j.mfglet.2021.10.002

16. Aguilera, A., P. J. Me´ausoone, A. Rolleri, J. L. Barros, F. Burgos, and C. Aguilar. 2016. Advances on indirect methods to evaluate tool wear for Radiata pine solid wood molding. Wear 350–351:27–34. https://doi.org/10.1016/j.wear.2015.12.011
17. Eschelbacher, S., J. Duntschew, and H.-C. Möhring. 2019, Recognition of wood and wood-based materials during machining using acoustic emission. In: Production at the Leading Edge of Technology, Proceedings of the 9th Congress of the German Academic Association for Production Technology (WGP), J. P. Wulfsberg, W. Hintze, and B.-A. Behrens (Eds.), September 30–October 2, 2019, https://doi.org/10.1007/978-3-662-60417-5_32
18. Fischer, B. 2016. Optical microphone hears ultrasound. Nature Photon. 10:356–358.
19. Derbas, M., Jaquemod, A., Frömel-Frybort, S., Güzel, K., Möhring, H.-C., Riegler, M. (2023) Multisensor data fusion and machine learning to classify wood products and predict workpiece characteristics during milling. CIRP Journal of Manufacturing Science and Technology, 47, 103-115. https://doi.org/10.1016/j.cirpj.2023.09.003
20. Derbas, M., Frömel-Frybort, S., Laaber, C., Möhring, H.-C., Riegler, M. (2023) Supervised classification of wood species during milling based on extracted cut events from ultrasonic air-borne acoustic signals. Wood Material Science & Engineering, 18(6). https://doi.org/10.1080/17480272.2023.2214118
21. Derbas, M., Jaquemod, A., Frömel-Frybort, S., Güzel, K., Möhring, H.-C., Riegler, M. (2024) A Machine Learning Approach to Predict Properties of Wood Products during Milling. Forest Products Journal, 74(2). https://doi.org/10.13073/fpj-d-24-00012
22. Derbas, M., Frömel-Frybort, S., Möhring, H.-C., Riegler, M. (2025) Accelerated Singular Spectrum Analysis and Machine Learning to investigate wood machining acoustics. Mechanical Systems and Signal Processing, 223. https://doi.org/10.1016/j.ymssp.2024.111879
23. Jaquemod, A., Palalić, M., Güzel, K., & Möhring, H.-C. (2024). In-Process Monitoring of Inhomogeneous Material Characteristics Based on Machine Learning for Future Application in Additive Manufacturing. Journal of Machine Engineering. https://doi.org/10.36897/jme/187872

Wood-Based Materials for Machine Components like Enclosures

Matthias Schneider[1], André Jaquemod[1], Thomas Stehle[1] and H.-Christian Möhring[1]

[1]University of Stuttgart, Institute for Machine Tools (IfW), Stuttgart 70174, Germany
matthias.schneider@ifw.uni-stuttgart.de

Abstract. The use of materials made from renewable raw materials opens up interesting possibilities for substituting metal materials in machine tool design, particularly in lightweight design. Machine enclosures, for example, are components that can be made of sustainable materials. Particularly in the case of machine tools for machining wood and composite materials, the machine enclosure is often designed as a moving partial enclosure. It encloses the direct working space, protects against ejected parts and reduces noise emissions as well as dust pollution.

These properties ensure an extensive protection for the operator. However, the mass of the moving partial enclosure has an influence on the dynamic behaviour as well as the acceleration and braking processes of the machine. The use of lightweight materials made from renewable raw materials is therefore very promising. The sandwich structure developed here allowed a reduction in the weight of machine enclosures compared with steel designs. Furthermore, the enclosures did not only fulfil protective functions but also improved the acoustic properties, as the propagation of sound emissions from the machine was reduced.

A reduction in weight opens up the possibility for further optimising the machine enclosure, for example, by reducing the open areas in the enclosure to improve the collection of chips and dust. By using wood-based materials in machine enclosures, it is possible to make a contribution to the ecological transformation of the industry and the manufacture of products. In addition, the carbon footprint can be reduced, making the machine enclosure a carbon neutral machine component.

Keywords: Wood material, Machining, Sustainable development, Safety

1 Introduction

The industrial transformation is also affecting machine building and is largely driven by political and social requirements. In particular, sustainable production processes are increasingly gaining importance. The approach presented here examined the potential of renewable raw materials as building materials in machine building, using the example of machine enclosures. The focus was on the use of wood-based materials for machine enclosures in CNC machining centres for woodworking. This type of machine typically features a partial enclosure that moves synchronously with the movement of the x-axis. Due to the large, panel-shaped workpieces, such as wood-based panels in furniture or door production, partial enclosures have become established over large-volume complete enclosures (see Figure 1). They enable an economical implementation of safety regulations without requiring a complex complete enclosure [1] [2].

Moving partial enclousre	Complete enclosure
	
- Higher moved masses → Deterioration of the dynamics + Low costs + Handling	- High costs + No additional moved masses, less energy consumption + Lower noise immission + Improves extraction

Fig. 1. Machines with complete and moving partial enclosures [2]

Another advantage of partial enclosures is the improved accessibility during manual workpiece changes, which also enables the performance of alternating operations by these machines. However, as machines are increasingly equipped with additional units, such as drilling units with up to 32 tool positions, saw units, edge banding systems, and postforming units, the dimensions of partial enclosures are constantly increasing. This development leads to a rise in moving masses, including those moved by the machine enclosure itself, which can have a negative impact on the machine's dynamic properties [3]. Lightweight machine enclosures made of fibre-reinforced plastics, such as glass fibre or carbon fibre reinforcements, have not gained market acceptance due to their high costs [4] [5]. The new approach presented here examined the use of renewable raw materials for safeguarding protective devices in partial enclosures. To assess the suitability of these new materials, comprehensive tests were conducted with specimen materials.

According to the Directive 2006/42/EC of the European Parliament and Council, machine enclosures must explicitly protect against ejected or falling workpieces and objects. Additionally, safeguarding devices must also limit emissions generated by the machine. Machine enclosures for woodworking centres must be designed and marketed in accordance with the state of the art, as specified in the DIN EN ISO 19085-1 [1] [6] and DIN EN ISO 19085-3 [2] standards.

Currently, the most commonly used materials for safeguarding devices are 2 mm thick sheet steel and 5 mm thick polycarbonate, which is used for viewing panels. The dimensions required for a safe machining of these materials are specified in the standards [1] [7].

The noise emissions generated by the machine are reduced by the machine enclosure to ensure compliance with legal noise limits at the workplace. According to occupational safety regulations, noise protection measures are required when the daily noise exposure level $L_{EX,8h)}$ reaches 80 dB(A) (lower action level) so that personal protective equipment (e.g. ear protection) must be worn [6] [7]. If the noise level exceeds $L_{EX,8h}$ = 85 dB(A), appropriate protective measures must be mandatorily implemented.

The material properties and structure of the machine enclosure play a crucial role in shielding noise sources from the operator [7] [4]. Additionally, an ecological assessment of the materials is conducted by evaluating the CO_2 equivalent of the materials used in the wall construction of the machine enclosure.

2 Methods

2.1 Structure of the machine enclosure made from renewable raw materials

The schematic structure of a sandwich material for machine enclosures is shown in Figure 2. A wood veneer material served as the carrier layer of the sandwich structure. An elastic intermediate layer was integrated to absorb the kinetic energy generated when ejected parts from the working space impact the surface. The intermediate layer was designed to be open-pored to meet functional requirements regarding acoustic properties. To protect against process-related influences such as dust and chip deposits and to prevent damage from contact with workpiece edges (e.g. during workpiece handling), the intermediate layer on the back side of the working space was protected by a protective textile [8].

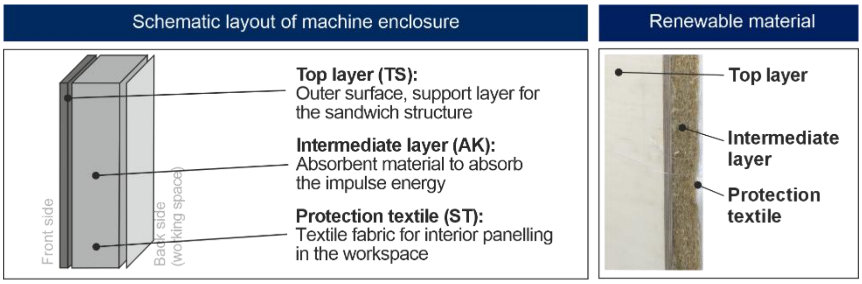

Fig. 2. Schematic structure of the safeguard made from renewable raw materials, here using the example of wood-based raw materials [8]

Table 1 lists the materials considered in this study for the use in the machine enclosure. Steel sheet (Ref01) and polycarbonate (Ref02) were used as reference materials. The investigated intermediate layer AK01 consisted of a polyurethane foam designed as an acoustic foam to enhance the acoustic properties compared with conventional materials. The renewable raw materials for the machine enclosures were implemented in a sandwich structures using a three-layer system. To meet the specific requirements for machine enclosures, a specific variation of the layer arrangement within the sandwich structure was carried out. The carrier layers varied between TS07 with a thickness of d_{TS} = 18 mm and TS10 with d_{TS} = 6.5 mm. In the intermediate layer, the raw density was reduced from AK03 with ρ = 195 kg/m³ to AK04 with ρ = 115 kg/m³, both with a thickness of d_{ST} = 40 mm [8].

Table 3. Overview of the materials analysed for the use in safeguards on machine tools [8]

Material	Reference	Dimension: material thickness (mm)	Specific mass (g/m^2)
Steel sheet (reference material)	Ref01	2	15 700
Polycarbonate (reference material)	Ref02	5	6 000
Polycarbonate + PUR foam	Ref02-AK01	20	6.360
Renewable raw material	TS07-AK04-ST01	58.7	20 481
Renewable raw material	TS09-AK03-ST01	52.7	13 321
Renewable raw material	TS09-AK04-ST01	52.7	16 521
Renewable raw material	TS10-AK03-ST01	47.2	9 455

The test samples with a sandwich structure made from renewable materials were examined for their suitability as safeguarding devices. To assess the retention capacity, impact resistance tests were conducted according to the DIN EN ISO 19085-1 standard [2]. To determine the acoustic properties of the materials for reducing machine-induced noise emissions, the insertion loss I_L was measured.

2.2 Investigation of the retention capacity

The requirements for safeguarding devices in equipment for metal and wood machining are fundamentally identical in terms of the protection against ejected objects. However, differences exist in the impact resistance testing according to the DIN EN ISO 19085-1 standard [1]. For this purpose, a test samples was hit with a test projectile weighing $m_{test\ projectile}$ =100 g. The standardized test velocity was $v_{test\ projectile}$ = 70 m/s, corresponding to a kinetic energy of E_{kin} = 245 J, which must be absorbed by the safeguarding devices [1].

Due to the high rotational speeds in woodworking, reaching up to n = 24 000 rpm, significant circumferential speeds occur at the tools or cutting edges. In the event of tool breakage, fragments can be ejected from the working space at high velocity due to the resulting energy. The experimental investigation of the test samples was conducted in the test facility, which is schematically illustrated in Figure 3 [3].

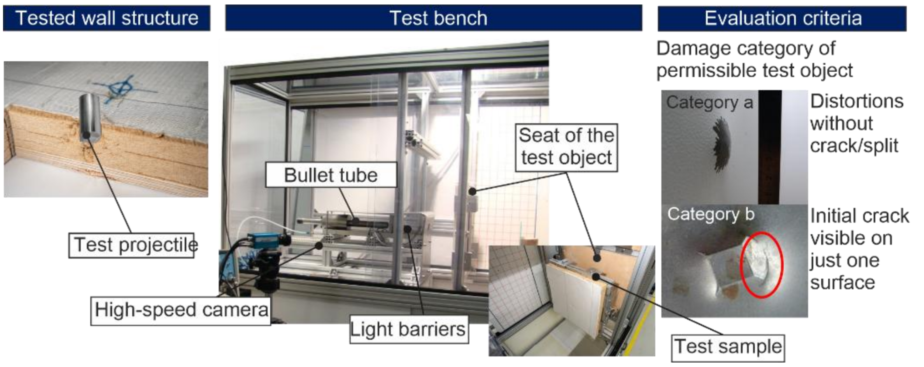

Fig. 3. Test setup for determining the impact resistance of materials for machine enclosures in accordance with DIN EN ISO 19085-1; damage of safeguards [1] [4]

The evaluation of the investigated materials was carried out according to the impact resistance test by means of a visual inspection of the test samples and a standardized documentation of the damage patterns. Figure 3 illustrates the exemplary damage categories a) and b). If a test sample showed bulging, bending, or plastic deformation without a visible crack after testing, it was assigned to damage category a). However, if a crack was detected that was only visible on one surface, the specimen was classified under damage category b). If the crack fully penetrated the material and was visible at both sides (front and rear), the specimen was categorized as damage category c). If the test projectile perforated the specimen completely, this corresponded to damage category d). The test was considered to be passed if the damage categories a) or b) were recorded. For machine enclosures, only materials should be used that passed this test and demonstrated the corresponding damage category [1] [9].

2.3 Investigation of the acoustic performance of the materials

In addition to the criterion of the material's retention capacity, the acoustic properties (insulation, loss) also played a role in selecting suitable materials for the wall design of a machine enclosure. To assess the sound insulation performance of machine enclosures, the reduction in the sound power level ΔL_W achieved by installing test samples in the test setup was determined. This is also referred to as the insertion loss I_L. The insertion loss here was the difference between the sound power level L_W emitted by the noise source with and without the test sample used as enclosure [10].

The insertion loss I_L was determined to analyse the acoustic properties of the materials. For partial enclosures with openings in the enclosure structure that move with the machine, this parameter was suitable for quantifying the noise reduction in the immediate vicinity of the machine. In the context of the legally defined noise exposure level, the A-weighted sound power level $L_{W,A}$ was determined at these positions, thus evaluating the effectiveness of the machine enclosure with regard to occupational safety. This measure was derived from the sound pressure reduction in accordance with DIN EN ISO 717-1 [11]. Both the reduction in sound pressure level and the insertion loss were measured and specified as standard in third octave or octave bands [11] [12].

In order to experimentally investigate the effects of openings in the machine enclosure on the acoustic properties, a test bench was developed at the IfW. This was designed in the form of a machine enclosure and took the structural conditions of modern CNC machining centres for woodworking into account. These often have no complete enclosure but are designed with an open construction at the top and rear in addition to the openings for workpiece infeed and outfeed. As shown in Figure 4, the test setup allowed the integration of test samples measuring 500 mm × 500 mm [8].

The test setup included a centrally positioned sound source, which was designed as a dodecahedron loudspeaker with uniform sound radiation. Depending on the number of installed test samples (closed sides within the test setup), it was possible to model either a partial or a complete enclosure and to take different opening ratios θ of the machine enclosure into account. The opening ratio θ represented the proportion of the open area on the machine enclosure A_0 to the entire inner surface of the enclosure [10].

$$\theta = \frac{A_0}{A_{ges}} \tag{1}$$

This model of a machine enclosure allowed to directly compare the test samples used with the previously tested impact test samples.

The acoustic measurements were carried out using the enveloping surface method in accordance with DIN EN ISO 3744 [13]. The test setup consisted of a semi-open room with a sound-reflecting floor surface and no other reflective surfaces or objects that could influence the measurements. As part of the enveloping measurement method, the microphones were arranged like a square measurement envelope around the reference cuboid, which enclosed the entire sound source. The test bench itself was not part of the sound source or the reference measurement [8].

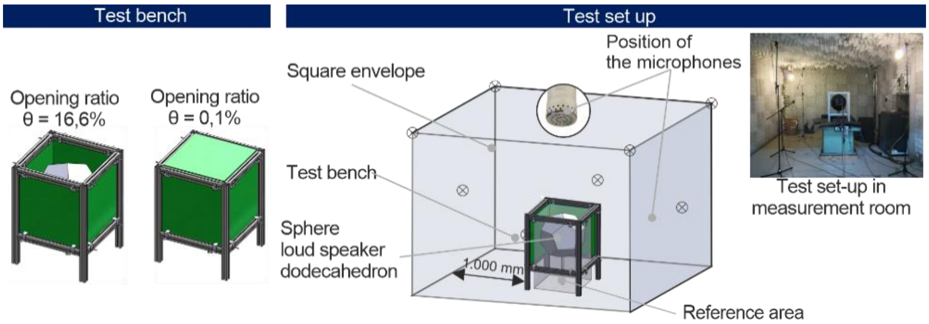

Fig. 4. Test bench and test environment for measurements using the enveloping surface method [8]

3 Results

3.1 Retention capacity of materials

In the impact resistance test, the materials made of renewable raw materials showed a better performance than the reference materials. Figure 5 compares the results of the impact resistance tests for the materials. Except for the test sample of TS10-AK05-ST01, the test samples of renewable raw materials passed the impact tests in accordance with the standard and were classified under damage category a). For the test specimen of TS10-AK05-ST01, the damage category c) was determined after the impact test as there was a visible crack at the front and rear of the test sample. This showed that the sandwich structure of TS09-AK03-ST01 was around 20 % lighter than Ref01. Both test samples had the same damage pattern (damage category a)) after the test. This shows that a weight-reduced machine enclosure made from renewable raw materials protects against ejected parts [8].

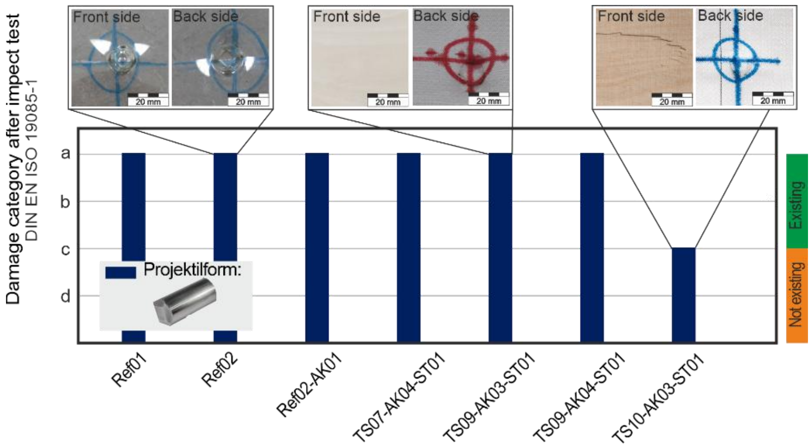

Fig. 5. Test results regarding the impact resistance of materials out of renewable raw materials for machine enclosures [8]

3.2 Acoustic performance of materials for machine enclosures

Figure 6 shows a comparison between the renewable material of TS09-AK03-ST01 with sandwich structure and the reference materials of Ref02 and Ref02-AK01. The test bench was closed on five sides with the respective test samples and therefore had a lower opening ratio of $\theta = 16.7$ %. The potential of the wood-based material was clearly recognisable in the evaluation of the measurement data, as its insertion loss was better than the results of the reference materials for all frequency ranges. This was also the case when the reference materials were acoustically modified with the AK01 acoustic foam [8].

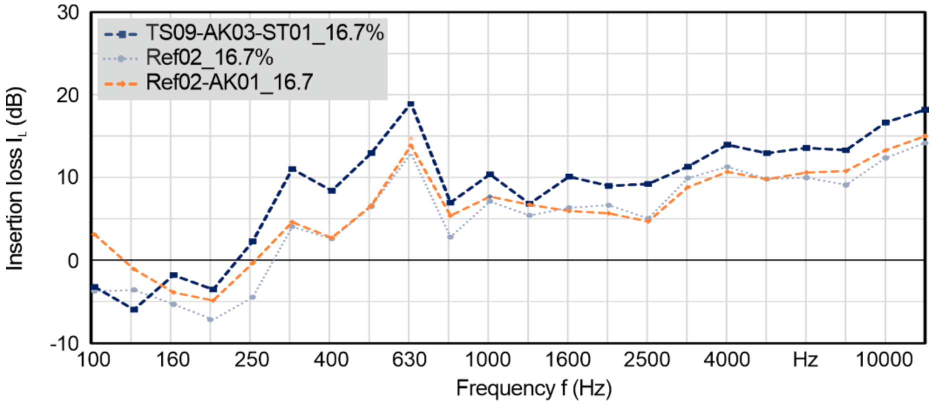

Fig. 6. Determination of the insertion loss I_L using the enveloping surface method (DIN EN ISO 3744); comparison between the materials TS09-AK03-ST01, Ref02 and Ref02-AK01 [8]

The comparison of the maximum achievable noise reduction as a function of the opening ratios shows that the new materials have very good acoustic performance due to their intermediate layer and sandwich structure. Figure 7 compares the values for the respective opening ratios to the theoretically achievable maximum noise reduction. It can be seen here that the test samples made from renewable raw materials performed better than the reference materials. In the tests, the new materials achieved a higher insertion loss across the varying opening ratios [8].

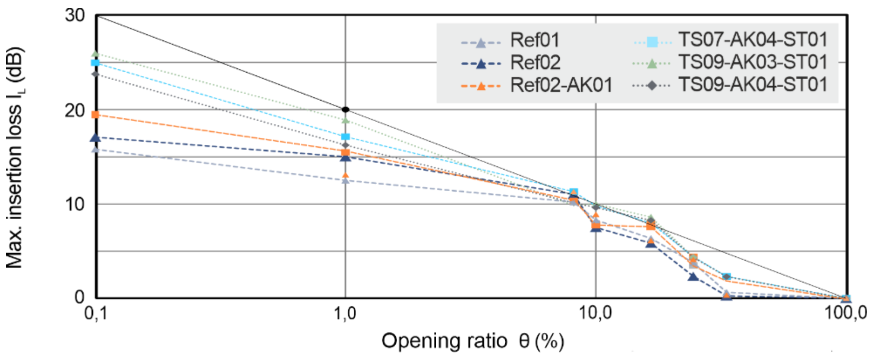

Fig. 7. Achievable noise reduction through the materials with different opening ratios in the machine enclosure [8]

The sustainability of the materials was assessed by analysing the CO_2 equivalents. The scope of the analysis comprised a cradle-to-gate approach, which includes the extraction of the raw materials, the production of the materials, their manufacture into a machine enclosure and the delivery of the machine to the customer [14]. The CO_2 equivalents per square metre of machine enclosure, as presented in Table 2, showed that the materials made of renewable raw materials had lower or negative CO_2 values compared with the reference materials. This was due to the fact that the production of the reference materials of Ref01 and Ref02 already includes high carbon emissions, which meant that a positive CO_2 equivalent was attributed to them from the outset. In contrast, the raw materials of renewable materials bind CO_2 during their growth, which was partially released during treatment and processing. How-ever, the originally stored CO_2 amount was not fully consumed by the gate, so that the negative carbon footprint was reduced. In addition, the carbon footprint ratio of the weight-reduced materials improved further over the utilisation phase, compared with the reference materials. As a reduced mass of the machine enclosure led to lower acceleration and deceleration forces, further emission savings could be achieved during operation. However, these effects were not taken into account in the present analysis [8].

Table 4. carbon footprint of the materials through the carbon equivalent [8]

Material	CO_2-equivalent (kgCO_2e)	Damage category
Ref01	29.8742	a)
Ref02	30.0792	a)
TS09-AK03-ST01	-8.0401	a)
TS10-AK05-ST01	-7.9212	c)

4 Summary and outlook

The approach of designing machine enclosures from renewable raw materials does not only have the advantage of a lightweight design variant but also that these components in the machine tool are made from an ecological material. The component of the machine enclosure has no influence on the accuracy-determining properties of the machine tool. This machine component therefore offers a great potential for establishing materials made of renewable raw materials for machine tool building. The weight saving of 20 % compared with the reference material of Ref01, which is predominantly used as a material for safeguards today, demonstrated the lightweight design potential of this material group. The test results from Chapter 3 showed that these materials are suitable for the use in machine enclosures. The test samples analysed demonstrated that they offer protection against ejected parts when tested for impact resistance in accordance with the standard. The structure of the sandwich design also gave these materials an advantage over the reference materials analysed.

The advantages of the material group, such as the lightweight design potential and the good damping properties against vibration loads, will be of interest for further applications for components and assemblies in machines.

References

1. DIN EN ISO 19085-1: Woodworking machines – Safety – Part 1: Common requirements. German version. Berlin (2021).
2. DIN EN ISO 19085-3: Safety of woodworking machines – One side moulding machines with rotating tools – Part 3: Numerically controlled (NC) boring and routing machines; German version, Berlin (2022).

3. Rapp, M.; Gerold, J.: Marktübersicht CNC-Bearbeitungs-Zentren 2023. In. HOB Die Holzbearbeitung 70(2023), Nr.7 pp 38-52 (2023).
4. Möhring; H.-C.; Stehle, T.; Schneider, M.: Lightweight machine housings for dynamic and efficient production processes: XXX CIRP sponsored Conference on Supervising and Diagnostics of Machining Systems. Karpacz, Polska (2019).
5. Forcillo, V.: Steigerung der Arbeitssicherheit an stationären Holzbearbeitungsmaschinen durch Maschinenumhausungen aus Faserverbundwerkstoffen. Doctoral thesis. University of Stuttgart (2013).
6. Directive 2006/42/EC of the European Parliament and of the Council of 17 May 2006 on machinery, and amending Directive 95/16/EC. Decision of the European Parliament and Council, Brussels (2006).
7. Kuolt, H. Geräuschentstehung und Maßnahmen zur Lärmminderung an Holzbearbeitungsmaschinen, Doctoral thesis. University of Stuttgart (2006).
8. Schneider, M. A holistic examination of materials made from renewable raw materials for the use as safe machine enclosures. Doctoral thesis (unpuplished). University of Stuttgart (2025).
9. DIN EN ISO16090-1: Machine tools safety - Machining centres, milling machines, transfer machines - Part 1: Safety requirements; German version, Berlin (2023).
10. Schirmer, W.: Technischer Lärmschutz - Grundlagen und praktische Maßnahmen zum Schutz vor Lärm und Schwingungen von Maschinen; Springer-Verlag Berlin Heidelberg. Berlin, Heidelberg, (2006).
11. DIN EN ISO 717-1: Acoustics - Rating of sound insulation in buildings and of building elements - Part 1: Airborne sound insulation; German version, Berlin (2021)
12. DIN EN ISO 15667: Acoustics - Guidelines for noise control by enclosures and cabins. German version, Berlin (2021).
13. DIN EN ISO 3744: Acoustics - Determination of sound power levels of noise sources using sound pressure - Engineering methods for an essentially free field over a reflecting plane; German version, Berlin (2011).
14. Forster, P.; Ramaswamy, V.; Artaxo, P.; Berntsen, T.; Betts, R.; Fahey, D. W. et al.: Changes in atmospheric constituents and in radiative forcing. In: Climate Change 2007: The Physical Science Basis. Contribution of Working Group I to the Fourth Assessment Report of the Intergovernmental Panel on Climate Change. pp 130–234. Cambridge, United Kingdom and New York, USA: Cambridge University Press (2007)

Effect of sawing and drying processes on bow and crook of dimension lumber from large-diameter sugi (*Cryptomeria japonica*) logs

Yukari Matsumura [1], Yosuke Matsuda [1], Kana Yamashita [1], Erina Kojima [1], Hideo Kato [1], Hirofumi Ido [1], Yuji Ikami [1]

[1] Forestry and Forest Products Research Institute, 1 Matsunosato, Tsukuba, Ibaraki, Japan
myukari@ffpri.affrc.go.jp

Abstract. The supply of large-diameter sugi logs is expanding with the increasing ratio of the aged-class planted forest area in Japan. The purpose of this study was to improve productivity of dimension lumber from the large-diameter sugi logs. Eight sugi logs, 36 cm or 38 cm in diameter and 5 m in length were used. Four of the logs were cut to 2.5 m in length. Five or six wide lumbers were sawn from each log. Half of the wide limbers sawn from each log were kiln-dried, and the other half of wide limbers were kiln-dried after being sawn into half-widths. The process of ripping wide lumbers into half-width before drying, and the process of ripping them into half-width after drying, were compared from the view point of the tendency of bow and crook. There was little difference in bow between the lumbers from two processes. It was found that the process of ripping after drying resulted in smaller crook in lumber. In the case of the 5 m length, some lumber might not meet target size because of larger bow and crook.

Keywords: Large-diameter log, Dimension lumber, Bow, Crook.

1 Introduction

The supply of large-diameter logs is expanding with the increasing ratio of the aged class planted forest area in Japan. Sustainable use of mature forest resources is necessary. Sugi (*Cryptomeria japonica*) is one of the most common planted tree species in Japan and is used as a wooden building material. The share of light-frame construction was about 20% in wooden houses in 2023. Imported SPF lumber has been used mainly for light-frame construction in Japan; however, use of sugi is gradually increasing recently. Production of 16ft lumber is also required for expanding the share of sugi dimension lumber. The purpose of this study was to improve productivity of dimension lumber from large-diameter sugi logs. The Saw-Dry-Rip (SDR) method has been used in for the sawing hardwoods, and eliminated the problem of crook [1]. The SDR process, together with high-temperature drying, resulted in higher volume recovery, and product quality was compared to the conventional live sawing process for rubberwood [2]. The effects of the SDR method on reduction of warp of sugi 2-by-4's was investigated for the case of medium-diameter (24 cm diameter) logs [3]. This study investigated the effect of sawing and drying processes on warp of dimension lumber from large-diameter sugi logs.

2 Materials and methods

2.1 Materials

Eight sugi logs, 36 cm or 38 cm in diameter and 5 m in length were used. The number of growth rings that was counted at the top end ranged from 41 to 62. The heartwood percentage ranged from 69% to 77%. The heartwood percentage is defined as the ratio of the heartwood radius to the short radius through the pith on the top end. The eccentricity on the top end ranged from 1.1% to 2.7 % and that on the butt end ranged from 1.0% to 6.5%. Eccentricity was calculated as the distance between the pith and the geometric center per short diameter. The Young's modulus by the longitudinal vibration method of the log ranged from 7.3 to 10.7 GPa. Four of the logs were cut to 2.5 m in length, the other four logs were used as 5 m in length.

2.2 Sawing pattern

A 1,200 mm band mill with an auto feed carriage was used for sawing. Logs were sawn using the sawing pattern shown in Fig. 1. The numbers in the figure show sawing order and the dashed line indicates the ripped line. The main products of primary sawing were five or six wide lumbers (47 mm thick and 218 mm wide).

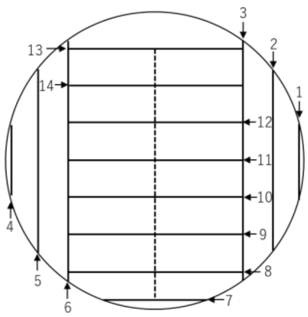

Fig. 1. Sawing pattern for wide lumbers.

2.3 Drying and ripping process

The lumbers sawn from each log were divided into groups A and B. Group A lumbers were ripped into half-width immediately after sawing and then kiln-dried. Group B lumbers were kiln-dried and then ripped into half-width (Figure **Errore. L'origine riferimento non è stata trovata.**2). The lumbers were dried in a conventional steam-heated kiln at 85 °C for 80 hours. The dried half-width lumbers were surfaced to standard lumber sizes, 38 mm thick and 89 mm wide, for a nominal 2 by 4 [4]. The weight, width, thickness, length, bow, and crook of the lumbers were measured at each stage after sawing, drying, ripping, and surfacing. The bow and crook were measured in units of 1 mm using a thread and ruler. The numbers in Fig.2 indicate the timing of the measurements.

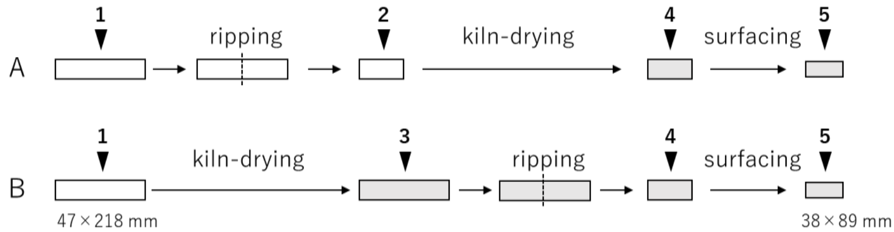

Fig. 2. Drying and ripping methods.

3 Results and discussions

Bow and crook measured after sawing, drying, ripping, and surfacing are shown in Figs. 3 and 4. The bow decreased after drying in both groups A and B. Little differences in bow were observed between both groups. The crook of lumber ripped immediately after sawing had clearly increased, and the crook increased further after drying in group A. In group B, the crook of wide lumbers hardly increased after drying. The average crook for lumbers ripped after drying increased slightly and varied more widely than wide lumbers before ripping. The crook for group B did not decrease after surfacing.

Bow and crook of 2-by-4 lumber after surfacing are shown in Table 1. The crook was expressed as the percentage of the cord height to the lumber length. Warp limits for A class structural lumber (requiring high bending performance) [4] are shown in Table 2. Based on bow, only one piece of 5 m lumber ripped before drying was rejected at the select structural grade. On the other hand, based on crook, the percentage of rejects for the 5 m select structural grade were 70.8% of the lumbers that were ripped before drying and 20.8% of the lumbers that were ripped after drying. The 12.5% of the 5 m lumbers that were ripped before drying were rejected even at the No. 2 grade. As for the 2.5 m lumber, only one piece that was ripped after drying was rejected based on crook.

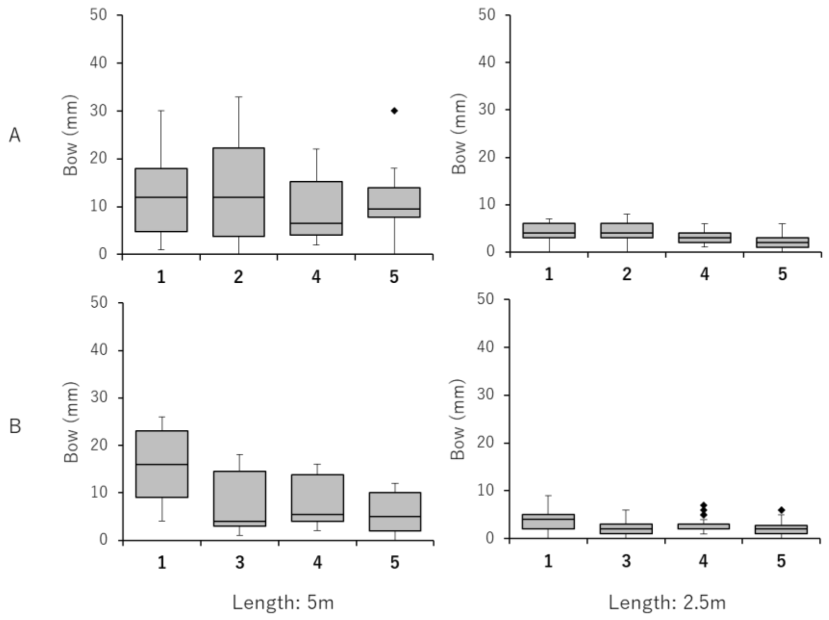

Fig. 3. Bow measured after sawing, drying, ripping, and surfacing.
(See Fig. 2 for the numbers on the horizontal axis.)

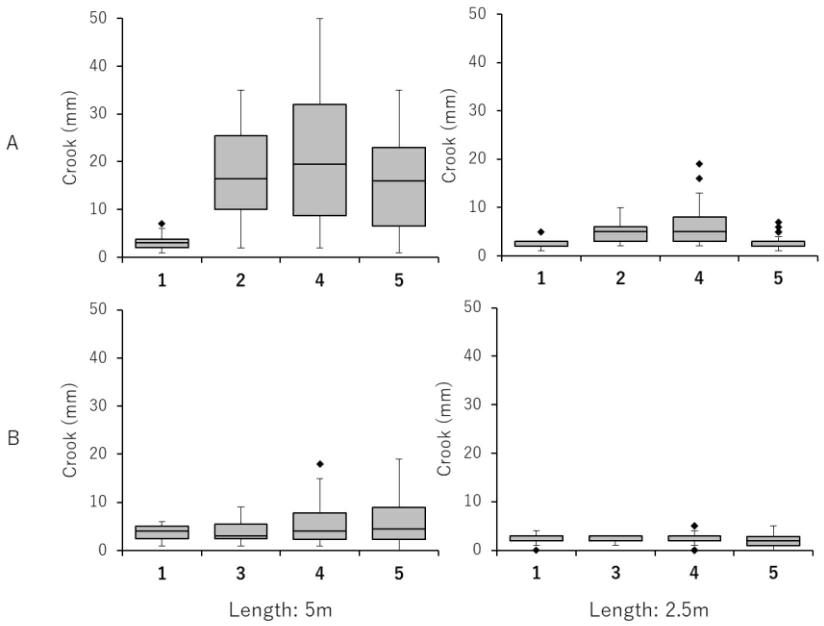

Fig. 4. Crook measured after sawing, drying, ripping, and surfacing.
(See Fig. 2 for the numbers on the horizontal axis.)

Table 1. Bow and crook of 2 by 4 lumbers after surfacing.

		Ripped before drying		Ripped after drying	
Length		5 m	2.5 m	5 m	2.5 m
n		24	42	22	42
Bow (mm)	mean	10.3	2.4	6.0	2.0
	SD	6.37	1.53	3.98	1.70
Crook (%)	mean	0.31	0.11	0.12	0.07
	SD	0.192	0.051	0.109	0.042

Table 2. Warp limits for A class structural lumber [4].

Grade		Select structural	No. 1	No. 2	No. 3
Bow (mm)	2.4-3.0 m	6	6	10	13
	4.8-5.4 m	19	19	25	38
Crook (%)		0.2	0.2	0.5	0.5

4 Conclusion

In the case of 2.5 m length lumber, the effect of the sawing and drying processes on crook was not significant. Therefore, the order of the ripping processes should be determined based on the production efficiency of each sawmill. For 5 m length lumber, ripping after drying would be recommended because ripping before drying causes larger crook. However, even in the case of the ripping after drying, the percentage of rejects based on crook is high. Therefore, the rough sawn size of wide lumber before drying needs to be larger.

Acknowledgements

This research was supported by the research grant #202102 of the Forestry and Forest Products Research Institute, and MAFF Commissioned project study on “Development of a stable supply system for domestic lumber by utilizing large-diameter logs” Grant Number JPJ012040.

References

1. Layton, T. F., Smith, W. R., Maeglin, R. R.: An evaluation of the saw, dry and rip process to convert red alder into studs. Wood Sci. Technol. 20, 185-200 (1986).
2. Ratnasingam, J., Scholz, F.: Yield improvement in Rubberwood sawmilling through the saw, dry and rip (SDR) technique. Eur. J. Wood Prod. 70, 525–526 (2012).
3. Ishiguri, F., Mitani, A., Iizuka, K., Yokota, S., Yoshizawa, N.: Effects of Saw-dry-rip Process on Warp Reduction in Japanese Cedar 2 by 4's. Bulletin of the Utsunomiya University Forests 40, 95-91 (2005).
4. Japanese Agricultural Standards: Structural Lumber and Finger Jointed Structural Lumber for Wood Frame Construction, JAS 0600 (2020).

Deep learning approaches for the automation of lathe check detection in wood veneers

Caroline Marc[1], Hugo Curial[1], Bertrand Marcon[1], Louis Denaud[1], Stéphane Girardon[1]

[1] Arts et Metiers Institute of Technology, LABOMAP, F-71250 Cluny, France

Abstract. Lathe checks are cracks that develop in veneers during the peeling process due to mechanical traction stresses, affecting both mechanical performance and adhesive bonding. Their detection is needed for optimizing veneer grading and ensuring product reliability especially glue consumption. Traditional assessment methods, such as dye penetration or acoustic analysis, are either labour-intensive, destructive, or indirect. Imaging-based techniques have shown promising results but remain challenging to automate due to variations in wood properties and surface conditions. This study proposes a deep learning approach for real-time lathe check detection. A U-Net-based convolutional neural network is trained on veneer images to segment lathe checks with high precision. The method is validated using a high-speed imaging system installed directly on the peeling lathe, allowing continuous monitoring of veneer quality. In addition, manual offline analyses are conducted to cross-validate predictions. Results show that the proposed approach accurately detects lathe checks, demonstrating a strong correlation with reference measurements. The model is robust to variations in wood species and cutting parameters, making it suitable for industrial applications. This automated method provides a scalable and reliable solution for veneer quality control, enabling manufacturers to optimize production and reduce defects in laminated wood products.

Keywords: convolutional neural network, lathe check, semantic segmentation, U-Net, wood veneer, peeling

1 Introduction

During the peeling process for veneer production, cracks known as lathe checks develop in the cutting zone due to a combination of mechanical stresses, particularly a traction stress field ahead of the knife [1]. The extent and frequency of these lathe checks are influenced by several parameters, including veneer thickness, wood characteristics, and processing conditions [2]. Since lathe checks affect both the mechanical performance and adhesive bonding quality of veneers [3], [4], [5], [6], [7], their detection and quantification are essential for optimizing veneer grading and ensuring product reliability.

Historically, lathe check assessment has relied on dye penetration techniques followed by microscopic examination [8], [9]. While effective, these methods are labour-intensive and impractical for large-scale industrial applications, prompting research into alternative techniques such as acoustic analysis [10], [11]. By monitoring sound emissions and cutting forces, Denaud et al. [12] estimated lathe check frequency, though these methods primarily infer their presence rather than directly measuring their geometry. Imaging-based solutions have also been explored, such as transillumination [13], which achieved a coefficient of determination (R^2) of 0.86 when estimating lathe check depth.

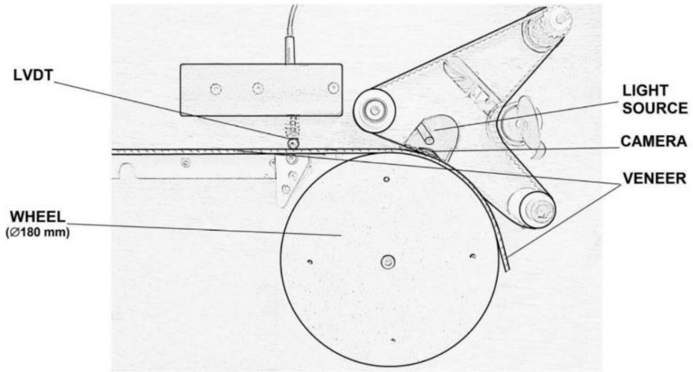

Fig. 1. Lathe checks opening measurement system (SMOF) [2] (LVDT : linear variable differential transformer)

A different imaging technique, using a lathe checks opening measurement system called SMOF (for "Système de Mesure d’Ouverture des Fissures" in French) , illustrated in Figure 1, was introduced at LaBoMaP to visualize lathe checks in the radial-tangential (RT) plane [14]. By capturing veneer edge images over a curved support, this system enhances lathe check visibility. However, despite its ability to provide detailed mappings, the automated detection process remains inconsistent across different wood types and lathe check morphologies, often requiring manual adjustments [13]. Moreover, the use of a pulley to slightly open lathe check may have an influence on the real depth of lathe checks.

Previous studies have explored lathe check detection on veneer surfaces [13] or within veneer-based panels [15], as well as cross-sectional imaging techniques using image processing after contrast enhancement [14], [16]. More broadly, crack detection in wood and other porous materials has leveraged both classical image analysis and deep learning methods [17]. While traditional approaches rely on grayscale thresholding and orientation-based filtering [18], [19], [20], recent advances in convolutional neural networks (CNNs) have significantly improved crack segmentation [21], [22], [23], [24].

A deep learning-based method for lathe check detection was recently proposed [25], demonstrating high segmentation accuracy on veneer cross-sections images obtained with the SMOF. This study investigates the applicability of that approach to real-time detection of lathe checks during the peeling process. This approach should give the true lathe check depth and distribution since the measurement is performed during the cutting process. High-speed imaging is used to capture lathe checks as they form at the cutting zone, and lathe check detection is performed using the method described in detail by Marc et al. [25] and presented in the following sections.

2 Materials and methods

2.1 Presentation of the detection method

The detection method proposed by Marc et al. [25] takes as input a grayscale image of the veneer edge (transverse plane) and produces an accurate mapping of the lathe checks present in this image. The maps are obtained through semantic segmentation, which classifies pixels into two categories: "lathe check presence" (white pixel) or "lathe check absence" (black pixel). This segmentation is performed using a state-of-the-art neural network specialized in this task, the U-Net network, developed by Ronneberg et al. [26].

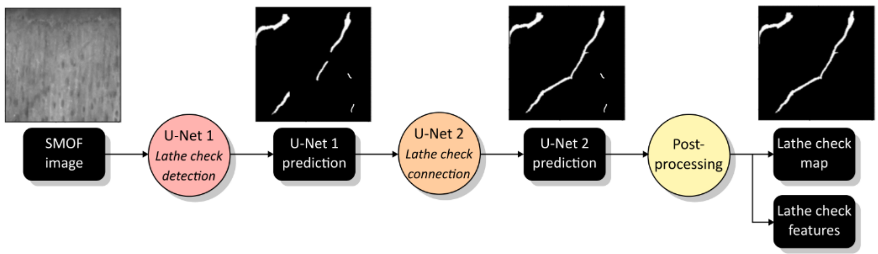

Fig. 2. Block diagram of the lathe checks detection process [25]

More specifically, detection is carried out using two consecutive U-Nets, as the method consists of three steps, illustrated in Figure 2:

1. The first U-Net aims to detect lathe checks. In some cases, when lathe checks are difficult to discern, they may appear on the U-Net prediction as "discontinuous", meaning they are divided into several groups of white pixels.
2. The second U-Net is therefore designed to connect these groups of pixels.
3. The final step is post-processing, which refines the mapping by denoising and linking the remaining lathe checks so that, in the end, each group of white pixels corresponds to a complete lathe check. This step also generates a table (in CSV format) containing the characteristics of each lathe check, such as depth and position.

Before being used, a supervised network must be trained on a dataset comprising a large number of input-output pairs to adjust the network parameters to the studied problem. Two datasets were thus created to train each of the two U-Nets separately. The first dataset consists of images obtained using the SMOF on the edge of peeled poplar veneer under pressure rates of 10% and 15%, along with their corresponding binary masks (ground truth). These masks were generated by manually labeling each pixel belonging to a lathe check. Poplar was chosen for this study due to its mesoscale homogeneity, which simplifies lathe check detection. The second dataset, used for training the second U-Net, consists of images predicted by the first U-Net and their corresponding manually labelled images, ensuring the connection of discontinuous lathe checks. The details regarding the training process and network performance evaluation are provided in [25].

2.2 Data collection

To capture images of lathe checks during the peeling process, a micro-peeling lathe from LaBoMap was used, equipped with a high-speed camera to record the cutting zone. Three poplar (Populus × canadensis, clone I-214) discs from the same tree were used, ensuring consistency with the dataset that trained the model. From each disc, a veneer ribbon was obtained and analysed. The widths of the veneers are provided in Table 1. Peeling was performed at a pressure rate of 10%, with a veneer thickness of 3 mm, matching the conditions used for the training images. The high-speed camera was operated at a frame rate of 1200 fps, with an exposure time of 250 µs. The peeling speed was 500 $m.s^{-1}$, meaning that an image was captured every 0.42 mm of peeled veneer.

Table 1. Veneer width

Veneer ID	Width (tangential direction, mm)
1	454
2	456
3	490

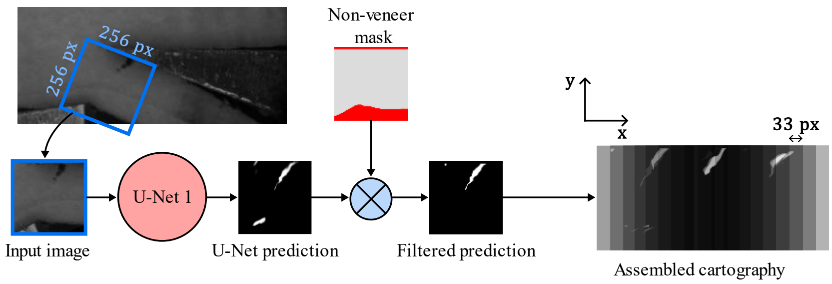

Fig. 3. Process of transforming peeling images into peeling lathe checks maps

To transform the large number of cutting zone images into a lathe checks map for each veneer, the steps illustrated in Figure 3 are followed. First, the images are rotated by 20.7°, corresponding to the knife attack angle. This adjustment ensures that the veneer's tangential direction appears horizontal, aligning with the images used for training the network and facilitating post-processing. Next, a 256×256 px window —

matching the network's input dimensions — is extracted from each image at the cutting zone and processed by U-Net 1 to generate a lathe checks map. In this image, pixels corresponding to the knife, the pressure bar, or areas outside the veneer are set to zero, as they cannot belong to a lathe check. Then, all images from the same veneer sheet are sequentially assembled with an offset of 0.42 mm (33 px) in the x-direction of Figure 3, corresponding to the veneer's tangential direction. Finally, a post-processing step is applied to the final image to denoise it and extract lathe checks characteristics — such as depth and position — in the form of a table.

The U-Net 2, designed to connect fragmented lathe checks, was not used in this study, as it was observed that the lathe checks were sufficiently "open" at the time of their formation for the U-Net 1 alone to be sufficient.

2.3 Reference measurement

To compare the lathe checks maps obtained through deep learning with a reference value and a complete image of the veneer, the three veneer sheets were analysed using the SMOF system. This system images the veneer edges with the lathe checks opened by passing the veneer over a pulley. The pulley diameter was chosen based on the veneer thickness to prevent additional cracking [14].

The resulting images are 12-bit grayscale with a resolution of 115 px.mm^{-1} in the wood's radial direction and 69 px.mm^{-1} in the tangential direction. The SMOF software allows for the manual detection of lathe checks in these images and generates a table containing the depth and position of each lathe check.

3 Results and discussions

3.1 Detection method performance

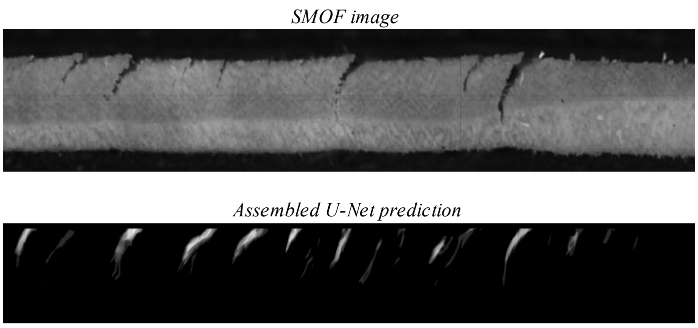

Fig. 4. SMOF image of a part of veneer *1* and the corresponding part of the assembled U-Net lathe checks prediction

Figure 4 shows the edge image of a veneer produced by the SMOF and the corresponding lathe check map obtained using the method described in Section 2.2. Even though the mapping is still somewhat noisy, most of the lathe checks appear to be correctly detected, even those that are difficult to discern in the SMOF photograph.

3.2 Comparison with the reference measurements

Table 2 and Figure 5 provide a more quantitative assessment of the accuracy of automatic lathe check detection, considering the entire length of the veneers. Table 2 presents the number of lathe checks detected for each veneer and each detection method. For all three veneers, the number of detected lathe checks is very similar across methods.

Table 2. Number of lathe checks detected by detection method

Veneer ID	1	2	3
SMOF	173	174	164
U-Net	174	170	165

Figure 5 illustrates the distribution of lathe check depths for each veneer and detection method. It can be observed that the U-Net tends to detect slightly deeper lathe checks compared to manual detection. This discrepancy could be due either to a limitation of the developed method, or to the fact that some lathe checks appear more open and thus more visible at the moment of their formation than when imaged by the SMOF. In the latter case, in-line detection using image analysis would not only be more optimized but also more reliable than offline manual detection.

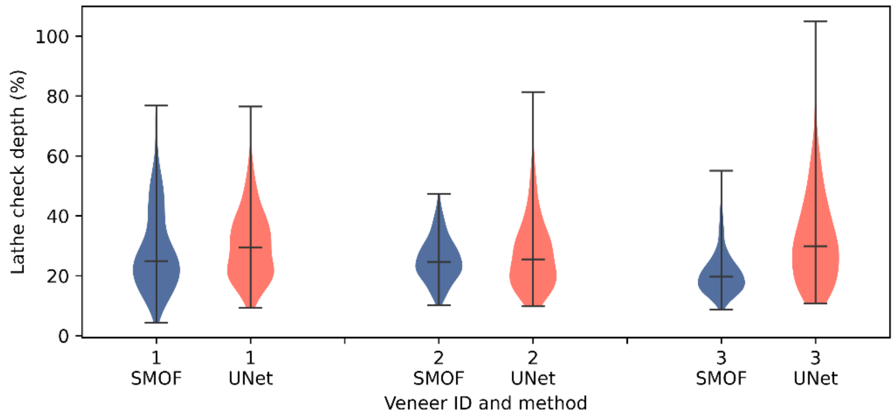

Fig. 5. Comparison of the distribution of lathe check depths, for lathe checks detected with the proposed method (U-Net) and the SMOF (manual method)

3.3 Discussions

This study was highly exploratory, as it was conducted on only three veneer samples, a single wood species, and a single pressure bar setting. Despite these limitations, the results indicate that in-line lathe check detection using deep learning is a promising approach. The number of detected lathe checks was similar between the automatic and manual methods, and the U-Net-based detection provided clear defect maps.

One key observation is that the U-Net model, originally trained on veneer images where lathe checks were enhanced through laser cutting for better visibility, was successfully applied to rabbeted veneer surfaces. This indicates that the method is robust to variations in surface conditions, at least within the scope of this study. Moreover, not using a pulley ensures that the depth of the measured cracks does not exceed the depth of the lathe checks generated.

Regarding processing time, both detection methods require only a few minutes. However, the automated approach has a significant advantage: it does not require an operator and can be performed in the background while other tasks proceed in parallel. In contrast, manual detection with the SMOF demands active intervention, making it less practical for industrial implementation.

4 Conclusion

This exploratory study explored the feasibility of using deep learning for real-time lathe check detection during the veneer peeling process. The proposed method, based on high-speed imaging and U-Net segmentation, successfully identified lathe checks as they formed at the cutting zone. The results showed a strong agreement with the manual reference detection method using SMOF imaging, with similar lathe check counts and depth distributions. These findings are highly promising for the industry, especially if the fissuring observed at the veneer edge is considered representative of what occurs along the entire veneer length.

Further research should focus on extending the dataset to various wood species and peeling parameters, improving detection accuracy, and assessing integration into an industrial workflow. Implementing such a system could ultimately enhance veneer quality control while reducing manual inspection efforts.

Acknowledgements

This study is funded by the ANR21-CE43-0008-02 BOOST project and the ADEME (French agency for ecological transition). The authors thank the technical platform Xylomat of the scientific network Xylomat financed by the ANR-10-EQPX-16 XYLOFOREST, which was largely used to carry out this study.

References

1. B. Thibaut et J. Beauchêne, « Links between Wood Machining Phenomena and Wood Mechanical Properties: The Case of 0°/90° Orthogonal Cutting of Green Wood », in *Proceedings of the 2nd Int. Symposium on Wood Machining*, Vienna, Austria, 2004, p. 149-160.

2. A. Rohumaa, J. Viguier, S. Girardon, M. Krebs, et L. Denaud, « Lathe check development and properties: effect of log soaking temperature, compression rate, cutting radius and cutting speed during peeling process of European beech (Fagus sylvatica L.) veneer », *Eur. J. Wood Wood Prod.*, vol. 76, nº 6, p. 1653-1661, nov. 2018, doi: 10.1007/s00107-018-1341-9.
3. D. DeVallance, J. Funck, et J. Reeb, « Douglas-fir plywood gluebond quality as influenced by veneer roughness, lathe checks, and annual ring characteristics », *For. Prod. J.*, vol. 57, nº 1/2, p. 21, 2007.
4. G. Pot, L. E. Denaud, et R. Collet, « Numerical study of the influence of veneer lathe checks on the elastic mechanical properties of laminated veneer lumber (LVL) made of beech », *Holzforschung*, vol. 69, nº 3, p. 247-316, 2015, doi: 10.1515/hf-2014-0011.
5. I. Rahayu, L. Denaud, J. C. Butaud, et G. Pot, « Qualités technologiques des panneaux contreplaqués et LVL réalisés avec les nouveaux cultivars de peuplier », *For.-Entrep.*, nº 213, p. 39-42, 2013.
6. A. Rohumaa, C. G. Hunt, M. Hughes, C. R. Frihart, et J. Logren, « The influence of lathe check depth and orientation on the bond quality of phenol-formaldehyde–bonded birch plywood », *Holzforschung*, vol. 67, nº 7, p. 779-786, 2013.
7. A. Rohumaa, T. Antikainen, C. G. Hunt, C. R. Frihart, et M. Hughes, « The influence of log soaking temperature on surface quality and integrity performance of birch veneer », *Wood Sci. Technol.*, vol. 50, nº 3, p. 463-474, mai 2016, doi: 10.1007/s00226-016-0805-5.
8. J. F. Lutz, « Heating veneer bolts to improve quality of Douglas-fir plywood », Rapport d'étude, 1960.
9. E. Movassaghi, « Influence des paramètres microdensitométriques du bois sur les efforts de coupe et la qualité des placages de Douglas et de Châtaignier obtenus par déroulage », Thèse, 1985.
10. L. Tomppo, M. Tiitta, et R. Lappalainen, « Ultrasound evaluation of lathe check depth in birch veneer », *Eur. J. Wood Wood Prod.*, vol. 67, nº 1, p. 27-35, 2009.
11. J. Wang, J. Biernacki, et F. Lam, « Nondestructive evaluation of veneer quality using acoustic wave measurements », *Wood Sci. Technol.*, vol. 34, nº 6, p. 505-516, 2001.
12. L. Denaud, L. Bleron, A. Ratle, et R. Marchal, « Online control of wood peeling process: Acoustical and vibratory measurements of lathe checks frequency », *Ann. For. Sci.*, vol. 64, nº 5, p. 569-575, 2007.
13. T. Antikainen, J. Eskelinen, A. Rohumaa, T. Vainio, et M. Hughes, « Simultaneous measurement of lathe check depth and the grain angle of birch (Betula pendula Roth) veneers using laser trans-illumination imaging », *Wood Sci. Technol.*, vol. 49, nº 3, p. 591-605, mai 2015, doi: 10.1007/s00226-015-0718-8.
14. B. Pałubicki *et al.*, « A Method of Lathe Checks Measurement; SMOF device and its software », *Eur. J. Wood Wood Prod.*, vol. 68, nº 2, p. 151-159, mai 2010, doi: 10.1007/s00107-009-0360-y.
15. M. D. Burnard, L. Muszyński, S. Leavengood, et L. Ganio, « An optical method for rapi examination of check development in decorative plywood panels », *Eur. J. Wood Wood Prod.*, vol. 76, nº 5, p. 1367-1377, sept. 2018, doi: 10.1007/s00107-018-1327-7.
16. V. Grubîi et J. Johansson, « An image processing algorithm for detection and analysis of slicing checks », *Eur. J. Wood Wood Prod.*, vol. 79, nº 4, p. 999-1006, juill. 2021, doi: 10.1007/s00107-021-01672-8.
17. H. S. Munawar, A. W. A. Hammad, A. Haddad, C. A. P. Soares, et S. T. Waller, « Image-Based Crack Detection Methods: A Review », *Infrastructures*, vol. 6, nº 8, p. 115, août 2021, doi: 10.3390/infrastructures6080115.

18. S. M. Bhandarkar, T. D. Faust, et M. Tang, « CATALOG: a system for detection and rendering of internal log defects using computer tomography », *Mach. Vis. Appl.*, vol. 11, nº 4, p. 171-190, déc. 1999, doi: 10.1007/s001380050100.
19. S. M. Bhandarkar, X. Luo, R. Daniels, et E. W. Tollner, « Detection of cracks in computer tomography images of logs », *Pattern Recognit. Lett.*, vol. 26, nº 14, p. 2282-2294, oct. 2005, doi: 10.1016/j.patrec.2005.04.004.
20. P. Wang et H. Huang, « Comparison Analysis on Present Image-based Crack Detection Methods in Concrete Structures », *3rd Int. Congr. Image Signal Process. CISP2010*, 2010.
21. G. Doğan et B. Ergen, « A new mobile convolutional neural network-based approach for pixel-wise road surface crack detection », *Measurement*, vol. 195, p. 111119, mai 2022, doi: 10.1016/j.measurement.2022.111119.
22. R. Ehtisham *et al.*, « Computing the characteristics of defects in wooden structures using image processing and CNN », *Autom. Constr.*, vol. 158, p. 105211, févr. 2024, doi: 10.1016/j.autcon.2023.105211.
23. T. He, Y. Liu, Y. Yu, Q. Zhao, et Z. Hu, « Application of deep convolutional neural network on feature extraction and detection of wood defects », *Measurement*, vol. 152, p. 107357, févr. 2020, doi: 10.1016/j.measurement.2019.107357.
24. Y. Lin, Z. Xu, D. Chen, Z. Ai, Y. Qiu, et Y. Yuan, « Wood Crack Detection Based on Data-Driven Semantic Segmentation Network », *IEEECAA J. Autom. Sin.*, vol. 10, nº 6, p. 1510-1512, juin 2023, doi: 10.1109/JAS.2023.123357.
25. C. Marc, B. Marcon, L. Denaud, et S. Girardon, « U-NET-based deep learning for automated detection of lathe checks in homogeneous wood veneers », *Eur. J. Wood Wood Prod.*, vol. 83, nº 2, p. 54, avr. 2025, doi: 10.1007/s00107-025-02208-0.
26. O. Ronneberger, P. Fischer, et T. Brox, « U-Net: Convolutional Networks for Biomedical Image Segmentation », Munich, Germany: Springer International Publishing, oct. 2015, p. (pp. 234-241).

Attempts at controlling the size of Japanese cedar chip by adjusting cutting conditions of a disc chipper

Yosuke Matsuda[1[0000-0003-3160-7158]], Yukari Matsumura[1], Takashi Yanagida[1[0009-0007-3362-6754]], and Kiyohiko Fujimoto[1]

[1] Forestry and Forest Products Research Institute, Tsukuba City, Ibaraki 305-8687, JAPAN
yosukem@ffpri.affrc.go.jp

Abstract. In recent years, the number of small-scale, wood chip gasification combined heat and power plants is increasing in Japan. However, it is known that the annual operating hours of such plants are shorter than that of conventional large-scale biomass power plants, due to the difficulty in supplying chips of the ideal size that would guarantee the stable operation of gasification combined heat and power plants. Our goal is to develop a technique for efficient production of optimized chips for the combined heat and power plants by optimizing cutting processes. Here, we investigated the effects of some cutting conditions on the chip size distribution. The experimental setup involved three rotation speeds (560, 720, and 880 rpm), three board feed speeds (0.3, 0.7, and 1.0 m/s), and two sharpness angles (38° and 40°). The particle size distribution of wood chips was measured using a screening method and approximated to a Rosin-Rammler distribution. Two types of screening sieves, woven wire mesh sieve and perforated plate sieve, were used for the screening. The results suggested that chip size decreased with increasing the rotation speed. The smaller chip was produced when the smaller sharpness angle was employed.

Keywords: chip, particle size distribution, Rosin-Rammler distribution.

1 Introduction

Wood chips are used as fuel for biomass power generation, which contributes to reductions in greenhouse gas. Recently, locally available wood biomass is attracting attention as a small-scale, decentralized energy source in Japan, as it has the potential to stimulate the local economy [2]. Japan's feed-in tariff system, implemented in 2015, offers preferential treatment to the electricity generated by small-scale power plant with a capacity of less than 2000 kW [3]. These small-scale biomass power plants in Japan often utilize wood chip gasification combined heat and power (CHP) plants that were originally designed in Europe [3,4]. However, these power plants have shorter annual hours of operation compared to large-scale power plants, due to the difficulty in achieving stable gasification; this is attributed in part to the difficulty in supplying chips of a particular size that ensure the stable operation of gasification CHP plants [3,4]. The chips produced in Japan are primarily optimized for pulp production, and therefore may not fully meet the regulations for gasification CHP plants [3]. The presence of oversized or undersized chips can lead to turbulence in the gas flow within the gasifier, which would result in tar formation [4]. This necessitates the removal of oversized or undersized chips through screening, which consequently reduces the yield. For the stable operation of gasification CHP plants, a technique to control chip size by optimizing cutting conditions is necessary. By using the technique, a wood chip supplier may efficiently produce ideally sized chips for the stable operation of CHP plants without large capital investments such as acquiring a new chipper.

Several studies have investigated the relationship between cutting conditions and the particle size distribution of chips produced by a disc chipper [5-7]. In our previous study [7], we investigated the effects of disc rotation speed and board feed speed on the size of chips produced by a disc chipper. It is necessary to identify other cutting conditions that can substantially alter the chip size, and to clarify the impact of those conditions. Here, we conducted a review of the methods and results of the previous study. Additionally, we present new experimental results, which include the measurement of chip dimensions. The knife with a sharpness angle different from the one used in the previous study was newly tested.

2 Materials and Methods

2.1 Specimens

The raw material for the chips were 105 boards, including 86 flat-sawn boards, seven rift-sawn boards, and 12 boards with pith. The boards were converted from Japanese cedar (Cryptomeria japonica) logs harvested in Ibaraki Prefecture, Japan. The dimensions of the boards were 900 mm in length, 35 mm in height, and 105 mm in width. The mean and standard deviation (SD) of moisture content were 77.1% and 28.4%, respectively. The mean of green density was 598 kg/m3 (SD = 108).

2.2 Conversion of boards into chips

A disc chipper (800DK, CKS Chuki Co., Ltd.) with a board feeding belt conveyor was used to convert boards to chips. The diameter of the disc was 762 mm. Four chipper knives were installed radially on the disc. The length of the cutting edge was 230 mm. The distance from the middle of the cutting edge to the rotation axis of the chipper was 235 mm. Figure1 shows the schematic diagram of the cutting process. Two sharpness angles (38° and 40°), three rotation speeds (560, 720, and 880 rpm) and three board feed speeds (0.3, 0.7, and 1.0 m/s) were tested. The tested combinations of sharpness angle, rotation speed, and board speed are shown in Table 1. For each combination, 15 boards were converted into chips. The clearance angle was 3°, and the spout angle was 35°.

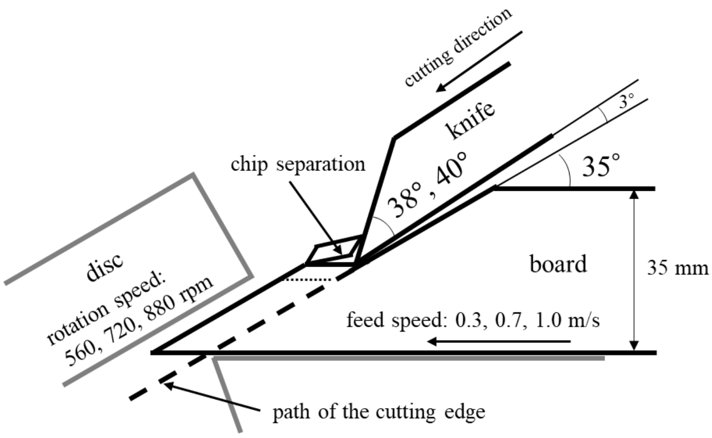

Fig. 1. A schematic diagram of the cutting process.

Table 1. Combinations of sharpness angle, rotation speed, feed speed.

Sharpness angle (°)	Rotation speed (rpm)	Feed speed (m/s)
38	720	0.7
40	560	0.3
40	560	0.7
40	560	1.0
40	720	0.3
40	720	0.7
40	720	1.0
40	880	0.3
40	880	0.7
40	880	1.0

2.3 Measurement of chip size distribution

For each combination of sharpness angle, rotation speed, and feed speed, approximately 2 kg of representative chips were extracted from the overall sample using a sample splitter (RT75, Retsch GmbH). Half of the representative chips (approximately 1 kg) was screened using six woven wire mesh sieves (φ = 300 mm) with square aperture (Tokyo Screen Co., Ltd) and the other half was screened using six perforated plate sieves (φ = 305 mm) with circular aperture (Retsch GmbH). The side lengths of the square apertures were 2, 4, 8, 16, 26.5, 31.5 mm. The diameters of the circular apertures were 2, 4, 8, 16, 26.5, and 31.5 mm. The sieves were stacked so that the coarser sieve was above the finer sieves. The chips were allocated on the top sieve, which has the largest aperture. The stacked sieves were shaken for 10 min using a sieve shaker (AS 300, Retsch GmbH) at an amplitude of 1.0 mm. Since wet dusts and other small chips often adhered to screens and larger chips, chips were kiln-dried before screening. The chip samples were screened in six batches, as the sieve was of inadequate size to screen the entire sample. After shaking, the weight of the chips retained on each sieve was measured and the chip size distribution was determined.

The Rosin-Rammler distribution model [8] quantifies the relationship between the chip size x (mm) and the weight-based percentage of the chip larger than x, or cumulative oversize, $R(x)$ (%). The model is expressed by the following formula using constants x_e and n:

$$R(x)=100\times\exp\{-(x/x_e)^n\}. \qquad (4)$$

By taking the logarithm of both sides of eq. (1) twice, this relationship can be expressed as follows:

$$\ln(\ln 100/(R(x))) = n \times \ln(x/x_e) = n\times\ln x - n \times \ln x_e\,,\ x > 0. \qquad (2)$$

Equation 2 demonstrates a linear relationship between $\ln x$ and $\ln(\ln 100/(R(x)))$. When $R(x)$ is given for x = 2, 4, 8, 16, 26.5, 31.5 mm, the slope (n) and intercept ($-n \times \ln x_e$) of eq. (2) were estimated using the least-squares method, and values of x_e and n were determined [8]. The chip size at which R is equal to 50% (x_{50}), was calculated by solving the following equation:

$$50 = 100 \times \exp\{-(x_{50}/x_e)^n\}. \qquad (3)$$

2.4 Measurement of dimensions of chip

The length, width, and thickness of 100 chips passed through sieves with an 8-mm aperture and remained on the sieve with a 4-mm aperture were measured using a digital caliper. The same number of chips that remained on sieves with 8- and 16-mm apertures were also extracted, and their three dimensions were measured. The chip samples were produced when the sharpness angle was 40°, rotation speed was 720 rpm, and feed speed was 0.7 m/s.

3 Results and discussion

Figure 2 shows the fitted Rosin-Rammler curves of cumulative oversize distribution ($R(x)$) for sharpness angle of 38° (dotted line) and 40° (solid line). The darker line shows the result from the woven wire mesh sieves (square aperture) and the lighter line shows the result from the perforated plate sieves (circular aperture). The coefficient of determination (R^2) for the four fitted curves in Fig. 2 exceeded 0.99, which was similar to the results from the previous study [7]. This result confirmed that the Rosin-Rammler equation is a reliable model for explaining the chip size distribution produced by a disc chipper. The chips produced when the sharpness angle was 38° were slightly smaller than those produced when the sharpness angle was 40°. It was considered that the chips size would be changed more drastically by adjusting the sharpness angle over a wider range.

The overall chip size measured by the woven wire mesh sieves was smaller than that measured by the perforated plate sieves, as shown in Fig. 2. This tendency was also observed in the previous study [7]. Since the chips were thin flake-shaped particles, they were assumed to pass diagonally across the square aperture. This indicates that some chips which were too large to pass through a circular aperture may be able to pass through the same-sized square aperture. As a result, the woven wire mesh sieves may produce an underestimate of the chip size. The ratio of x_e for woven wire mesh sieve to x_e for perforated plate sieve was 0.79 for sharpness angle 38°. The ratio of n was 1.00. These results were similar to those of the previous study [7]. This result confirmed that a Rosin-Rammler equation derived from woven wire mesh sieve could be converted into the equation for perforated plate sieve [7]. This means that chip suppliers can evaluate the compliance of their chips with CHP plant regulations, regardless of the type of screen they use.

Figure 3 shows the means of the dimensions of chips that remained on the sieves with 4, 8, and 16 mm apertures. The figure indicates that the lengths of the chips were constant, while their width and thickness varied. This variability occurred despite the chips being produced under the same cutting conditions. The consistency of the length should be the result of the constant feed per knife, which was controlled by the rotation speed and feed speed. The thickness depended on the frequency of the chip separation along the grain direction (Fig. 1), and was therefore difficult to control. The width was also considered difficult to control, as the chips were struck by the disc and broken in the width dimension before being released from the chipper.

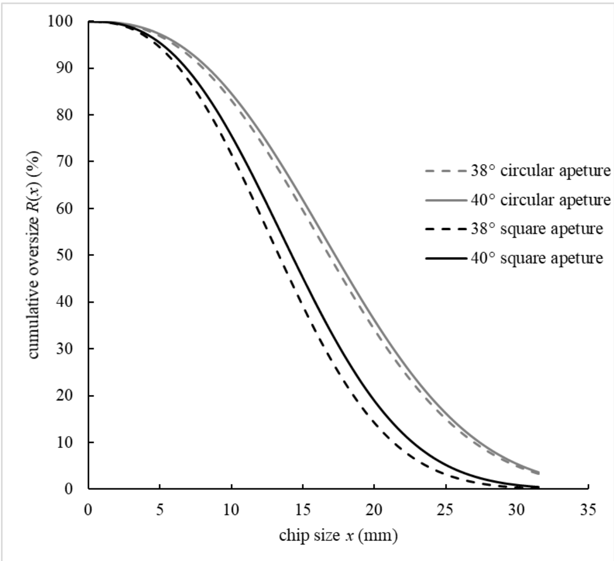

Fig. 2. Chip size distributions for two sharpness angles.

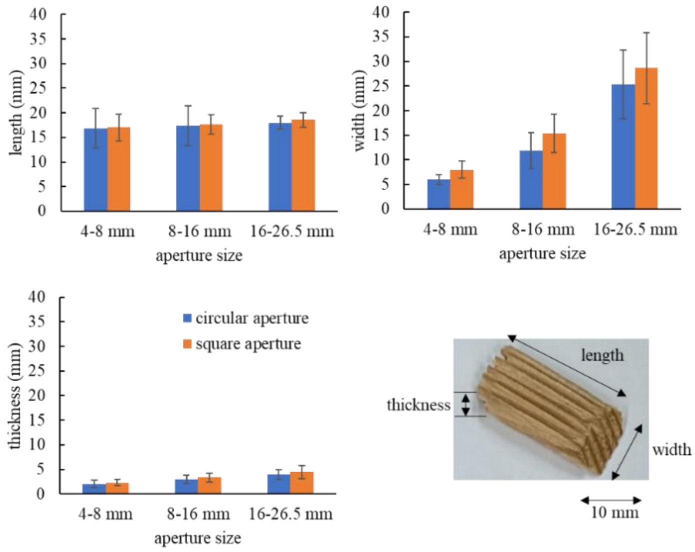

Fig. 3. Length, width, and thickness of chips produced when the sharpness angle was 40°, rotation speed was 720 rpm, and feed speed was 0.7 m/s.

Figure 4 shows the relationships of the rotation speed and feed speed on x_{50}. The chip size decreased with the increase in rotation speed. This was likely due to the feed per knife decreasing with increasing rotation speed, leading to decreased chip length.

Since the difference in x_{50} between 720 and 880 rpm was smaller compared to the difference between 660 and 720 rpm, further increases in rotation speed may not have a notable effect on chip size. The feed speed was also predicted to affect the feed per knife, although clear relationship between the feed speed and the chip size was not observed. The feed speed was controlled by a belt conveyor, but it was suggested that the boards were not being fed by the conveyor, but rather were self-fed by the rotation of the disc chipper once the cutting started [7].

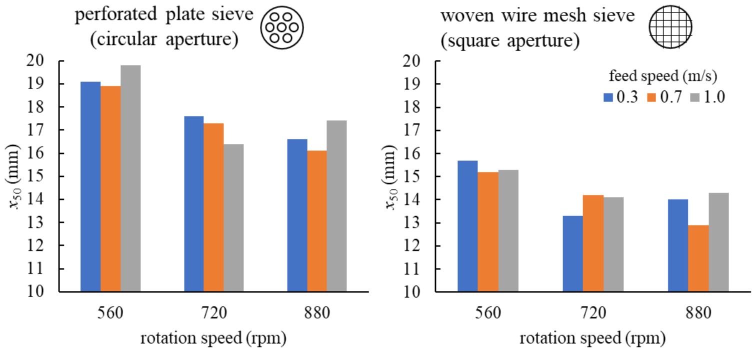

Fig. 4. Relationships of rotation speed and feed speed on x_{50}.

4 Conclusions

The results regarding the difference in chip size distribution between the sharpness angles of 38° and 40° indicate a potential relationship between the sharpness angle and the chip size. Its effect shall be further examined in subsequent research by varying the sharpness angle over a wider range. This study demonstrated that the production rate of the ideally sized chips for CHP plants can be enhanced by adjusting cutting conditions. However, it was challenging to achieve substantial effects of those adjustments within the range of parameters that were tested in this study. Moreover, it was found that the width and thickness of chips produced under identical cutting conditions are not uniform. For more efficient production of ideally sized chips for CHP plants, the effects of additional parameters shall be investigated in future studies.

Acknowledgements

This research was supported by the research program on the development of innovative technology grants (JPJ007097) from the Project of the Bio-oriented Technology Research Advancement Institution (BRAIN).

References

1. Kuboyama, H., Komata, H., Yanagida, T.: Conditions for establishing a combined heat and power station by using unutilized wood biomass. Journal of the Japanese Forest Society 99, 226–232 (2017).
2. Koido, K.: Technical, environmental, and economic sustainability in the use of energy from wood gasification combined heat and power. Wood Industry 77(8),292–297 (2022).
3. Yanagida, T.: The massive introduction of renewable energy and the current status of woody biomass power generation. Wood Industry 76(10), 370–375 (2021).
4. Sasauchi, K.: Latest trends and challenges of small-scale biomass gasification CHP in Japan. Nihon Enerugii Gakkai Kikanshi Enermix 101(6), 660–668 (2022).
5. Georges, R., Auchet, S., Méausoone, P.J.: Experimental study about the effects of disc chipper settings on the distribution of wood chip size. Biomass Bioenergy 35, 843–852 (2011).
6. Nati, C., Eliasson, L., Spinelli, R.: Effect of chipper type, biomass type and blade wear on productivity, fuel consumption and product quality. Croatian Journal of Forest Engineering 35(1), 1–7(2014).
7. Matsuda, Y., Matsumura, Y., Yanagida, T., Fujimoto, K.: Particle size distribution of Japanese cedar chip converted from boards using a disc chipper and its relationships with disc rotation speed and board feed speed. Journal of Wood Science 71, 1 (2025).
8. The Society of Powder Technology: Funtai Kougaku Binran. 2nd edn. Nikkan Kogyo Shimbun, LTD, Tokyo (1998).

Systematic and comprehensive quality specification and verification for furniture industry – DIN 919, DIN 68100, VDI 3414, VDI 3415

Adrian Riegel[1], Christian Kortüm[2], Frieder Scholz[2] and Karsten Binninger[2]

[1]Technische Hochschule Ostwestfalen-Lippe, Campusallee 12, 32657 Lemgo, Germany
[2]Technische Hochschule Rosenheim, Hochschulstraße 1, 83024 Rosenheim, Germany
adrian.riegel@th-owl.de

Abstract. Mostly in the furniture industry the quality approach is anecdotical. A systematic convergence of specifications for claims of functions and design is missing. With the mentioned German standards a system is now drafted or agreed, which follows the system of the Geometrical Product Speciation (GPS, ISO 8015) and offers new possibilities for coding on technical drawings but as well downstream the chain of standards to measuring or testing and in case process capability analysis. DIN 919-2 as a new drafted German standard for technical drawing in wood industry is opening up the whole tool set of GPS coding elements. DIN 68100 is adding a geometrical tolerance system including swelling or shrinkage. DIN68100-2 will propose statistical tolerancing to convolute variances in geometry caused e.g. by production with distributions in moisture content or shrinkage coefficients. VDI 3414 is offering specifications and corresponding verifications for attributive quality characteristics of wooden surfaces including a naming and coding system. Finally VDI 3415-2 is referring to measuring and production capability analysis esp. for the wood industry and related research. As far as possible the German standardization activities will be presented in the paper. The selected use case will be the edge banding and profile wrapping where the new guideline VDI 3412 will assist the practitioners and scientists concerning specification, verification but as well in trouble shooting.

Keywords: technical drawing, geometrical product specification and verification GPS, process capability, standards and guidelines, edge banding.

1 Introduction

The globalization is continuing also in the furniture branch. A precise specification of the needed part is a condition precedent to avoid misunderstandings and reclamations. Especially in the furniture branch due to a high number of variants the representation of a single part or article is only given in the ERP-system and drawings, which are mostly only similar. Besides these data additional specification are often given by textual description. During the IWMS 2019 in Oregon we gave already a brief introduction in several standardization activities ongoing in DIN and VDI [1]. These standards and guidelines will come soon to an end and provide then hopefully a comprehensive set for the specification of parts not only in the furniture industry but as well in the other wood branches. These set is based on the system of geometrical product specification and verification but is not totally limited to geometrical characteristics of the workpiece.

2 GPS Masterplan, GPS Matrix, GPS Chain

The ISO Committee ISO/TC 213 responsible for creating, updating, and maintaining the ISO GPS standards for geometrical product specifications and verification. These activities are nonspecific for a branch but the origin is the metal branch esp. the automotive and aerospace industry. The GPS system is fundamental, highly sophisticated and coherent but complex. For most standard use cases in the branch the GPS system maybe to complex but useful for consistent definitions of macro and micro geometry of workpieces in international contexts.

The masterplan (ISO 14638) combines different standards on the same field to chains [2]. The chain elements are defined for certain usage-related topics for the specification (first three elements) or verification (last three elements):

- Chain link A: symbols and indications;
- Chain link B: feature requirements;
- Chain link C: feature properties;
- Chain link D: conformance and non-conformance;
- Chain link E: measurement;
- Chain link F: measurement equipment;
- Chain link G: calibration;

The principles of the GPS system is defined by rules in ISO 8015; ISO 14638 provides an additional explanation [2, 3]The fundamental principles are invocation principle; principle of GPS standard hierarchy; definitive drawing principle; feature principle; independency principle; decimal principle; default principle; reference condition principle; rigid workpiece principle; duality principle; functional control principle; general specification principle; responsibility principle. Applying these principles leads to a consistent definition of geometric features of a workpiece up to final verification by testing or inspection [4].

A small overview of some key standards to understand the GPS system is listed in references. [5]. The GPS system is now consisting out of more than 200 standards, which are more or less linked to chains accordingly to geometrical characteristics as size, distance, form, orientation, location, run-out, profile surface texture, areal surface texture and surface imperfections. The GPS matrix is built up in that way and consistent system for geometrical specification is generated. To improve the application of the GPS standards, sometimes rules are given leading the reader thru the use cases.

The thesis of the activities in DIN and VDI is, that the principles, rules and the systematic of the GPS system will also be beneficial in the wood and furniture branch and will enhance or specify the specifications.

3 Geometry (DIN 919 and DIN 68100)

The GPS system is now partly adapted to the needs of the wood and furniture branches. Firstly, the geometrical definitions are consistently improved by rewriting and enhancing implemented DIN standards to the GPS standard.

3.1 Symbols and indications (A)

Since 1939 DIN 919-1 [6] is a national branch specific standard for drawings in the furniture craft. DIN 919-2 [7]:1972 was dedicated to the furniture industry esp. serial production but never was used very often and finally retreated 1986. Due to the usage in craft the DIN 919-1 will remain without GPS and will only be enlarged by several additional features. The new DIN 919-2 will be a GPS Standard fully implemented in the system. The full set of standards for chain elements A-G – mostly ISO standards for drawings e.g. ISO 129 [8] and tolerances e.g. ISO 1101 [9]. But DIN 919-2 offers also solutions for surfaces specifications for varnish, lacquer and divers laminates or veneer. A system will be proposed to work with variants without a drawing for each individual item. A syntax to work with equations for measures as well as for different surface layers will be defined.

3.2 Feature requirements and tolerances for dimensions (B-C)

Since 1984 DIN 68100 [10] is a national branch specific standard for dimensional tolerances in the furniture industry and other branches. DIN 68101 [11] enlarged the tolerance system to non-symmetrical tolerance fields according to ISO 286-1 [12] and -2 [13]. Apart from education DIN 68101 was not really used in wood and furniture industry and is now retreated. DIN 68100 is at the moment in rework and will be splitted to DIN 68100-1 defining a consistent system for measures of distances including swelling and shrinking. The used model with differential factors is well known in the branch but not yet described in a standard with listed factors for many wood species and wood based materials. DIN 68100-2 will still offer a tolerance system similar to IT-tolerances of ISO 286. But the intention is more to standardize a tolerance system according to ISO 22081 [14] – general tolerances based on profile form tolerances. The so toleranced workpieces are linearly scaled in size by the same factor, a systematic which fits better to the needs of the cabinet industry. Both parts of DIN 68100 are rule-based. DIN 68100-2 will describe in the appendix the method of statistical tolerancing. This method offers by convolution the statistical calculation of tolerance distributions for scattering of distances, moisture and differential shrinkage coefficient at the same time. The resulting distribution as a probability gives an idea what will happen to the workpiece or function during practical use.

4 Surface Characteristics (VDI 3414)

The surface characteristics of wood and wood-based materials play a crucial role in various applications, particularly in the furniture, door, and flooring industries. Unlike purely functional surfaces such as those of metal sheets, where GPS roughness parameters like Rz or Ra can be easily defined, the evaluation of wooden surfaces is far more complex. In addition to functional requirements, aesthetic aspects significantly influence the perception and acceptance of these products.

To address these complexities, the VDI 3414 guideline series provides a structured approach to the quality evaluation of wood and wood-based surfaces. Part 1 of this series, titled Quality Evaluation of Wood and Wood-Based Surfaces – Surface Characteristics [15], describes various surface characteristic through verbal descriptions. These descriptions are supplemented by figurative representations that illustrate specific characteristics, making it easier to classify and assess surface quality. In the latest revision of this guideline, numerical descriptions have been introduced to enable a more mathematical and objective quality definition. This development aims to establish a standardized approach for evaluating wooden surfaces according to the GPS System, esp. for chain link A-C .

Part 2 of the VDI 3414 series, titled Quality Evaluation of Wood and Wood-Based Surfaces – Testing and Measuring Methods [16], focuses on the practical aspects of evaluating surface characteristics. It outlines the procedures and techniques used to measure and quantify these features, ensuring consistency and reliability in quality assessment. Many surface characteristics can be measured using sensory analysis; therefore, Part 2 also provides methodologies for sensory quality testing, which is widely used in the food industry. This methodology includes training and calibration of inspectors and testing panels, as well as the actual sensory evaluations, allowing specific characteristics to be assessed objectively through human perception in both qualitative and quantitative terms. As a result, both parts of the VDI 3414 guideline fulfill the GPS Chain Links A to G, ensuring comprehensive and standardized surface quality assessment.

Furthermore, Parts 3 and 4 of the VDI 3414 series relate surface characteristics to specific processes and their evaluation. Part 3, titled Quality Evaluation of Wood and Wood-Based Surfaces – Milled, Sawn, Planed, Drilled, and Turned Surfaces [17], focuses on surface characteristics resulting from various machining processes, providing guidelines for assessing quality in these operations. Part 4, titled Quality Evaluation of Wood and Wood-Based Surfaces – Sanded Surfaces, specifically addresses the evaluation of sanded surfaces and their unique properties [18]. Both parts will be aligned with GPS standards in the next revision, similar to Part 1, ensuring a consistent and standardized approach to surface quality assessment.

By integrating verbal, figural (visual), and numerical descriptive approaches, VDI 3414 provides a comprehensive framework for defining and assessing the quality of wood and wood-based surfaces. This guideline helps manufacturers, quality control professionals, and researchers establish consistent standards, ensuring that both functional and aesthetic requirements are met in industrial applications.

5 Use case Narrow Surface Coating

5.1 VDI 3412 for Hotmelt applications

In the VDI committee GPL FA 102 a need for a new guideline in process optimization was identified: Hot melt application in surface coating. These activities should be guided by the GPS system already implemented in DIN 919, VDI 3414 and if possible DIN 68100. So far two sheets of VDI 3412 have been finished:

- Part 1, Basics for coating with hot melt glue applicable for all particular cases. Chapters: Gluing process, graphic representation, process input parameters, joining process and process parameters, quality indicators and assessment methods for furniture production and last not least causal research and trouble shooting [19].
- Part 2: Edgebanding and Softforming for the edges of flat workpieces. Chapters: Process technologies, materials, process control and corresponding quality indicators, process correlations, process output parameters and quality indicators, quality assessment and troubleshooting [20].

Further sheets in process will address profile wrapping (3) and 3D lamination (4).

5.2 Process correlations

The complexity of hotmelt applications is very high. Many input variables have to work coordinately together. It is difficult to calculate the influence of the process parameters on quality issues in a precise way. However, tendencies of a variety of variables on the peeling resistance F_s can be identified:

Table 1. Process correlations in the edgebanding process

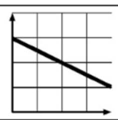	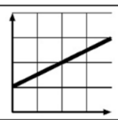	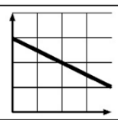	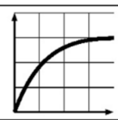	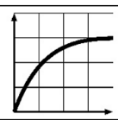
F_s = f(workpiece temperature)	F_s = f(heat conduction capacity of workpiece)	F_s = f(moisture of workpiece)	F_s = f(loose particles)	F_s = f(temperature of coating material)
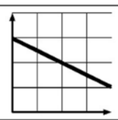	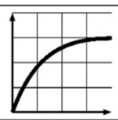	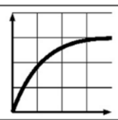	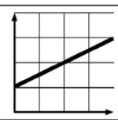	
F_s = f(moisture of coating material)	F_s = f(quantity of glue)	F_s = f (application temperature)	F_s = f (pressure)	

So VDI 3412-2 works also as a best practice guideline for process optimization.

5.3 List of Imperfections, figuratively expressed

In addition and acc. to VDI 3414-1 the guideline provides a large list of product imperfections like poor alignment or projection of the edge and the correlated reasons supplemented by images as far as possible, examples:

Table 2. Imperfections

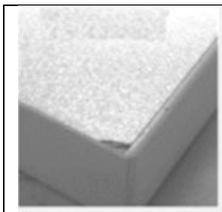		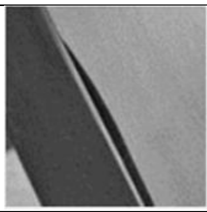	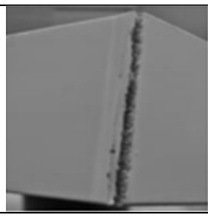
Chipping of cover	Open glueline	Edge not straight	Loose edge

5.4 Geometric product specification (GPS)

It is advisable to specify the product precisely before taking any further steps. This may seem trivial at first, as edge banding has been practiced for a long time. Nevertheless, it is generally useful to clearly define the characteristics within the respective limits (tolerances). The GPS standards system provides the necessary and clear representation of the geometry with characteristics and tolerances. Examples:

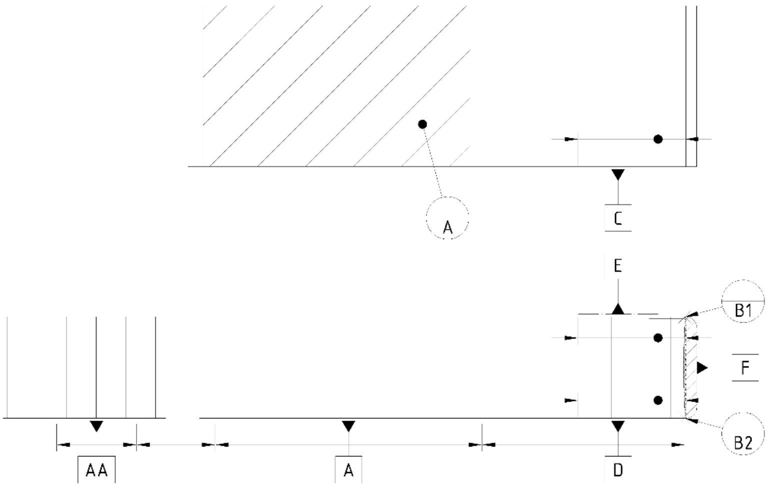

Fig. 1. Definition of workpiece geometry and tolerances within a predefined reference system

In particular, the parameters required to control automatic measuring machines can be defined in this way. The product (substrate with joined edge band) and the quality definition using form and position tolerances are shown graphically in accordance with GPS above. Additional notes are indicated by numbers in triangles. Indexed Greek lowercase letters refer to dimensions that must be replaced by the desired characteristics in the specific case. The tolerances corresponding to the dimensions can be recognized by the preceding "t". These must also be determined by specific information.

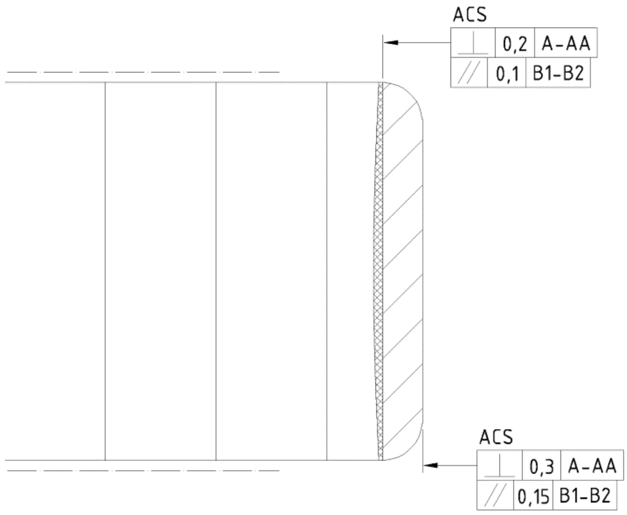

Fig. 2. Geometric definition of the edgeband

6 Outlook

The activities in DIN NA 042-04-03 and VDI GPL FA 102 are still on going. Releases are expected next year. But what already has been proved, a clear specification, better a consistent quality definition leads to a better understanding of the (customers) needs and on the other hand to a systematic approach for the verification. During the work on the guidelines and standards progress in science and technology concerning measurement and testing was elaborated.

Other experiences made in the working groups concern the degree of sophistication. The GPS system needs education and training like a new language or dialect. Maybe some practitioners will be overwhelmed but the best in class can surely benefit. On the long run, after the new standards and guidelines have been accepted and integrated in the education by Universities and Polytechnics, the whole branch can profit.

References

1. Riegel, A., Kortüm, C.: Geometric Dimensioning and Tolerancing of Furniture Components. In: IWMS-24 Proceedings, pp. 145–156. Oregon State University, Corvallis, OR, USA (2019).
2. DIN EN ISO 14638:2015-12-00: Geometrical product specifications (GPS) - Matrix model (ISO 14638:2015). Deutsches Institut für Normung e.V. Beuth Verlag, Berlin (2015)
3. DIN EN ISO 8015:2011-09-00: Geometrical product specifications (GPS) - Fundamentals - Concepts, principles and rules (ISO 8015:2011). Deutsches Institut für Normung e.V. Beuth Verlag, Berlin (2011).
4. Creo Parametric Online Help: Model-Based Definition – ISO2012 Rule Set. http://support.ptc.com/help/creo/creo_pma/german/index.htm#page/model-based_definition/ISO2012/Rule_Set.html last accessed 2019/05/15.
5. Weckenmann, A., Hunmienny, Z. (eds.): Geometrische Produktspezifikation (GPS) – Kurs für Technische Universitäten. Lehrstuhl QFM, Erlangen (2001).
6. DIN 919-1:2014-08-00: Technical drawings – Wood processing – Principles. Deutsches Institut für Normung e.V. Beuth Verlag, Berlin (2014).
7. DIN 919-1:1972-03-00: Technical Drawings for Woodworking; Series Production. Deutsches Institut für Normung e.V. Beuth Verlag, Berlin (1972).
8. DIN EN ISO 129-1:2020-02-00: Technical product documentation (TPD) - Presentation of dimensions and tolerances - Part 1: General principles (ISO 129-1:2018); German version EN ISO 129-1:2019. Deutsches Institut für Normung e.V. Beuth Verlag, Berlin (2020).
9. DIN EN ISO 1101:2017-09-00: Geometrical product specifications (GPS) - Geometrical tolerancing - Tolerances of form, orientation, location and run-out (ISO 1101:2017); German version EN ISO 1101:2017. Deutsches Institut für Normung e.V. Beuth Verlag, Berlin (2017).
10. DIN 68100:2010-07-00: Tolerance system for wood working and wood processing - Concepts, series of tolerances, shrinkage and swelling. Deutsches Institut für Normung e.V. Beuth Verlag, Berlin (2010).
11. DIN 68101:2012-02-00: Fundamental deviations and tolerance zones for wood working and wood processing. Deutsches Institut für Normung e.V. Beuth Verlag, Berlin (2012).
12. DIN EN ISO 286-1:2019-09-00: Geometrical product specifications (GPS) - ISO code system for tolerances on linear sizes - Part 1: Basis of tolerances, deviations and fits (ISO 286-1:2010 + Cor 1:2013); German version EN ISO 286-1:2010 + AC:2013. Deutsches Institut für Normung e.V. Beuth Verlag, Berlin (2019).
13. DIN EN ISO 286-2:2019-09-00: Geometrical product specifications (GPS) - ISO code system for tolerances on linear sizes - Part 2: Tables of standard tolerance classes and limit deviations for holes and shafts (ISO 286-2:2010 + Cor 1:2013); German version EN ISO 286-2:2010 + AC:2013. Deutsches Institut für Normung e.V. Beuth Verlag, Berlin (2019).
14. DIN EN ISO 22081:2022-11-00: Geometrical product specifications (GPS) - Geometrical tolerancing - General geometrical specifications and general size specifications (ISO 22081:2021); German version EN ISO 22081:2021. Deutsches Institut für Normung e.V. Beuth Verlag, Berlin (2022)
15. VDI 3414 Blatt 1:2019-02-00: Quality evaluation of wood and wood-based surfaces - Surface characteristics. VDI Verein Deutscher Ingenieure e.V. Beuth Verlag, Berlin (2019).
16. VDI 3414 Blatt 2: 2019-02-00: Quality evaluation of wood and wood-based surfaces - Testing and measuring methods. VDI Verein Deutscher Ingenieure e.V. Beuth Verlag, Berlin (2019)

17. VDI 3414 Blatt 3:2019-02-00: Quality evaluation of wood and wood-based surfaces - Milled, sawn, planed, drilled, and turned surfaces. VDI Verein Deutscher Ingenieure e.V. Beuth Verlag, Berlin (2019).
18. VDI 3414 Blatt 4:2019-02-00: Quality evaluation of wood and wood-based surfaces - Sanded surfaces. VDI Verein Deutscher Ingenieure e.V. Beuth Verlag, Berlin (2019).
19. VDI 3412 Blatt 1:2025-02-00: Coating of wood-based substrates using thermally reactivable adhesives and functional layers - Quality assurance and optimization – Fundamentals. VDI Verein Deutscher Ingenieure e.V. DIN Media, Berlin (2025).
20. VDI 3412 Blatt 2:2025-02-00: Coating of wood-based substrates using thermally reactivable adhesives and functional layers - Quality assurance and optimization - Edge banding and soft forming. VDI Verein Deutscher Ingenieure e.V. DIN Media, Berlin (2025).

Evaluation of the capability of poly-articulated robot for wood machining and identification of parameters correlated with surface quality in robotic wood machining

Nasri Linda[1], Curti Rémi[1], Larricq Pierre1, Eyma Florent1

[1] Institut Clément Ader (ICA) ; Université de Technologie Tarbes Occitanie Pyrénées ; CNRS, IMT Mines Albi, UPS, INSA, ISAE-SUPAERO ; IUT de Tarbes, 1 Rue Lautréamont, 65000 Tarbes, France
linda.nasri@iut-tarbes.fr

Abstract. Industrial robots have become a key technology across sectors for their cost efficiency availability and multi-axis flexibility, but their application in wood machining remains limited, with no studies on the quality of solid wood machined by robots. Achieving satisfactory surface finishes in wood machining is complex due to grain direction, often requiring sanding. While many sanding processes are automated, manual operations dominate for complex shapes. This study aims to evaluate the capability of a 6-axis robot in wood machining by comparing its dimensional, geometrical, and surface quality to the CNC router, the industry benchmark. It also aims to investigate the relationship between the roughness indicators of parts machined with different grain direction and signals measured during machining, determining the parameters correlated with the wood surface quality, and establish threshold values for roughness indicators beyond which sanding is required, allowing the identification of areas requiring finishing. To assess the robot's capability, oak, and fir samples were machined under identical conditions in six robot positions and with a CNC router, followed by dimensional, geometrical, and surface quality evaluations. The results show that a poly-articulated robot produces sufficient dimensional and geometrical quality for various wood applications, as well as surface quality comparable to that achieved by CNC router.

Keywords: Robotic machining, Dimensional and geometrical quality, Surface roughness

1 Introduction

Industrial robots have become a critical technology, particularly in the electronics and automotive sectors [1]. Industrial robots have been used for machining operations because they offer many advantages, such as large workspaces, high degree of freedom (DOF), and flexibility compared to computer numerical control (CNC) machines [2].

However, only 0.2% of all industrial robots worldwide are used in wood machining processes [3]: Their specific interest in this sector is not well defined. In the literature, some studies have evaluated the machining quality obtained by using a poly-articulated robot on different materials, some of which have compared these results with those obtained using a CNC machine. The surface quality obtained when machining with a poly-articulated robot can be equivalent to that of a CNC machine, as shown by a study on laminated composites [4]. However, in some cases it may be lower, particularly when machining aluminium [5]. In addition, it is noteworthy that in robotic machining, the robot's configuration also affects both dimensional accuracy and surface quality [6–8]. These two criteria can be important depending on the intended use of the machined wood (construction, carpentry, or furniture). At present, there is no assessment of the quality of solid wood resulting from robotic machining. This study aims to evaluate the capability of a 6-axis poly-articulated robot for wood machining in terms of dimensional, geometrical, and surface quality by comparing the results from machining parts with various characteristic features to those achieved using a CNC router.

2 Materials and Methods

2.1 Machining and metrological control

Specimens. In order to evaluate the robot capability in wood machining, two local wood species were chosen: a hardwood, oak, and a softwood, fir. The fir specimens each measure 200 × 180 × 19 mm3, and the oak specimens each measure 200 × 180 × 36 mm3. All of the oak and fir specimens come from rift-sawn boards. Their geometry was designed to allow for the verification of the main geometric specifications characteristic of a milled part, as detailed in the paragraph « **Control / Measurement methods** ». The specimens were conditioned in the laboratory at a temperature of 20 °C and a relative humidity of 65%.

Machining (Robot and CNC router). The specimens were machined using a CNC router (Dubus 3-axis) and a 6-axis poly-articulated robot (Kuka Kr 70) with a maximum payload of 70 kg and a theoretical position repeatability of +/- 0,05 mm, equipped with an electrospindle (HSD MT 1090 HSK A40). On the machining robot, 6 machining positions (Fig. 1 and 2)) were tested, to place the robot in different postures in order to determine the influence of its axis positions on the machining quality achieved. The reference frame of the workpiece in position 6 (Fig. 2), mounted on a 7^{th} axis (rotating table), was oriented at -45° around the Z-axis relative to the robot's base frame. These tests were repeated 5 times for a total of 30 specimens of each species, oak and fir. In addition, each position included a test without a workpiece. During the tests performed on the robot (including without the workpiece), various data were recorded in real time, including the theoretical and calculated cartesian positions of the robot, the angular positions of the joints, the robot's speed, as well as the torques and motor currents. This was achieved using the KUKA RobotSensorInterface (RSI) and the robot's internal sensors. On the CNC router, only one position, central on the worktable, was used as a reference for comparison. This test was also repeated 5 times. In total, 35 specimens of each species were machined. All the specimens were machined using the same cutting parameters (Table 1), typical for a semi-finishing operation. The selected cutting mode is up-milling for contour milling operations. The cutting tool used is a 2-teeth high-speed steel cutter with a diameter of 16 mm and a helix angle of 30°.

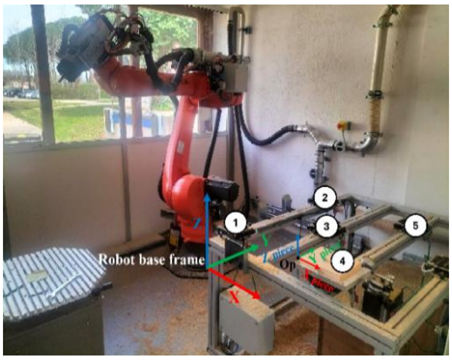

Fig. 1. The five positions on the machining table with the robot

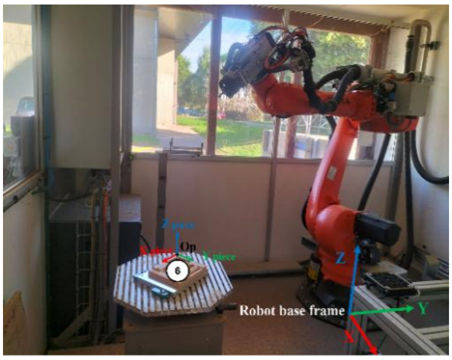

Fig. 2. The 6[th] machining position with the robot

Table 1. Machining parameters for the robot and the CNC router

Parameter (Unit)	Value
Rotational speed (rpm)	15 000
Cutting speed (m/s)	12,57
Feed rate (m/min)	10
Plunge feed speed (m/min)	0,5
Average chip thickness (mm)	0.14
Axial depth of cut (mm)	3
Radial depth of cut (mm)	3

Control / Measurement methods. The evaluation of the robot's capability for wood machining was conducted through three types of controls: dimensional, geometrical, and surface quality controls (Fig. 3).

Dimensional. Dimensional control was performed using a coordinate-measuring machine (GLOBAL Lite). Eight dimensions were controlled (Figure 3): The lengths and depths of slotted holes R1 and R2, machined along the Y-axis and X-axis of the robot respectively (except in position 6, where R1 and R2 are oriented at -45° around the Z-axis relative to the robot's cartesian base frame), with nominal lengths of 70 mm and nominal depths of 10 mm and the center-to-center distances between the four holes (nominal lengths C1C2 = C3C4 = 77 mm and C1C3 = C2C4 = 54 mm)

For each controlled dimension, the mean absolute error was calculated during machining with the CNC router and for each position during machining with the robot (Equation 1).

$$E_d = \frac{\sum_{i=1}^{n} |d_i - D|}{n} \quad (1)$$

Where:

E_d: The mean absolute error of the controlled dimension

d_i: Measured length of specimen number i (ranging from 1 to 5)
D: Nominal length

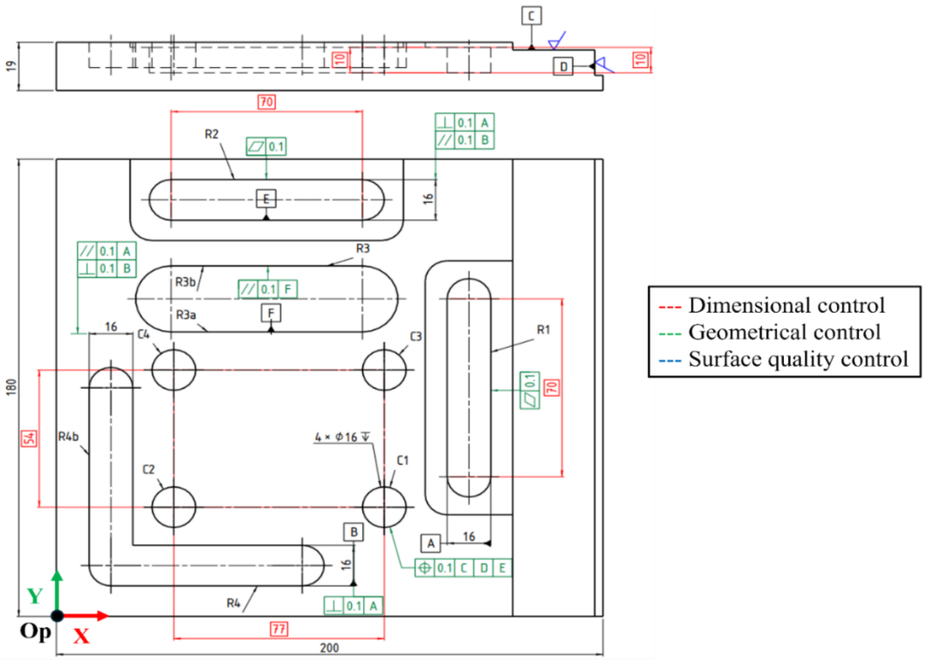

Fig. 3. Controlled dimensions, geometric specifications, and surface quality

Geometrical. Geometrical control was also performed using the same coordinate measuring machine. Twelve geometrical controls were carried out (Fig. 3): flatness of one side face of slotted holes R1 and R2, control of perpendicularity errors between distinct slotted holes (perpendicularity between R1 and R2, and between R4 and R1), control of perpendicularity error between contiguous slotted holes to evaluate the robot's ability to change direction during machining (perpendicularity between R4b and R4), control of parallelism errors between distinct slotted holes (parallelism between R4 and R2, parallelism between R4b and R1), parallelism between the two planes R3a and R3b of the R3 pocket to assess the robot's contouring capability, and finally, the locations of the four holes.The average errors E_g were calculated for flatness, perpendicularity, and parallelism errors, and the mean absolute error was calculated for hole location errors along X-axis and Y-axis, during machining with the CNC router and for each position during machining with the robot (Equation 2).

Surface quality. The topographic parameters were measured using a MarSurf CM mobile 3D surface measurement device. For each specimen, the roughnesses of two surfaces were measured in end milling and contour milling, respectively. The evaluated surfaces measure 11×11 mm^2 for end milling and 7×7 mm^2 for contour milling. A high-pass filter with a cut-off wavelength of 2.5 mm was used to filter the roughness of oak and fir, with a Gaussian filter applied (ISO 16610-61). The roughness parameter represented in this study is the arithmetical mean roughness (Sa), as described in ISO 25178-

2 [9]. This parameter is commonly used to describe general roughness of wood machined surfaces [10].

3 Results and Discussion

One result for each type of control is detailed in this chapter: deviations in lengths for dimensional results, parallelism errors for geometrical results, and Sa roughness parameter for end milling in surface quality control.

3.1 Dimensional results

In the machining of oak and fir, the deviations between the measured and nominal lengths of slotted holes R1 et R2 (Fig. 4) are generally greater in robotic machining compared to machining with the CNC router.

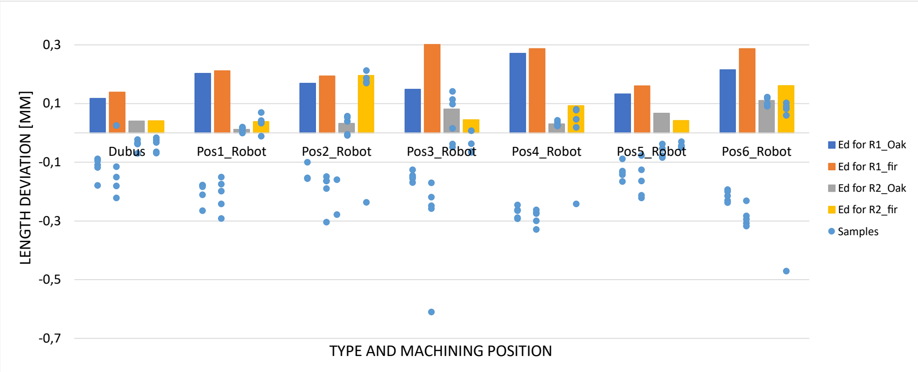

Fig. 4. Length deviations of slotted holes R1 and R2 from their nominal length (70 mm) in machining oak and fir

In addition, length accuracy was affected by the robot's posture (which varies with the machining position). The lengths obtained are closer to the nominal value along the X-axis (corresponding to the arm extension) than along the Y-axis. In the literature, the cutting direction in robotic machining has also shown an influence on the dimensional quality obtained, as shown by a study of glued laminated timber [7], where pockets were machined parallel to the grain in two different directions, and it was observed that the pocket lengths machined in the arm extension direction are more accurate than those machined in the perpendicular direction. This was explained by the fact that when machining along the first direction, the robot only needs to adjust its reach, whereas in the second direction, the robot not only has to extend its arm but also change its lateral position and perform rotations, which increases the influence of mass inertia. Length errors also vary for a given position across the five repeatability tests. The dispersion is relatively constant for each of the positions, with a maximum Average Absolute Deviation (AAD) of 0.18 mm. This may be attributed to the robot's positioning repeatability (theoretically 0.05 mm), the cutting operation itself (variation in cutting forces between specimens or in the quality of the cut in the measured areas), or measurement inaccuracies (likely in the range of microns or hundredths of a millimeter). The length deviations obtained are for the most part below 0.3 mm.

3.2 Geometrical results

For both machined wood species, the parallelism errors measured between R4b and R1 are generally comparable to those obtained with the CNC router (Fig.5 et Fig.6). The largest parallelism errors are generally measured between the two sides of pocket R3 (R3a and R3b). These errors are generally larger than those observed with the CNC router although certain robotic machining positions exhibit comparable parallelism errors. These errors vary not only from one position to another but also within the same position, with a maximum average absolute deviation of 0.12mm. The parallelism errors obtained are, as for the lengths, mostly less than 0.3 mm.

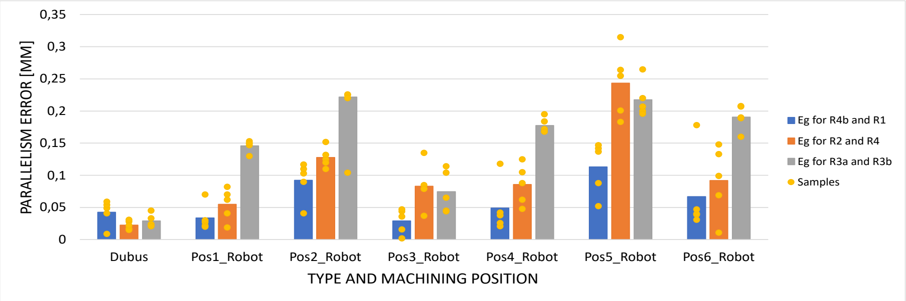

Fig. 5. Parallelisms errors of slotted holes in oak machining

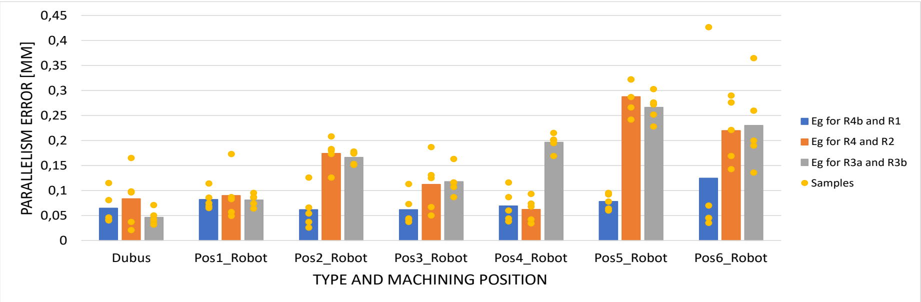

Fig. 6. Parallelisms errors of slotted holes in fir machining

3.3 Surface quality results

The surface quality achieved through end milling of oak and fir using the robot is comparable to that obtained with the CNC router (Fig.7). These results are consistent with those in [4], which found a surface quality in robotic machining of laminated composites comparable to that obtained with a CNC machine. Furthermore, in robotic machining, the machining position did not show a significant effect on the average surface roughness (Sa) of oak and fir. In solid wood machining, the results are heterogeneous, independently of the machine or position used. The variation in the results is mainly due to the material variability, not the type or position of machining. End milling was always performed perpendicular to the growth rings, which vary in width from one specimen to another, as well as within the same specimen. Although the size of the measurement area was chosen to contain several growth rings in order to limit this effect, the variability in ring width within a tree remains a significant source of variation in the basic properties of the wood (such as density) and its machinability [11], and therefore in the surface roughness measured locally.

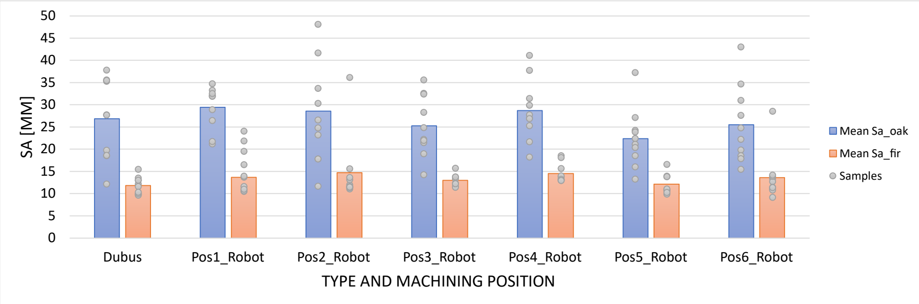

Fig. 7. Sa parameter roughness in oak and fir end milling

3.4 Additional Analyses to identify the origin of the observed defects

Effect of robot's posture and speed on the machining path accuracy. When machining with the robot, the most severe defects were located on pocket R3 at the entry and exit points, as well as during transitions between linear and circular motions. The analysis of recorded signals (both without the workpiece and during machining) allowed for a comparison of the paths and showed the effect of the robot's posture and speed on path accuracy. During machining, the path deviates from the target path (Fig. 8 et Fig. 9), even without the workpiece, where no significant difference was observed between the trajectory with or without the workpiece. This suggests that the rigidity of the robot is probably not the cause of the deviations obtained. The robot's posture has an influence on path accuracy, even without the workpiece. This effect is more pronounced during direction changes when machining the R3 pocket (Fig.10), with a maximum deviation of 0.02 mm at position 3, 0.2 mm at position 6, around 0.25 mm at positions 1, 2, 4, and 5, and around 0.3 mm at position 6 (same orientation as the workpieces on the machining table). The effect of four speeds (3 m/min, 5 m/min, 7.5 m/min, and 10 m/min) on the path (run without the workpiece) at position 3 was studied. Our results showed that the robot speed influenced the path accuracy, particularly at the R3 pocket (Fig.11), where the deviation from the target path increased with the speed, with a maximum deviation of 0.5 mm at 3 m/min and 2.7 mm at 10 m/min. These results allow for a conclusion regarding the level of deviations observed, which are probably caused by inertia effects or limitations in the robot's control system.

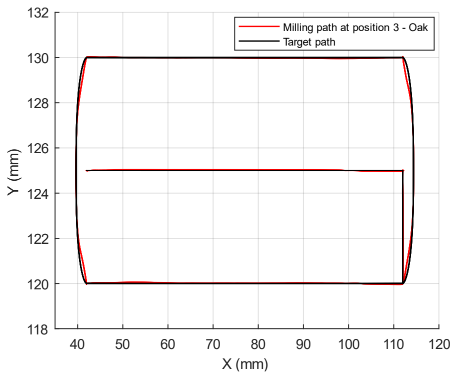

Fig. 8. Zoom in on pocket R3 path when machining an oak specimen at position 3

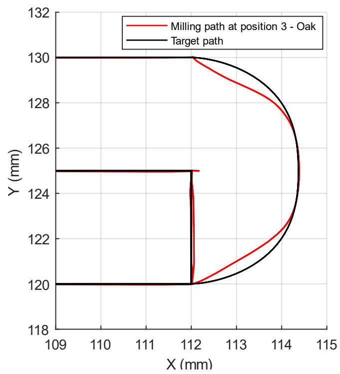

Fig. 9. Zoom in on the semicircular path

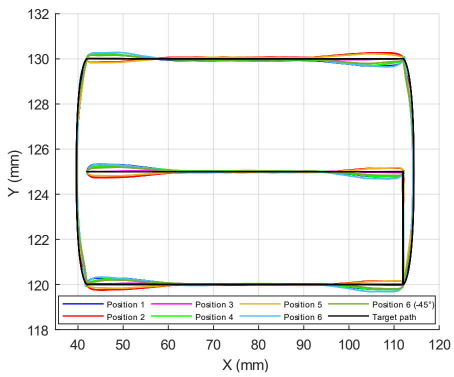

Fig. 10. Zoom in on pocket R3 path during machining without workpiece in different positions

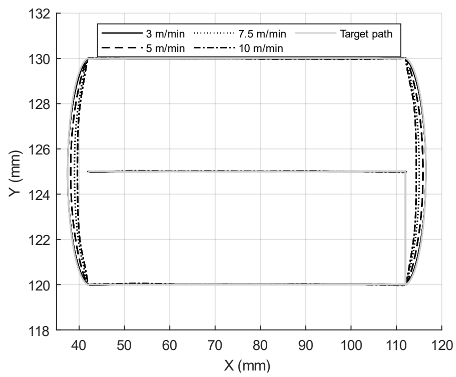

Fig. 11. Zoom in on pocket R3 path during machining without workpiece at different robot speeds

4 Conclusion

Machining oak and fir using a 6-axis poly-articulated robot has achieved dimensional and geometrical accuracy generally less than or equal to 0.3 mm. This level of accuracy is sufficient for many wood machining applications (construction, carpentry, cabinetry, ...). A surface quality similar to that achieved with the CNC router was also observed. This research provides a starting point for evaluating the capability of a poly-articulated robot in wood machining. The results obtained provide a basis for understanding the quality achievable in wood machining using a poly-articulated robot. It highlights the potential for future work aimed at exploring how to leverage this technology and its complex automation capabilities to overcome the current scientific and technological barriers in the field. The next objective is to study the relationship between the surface quality of machined wood at different grain orientations and the signals measured during machining (cutting forces, acoustic emission), and determine the parameters correlated with surface roughness parameters. This will enable the estimation of surface quality in machined wood by monitoring these signals and, consequently, identify areas with satisfactory surface quality for a given objective, as well as those requiring finishing, in order to establish an optimized sanding procedure based on the surface quality obtained during the previous milling operations.

References

1. International Federation of Robotics. World robotics 2022 - industrial robots. 2022.
2. Kim SH, Nam E, Ha TI, Hwang S-H, Lee JH, Park S-H, et al. Robotic Machining: A Review of Recent Progress. Int J Precis Eng Manuf. 2019;20:1629-42.
3. Landscheidt S, Kans M, Winroth M. Opportunities for Robotic Automation in Wood Product Industries: The Supplier and System Integrators' Perspective. Procedia Manufacturing. 2017;11:233-40.
4. Slamani M, Gauthier S, Chatelain J-F. Comparison of surface roughness quality obtained by high speed CNC trimming and high speed robotic trimming for CFRP laminate. Robotics and Computer-Integrated Manufacturing. 2016;42:63-72.
5. Behrang M. Robotic machining: evaluation of the positioning accuracy and the machined surface quality. 2014;
6. Feng L, Zhao W, Zhang Z, Yan P, Cheng M, Jiao L, et al. Effect of Postures and Cutting Process on Robot Milling Performance and Surface Quality. In: Liu X-J, Nie Z, Yu J, Xie F, Song R, éditeurs. Intelligent Robotics and Applications. Cham: Springer International Publishing; 2021. p. 639-47.
7. Pantscharowitsch M, Linzer F, Neuner H-B, Kromoser B. On the utilisation of the workspace of an industrial robot for milling structural timber components - experimental trials with different arm positions and evaluation of machining quality. World Conference on Timber Engineering (WCTE 2023) [Internet]. Oslo, Norway: World Conference on Timber Engineering (WCTE 2023); 2023 [cité 27 juin 2023]. p. 599-608. Disponible sur: http://www.proceedings.com/069179-0082.html
8. Xu P, Gao Y, Yao X, Ng YH, Liu K, Bi G. Influence of process parameters and robot postures on surface quality in robotic machining. Int J Adv Manuf Technol. 2023;124:2545-61.
9. ISO 25178-2. Spécification géométrique des produits (GPS) - État de surface: Surfacique - Partie 2: Termes, définitions et paramètres d'états de surface. 2022.
10. Ramanakoto MF, Andrianantenaina AN, Ramananantoandro T, Eyma F. Visual and visuo-tactile preferences of Malagasy consumers for machined wood surfaces for furniture: acceptability thresholds for surface parameters. Eur J Wood Prod. 2017;75:825-37.
11. Khazaien A. Caractérisation 3D de l'état de surface du bois: stratégie de mesure–influence des paramètres liés à l'essence et à l'usinage [PhD thesis]. IUT GMP de Tarbes, Toulouse III. France; 2006.

Cutting area observation coupled with dynamically compensated cutting forces to characterize the chip formation in wood peeling

[1] Curial Hugo[0009-0009-4356-6614], [1] Marcon Bertrand[0000-0003-1951-1663], [1] Viguier Joffrey[0000-0001-7926-599], [1] Girardon Stéphane [0000-0003-2990-6781], [2] Curti Rémi[0000-0002-8997-9248], [1] Denaud Louis[0000-0002-4370-6076]

[1] Arts et Metiers Institute of Technology, LABOMAP, F-71250 Cluny, France
[2.]Institut Clément Ader, Université de Toulouse, F-65000Tarbes, France

Abstract. The presented work is part of a PhD thesis on second-grade hardwood valorisation by mean of peeling to manufacture engineered wood products for construction and furnishing. This study is state-funded by the ADEME (French agency for ecological transition) to grow outlets of a broader variety of hardwood species which constitute the majority of French forestry resources (2/3 of the wood volume in French Forests).To study the multiple parameters of the wood peeling process, a micro-lathe peeling machine was developed to correlate camera observations of the cutting zone with the measured efforts during machining.in the present study focusses on hardwood with a high intra-ring density heterogeneity. However, the band-bass of the measured efforts is limited due to internal resonance of the machine. This work aims first to characterize the vibratory behavior of the dynamometer and the whole structure response to dynamic loadings and secondly to extend the overall band-pass using the dynamic compensation method to match the cutting force acquisition frequency with the video camera one. This step being a strong requirement before affronting the subsequent challenge to perform inverse identifications for instance.

Keywords: Experimental micro-lathe, Dynamic compensation, Cutting forces,

1 Introduction

The peeling process is one of the first transformation process which consists in turning logs into wood sheets called veneers. It involves rotating a section of log (bolt) along its longitudinal axis while a knife, moving at a continuous feed rate, cuts it. The cutting edge of the knife remains parallel to the axis of rotation, producing continuous veneer ribbon.

This study explores the potential of second-grade hardwood species for engineered wood production through peeling. The efficiency and quality of the peeling process depend significantly on process parameters such as machine geometry and pre-heating treatments. To gain deeper insights into the chip formation mechanisms, a specialized micro-lathe was designed and built at LaBoMaP [1], see Fig. 1. This system has previously been used during the past twenty years to study the influence of soaking temperature on Douglas-fir peeling [2], as well as for vibratory and acoustic analysis of the peeling process [3] and the investigation of transient regimes during wood peeling [4].

A recent enhancement to this setup includes a high-speed video camera to capture the cutting zone during peeling. This orthogonal cutting configuration enables direct observation of key phenomena such as variation of cutting condition within ring transitions. However, to accurately synchronize the cutting forces measurements with the recorded images, a precise characterization of the dynamometer's vibratory behavior together with the structure of the whole device (micro-lathe) is required. A previous study [3] identified the limitation in the frequency bandwidth and lead to the necessity of applying corrections capable of extending it. The dynamic compensation method is commonly applied in piezo-electric multicomponent dynamometers and was implemented with a varying degree of refinement for metal milling studies in [5–7] or for canter chipping in [8]. It is here adapted to the micro-lathe architecture and the correction is assessed using known sine waves input and real machining experiments.

2 Material and method

2.1 General architecture of the micro-peeling lathe and its acquisition

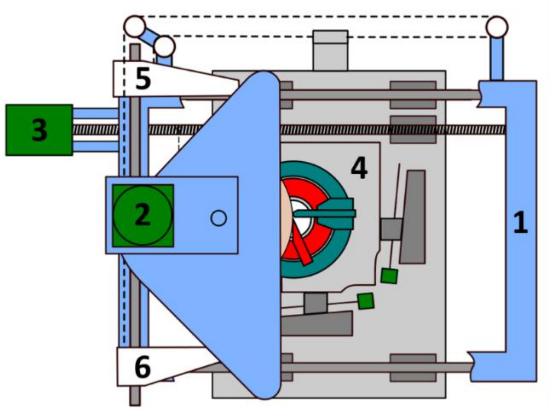

Main components of the lathe
1. Machine Frame
2. Spindle motor
3. Feed motor
4. Knife and pressure bar carriage
5. Profilometer harm
6. Slipping sled harm

Fig. 1. : Global architecture of the experimental micro-lathe

The experimental micro-lathe [1] allows the peeling of disks instead of bolts from 15 to 45 mm in width (longitudinal dimension of the bolt) while maintaining the diameter up to 500 mm. Such dimensions have the advantage to increase the number of feasible tests in a single bolt while maintaining an industrial-like scale in the Radial-Tangential plane. Moreover, variability between specimens is smaller as these originate from closer location in the tree.

The architecture of the machine is presented in Figure 1. Wood-disk specimens are bolted to the spindle and rotated by the spindle motor via a gear reductor (2). The knife can rotate around its cutting edge axis to adjust the clearance angle and the pressure bar translates in X-Y direction to adjust the pressure rate and the advance relative to the knife. It also can rotate to change the apparent nose angle of the pressure bar. The two tool-holders are each mounted on a pair of triaxial piezoelectric dynamometers (Kistler 9067) to measure the cutting forces as displayed in Figure 2. The orthogonal cutting configuration in the X-Y plane means that all dominant forces are confined in the cutting plane and that out-of-plane forces are negligible. It is however probable that vibration modes of the machine structure involve out of plane deformations and forces. There is however no interest in correcting them as they are not studied afterward. Both tools are mounted on the tool carriage (4) which is translated back and forth thanks to a ball screw and brushless unit. $\vec{X}$ et $\vec{Y}$ charges emitted by the corresponding sensors directions are summed-up and amplified in a Kistler charge amplifier to return the in-plane forces of the orthogonal cutting. To access the fresh cut wood surface to metal friction coefficient in machining, a slipping sled made of the same material as the knife is used. It is mounted on a moving arm which loads it radially on the bolt. One smaller piezoelectric sensor (Kistler 9251A) measures the tangential and the radial forces to calculate the friction coefficient assumed to be equivalent to the one at the knife/wood interface.

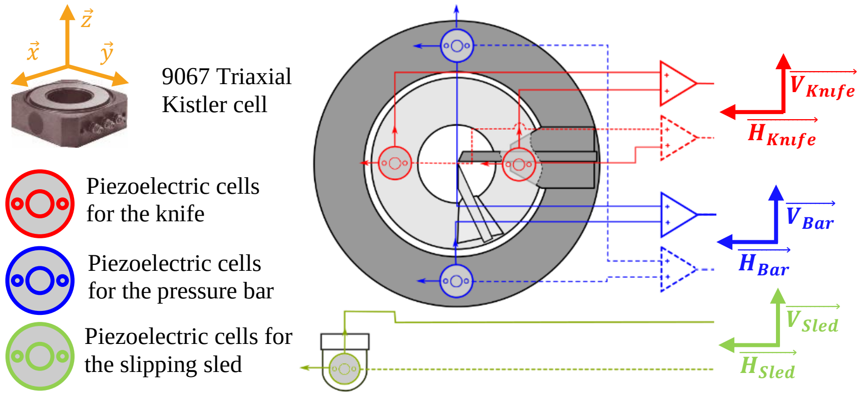

Fig. 2. Machining dynamometer principle

2.2 Video acquisition

Coupled to forces measurement, the video acquisition is a way to improve the qualitative understanding of some of the cutting phenomena in peeling like lathe checks formation, especially in growth ring transition for wood with a high intra-ring density heterogeneity. In a second step, Digital Image Correlation (DIC) is to be performed on the films to access strains and strain rates at industrial-like cutting speed (0.5 m/s in our case) in the vicinity of the tools as upscaling from qualitative to quantitative uses of the frames grabbed in-situ during peeling.

The camera installed is a Baumer VLXT-17M equipped with an adjustable zoom telecentric optic which gives, with the adopted position, a spatial resolution of 51.5 px/mm. Under current illumination, shutter speed cannot underpass 250 µs which lead to a maximum frame rate of 1800 fps for this camera with a region of interest (ROI) of 27×9.4 mm^2 (1392×477 px^2). The calculated blur under these circumstances is 6.45 px (0.124 mm) and a displacement of 14.32 px (0.277 mm) between each frame. The performances of the system will be improved soon with the addition of a new, more powerful illumination.

2.3 Bandwidth limitation

Past studies on the micro-lathe showed that major resonances of the machine are situated well under 2 kHz which leads to high distortions of the forces signals [9]. These are limiting to corelate any phenomenon on the camera acquiring at such speed with respect to measured forces. Therefore, the machine frequency response is therefore characterised to measure the actual bandwidth available and the necessary correction. The frequency behavior is obtained by performing a modal analysis of the structure of the machine. As the machine has 5 degrees of freedom (4 tool settings and the feed), a complete vibrational characterisation would entail to test both tools in every direction for every possible configuration (diameter, clearance angle, X-Y, and pressure bar angle). This perspective may not be entirely realistic, and the study will proceed with the following assumptions: The tool carriage position (diameter) is considered to have no influence on vibrational behavior. The pressure bar is positioned horizontally, and any translation relative to the knife is assumed to be negligible. Additionally, variations in the knife's clearance angle within the range of -1° to +3° are disregarded. Further vibratory tests should be conducted to assess the potential errors introduced by these assumptions.

Modal analysis setup

The setup used for modal analysis, also referred to as the ringing , is illustrated in Fig. 3. A white noise input, spanning a frequency range of 1 Hz to 5 kHz ,is emitted from a frequency analyser card running NVgate software. The signal is then amplified with an LSD PA25E power amplifier before being transmitted to a Modalshop 2007E shaker which has a maximum frequency of 9 kHz and a peak force of 7 N. As shown in Fig. 3, the shaker (1), isolated from the machine structure, is connected to a pushrod (2) on which a force sensor (3) is mounted. The sensor is magnetically attached to the tools as close as the wood enters in contact with the during a real peeling test.

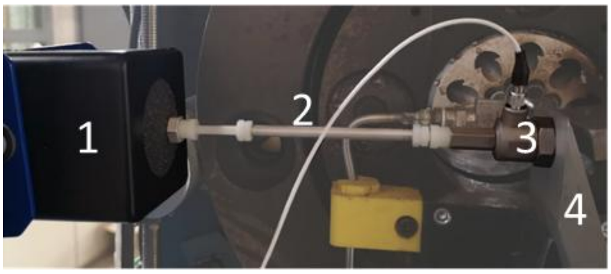

3	Ringing device
1.	Shaker
2.	Pushrod
3.	Force sensor
4.	Knife

Fig.3. Ringing setup for the knife horizontal direction

The input and output forces are recorded using the same card that generates the input signal, operating at a sampling frequency of 25.6 kHz per channel for 90 seconds. Each component, such as the pressure bar and knife holder, is excited separately in both vertical and horizontal directions. Due to the limited number of input channels on the card, the output forces of only three out of four components can be recorded at a time. Therefore, two separate tests are conducted for each input to capture all four output responses.

Computation of the transfer function

Fourier transforms of the input and output signals are computed, and the transfer function is estimated using the H_1 estimator in the frequency domain. This approach assumes that the input signal is noise-free, meaning all input measurements are considered accurate, while any noise is attributed solely to the output signals (i.e., originating from the machine). The H_1 estimator is computed using spectral power densities—cross-spectrum S_{KiFj} for the output and auto-spectrum S_{FjFj} for the input [10]. Welch's method [11],with a 75% overlap, is applied to obtain a numerical transfer function with a frequency resolution of 1/10 Hz.

Similar formalism as in [5] is used to describe the problem. K is known as the vector of measured efforts by the dynamometer, H is the transfer matrix which represents the behavior of the dynamometer that, if was ideal, would be equal to the identity matrix, and F is the input force vector obtained by the force sensor which is considered to be the true effort applied. The first index specifies the direction, h for horizontal and v for vertical, and the second one, specifies the tool with k for knife and p for pressure bar. Due to numerical computation, separate transfer matrix H exists for every discrete frequency where $H_{i,j}(f)$ is a complex term. Each term is computed by exciting one input force direction (F) and measuring all corresponding output force components (K).

$$
\begin{pmatrix} K_{hc}(f) \\ K_{vc}(f) \\ K_{hp}(f) \\ K_{vp}(f) \end{pmatrix} =
\begin{pmatrix}
H_{hc,hc}(f) & H_{hc,vc}(f) & H_{hc,hp}(f) & H_{hc,vp}(f) \\
H_{vc,hc}(f) & H_{vc,vc}(f) & H_{vc,hp}(f) & H_{vc,vp}(f) \\
H_{hp,hc}(f) & H_{hp,hc}(f) & H_{hp,hp}(f) & H_{hp,vp}(f) \\
H_{vp,hc}(f) & H_{vp,hc}(f) & H_{vp,hp}(f) & H_{vp,vp}(f)
\end{pmatrix}
\begin{pmatrix} F_{hc}(f) \\ F_{vc}(f) \\ F_{hp}(f) \\ F_{vp}(f) \end{pmatrix} \quad (5)
$$

Extension of the bandwidth with dynamic compensation

The basic principle of the dynamic compensation method is presented in Fig. 4. The reverse transfer matrix is computed to achieve a correction both in gain and phase of the input signal. A low pass Butterworth [12] filter is applied to the measured signal to cut frequencies over 2 kHz. It is then back transformed in the time domain to obtain a greater estimate of the real applied efforts than the ones directly measured (corrupted by structural dynamical effects)

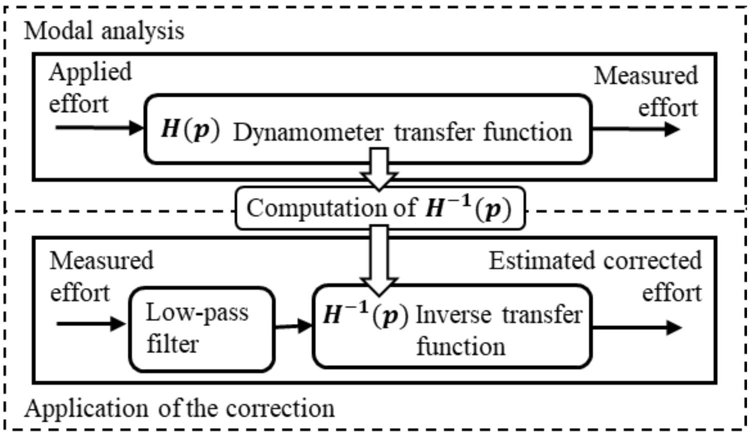

Fig. 4. Principle of the dynamic compensation, adapted from [8]

Evaluation of the frequency response and the correction benefits

The dynamic behavior of the dynamometer is first presented. Gain and phase are displayed to spot the main proper frequencies and coherence is used to assess the quality of the signal acquired while ringing.

To evaluate the capability of the correction, the proper frequencies are first used to excite the system with the corresponding sine signal using the same ringing setup. The measured and corrected forces signals (arising from the micro-lathe embedded dynamometers) are then compared to the real input signal measured with the force sensor (referenced as 3 in Fig. 3).

The compensation is then tested on poplar (Populus canadensis, clone I-214) peeling at the moment of a lathe check opening. The video acquisition is used to correlate the phenomenon to the corresponding efforts. To do so, a reduced 200-frames video acquisition of the scene is taken after two revolutions the knife in the bolt to avoid unsteady cutting conditions. The settings of the camera and the cutting parameters are displayed in Table 1. The exposure time is recorded synchronously with the forces signals via its IO ports to ensure the synchronization of forces measurements and frames.

Table 1. Acquisition settings during poplar peeling

Video		
Acquisition frequency	1200	fps
Resolution	51.5	px/mm
ROI	1376×456	px^2
	26.7×8.84	mm^2
Exposure time	250	µs
Efforts and frames exposure		
Acquisition frequency	30	kHz
Lathe settings		
Cutting speed	650	mm/s
Feed (aimed thickness)	3	mm/rev
Clearance angle	0	degrees
Cutting angle	20	degrees

3 Results and discussions

3.1 Frequency response of the dynamometer

The frequency response of the dynamometer is evaluated by examining each term of the transfer matrix *H*. The terms of the transfer function are categorized into three distinct groups, each represented by a different color, as shown in **Eq 5** Diagonal terms (purple) indicate the influence of a force component on itself. Intra-tool coupling terms (gray) represent the effect of one direction on the other within the same tool. Inter-tool coupling terms (black) account for the influence across both directions on the other tool.

Transfer functions of diagonal terms of H are displayed in Fig. 5 with gain frequency and coherence. The first resonances are visible as early as 120 Hz across all tools (highlighted in green), with significant resonances occurring at 550 Hz vertically on the knife and at 860 Hz horizontally on the pressure bar.

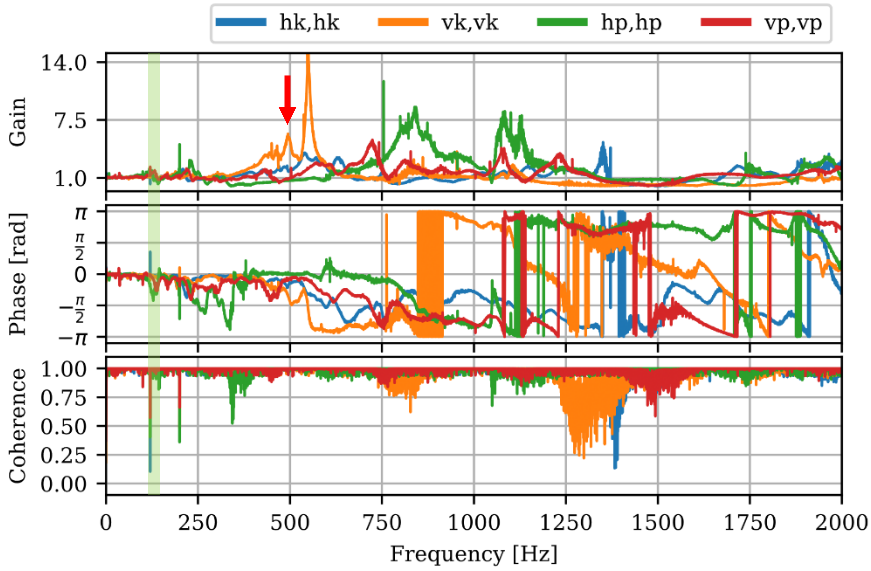

Fig. 5. Gain, phase and coherence of the H transfer matrix terms

3.2 Evaluation of the correction

The performance of the dynamic compensation is evaluated by exciting the system at its main resonant frequencies. The known input signal is compared to the measured signal and the corrected one both in terms of amplitude and phase correction.

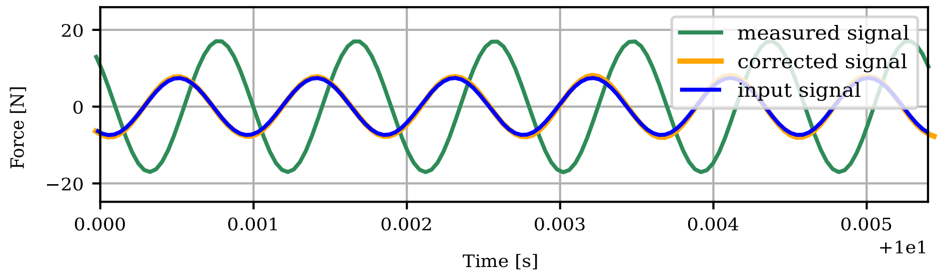

Fig. 6. 1111 Hz sine input vertically on the knife in blue, the direct measured signal by the piezoelectric dynamometers, and the corrected signal (using the identified transfer matrix) by dynamic compensation

Fig. 6 displays the correction achieved using dynamic compensation on the vertical-knife direction. The corrected signal compensates for most of the delay and amplification in this particular case. However, for some directions and at certain frequencies, the correction shows worse performing results, especially at antiresonances where the coherence drops. Extended work should be performed to improve the acquisition and the computation of the vibratory behavior in this case.

3.3 Dynamic response on a lathe check formation

The direct application of the method exemplified on the sine-waves is the measurement of efforts during the propagation of a lathe-check without pressure bar. The almost instantaneous propagation of the crack excites the system as a Dirac pulse would and very little contact with wood remains to dampen the system which consequently resonates freely.

Over the 200 images taken during the peeling phase, 4 consecutive ones are chosen in Fig. 7 to illustrate the phenomenon. The four images are synchronized with the cutting force measurement via the exposure time represented by a pair of dashed gray lines for each. For visibility purposes, the opening lathe-check are highlighted in red.

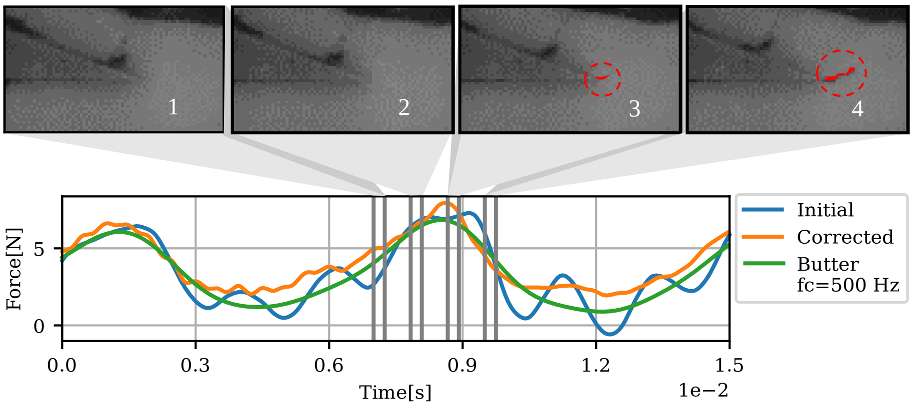

Fig. 7. Knife vertical force to time acquisition of a lathe check (red highlighted) formation with the corresponding images of the cutting zone. Vertical dashed lines are the respective frame exposure times being set at 250 µs.

The corrected signal is displayed alongside the initial 2 kHz low-pass filtered signal used for correction and a more restrictive 500 Hz low-pass filtered. Two key benefits of the correction are observed.

First, in Picture 3, the synchronization of the check opening corresponds to a noticeable drop in vertical efforts on the knife, whereas the efforts remain unchanged or even higher in the initial signal. The second benefit becomes apparent after the fourth picture, when the lathe check is fully opened (or before the studied check forms). At this stage, a significant oscillation is visible, with a frequency approximating 500 Hz in the initial frequency response. As seen in Fig. 5, this frequency closely aligns with the second-highest resonance frequency for the knife in the vertical direction (marked with a red dart). Applying a corresponding third order low-pass Butterworth filter suggests that the 500 Hz low-pass filter may however be too suppressive to fully capture the phenomenon of interest.

4 Conclusion

To synchronize the frames recorded with the cutting force measurements on the experimental micro-lathe, dynamic compensation was implemented. This adjustment was necessary after the resonance frequency behavior of the entire testing setup was found to be too restrictive for studying the cutting phenomenon. While the correction in the frequency domain, particularly where coherence is low (mainly at anti-resonances), could be further improved, the highest resonant peaks were effectively corrected in both phase and gain and a real machining test demonstrated that phase correction successfully resynchronized the lathe check openings with the measured cutting forces. Additionally, resonances occurring after rupture were significantly dampened. This enhanced time-response fidelity marks a significant step forward in identifying wood behavior at high cutting speeds, especially when integrating microdensitometric data of the peeled bolt.

Acknowledgements

The results and the study described here are part of the results obtained in the « Valorisation des feuillus en construction par une approche holistique, collaborative et entrepreneuriale » (2023-2027) project. The ADEME (French agency for ecological transition) is thanked for its financial support (Grant N°2282D0474-A).

References

1. Butaud JC: Conception d’une dérouleuse instrumentée. CNAM, Cluny, France (1994)
2. Frayssinhes, R.: Optimisation des paramètres de déroulage du douglas et modélisation des propriétés mécaniques de panneaux de LVL intégrant les données sylvicoles, https://pastel.archives-ouvertes.fr/tel-03132767/document, (2020)
3. Denaud, L.: Analyses vibratoires et acoustiques du déroulage, (2006)
4. Decès-Petit, C.: Etude des phases transitoires au cours du déroulage de bois, (1996)
5. Girardin, F., Remond, D., Rigal, J.-F.: High Frequency Correction of Dynamometer for Cutting Force Observation in Milling. Journal of Manufacturing Science and Engineering. 132, 031002 (2010). https://doi.org/10.1115/1.4001538
6. Jullien-Corrigan, A., Ahmadi, K.: Measurement of high-frequency milling forces using piezoelectric dynamometers with dynamic compensation. Precision Engineering. 66, 1-9 (2020). https://doi.org/10.1016/j.precisioneng.2020.07.001
7. Scippa, A., Sallese, L., Grossi, N., Campatelli, G.: Improved dynamic compensation for accurate cutting force measurements in milling applications. Mechanical Systems and Signal Processing. 54-55, 314-324 (2015). https://doi.org/10.1016/j.ymssp.2014.08.019
8. Curti, R.: Analyse, modélisation et simulation de la coupe orthogonale du bois vert en vue de son application au fraisage par canter, (2018)
9. Denaud, L., Bleron, L., Ratle, A., Marchal, R.: Online control of wood peeling process: Acoustical and vibratory measurements of lathe checks frequency. Annals of Forest Science. 64, 569-575 (2007)
10. Ewins, D.: Modal testing theory, practice and application. Research Studies Press Ltd., Baldock, England (2000)

11. Welch, P.: The use of fast Fourier transform for the estimation of power spectra: A method based on time averaging over short, modified periodograms. IEEE Trans. Audio Electroacoust. 15, 70-73 (1967). https://doi.org/10.1109/TAU.1967.1161901
12. Butterworth, S.: On the theory of Filter Amplifiers. In: On the theory of filter Amplifiers. p. 536-541 (1930)

Steam Softening for Solid Wood Bending, focussing on kiln dried lumber

Otto Eggert[1]

[1] GHEbavaria Maschinen GmbH, 97246 Eibelstadt, Germany

Abstract. In certain areas around the world, wood from local saw- mills is not really available for the furniture production. It has to be imported, even crossing oceans. In this case, wood comes quite usually cut and milled to standardized dimensions, dried to some +/- 8 % moisture content (m/c).

The question is, is it possible to bend dry hardwood with good results, no matter if this is kiln dried, pre-bend (no matter if this happened recently or hundreds of years ago)? This question is quite important given that there is a high interest to introduce Solid Wood Bending as a production process to countries that do not have relevant wood sources at their doorstep for their furniture production.

Based on the today established understanding that wood has visco-elastic and visco-plastic properties, it is suggested, that wood can be re- softened and then be bend. On the other side, there are theories about the role of lignin to resist compressive forces and its behavior after wooden parts have been initially dried below a m/c of 10%. In that case, the question is, to what extend does the behaviour of lignin influence the re-softening and bending process to eventually bend dry-aged, kiln dried or previously bend wooden parts in whatever direction?

To understand the influences of the different softening processes, samples of kiln-dried wood were softened and bend. The test criteria were the quality of a typical bend part in U-shape for a standard chair frame.

Keywords: Solid Wood Bending, Steam Softening, visco-plastic properties of wood, visco-elastic properties of wood, lignin reaction, kiln-dried wood.

Fig. 1. Solid Wood Bending Machine (GHEbavaria, Stuzama I, Model 2025), at 0-position

1 Introduction: Stress and strain during the Solid Wood Bending Process (Thonet Method)

Steam Bending of Solid Wood is a generally accepted and widely used method for the industrial production of chairs and other curved wooden elements. It was developed and introduced by Michael Thonet around 1850 because the glue in glue-laminated bend parts did not last.

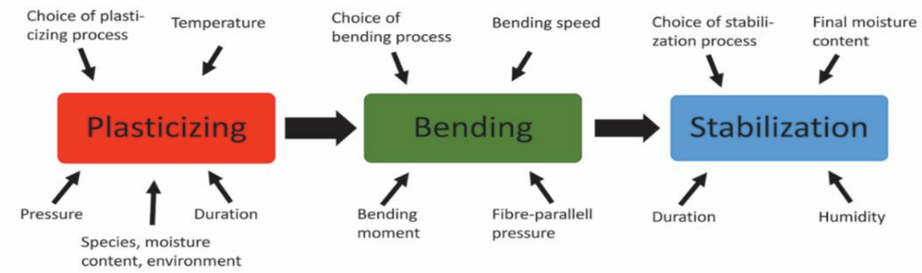

Fig. 2. Process Steps of Solid Wood Bending [1]

The bending process has three steps: plasticizing (softening) - bending- stabilizing (drying), Figure 2. Plasticizing (softening) is usually done in a steam atmosphere. In a professional steam autoclave the softening process takes approx. 1 min per mm thickness. There are other ways to heat up wood, too, e.g. using radio- frequency more or less like in a microwave oven. That's the faster way, however it's most important to make sure that the moisture content doesn't decrease too much [1]. That's why the initial moisture content (m/c) should be in the range of 16 … 18% (+/- 1 %) to achieve nice and soft bending properties.

During the actual shape change / bending phase, there is only one thing to be kept in mind: wood doesn't allow strain caused by tensile stress. Simply said, wood doesn't tolerate elongation. It simply breaks as soon as acceptable loads are exceeded. Since bending always has a neutral line, inside of it, there is densification, outside elongation. Thonet's idea was to combine a metal strap on the convex side of the bending to cover the tensile stress, so that the wooden part on the inside is kept under compression stress exclusively.

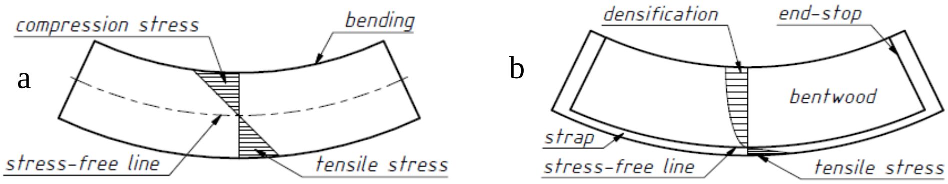

Fig. 3. Bending: a) general; b) Solid Wood bending, Thonet Method with a strap to cover tensile stress [1]

Stabilizing / drying after steam softening and bending is not that much of a big deal. The only thing to take into account is wood has to stay in the desired shape, e.g blocked by any kind of die and hook or just hook, otherwise there is either a relaxation ("spring back") or if a certain point in the drying phase is crossed, the bend parts is closing further, bending e.g. from 190° to 195° or so [2].

2 Materials

Solid Wood Bending can be applied on Northern Hardwoods, such as Ash, Beech, Oak, Walnut etc. Softwoods generally don't work, and tropical hardwoods, such as Teak (Tectona grandis) or Hevea (Hevea brasiliensis) are quite complicated to be bend. It works on lab- scale, but so far not in industrial production scale.

2.1 Lignin inside the wooden structure

Without getting too much into details, Lignin (from Latin *lignum*, meaning wood) is an aromatic phenylpropanoid polymer, which provides rigidity and water resistance to wood [3]. Lignin is fundamental for the solidity of plant tissue, the compressive strength in the first place, while the embedded cellulose fibres cover the tensile strength. Tear resistant flexible fibres (cellulose) are penetrated by a dense and stiff polymer filler (lignin) [44].

It is widely known that wood can be softened by using steam. Like polymers, wood has a glass- transition temperature, that allows bending when exceeded.

2.2 Visco- elastic and visco- plastic properties of wood

For the progression of forces during solid wood bending process see Fig. 4:

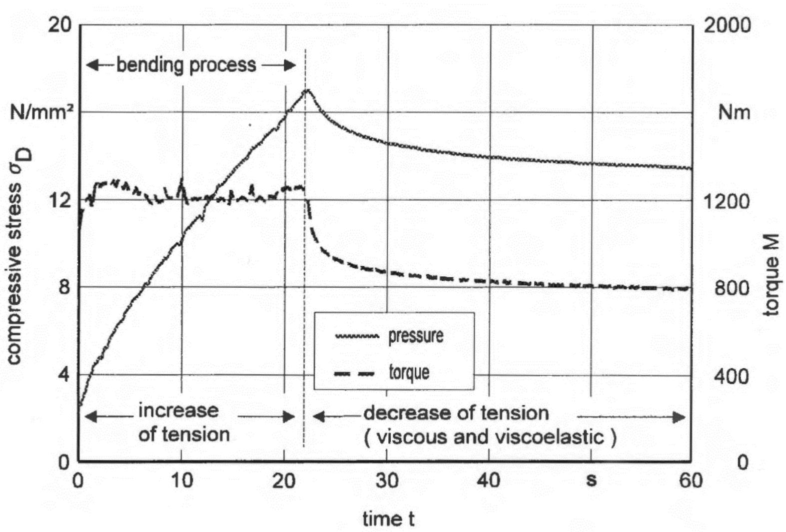

Fig. 4: Progression of Forces while bending and relaxation [1]

To compare, the progression of forces in the Burgers-Kelvin Model of viscoelastic behaviour see Fig. 5:

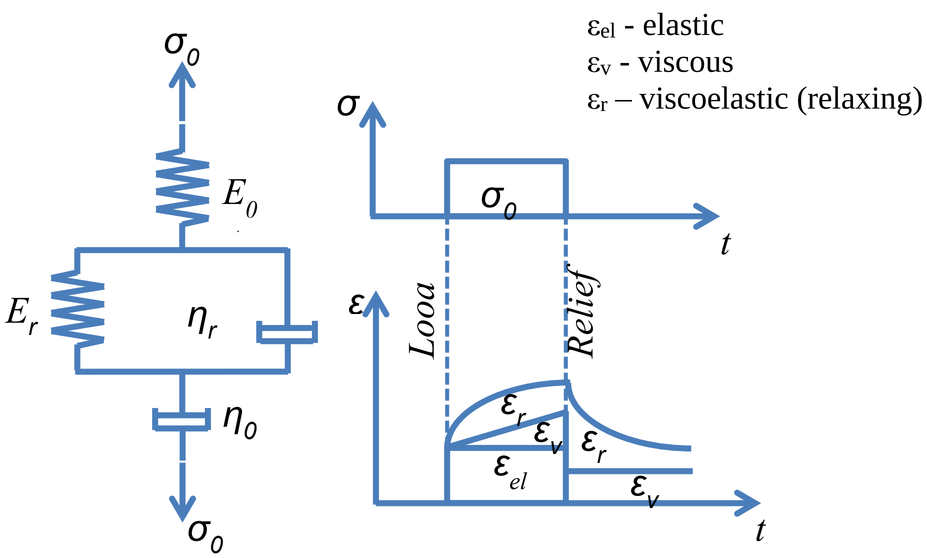

Fig. 5. Burger- Kelvin- Model of viscoelastic material behavior [5]

The similarities in progression are quite obvious, in particular during the relaxation phase: In other words, seen from this point of view, during the bending process, wood shows visco-elastic properties that are converted into a visco-plastic state during the stabilization phase that comes with cooling and drying. While the behaviour of visco-elasticity and visco- plasticity come in polymers with a thermo- induced component, such as a glass- transition temperature of approx. 82°C, it is known that these effects exist in wood, too [3].

In other words, it can be assumed that wood can be heated over that glass- transition temperature and, with some adding of water it softens and then allows deformation that can be permanent as long as the deformation forces remain until the part is cooled and dried. And, this deformations are change- and reversible when the same hygrothermal conditions are applied.

3 Methods

3.1 Re-Softening of Kiln- Dried Lumber

Immersing in Water

It can be regarded as common knowledge that one of the parameters for wood allowing deformation is a moisture content of approx. 16% or more. Since kiln- dried lumber as well as bend parts in general are usually stored between 6 … 9 % moisture content, that content has to be increased in the first place for and shape change. To do so, a widely seen method is soaking of wood in water. In that case, the lumber is immersed in a water tank, where it can soak. The time for soaking depends on the temperature of the water in the tank. For example, in hot countries where tap water has a temperature of approx. 36°C, wood is ready for the next process step, steam softening, within 30 min., while in a cold workshop in a northern country with a water tank of 10°, the whole process takes about 5 h.

Steam Softening

During the steaming process, steam has two positive effects on lumber: moisture (water) is received by the wood to increase the m/c, while the heat that comes with the steam is increasing the temperature of the object.

For the test, a standard Compact Steamer, Type HODA, made by GHEbavaria, Germany was used. In the rear part, water is heated to the steam point and then led by a pipe to the autoclave, both of them in the same housing and operating at a temperature of approx. 100 °C.

3.2 Bending Tests

For the tests, a Solid Wood Bending Machine, type Stuzama I, made by GHEbavaria, Germany, was used. The die offers a 180° bending with a radius of 170 mm. All parts were bend to an angle of 180° (the design of a chair seat frame).

All parts had a length of 800 mm, a thickness of 24 and 36 mm and a width of 54 mm. According to its specification, the Lumber came in 7 … 9% moisture content. The lumber used in these tests was supplied by Pollmeier Massivholz GmbH, Germany. In total, 40 parts were tested.

Fig. 6: Compact Steamer HODEL,

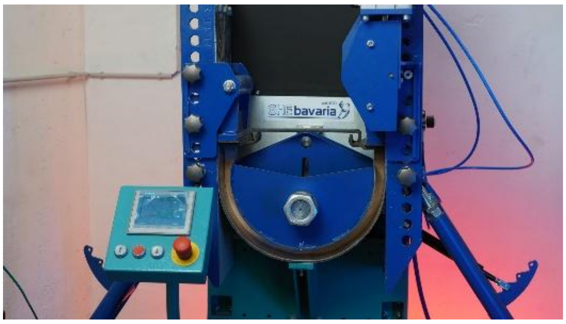

Fig. 7: Solid Wood Bending Machine (GHEbavaria, Stuzama I) at bending 180° position

4 Results

For the test, a number of data had to be acquired, Table 1:

- Measuring the moisture content U of each part by the use of a moisture meter (Gann Hydromette)
- Measuring the mass m of each part by a calibrated Satorius scale
- Immersing the parts in a water tank
- Measururing the mass of each part again after watering and after steam softening

Table 1. Bending tests with kiln-dried lumber (typical selection, total 40 pieces)

No.	U_0	m_1, g	m_{0darr}, g[1]	$t_{\text{water immerse}}$, h	m_2, g	U_2, %	m_D, g[2]	U_D, %[2]	$\Delta\%_D$	Remark
14	10,3%	776	703,54	05:03	853	21,2%	854	21,4%	0,142%	O.K.
15	6,5%	668	627,23	04:56	724	15,4%	739	17,8%	2,391%	O.K.
16	7,7%	756	701,95	04:54	842	20,0%	859	22,4%	2,422%	m.c.[3]
17	8,0%	764	707,41	04:53	847	19,7%	871	23,1%	3,393%	O.K.
18	11,0%	713	642,34	04:51	774	20,5%	798	24,2%	3,736%	O.K.
19	8,30%	738	681,44	04:48	806	18,3%	820	20,3%	2,054%	O.K.

[1] m_{0darr}: dry mass of wood

[2] Steaming: 30 min

[3] m.c.: minimal collapse of cells

The chart shows 6 typical parts out of a total of 40 tests. It can be said that with re-moisturing the lumber prior to steaming and bending, the pre-kiln-dried lumber is as suitable for bending as wood that was initially naturally dried and then moistured or as naturally dried wood down to 16…18 % m/c and then softened by steam prior to bending. In other words, the behavior of re-moisturized lumber to approx. 15 … 24% is identical, no matter if previously kiln dried or naturally dried, if previously bend or unbend. This understanding is supported by the understanding of Lignin as being a thermoplastic component and the visco- elasto-plasticity of wood.

Fig. 7: bend part no. 14, inside

Fig. 8: bend parts, outside

Fig. 9: bend part no. 19, inside

Fig. 10: bend part no. 19 with knots

Among the delivered lumber, there was one part (no. 19) having knots. It is a common understanding, that lumber with knots can't be bend. Because of the densification during the bending process, see fig. 3b), the part will crack. According to our long-term experience, this is applies only to parts with knots tangential to the bending, or if the knots are growing to the inside. If a knot is growing to the outside (in radial direction), wood can usually be bend, see fig. 9, 10.

There are two practical remarks, that have to be kept an eye on:

- Fresh wood with a m/c of 24% is way much softer than re-moistened wood. It does not have the internal stability that is required for bending. It will buckle under longitudinal load according to the Eulerian load case. Fresh wood has to be initially dried to less than approx. 18% prior to steam softening.
- During the stabilization phase that includes drying, wood will shrink. In particular, if the lumber used for bending has a radial thickness of > 20 mm, shrinking in longitudinal direction may occur, and that shrinking may decrease the necessary longitudinal pressure that pushes the neutral zone to be on the outside of the bend part. As a result, the pressure will decrease

and the neutral zone will shift to the inside of the part. As consequence, the part will crack on the outside. In that case, the only way to avoid those types of damages is, to take care that the m/c prior to bending is kept below 18% and the part fits exactly into the strap prior to start re-moistening and steam – softening.

5 Conclusion

Re- softening and then stabilizing dried wood is practically reversible, no matter if after 1 h or 100 years. As soon as wood is softened, it has visco-elastic and visco- plastic properies that are progressively coming to a halt during the stabilization phase with temperatures clearly below the glass transition temperature and environmental conditions that allow wood to dry to a m/c below approx. 15%.

Acknowledgments. The project on which this report is based is supported by funds of the German Federal Office for Agriculture and Food under the support code 2022HV051B. The author is responsible for the content.

References

1. Eggert O (1995) Untersuchung der Einflußgrößen beim Biegen von Vollholz [*Investigation of influencing Factors when Bending Wood*]. PhD Thesis, Universität Stuttgart
2. Iida I, Norimoto M, Imamura Y (1983) Wood Bending Utilizing Microwave Heating – Hygrothermal Recovery of Bentwood in the Direction Perpendicular to Grain. Wood Research Review 17: 99- 111
3. Niemz, P, Mai, C., Schmitt, U.: Introduction to Wood Science. In: Springer Handbook of Wood Science and Technology, p. 30. Springer Nature, Cham, Switzerland (2023).
4. Sekundärwände von Faser- und Holzzellen. In: Sitte et al. 2002, S. 95–96.
5. Saechtling H (1992) Kunststoff- Taschenbuch [*Handbook of Plastics*] 25. München, Hanser

The Modern Feed Systems Of Cross-Cut Optimizing Saws

Kazimierz A. Orlowski[1[0000-0003-1998-521X]] , Wojciech Blacharski[2],
Daniel Chuchala[1[0000-0001-6368-6810]], Przemyslaw Dudek[3], Jakub
Sandak [4[0000-0001-9190-677X]] and Gerhard Sinn [5[0000-0002-8365-3650]]

[1] Gdańsk University of Technology, Faculty of Mechanical Engineering and Ship Technology,
Gdansk Poland
kazimierz.orlowski@pg.edu.pl, daniel.chuchala@pg.edu.pl
[2] Technical consulting, private activity, Gdansk
wblachar@gmail.com
[3] REMA S.A., Reszel, Poland
przemyslaw.dudek@rema-sa.pl
[4] InnoRenew CoE, Izola, Slovenia
jakub.sandak@innorenew.eu
[5] Inst. of Physics and Materials Science, BOKU University, Austria
gerhard.sinn@boku.ac.at

Abstract. The work presents the development of kinematic systems for feed movements of cross-cutting optimizing saws. For efficient machining on a cross-cut saw with high feed speed values in contemporary machine tools pendulum-type kinematic systems are presently used. The arm of the pendulum with a circular saw blade on the spindle moves on a curved trajectory. There are well-known solutions for the design of the feed movement with a pneumatic actuator, or more modern ones with a crank mechanism driven by a rotary servomotor, as well as an innovative solution with a tubular linear motor. An advantageous feature of a feed system with an electric linear servo motor of mandrel design is that the pendulum arm angular travel and the saw stroke can be programmed to achieve the shortest possible time for a single cutting cycle, with the stroke adapting to the cross-sectional dimensions of the material currently being cut. The both feeding systems with a crank mechanism driven by a rotary servomotor and with a tubular linear motor are much more rigid than pneumatic actuator solutions. The optimization process in which a rotary servo motor or a tubular linear motor is applied could be led with extremely fast saw strokes (maximum value of the feed speed reaches even 4 m·s-1), therefore, some saw blades producers call this method cutting “a punching method”. There are no perfect solutions, therefore, the advantages and disadvantages of these applications will be discussed in a concise manner.

Keywords: Kinematic System, Cross-Cut Saw, Feeding System.

1 Introduction

Optimizing cross-cut saws, also called optimizers, belong to the group of cross-cut sawing machines often used in wood processing plants, and their purpose is to align the ends of lumber, trim to length and fast and precise cut out the anatomical defects during cross-cutting of single boards in solid wood. Thanks to the use of modern cross-cut saws and effective optimization for defect removal, it is possible to expect a reduction of raw material waste up to 8% [1].

Cutting power during cross-cutting of selected wood species was investigated by Kminiak and Kubš [2]. In this experiment he experiment, a constant feed force of 20 N was used. Kováč et al. [3] conducted experiments during cross cutting of beech wood and spruce wood with feed speed lower than 12 m·min^{-1}. Nasir and Cool [4] investigated the effect of feed speed, rotation speed, depth of cut, and the average chip thickness on the power consumption and waviness during the circular sawing process of green Douglas-fir wood. In the latter experiment maximum of feed speed in longitudinal direction was 180 m·min^{-1}. Although the results described in works [4] are valuable they cannot be utilized in the machine tools, which are the subject of this paper, since, in optimizing cross-cut saws fixed length cutting, defect cutting and optimization is conducted with extremely fast saw strokes, therefore, some saw blades producers call this method cutting “a punching method” [5].

The Polish manufacturer of machine tools for woodworking Rema SA (Reszel, PL) offers an optimizing cross-cut saw with an automatic pusher called Castor 500, in which a feed movement is realized by means of a pneumatic actuator. However, latterly the company has been financially supported by the European Regional Development Fund, and the improvement of the feeding system of the machine was one of the project goals. The target to be achieved was a maximum feed rate of 4 m·s^{-1}. The work presents the development of kinematic systems for feed movements of cross-cutting optimizing saws.

2 Theoretical background

Figure 1 presents general classification of drive feed systems in cross-cut saws, which was developed on the basis of our own observations and at the same time significantly expands on the information contained in the Manžos handbook [6]. The circular saw blade can move in an arc or in a straight line. However, the most common feed mechanisms at present are those with along the arc saw motion operating in pendulum based kinematic systems. The solid line in the diagram encompasses modern feed systems in which the actuator arms are driven by a pneumatic actuator or, in newer types, by rotary servo motor.

The marked area in Fig. 1 of contemporary feed drives can be extended to include linear motor drives (encompassed with a dashed line), which have been studied similarly to those driving systems described in the chapter [5].

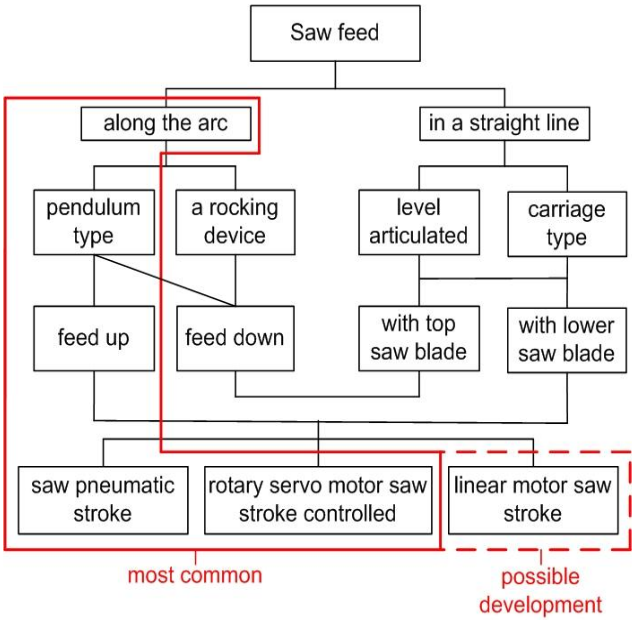

Fig. 1. Classification of drive feed systems in cross-cut saws

3 Concise description of the feed systems

In an optimising cross-cut saw with a feed system driven by a pneumatic cylinder (Fig. 2), the feed motion is performed by a pendulum with a bearing spindle and a circular saw blade mounted on it. The feed motion is performed by rotating the pendulum through a fixed angle around the axis of the joint fixed to the body. After the cut, the pendulum and the saw blade are retracted to their initial resting position.

The disadvantage of these systems is that the stroke in the vertical direction has a constant value. In addition, during the reversing movement of the pendulum arm, the pneumatic actuator is subjected to an inertial force that depends on the mass of the pendulum system including the saw and the accelerations realised. The possibility of achieving high accelerations is limited due to the flexibility of the pneumatic drive and the need to provide effective suspension in the turning movement. The flexibility of the system results in non-uniformity of the pendulum speed and increased cutting times for a single cycle.

The pendulum system of the optimizing cross-cut saw with the feed motion realized due to the crank mechanism driven with the rotary servo motor is presented in Fig. 3. The control system is programmed so that the shaft of the servomotor makes a single rotation of an angle of 360°, during which the pendulum arm together with the rotating saw cuts through the material and makes a return movement. The starting and stopping points of the servomotor rotor movement in successive cycles are programmed so that the pendulum arm occupies the bottom extreme position after cutting.

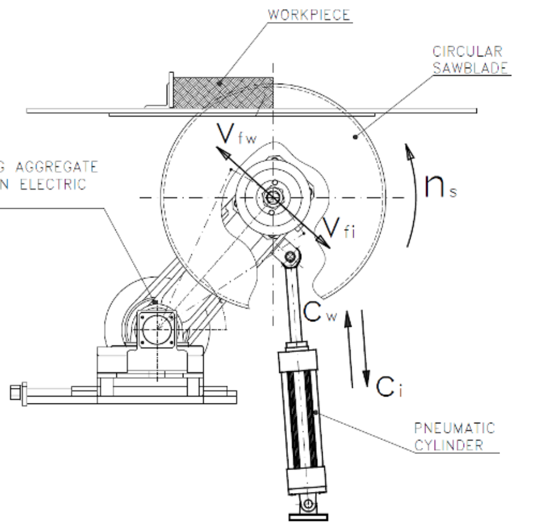

Fig. 2. The pendulum systems of optimizing cross-cut saws with the feed motion realized by means of a pneumatic actuator, where: v_{fw} – working feed speed, v_{fi} – idling feed speed, n_s – rotational speed of the circular saw blade, c_w – piston rod speed in the working stroke, c_i – piston rod speed in the idling stroke

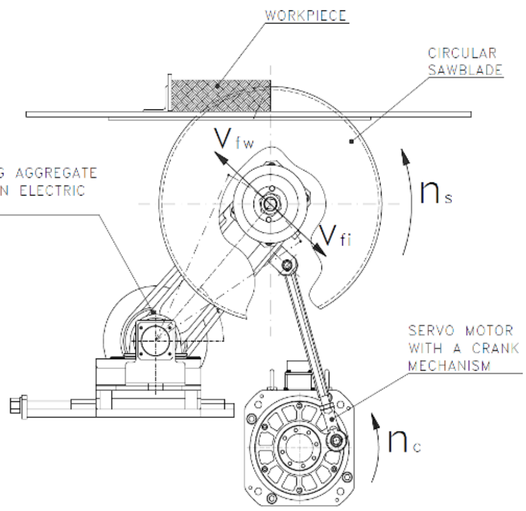

Fig. 3. The pendulum systems of optimizing cross-cut saws with the feed motion realized due to the crank mechanism driven with the rotary servo motor, where: v_{fw} – working feed speed, v_{fi} – idling feed speed, n_s – rotational speed of the circular saw blade

In these feed systems, the saw stroke in the vertical direction is fixed. It is not possible to reduce the single cycle time for smaller cross-sectional dimensions of the material being cut. Moreover, the pendulum arm reversal in the upper return position takes place at the highest servomotor speed, resulting in a high inertia force, the peak values of which are greater the shorter the time set for one cutting cycle. Reducing the speed of the shaft allows the value of the inertia force to be reduced, which results in longer cutting times. In this solution, the main criterion for the selection of the servo is the value of the permissible dynamic load on the shaft. For this reason, versions of servo motors with reinforced shaft bearings and increased parameters of permissible torque and acceleration in relation to the calculated values are used in known cross-cut saws. Hence, this is the reason for the increased cost of this design.

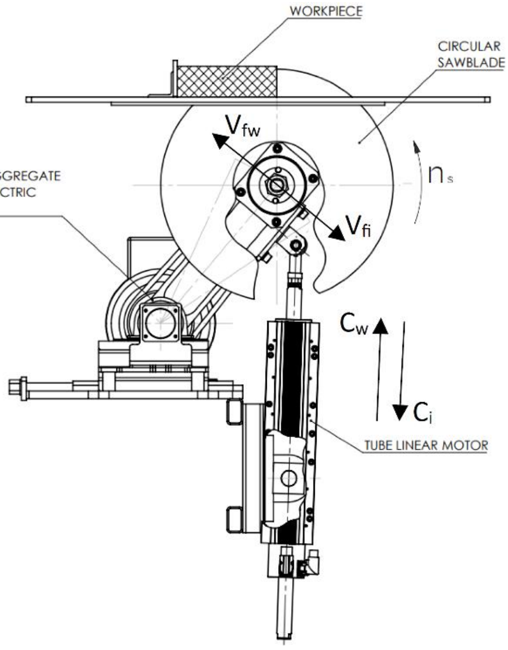

Fig. 4. The pendulum systems of optimizing cross-cut saws with the feed motion realized due to the tube linear motor, , where: v_{fw} – working feed speed, v_{fi} – idling feed speed, n_s – rotational speed of the circular saw blade, c_w – mandrel speed in the working stroke, c_i – mandrel speed in the idling stroke

Figure 4 presents the pendulum system of the optimizing cross-cut saws with the feed motion realized due to the tube linear motor. This design is protected by the patent PL239869 [7]. The feed movement is carried out by a movable pendulum with a bearing spindle and a circular saw fixed on it to a stationary body support. Once the cut has been made, it is retracted to its initial resting position. A linear motor of mandrel design is used to drive the pendulum arm, whose mandrel makes reciprocating movements (defined stroke and acceleration) controlled by an electronic control system. These values are selected to obtain the shortest time for a single cutting cycle, taking into account the dimensions of the workpiece. The programming of the saw stroke and the favourable characteristics of the mandrel-type linear servo motor, including the driving force achieved and the accelerations and decelerations realised during the reversing movement of the mandrel, make it possible to achieve shorter cutting cycle times than those achieved in known cross-cut saws with a comparable pendulum arm mass.

Since, in the case of the feeding system driven by the means of a pneumatic actuator the set-up of the feed speed is difficult and its changes are unpredictable because of the system flexibility [5]. For the design with a pneumatic actuator the maximum feed speed of 2 $m \cdot s^{-1}$ could be achieved. Henceforward, in the future in a new cross-cut saw the crank mechanism driven with the rotary servo motor should be recommended for application. The maximum feed speed in this case could reach values of 4 $m \cdot s^{-1}$. In the conducted experiments in the plant conditions if the mandrel-type linear servo motor was applied the maximum feed speed reached also values of 4 $m \cdot s^{-1}$.

4 Conclusions

An analysis of the current offerings from various cross-cut saws manufacturers has shown that pneumatic drives and rotary servo drives are king among the feed system solutions for today's cross-cutting saws.

In addition, the use of a mandrel-type linear motor would allow the feed drive to be made more flexible, in comparison to the rotary servo drives, according to the size of the workpiece without compromising the maximum feed speed achieved.

Acknowledgements: It is kindly acknowledged that this work has been carried out within the framework of the project POIR.01.02.00-00-0091/17, which has been financially supported by the European Regional Development Fund. The authors also would like acknowledge the company REMA S.A. in Reszel (Poland), which was the beneficiary of this project.

References

1. Dimter OptiCut 450 Quantum https://falkenberg.no/media/produkter/produktark/sagbruk/73-prospekt-opticut-highspeed-serie-gbr.pdf, last accessed 2025.02.17.
2. Kminiak, R., Kubš, J.: Cutting power during cross-cutting of selected wood species with a circular saw. BioRes. 11(4), 10528-10539. (2016).
3. Kováč, J., Harvánek, P., Krilek, J., Kuvik, T., Melicherčík, J.: Analysis of cutting conditions in the process of cross-cutting wood by circular saws. BioReso, 16(1), 1029-1041. (2021).
4. Nasir, V., Cool, J.: Optimal power consumption and surface quality in the circular sawing process of Douglas-fir wood. Eur. J. Wood Prod. 77, 609–617 (2019).
5. Orłowski, K., Blacharski, W., Chuchała, D., Dudek, P.: Theoretical and actual feed per tooth during wood sawing on an optimizing cross-cut saw. In: Królczyk G., Niesłony P., Królczyk J. (eds) Industrial Measurements in Machining. IMM 2019. Lecture Notes in Mechanical Engineering. Springer, Cham. 259-267. (2020).
6. Manžos, F.M.: Derevorežuščie Stanki, (In Russian: Wood cutting machine tools), Izdatel'stvo Lesnaâ promyšlennost', Moskva (1974).
7. Blacharski, W., Orlowski, K., Chuchala, D., Dudek, P., Fidurski, M.: Sposób optymalizacji cięcia na długość i wycinania wad materiału drzewnego w pilarce tarczowej i układ posuwowy z serwomotorem liniowym w pilarce tarczowej. Patent PL2398

Water repellency of wood surfaces by high-speed friction processing

Tadashi Ohtani[1], Ryuichi Iida[2] and Doppo Matsubara[3]

[1] Tokyo Gakugei University, Japan,
[2] Polytechnic University, Japan
[3] Tokyo University of Agriculture and Technology, Japan
t-ohtani@u-gakugei.ac.jp

Abstract. This study investigated a new processing method that can produce functionality such as super-water repellency by effectively controlling the uneven shape of the wood surface and adding chemical components. The processing method was performed in friction by contacting a metal tool with wood sample. The wettability of the wood surface was measured in the friction-treated under different conditions. Spruce wood was used for the friction processing, and the wood surface was rubbed while a tool rotating at high-speed was contact with the wood sample. The result showed that the inherent hydrophilic properties of wood changed to water-repellent properties by rubbing the surface layer of the wood sample. In addition, the water repellency effect of the friction processing could be further improved by using a coated tool with containing fluorine components or applying fluorine paint to the wood surface before the friction processing. Furthermore, it was found that the effect of the friction processing could be further utilized to form a super-water repellent wood surface by adding fine processing to the wood surface.

Keywords: High-speed friction, Water repellency, Wood surface.

1 Introduction

Wood becomes deform or rot due to moisture. Therefore, when wood is used for exterior construction or outdoor flooring, it is currently treated with paint or chemicals to improve durability. In relation to moisture, the "wettability" of wood, which indicates how water penetrates the wood surface, is important for durability.

Regarding the wettability of materials, it has been revealed that the effect of excellent water repellency was known as a "lotus effect" in which the uneven surface of lotus leaves [1]. Focusing on such excellent properties of living things, surface treatment technologies related to biomimetics that control the unevenness of material surfaces to improve water repellency have been investigated [2-4]. In these studies, it has been reported that by controlling the unevenness of the material surface at the micro to nanometer-level, it is possible to achieve super-water repellency on the surface [3-4].

From the above reports on controlling the shape of material surfaces, our research have already conducted on controlling the unevenness of wood surfaces by rubbing the wood surface with a smooth metal tool and machining it [5]. This method of surface modification by friction treatment can easily improve the smoothness of the wood surface by using a rotary tool used in machining wood. Furthermore, by using the mechanical and thermal effects of friction to induce tribo-chemical reactions on the wood surface, it is possible to simultaneously smooth and modify the surface structure.

In contrast, research on imparting functionality to wood surfaces has been reported, including research on forming a superhydrophobic wood surface by plasma treatment and forming a thin film on the wood surface, and research on preventing the wettability of wood after UV exposure by applying metal nanoparticles to the wood surface [6-7]. These studies on wood surface treatment have shown that it is possible to develop new functionality such as super-water repellency by effectively controlling the unevenness shape and applying components that impart functionality, using machining.

Therefore, this study investigated the wettability of wood surfaces when rubbed at high-speed using a metal tool with a smooth surface. Furthermore, and attempted to form a super-water repellent surface by surface modification using the smoothness generated by friction treatment and the tribo-chemical reactions.

2 Material and methods

2.1 Wood sample

The sample material was air-dried spruce (Picea sitchensis Carr.) with 10.3 % moisture content and 0.46 g/cm3 density. Table 1 shows the sample wood specimen used in this experiment. The sample materials were cut into dimensions of 3 (T) × 50 (L) × 11 (R) mm for specimen A-D and 50 (T) × 100 (L) × 25 (R) mm for specimen E by using a circular saw. Surface pre-treatment of the sample wood specimens was finished in planer cutting, and specimen A was used for the control surface.

Table 1. Sample wood specimen used in this experiment.

Wood sample	Surface condition
Specimen A	Control (in planer cut surface)
Specimen B	Friction [Fr] + Lubrication oil (in wood surface) [L_{oil}]
Specimen C	[Fr] + Fluoridation (in tool) [F_{tool}]
Specimen D	[Fr] + [F_{tool}] + Fluorine oil (in wood surface) [F_{oil}]
Specimen E	[Fr] + [F_{tool}] + [F_{oil}] + Laser drilling [Ld]

The friction surface of the sample wood was set on the tangential section (LT) in the longitudinal (L) and tangential (T) directions to the fiber direction. The specimen B as shown in Table1 was rubbed in the friction [Fr] of wood surface after painted the lubrication oil [L_{oil}]. The specimen C was robbed in [Fr] by using the coated tool of PTFE with the fluoridation component [F_{tool}]. The specimen D was robbed in [Fr] ＋ [F_{tool}] of wood surface after painted the fluorine oil [F_{oil}]. The specimen E was set in the wood surface by Laser drilling [Ld] after robbed in [Fr] ＋ [F_{tool}] ＋ [F_{oil}].

2.2 Experimental conditions of friction test

To investigate functionality such as water repellency on the wood surface, a mechanical processing technology was used in which the surface layer of less than 1 mm was densified and rubbed. As for the mechanical processing of wood, the technology such as cutting using a rotating tool was mainly developed and used. Fig.1 shows schematic illustrations of the high-speed friction test apparatus and the detailed conditions of the rubbing system. The experimental test was conducted in the friction system where the sample wood specimen sliding to the round bar tool which was driven in a unidirectional manner. The rotation speed of the tool and the feeding speed were denoted by feed rate f and circumferential speed V, respectively. Tool surface was also denoted by amount of reduction t.

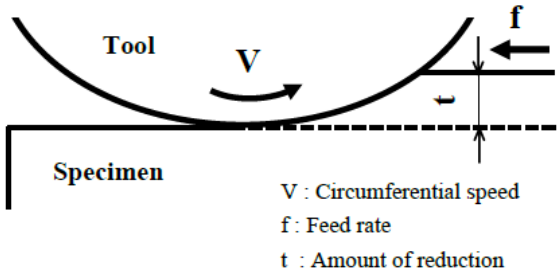

Fig. 1. Schematic illustration of experimental condition in friction treatment test.

Table 2 shows the processing condition of the sample wood specimens in this experiment. The tools for the friction test were used in the based material of SUS304, and the tool for the test of specimen B was conducted by using SUS-tool with the lubrication of linseed oil. Another tool was coated with the original paint, which included the main component, polytetrafluoroethylene (PTFE). The coating was performed by SURFCOAT Co., Ltd in Tokyo Japan. The friction test of specimen C-E was also conducted by using the PTFE coated tool.

The conditions of the friction test treatment were as follows: the feeding speed of the sample wood specimen was set in 0.012 m/s and tool circumferential speed was 490 [m/min], and the reduction amount that pressed tool against the wood specimen surface was set in 300 μm, The laser drilling for the specimen E was used of the femtosecond laser processing machine (LASER P400U manufactured by GF Machining Solutions). The drilling condition was set in the spot diameter of 50 μm by femtosecond laser among 75 μm pitch.

Table 2. Processing condition of the sample wood specimens in this experiment.

Experimental conditions	Conditions [Unit]
Base material of tools	SUS304
Coated material of tools	polytetrafluoroethylene (PTFE)
Circumferential speed (V)	490 [m/min]
Feed rate (f)	0.012 [m/min]
Amount of reduction (t)	300 [μm]
Lubricant	Flaxseed oil, Fluorine oil
Laser drilling	Spot diameter of 50 μm by Femtosecond laser among 75 μm pitch

2.3 Evaluation of wettability in rubbed wood surface

The water repellency of the friction treated wood surface was evaluated. The water droplet contact angle θ was determined in order to evaluate the wettability under the condition that water droplets adhered after the friction treatment. Fig.2 shows the measurement of the water droplet contact angle θ by the droplet method. In the droplet method experiment, distilled water was gently dropped under the condition that the droplet volume was 1.5 μl, and the droplet contact angle θ was evaluated. For the evaluation, the images were taken of the state when water was dropped, and the obtained images were analyzed. In the image analysis, the contact angle θ was calculated using the following equation (1) by obtaining the radius (r) and height (h) of the droplet at the interface where the droplet contacts the wood surface. In this experiment, the droplet method was conducted six times on the wood surface after friction treatment.

$$\theta\ (^\circ) = 2\tan^{-1}\left(\frac{h}{r}\right) \cdot \cdot \cdot (1)$$

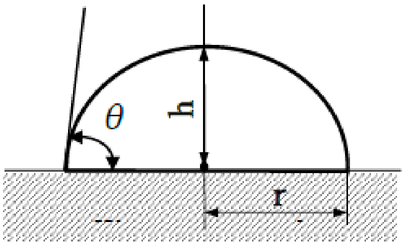

Fig. 2. Measurement of water droplet contact angle θ by droplet method.

The method for evaluating the water repellency used in this experiment was shown in Fig.3. For specimen A, the water repellency was evaluated on the control surface that had been planned. For specimens B and C, the water repellency was evaluated on the surfaces that had been rubbed in friction after planned. Specimen B was lubricated with linseed oil, and specimen C was rubbed with a PTFE-coated tool. For specimen D, the water repellency was evaluated on the surface that had been rubbed with a PTFE-coated tool after applying fluoridation paint to the wood surface. For specimen E, the water repellency was evaluated on the surface that had been machined with fine pits by laser after rubbed under the same conditions as specimen D

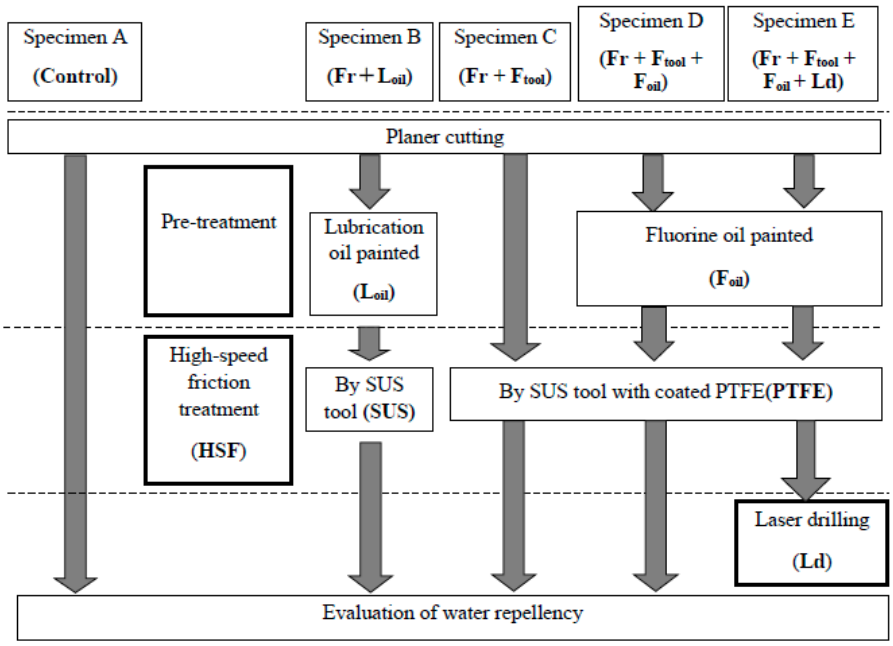

Fig. 3. Evaluation method of the water repellency for the specimens used in this experiment.

3 Results and discussions

3.1 Observation of wettability on rubbed surfaces

To investigate the water repellency of wood surfaces under various conditions, Fig.4 shows the photos of water droplets observed on specimens A to E. In the case of specimen A, a small amount of water droplets can be observed on the surface immediately after dropping the water and then disappearing. In the case of specimens B and C, both of which were subjected to friction treatment, droplets close to hemispheres can be observed immediately after the dropped on the wood surface. When fluorine components were added both to the tool and wood surface of specimen D, droplets on the wood surface were observed to be close to spherical. Furthermore, under the conditions of specimen E, almost spherical droplets could be observed on the wood surface. From the observation, it was indicated that by modifying the wood surface using friction treatment, the surface appears the different wettability for water droplets.

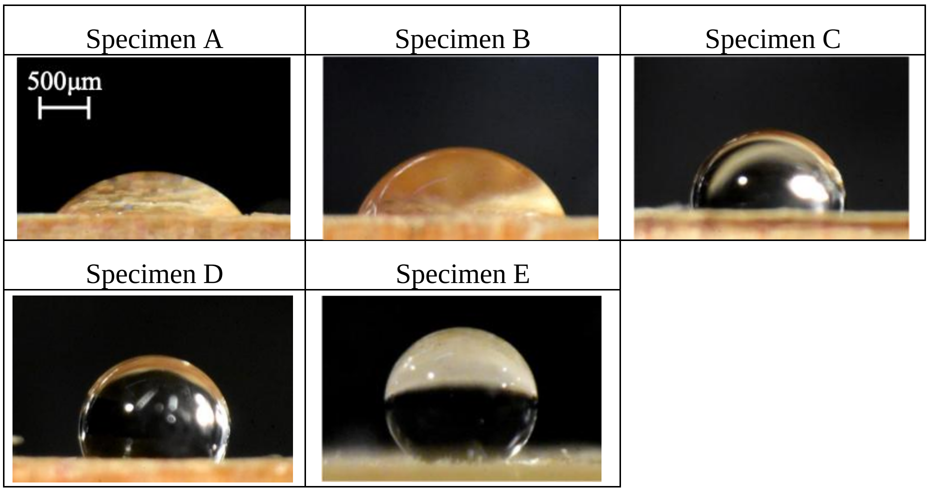

Fig. 4. Observation of the water droplet by droplet method.

3.2 Water repellency on friction-treated surfaces

Based on the observation of the water droplets on the wood surface under different friction treated conditions, the droplet contact angle was calculated using Eq. (1). Fig. 5 shows the average water droplet contact angle under various conditions. In the results for specimen A, the water droplet contact angle was about θ = 40°, while the θ value reached 70° or more for the friction-treated surface of specimen B and C. The θ value for specimen C, which was rubbed with a tool with a PTFE coated on its surface, was larger than the θ value for specimen B, which was rubbed under lubricated conditions by flaxseed oil. Furthermore, when fluorine components were added both to the tool and wood surface of specimen D, the θ value exceeded 100°, and the θ value for specimen E was even larger, reaching about 140°.

From the above results, the water droplet contact angle is small on the normal planer-cut wood surface, whereas the water droplet contacts angle increases when the friction treatment method is applied, and the surface can be modified from hydrophilic to water-repellent. Furthermore, the water repellency can be further improved by adding fluorine components that show water repellency to the tool surface and wood surface. In addition to the effects of smoothing and tribo-chemical reactions caused by friction treatment, it is found that a super-water-repellent surface can be formed by further micro-processing the wood surface.

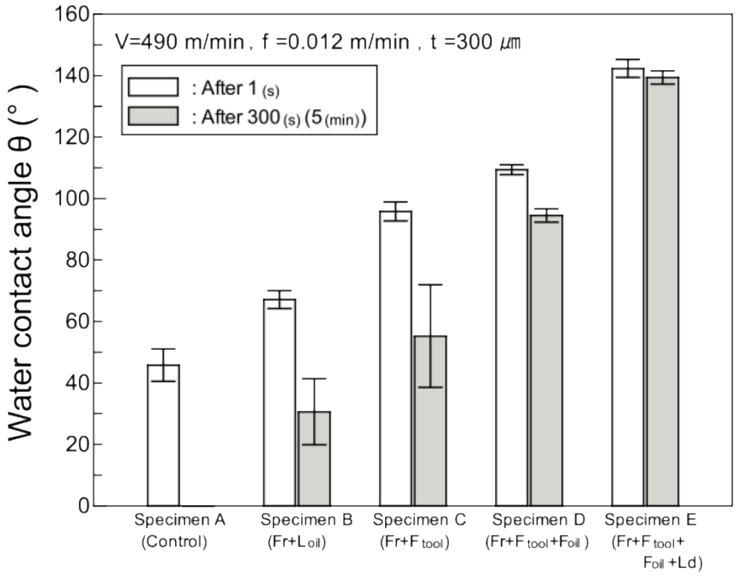

Fig. 5. Water droplet contact angle measured in each wood sample specimen.

4 Conclusions

As a new method of surface treatment, friction processing was performed by contacting a metal tool with wood, and the wettability on the wood surface in various friction treatments was evaluated. The results obtained were as follows:

(1) By rubbing the surface layer of the wood, the inherent hydrophilic properties of wood changed to water-repellent properties.

(2) By adding fluorine components that show water repellency to the tool and wood surface for friction treatment, the water-repellent properties of wood surface could be further improved.

(3) In addition to the above effect of friction treatment, it was found that a super-water-repellent wood surface could be formed by taking advantage of the surface smoothing caused by friction treatment and further applying fine processing to the wood surface.

Acknowledgments. Part of this research was funded by the Adaptable and Seamless technology transfer Program (A-STEP) industry-academia collaboration (training type) in Japan Science and Technology Agency (JST) subsidy for 2022, "Development of surface treatment technology by tribo-chemical reaction for utilization of decarbonized wood" (representative: Tadashi Otani).

References

1. Barthlott,W., & Neinhuis,C.: Purity of the sacred lotus, or escape from contamination in biological surfaces. Planta 202, 1-8 (1997)
2. Sheng X, Zhang J. : Directional motion of water drop on ratchet-like superhydrophobic surfaces, Applied Surface Sci. 257, 6811-6816 (2011)
3. Tang MK, Huang XJ, Guo Z, Yu JG, Li XW, Zhang QX. : Fabrication of robust and stable superhydrophobic surface by a convenient, low-cost and efficient laser marking approach, Colloids and Surface A, Physicochem Eng Aspects 484, 449-456 (2015)
4. Guo Z, Zhou F, Hao J, Liu W.： Effects of system parameters on making aluminum alloy lotus, J Colloid and Interface Sci. 303, 298-305 (2006).
5. Ohtani T, Iida R. : Effect of mechanical and thermal reaction in high-speed friction processing of wood surface, Proceedings of 25th International Wood Machining Seminar (2023).
6. Xie L., Tang Z., Jiang L., Breedveld V., Hess D.W. : Creation of superhydrophobic wood surfaces by plasma etching and thin-film deposition, Surface & Coatings Technology 281, 125-132 (2015)
7. Tengfei Y., Jeffrey J. M.:Ability of metallic nano-particles to provide UV protection to wood surface: a preliminary experiment, Journal of Coatings Technology and Research.19, 1535-1550 (2022)

Effects of the lubricant in high-speed friction processing

Ryuichi Iida[1][0000-0001-7564-7616] and Tadashi Ohtani[2]

[1] Polytechnic university, Japan
[2] Graduate School of Education, Tokyo Gakugei University, Japan
r-iida@uitec.ac.jp

Abstract. New wood surface treatment technology is being developed to improve functionality on wood surface by rubbing wood surface in high speed. This new technology which is called "high speed friction treatment" in our study, is conducted by rubbing wood surface with smooth metal round bar tool surface. During such processing, wood surfaces are heated by the effect of frictional heat and become smoother surface which reflected tool surface asperity by mechanical action of friction. However, some problems have been occurred when the friction condition become in unappropriated during processing and wood surface become rougher and less functionality. In this study, to solve such problem, it was tried to add the lubricants or to use coated tool in high-speed friction treatment. The effect of the lubricant addition was investigated with focusing on the processing accuracy and the functionality generated on wood surface. The treated wood surface colure, roughness and water repellency were evaluated. The results showed that change of wood surface colure was suppressed by adding lubricant in comparison with non-lubricated high speed friction processing condition. The lubrication affected to the change of wood surface asperity to the generation of smooth surface. Furthermore, smoothed wood surface showed the high performance in the water repellency. From above results, it would be considered that the appropriated lubricating condition are needed for high-speed friction treatment in the terms of processing accuracy and generating functionality on wood surface.

Keywords: Wood surface, High-speed friction, Lubricant, Accuracy

1 Introduction

The realization of a decarbonized society necessitates the long-term utilization of wood. Durability is particularly required when the wood is used outdoors, where exposure to ultraviolet rays, wind, and rain causes degradation. The retention of rainwater on the wood surface, in particular, leads to increased moisture content, accelerating decay. Therefore, to ensure the long-term utilization of wood, it is essential to implement treatments that prevent water retention on the wood surface and water infiltration into the wood.

Several studies have been conducted to enhance the water repellency of wood surfaces. Kúdela et al. reported that the wettability of beech wood was varied by changing the surface roughness using a CO2 laser [1]. Additionally, there are reports of studies attempting to improve water repellency through chemical changes in the wood surface using silane treatment [2,3].

We have also been developing a new surface treatment technology to impart water repellency to wood surfaces. Our method involves rubbing the wood surface with a smooth-surfaced metal round bar rotating at high speed. Using this new high-speed friction treatment method, it has successfully generated ultra-smooth wood surfaces [4] and improved water repellency at the laboratory scale wood samples [5]. This high-speed friction treatment technology causes thermal and mechanical effects due to friction. These effects are leading to changes in the roughness and chemical properties of the wood surface. Based on our research results, we expanded our technology from the laboratory scale to practical applications. However, when applying the friction treatment technology to practical-scale wood samples, roughened surfaces and surfaces with low water repellency were formed. This may be due to improper lubrication during friction.

Therefore, in this study, we investigated the effects of coating highly lubricating materials on the tool surface and applying lubricants during the friction treatment to solve the problems that arise when performing friction treatment on practical-scale wood samples.

2 Materials and methods

2.1 Sample material

Air-dried Spruce was used for the high-speed friction treatment. Sample specimens were cut to 100 mm in the longitudinal direction, 30 mm in the radial direction, and 20 mm in the tangential direction. All specimens were kept under the same conditions of 20℃ and 65% relative humidity (RH). The friction treated surface was conducted on the tangential section of the wood sample specimen.

2.2 High-speed friction treatment

High-speed friction treatment was conducted using the originally designed machine. Figure 1 shows the processing section of the friction processing machine. This machine was developed by modifying an existing wood planer, replacing the cutting blades with a metal cylinder with a smooth surface. The diameter of the metal cylinder was 52 mm. As shown in Figure 2, the high-speed friction treatment method was carried out by feeding wood specimens, fixed on a jig, against a rotating metal disc tool at a constant speed using an actuator. In this experiment, the tool rotation speed was configured at 8,000 rpm, and the tool reduction amount to the wood specimens was set to 0.3 mm. The feed speed of the wood specimens was maintained at 1 mm/s.

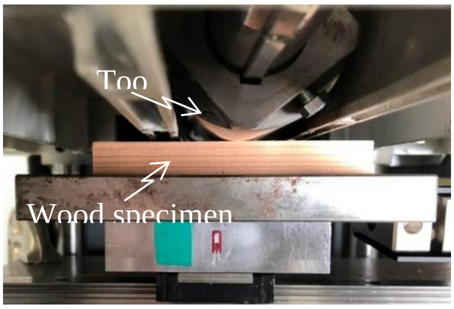

Fig. 1. Friction Treatment Section in high-speed friction treatment experimental apparatus

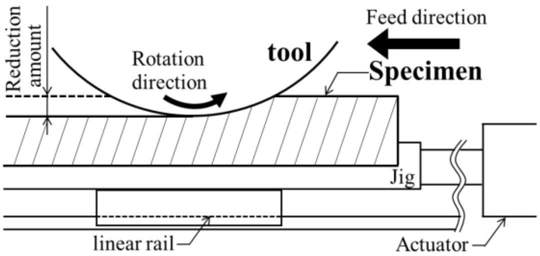

Fig. 2. Schematic illustration of high-speed friction treatment condition

Table 1 illustrates the lubrication conditions employed during friction processing in this experiment. We modulated the friction conditions during high-speed friction processing by applying various coatings to the tool surface and lubricant to the wood surface prior to high-speed friction treatment.

Table 1. Tool and lubricant condition in high-speed friction treatment

Symbol	Tool material	Coating on tool surface	Lubricant
F_{SUS}	SUS304	-	-
F_{TiN}		TiN	-
F_{PTFE}		PTFE	-
$F_{PTFE+Lub}$		PTFE	Fluorine oil

Under non-lubricated conditions, high-speed friction treatment was conducted using a metal disc tool made of SUS304 without any added lubricants. This experi-mental condition was denoted as "F_{SUS}" in this study. In the experimental conditon of applying the coated tool, the tool surface of SUS304 was coated with either titanium nitride or polytetrafluoroethylene to modify its frictional properties. These conditions are represented by "F_{TiN}" and "F_{PTFE}" respectively. Furthermore, in the condition where lubricant was applied, a specific amount of fluorine oil (A105 WAKO CHEMICAL CO., LTD.,) was applied to the wood surface before high-speed friction treatment. In this condition, a tool coated with PTFE was used and denoted as "$F_{PTFE+Lub}$" in this report.

2.3 Evaluation of surface properties

Method of Surface color measurements

The color of wood surfaces treated under different high-speed friction treatment conditions were evaluated. Surface color was assessed using a colorimeter based on the Lab color space. The measurement area was set to a diameter of 10 mm. D65 light source was used for measurement. The brightness $L*$ and chromaticity $a*$ and $b*$ were measured. The chroma was calculated as the square root of the sum of the squares $a*$ and $b*$. Measurements were taken at nine locations on each wood specimen.

Surface texture measurement

The surface roughness was measured using a surface roughness meter (surfcom130a Tokyoseimitsu) by tracing the stylus in directions both parallel and perpendicular to the wood fiber. The measurements were taken over a length of 4 mm with a cut-off value of 0.25 to evaluate the surface roughness. The surface profile was treated with a Gaussian filter, according to ISO 4287-1997. The surface roughness was measured at thirty points, both parallel and perpendicular to the grain, for each specimen.

Measurement of water repellency on wood surface.

The contact angles of water droplets on the wood specimen surfaces were measured. The sessile drop method was adopted, wherein a 1.5 μL deionized water droplet was slowly dropped onto the leveled wood specimen surface. The shape of the water droplet was observed from the LR surface of the specimen using a digital camera immediately after the water was dropped onto the wood surface. The radius r and height h of the water droplet in observed image, as shown in Figure 3, were measured by using the image analysis software ImageJ [6-7]. And the contact angle was calculated using the half-angle method in Equation 1.

$$\theta = 2\tan^{-1}\frac{h}{r} \qquad (6)$$

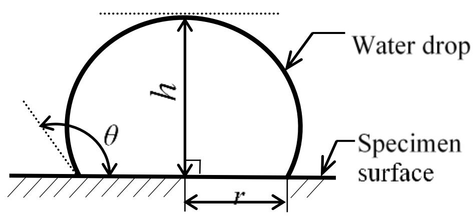

Fig. 3. Evaluation of water contact angle

3 Results and discussions

3.1 Change of surface appearances after high-speed friction treatment

High-speed friction treatments were conducted under various lubrication conditions, and the changes in surface coloration were evaluated. Figure 4 shows the surface of the wood specimens after high-speed friction treatment. Under the condition where the SUS tool was used without any lubricant (F_{SUS}), partial darkness of the wood surface was observed. Conversely, under the conditions of F_{PTFE}, F_{TiN}, and $F_{PTFE + Lub}$, no significant blackening was recognized.

To analyze the changes in surface coloration in detail, a colorimeter was used to evaluate the surface color of the wood. Figures 5 and 6 shows the Brightness ($L*$) and chroma ($C*$) of the wood surface, respectively. The $L*$ of the wood surface decreased under all conditions of high-speed friction treatment in comparison with non-treated surface (CR). This decrease in $L*$ can be attributed to the thermal effects exceeding 100 ℃ that occur between the wood and the tool during high-speed friction treatment [8]. The decrease in $L*$ was particularly pronounced under the F_{SUS} condition. On the other hand, the chroma of the wood surface increased after treatment. The increase in chroma was especially notable under the $F_{PTFE+Lub}$ condition. The greatest variation in coloration was observed under the F_{SUS} condition, resulting in an uneven surface color.

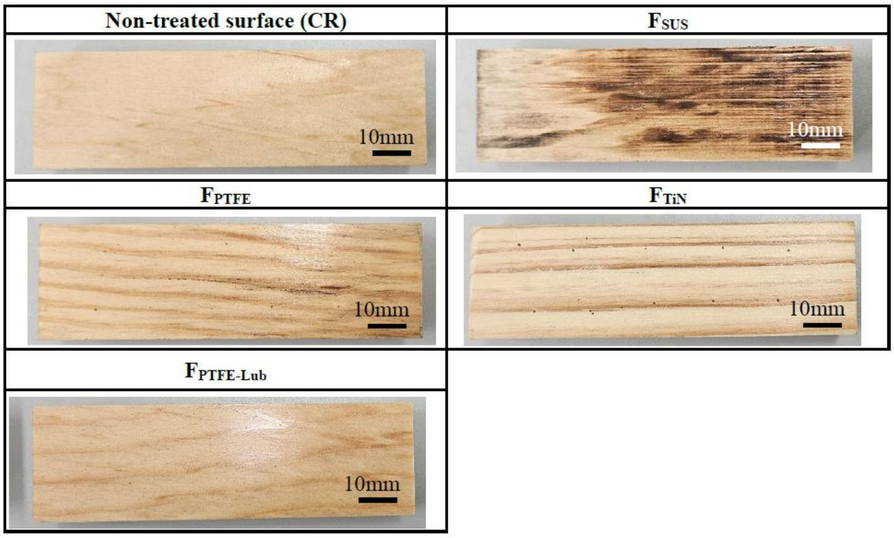

Fig. 4. Spruce surface after high-speed treatment.

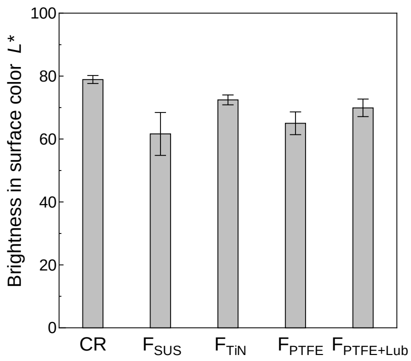

Fig. 9. Brightness in wood surface treated by high-speed friction in different condition

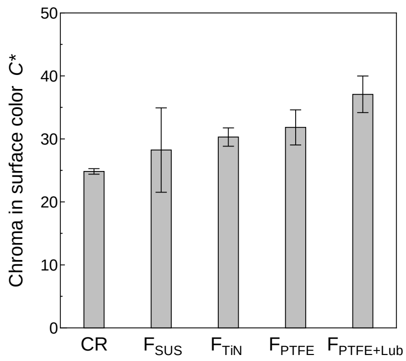

Fig. 10. Chroma in wood surface treated by high-speed friction in different condition

3.2 Surface texture change after high-speed friction treatment

The surface topography of wood was evaluated. Figure 7 shows the arithmetic average roughness *Ra* of the wood surface under various high-speed friction treatment conditions. The spruce surface after friction treatment was smoother than the untreated surface processed by planer cutting. The condition where a lubricant was added during friction treatment produced the smoothest wood surface, with *Ra* of less than 1 μm. On the other hand, the conditions with F_{SUS} and F_{TiN} resulted in higher *Ra* values compared to the condition using PTFE-coated tools. This is considered that the insufficient lubrication during the friction treatment caused wood adhesion to the tool surface, as shown in Figure 8.

From these results, it can be concluded that appropriate lubrication is essential to achieve a smoother wood surface through high-speed friction treatment.

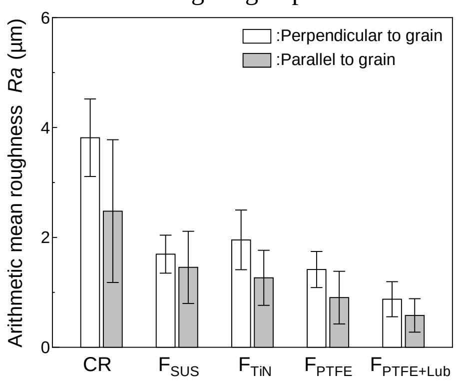

Fig. 7. Surface roughness of wood surface treated high-speed friction

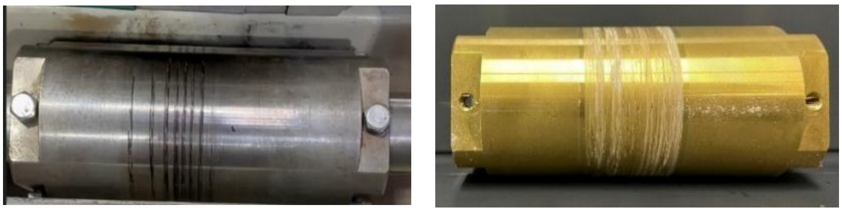

Fig. 8. SUS and TiN Tool surfaces condition after high-speed friction treatment

3.3 Water repellency on treated wood surface

The water repellency of the surface after friction treatment was evaluated. Figure 10 shows the measurement results of the water droplet contact angle on each wood surface. The water droplet contact angle on the wood surface increased after friction treatment. In particular, wood surface treated by the condition using PTFE-coated tools and with added lubricant during treatment showed larger water droplet contact angles. The $F_{PTFE+Lub}$ condition exhibited a water droplet contact angle of approximately 100 degrees. Furthermore, it was observed that the variation in measurement results was smaller under the F_{PTFE} and $F_{PTFE+Lub}$ conditions.

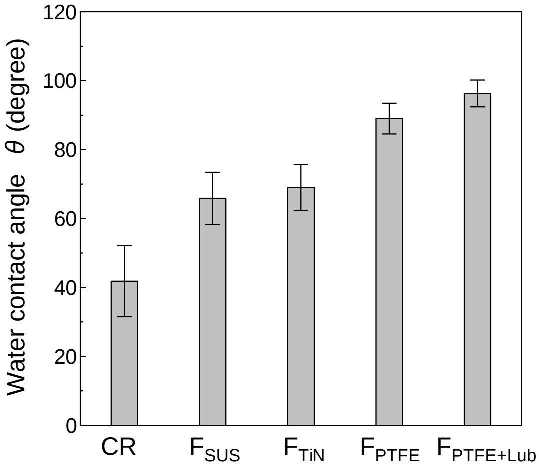

Fig. 9. Water contact angle on treated wood surface

To evaluate the uniformity of the processing during friction treatment, the ratio of the standard deviation of the measurements in treated surface and untreated surface was calculated for the values of surface roughness and water droplet contact angle. Table 2 shows the ratio of the standard deviation of measurement values in the treated surface to untreated surface. It is found that, under any friction treatment conditions, a surface with less variability is formed compared to the wood surface created by planer cutting. However, higher values were observed in the condition of F_{SUS} in comparison with F_{PTFE} or $F_{PTFE+Lub}$.

From these results, it was concluded that using the coated tools with highly lubricating substances or adding lubricants during friction treatment can consistently produce wood surfaces with stable functionality and less variability in roughness.

Table 2. The ratio of the standard deviation of each evaluation index for untreated wood surfaces

Evaluation index	High-speed friction treatment condition			
	$\mathbf{F_{SUS}}$	$\mathbf{F_{TiN}}$	$\mathbf{F_{PTFE}}$	$\mathbf{F_{PTFE+Lub}}$
Ra in parallel to grain	0.51	0.39	0.37	0.23
Ra in perpendicular to grain	0.49	0.77	0.47	0.45
Water contact angle $\boldsymbol{\theta}$	0.73	0.65	0.43	0.38

4 Conclusion

In this study, it was investigated that the effects of coating highly lubricating materials on the tool surface and applying lubricants during the friction treatment. The following results are obtained.

1) It is possible to prevent from surface color darker in high-speed friction treatment surface by using the coated tool.

2) It is essential to ensure appropriate lubrication by using a coated tool or adding lubricants to achieve a smoother wood surface through high-speed friction treatment.

3) The coated tools with highly lubricating substances or adding lubricants during high-speed friction treatment can consistently produce high quality wood surfaces.

References

1. Kúdela, J.; Kubovský, I.; Andrejko, M. Surface Properties of Beech Wood after CO_2 Laser Engraving. Coatings 10(1), 77 (2020).
2. Mengying, Z.; Jianxiong, L.; Ping, L.; Xianjun, L.; Guangming, Y.; Yingfeng, Z. Construction of high-efficiency fixing structure of waterborne paint on silicate-modified poplar surfaces by bridging with silane coupling agents. Prog. Org. Coat. 2022, 167, 106846.
3. Donath, S., Militz, H. & Mai, C. Weathering of silane treated wood. Holz Roh Werkst 65, 35–42 (2007).
4. Ohtani, T., Iida, R., Nakai, T. et al. Smoothness of a spruce surface rubbed with a metal tool under high-speed friction. J Wood Sci 62, 377–380 (2016).
5. Iida R, Ohtani T, Yurikusa M. Effect of High-Speed Friction Treatment with Fluorine Components on the Changes in Spruce Surface Properties. Buildings. 14(11), 3513 (2024).
6. Schneider, C.A., Rasband, W.S., Eliceiri, K.W. "NIH Image to ImageJ: 25 years of image analysis". Nature Methods 9, 671-675, 2012.
7. Abramoff, M.D., Magelhaes, P.J., Ram, S.J. "Image Processing with ImageJ". Biopho-tonics International, volume 11, issue 7, pp. 36-42, 2004.
8. Iida, R., Ohtani, T., Nakai, T. et al. Changes in wood temperature under high-speed friction. J Wood Sci 60, 313–320 (2014).

Calibration and Sensitivity Analysis of a Bonded Particle Model for the Simulation of Chip Ejection from Wood Cutting Tools

Julius Hausmann[1]

Dresden University of Technology, Dresden, 01069, Germany,
julius.hausmann@tu-dresden.de,
WWW home page: https://www.tu-dresden.de/hft

Abstract. The Bonded Particle Model (BPM) provides a novel method for simulating chip ejection in wood machining, but its accuracy relies on proper calibration of functional parameters. This work identifies critical model parameters using Design of Experiments methodology. Material parameters of spheres and bonds, as well as contact model parameters like the coefficient of restitution and friction coefficients are examined, to assess their effects on chip ejection dynamics. Key findings indicate that controlling the total number of broken bonds through strength ratios is essential, while strain to rupture and strength ratios also influence the median particle speed. Factors affecting flight angles are less clear. Simulation results show that flight angles in BPM closely match experimental data, while velocity magnitudes differ more significantly. This work enhances understanding of BPM parameters and their impact on chip ejection, highlighting calibration challenges.

Keywords: bonded particle method (BPM), chip ejection, parameter calibration, groove milling, particleboard

1 Introduction

The emissions of dust and chips from wood-cutting processes are of great importance for occupational health and safety, as well as the economic efficiency of machining processes in the wood industry. Owing to the significant volume of stock removal, even small fractions of uncaptured dust and chips can have severe consequences. The reason for the low capture rates often results from an insufficient design of the dust and chip hoods. Chips from saw-like tools have an initial velocity after chip formation that is usually higher than the cutting velocity [1]. The dispersity of chips from wood sawing processes is affected by a multitude of factors, including the geometry of the cutting tooth, internal structure of the wood, cutting direction, and moisture content [2], [3]. In most sawing processes, the average particle size by mass is typically larger than 100 µm [4]. These coarser particles have relatively high inertia and are not significantly affected by common suction flows, which can be depicted by an evaluation of the Stokes numbers [5]. It can be concluded that the particles released from a cutting tool inside the dust hood will likely strike the wall of the dust hood. Therefore, it is crucial to determine their initial conditions upon ejection from the cutting tool to better understand how particles interact with the tool chip space and how they collide with the walls. In a current research project, these conditions were studied both experimentally and numerically for the groove sawing process for both particleboard and medium-density fiberboard. Given the complexity of wood machining, numerical methods offer a promising approach for analyzing these dynamics. The Bonded Particle Method (BPM) can be applied to simulate the behavior of wood chips during and after the cutting process. This study contributes to the development of a surrogate model of chip ejection for coarser chips by examining the model proposed by [6] using MUSEN discrete element software [7]. The objective was to identify the appropriate parameters for the model and evaluate its performance with respect to real-world observations. At first, the considerations involved in the derivation process of the BPM model for the chip ejection of particleboard are outlined. The model is then treated as a black box, and a design of experiments (DoE) is applied to systematically investigate the influence of material definitions and contact model parameters on chip motion. Finally, the simulation results of the calibrated model are compared with real-world observations.

2 Material and Methods

2.1 Derivation of a BPM approach

To derive a surrogate model for the ejection of chips, a literature review of cutting simulations based on the discrete element method has been conducted [6]. Inspired by the preliminary work, a structural model for the simulation of chip ejection in particleboard milling was derived [6], wherein the chips formed are represented in a rudimentary manner, including the orthotropic structure of the particleboard. Previous studies have demonstrated that the utilization of regular cubic lattices facilitates a high degree of anisotropy, thereby defining the shear planes between layers along the main axis [8]. In contrast, in irregular packing's, interlocking spheres lead to a rupture that is less smooth or dynamic (cf. [8], [9]). Thus, a regular lattice was employed, with bonds in the xy-plane representing particleboard chips. The bonds in the z-direction represent the interparticle contacts belted by glue. The discrete representation of a continuous domain as a discrete assembly of spheres and bonds, inevitably introduces discretization error and is constrained by computational costs. Finer discretization not only increases computational costs owing to the increased number of discrete elements but also because a decreased critical time step is required for a stable simulation, which depends on the particle radius R_p. In MUSEN, the required time step is calculated based on either the Rayleigh time or a critical time step for bonds. In addition, the critical time step relies on the particles Poisson ratios ν, Young's moduli E, densities ρ, and stiffness of the bonds, which moreover depend on the initial bond length L_{init} and bond radius R_b. For further details, please refer to [7]. Choosing the right level of discretization in the BPM depends on a critical dimension that needs to be represented, such as the size of chips or even wood fibers inside the chips. The feet per tooth f_z is considered a characteristic length defining the cutting process. Therefore, the lattice formed here consists of monodisperse spheres with $D_p = 80\,\mu m$, similar to the feed per tooth for this particular application. This ensures that each engaging tooth interacts with at least one layer of particles. To reduce the computational costs, the spacing of the spheres inside the lattice is $2.5\,R_p$, which is $100\,\mu m$. The spacing in the z-direction differs by $-2\,\mu m$ to create individual bonds in this direction because the bond creation process is based on distance thresholds. The bonds between the spheres are defined with a diameter D_b equal to the sphere diameter D_p in the xy-plane and a smaller diameter in the z-plane, given by $0.667\,D_p$. The author initially wanted to represent the inherent material stiffness and strength properties of particleboard by reducing the bond diameter in the z-direction. However, scaling the bond diameters is unfavorable because it leads to a reduction in the transfer of moments between the contacting spheres [10]. Irrespective of this, the bond diameters were maintained, as stated before, to preserve the integrity of the initial model parameters established based on this structural model.

The elastomechanical properties of discrete bonds depend on the mathematical bond model implemented and employed in the simulation software. Here, the Kelvin-Voigt model implemented in MUSEN [7] was used. To calculate the reaction forces, the relative velocities between the particles are split into normal and tangential components. The elastic forces in both the normal and shear directions are proportional to the relative displacement following Hooke's law. The tangential stiffness is derived from the relationship for isotropic materials, $G = \frac{E}{2(1+\nu)}$, where G is the shear modulus. In the Kelvin-Voigt bond model, dissipation forces control energy loss during particle interactions by damping their relative motion, typically linked to real-world friction or viscosity. These forces impact the total magnitude of reaction forces, influencing the simulation's dynamics and stability. The dissipation forces are proportional to the relative velocities of two connected particles multiplied by a numerical damping coefficient η, which was set to 100 here. Finally, a bond-breakage criterion must be introduced. A bond is deemed broken if the normal or shear stress exceeds the maximum strength thresholds in the normal direction σ or tangential direction τ. The bond's mechanical behavior is defined by its geometry, Young's modulus E, Poisson ratio ν, and maximum strengths σ and τ. Further details can be found in the MUSEN documentation.

2.2 Exploration of BPM parameters by Design of Experiments

One of the biggest challenges of BPM is the calibration of the material properties of the discrete elements in the selected discretization scale for a specific structural model. In addition to the material stiffness, the number of bonds per sphere also has a direct effect on the mechanical behavior of the BPM structure.

In cubic sphere packing, only a portion of the space is filled with matter, making it feasible to enhance the elastomechanical properties and density of discrete elements to align with bulk properties. This is particularly necessary if realistic reaction forces are part of the model's objective. Yet the author assumes that the forces required for material breakage are less important for simulating chip ejection, as the main acceleration comes from the collision between the cut chip and the cutting tooth. Thus, matching a specific ratio of strength and stiffness properties is deemed more relevant for realistic chip formation. The initial material properties in table 1 (level 0) were based on spruce wood (*Picea abies* (L.) H. Karst) but were modified through trial and error due to excessive destruction observed in the BPM simulation. Curti [8] also applied density calibration for their cutting simulations. Given newtons second law, it seems advisable to include the density definitions into the calibration process. Here, the density of the spheres were set rather incidentally to $1000\,\mathrm{kg\,m^{-3}}$, close to the density of the surface layer of particleboard.

Table 1: Factors and factor levels used for the setup of the DSD. The factor levels -1 and 1 are calculated by either doubling or halving the initial level 0 parameters. Symbols: coefficient of restitution e, coefficient of friction μ, subscripts: kinetic k, rolling r, Wood - Wood $W-W$, Wood - Tool $W-T$

Factor	Factor levels			Unit
	-1	0	1	
E_{XY}	5.5×10^{9}	1.37×10^{10}	2.2×10^{10}	$\mathrm{N\,m^{-2}}$
σ_{XY}	1.0×10^{8}	2.05×10^{8}	4.0×10^{8}	$\mathrm{N\,m^{-2}}$
τ_{XY}	2.5×10^{7}	6.25×10^{8}	1.0×10^{8}	$\mathrm{N\,m^{-2}}$
ν_{XY}	0.05	0.25	0.45	
E_{Z}	2.0×10^{8}	3.5×10^{8}	5.0×10^{8}	$\mathrm{N\,m^{-2}}$
σ_{Z}	5.0×10^{7}	1.25×10^{8}	2.0×10^{8}	$\mathrm{N\,m^{-2}}$
τ_{Z}	5.0×10^{7}	1.25×10^{8}	2.0×10^{8}	$\mathrm{N\,m^{-2}}$
ν_{Z}	0.05	0.25	0.45	
$e_{\mathrm{W-W}}$	0.2	0.5	0.8	
$\mu_{\mathrm{k,W-W}}$	0.2	0.5	0.8	
$\mu_{\mathrm{r,W-W}}$	0.2	0.5	0.8	
$e_{\mathrm{W-T}}$	0.2	0.5	0.8	
$\mu_{\mathrm{k,W-T}}$	0.2	0.5	0.8	
$\mu_{\mathrm{r,W-T}}$	0.2	0.5	0.8	

To study the influences of the material properties and collision properties, Design of Experiments (DoE) was applied. The study is based on a Definitive Screening Design (DSD), a special partial factorial design with a very small experimental scope. A DSD is based on three factor levels and are primarily aimed at determining main effects but may also allow the evaluation of interactions and quadratic terms, which makes them suitable for initial investigations of non-linear relationships. For the 16 factors considered here, only 38 experiments are required for a basic analysis. As described in section 2.1, the simulation time step needs to be adjusted if sphere or bond stiffness definitions are changed. The "recommended time step" was calculated for each run and used for the simulation.

The groove milling of particleboard is used as a reference process for analysis and calibration, particularly a groove saw with a 150 mm diameter, 8 mm cutting width, and 12 cutting teeth, each with a flat top grind and 15° rake angle. In the simulation, the feed speed is $28.8\,\mathrm{m\,min^{-1}}$, and the tool rotates at $6000\,\mathrm{min^{-1}}$. Thus, the feed per tooth is 0.4 mm, and the cutting speed is $47\,\mathrm{m\,s^{-1}}$. The BPM assembly used for the DoE is initialized by a cuboid of (25 x 4 x 3.5) mm (xyz). The tool was positioned centered on the edge of the cuboid ($x = 0\,\mathrm{mm}$ and $z = 75.5\,\mathrm{mm}$). The spheres inside the tool domain were removed. This results in a cutting depth $a_\mathrm{e} = 3\,\mathrm{mm}$ and a remaining material thickness of 0.5 mm underneath the cutting line. This setup represents steady-state circumferential milling, where the effects of the minor cutting edges are neglected, as the cutting width is smaller than the width of the cutting tooth (see Fig. 1). The layer of spheres on the bottom surface of the cuboid is constrained by a boundary condition that prevents the assembly from moving during tooth engagement. The simulation consists of a total number of 189 000 discrete spheres and 465 000 bonds.

2.3 Postprocessing of simulation data and statistical evaluation procedure

A significant challenge arises when dealing with the substantial amounts of simulation data in post-processing. MUSEN does not provide the functionalities required for the analysis of agglomerate motion. A statistical analysis procedure calculating the desired metrics from exported simulation data was implemented in the programming language Python. This included the extraction of the 'actively" emitted particles or agglomerates from the rest of the spheres, filtered by their velocity component in x-direction $v_\mathrm{x} > 10\,\mathrm{m\,s^{-1}}$. Only this group of particles was used in the calculation of particle statistics. After postprocessing, a stepwise linear regression analysis was conducted using the software JMP to identify significant influencing factors on the median particle speed and flight direction, the mean agglomerate diameters, the number of agglomerates, and the total number of broken bonds. As stated before, the author believes the ratios between stiffness and strength parameters might be important for the prediction of particle ejection. Therefore, the following ratios were included in the regression analysis: strain to rupture in normal and tangential directions $\epsilon_{\mathrm{max,N}} = \frac{\sigma}{E}$ and $\epsilon_{\mathrm{max,T}} = \frac{\tau}{G}$, stiffness ratio $\frac{E}{G}$, and strength ratios in xy and z direction. In the following, the final models with only statistically significant ($\alpha = 5\,\%$) main effects are presented.

3 Results

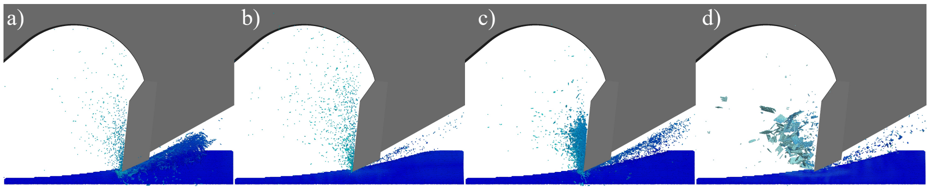

Fig. 1: Four snapshots of simulated trials conducted in the DoE.

The simulated experiments created quite diverse results regarding the chip formation and chip ejection (Fig. 1). The significant influencing factors on the total number of broken bonds are the ratio of normal to tangential strength $\frac{\sigma_Z}{\tau_{XY}}$, followed by strain to rupture $\epsilon_{\mathrm{max,N,XY}}$ and kinetic friction coefficient $\mu_{\mathrm{k,W-W}}$. Regarding $\frac{\sigma_Z}{\tau_{XY}}$, it was found that this ratio $\frac{\sigma_Z}{\tau_{XY}}$ should be smaller than unity and $\epsilon_{\mathrm{max,N,XY}} \leq 0.05$, because otherwise the breakage of bonds occurs far below the cutting line and a lot of passive particles are emitted; see Fig. 1 a) and c). In general, the number of broken bonds is inversely proportional to the agglomerate size. Thus, the number of total broken bonds should be minimized to retrieve larger chips; see Fig. 1, d).

The factors affecting the median particle speed and median flight angle are presented in figures 2 and 3. Higher strain to rupture in the tangential direction $\epsilon_{\mathrm{max,T,XY}}$ and bond strength σ_{XY} increase the median speed. Especially $\epsilon_{\mathrm{max,T,XY}}$ seems like an important factor to calibrate particle speed. Decreasing values of σ_{XY} lead to more breakage of bonds in the xy-direction, forming smaller agglomerates with lower overall kinetic energy (Fig. 1-c). It can be assumed that this relates to the increased amount of energy dissipated because of the increased number of inter-agglomerate collisions. It can be stated that $\epsilon_{\mathrm{max,T,XY}}$ should be in the range 3 % to 7 %. Restitution coefficients also contribute positively, while all friction coefficients reduce median particle speed with increasing values. The contact parameters influence the particle velocity as expected according to their physical definitions. The influencing factors on the direction of chip motion could not be depicted as clearly. Increased friction coefficients ($\mu_{\mathrm{r,W-W}}$, $\mu_{\mathrm{k,W-T}}$) reduce flight angles, which seems to be related to the interaction with the cutting tooth in the cutting zone. The ratio $\frac{\sigma_Z}{\tau_{XY}}$ has a strong negative effect on flight angles, whereas strain to rupture $\epsilon_{\mathrm{max,T,XY}}$ seems to have a positive impact. To better match experimental data, the friction coefficients should be low (≤ 0.3), $\epsilon_{\mathrm{max,T,XY}}$ should be in the range 3 % to 7 % while $\frac{\sigma_Z}{\tau_{XY}}$ should be ≤ 3.

3.1 Comparison between simulations and experimental data

Experimental studies of chip ejection similar to the situation simulated with the BPM were conducted in [1] using a digital high speed camera and particle

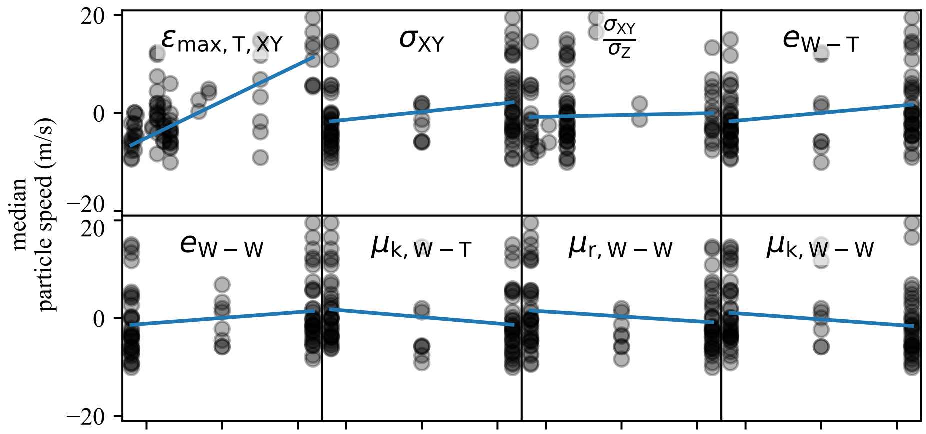

Fig. 2: The figure contains added variable plots showing the residuals of regressing median particle speed against the independent factors, excluding factor X_i, plotted against the residuals from regressing X_i against the other independent factors. The slope of each partial regression line corresponds to the regression coefficient for X_i in a regression of all covariates against median particle speed.

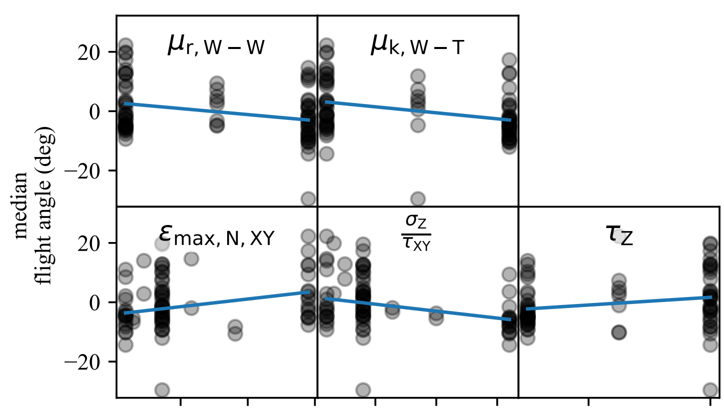

Fig. 3: Added variable plot for influencing factors on the median flight angle. The flight angle is defined as the angle of the velocity vector in respect to the x-axis. (cf. 2)

tracking velocimetry algorithms. If the analysis area is subdivided into a regular grid, the measured trajectory pieces lying in each grid field can be statistically summarized and visualized as a vector representation. The same procedure can be followed using the data from the BPM simulations. In Fig. 4, both particle speed and flight direction can be compared. The magnitudes of particle speed show larger differences, especially in the area above the cutting line and in the region towards the tool center. The particle velocities differ by $5\,\mathrm{m\,s^{-1}}$ to $10\,\mathrm{m\,s^{-1}}$ in the cutting zone. The flight angles are relatively similar throughout the area. The deviations here are on average less than 5 degrees. It should also be noted that the experimental data exhibits a measurement uncertainty. In addition, the resistance forces of the fluid cannot currently be mapped correctly in the BPM simulation. Furthermore BPM simulations in a multiprocessing framework are not deterministic. Multiple simulations of longer durations would reduce this uncertainty. Thus the degree of deviation between both methods can be expected. Finally, not only the velocity field but above all the mass flow should be compared. However, no experimental data is currently available for this.

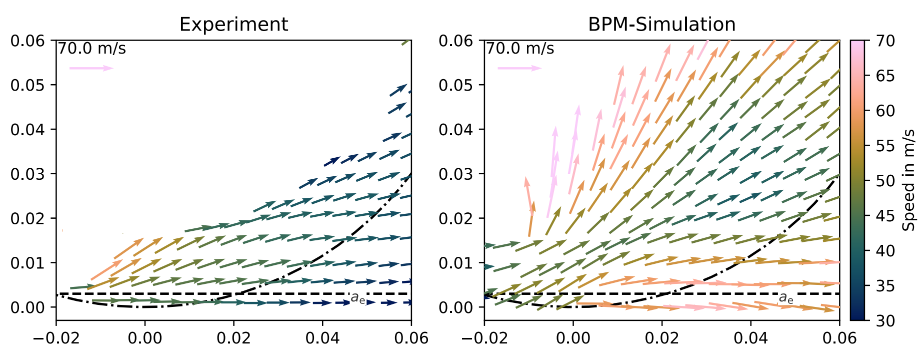

Fig. 4: Illustration of determined velocity vectors for the same cutting process with 3 mm depth of cut and n=6000 min^{-1}. Color and arrow length symbolize the velocity magnitude. For the experimental data only trajectories inside the chip space and the ambiance tool area are available.

4 Summary and outlook

The comparison of the experimental and numerical results shows the potential of the BPM simulation for the prediction of chip trajectories. DoE is applicable for the calibration of the BPM model. If the evaluation routines for post-processing exist, the time required for this is also manageable. The density of the particles as well as the influence of the fixed boundary condition should be included in future calibration procedures. At present, it remains an open question to what extent the model obtained can correctly reflect changes in feed per tooth, cutting edge geometry or other relevant process parameters. Therefore, the benefits of the approach presented here cannot yet be conclusively assessed.

5 Acknowledgement

The IGF project No. 22923 BG of the Forschungskuratorium Maschinenbau e.V. (FKM), Lyoner Straße 18, 60528 Frankfurt, Germany, was funded by the Federal Ministry for Economic Affairs and Climate Action through the German Federation of Industrial Research Associations (AiF) under the Industrial Collective Research (IGF) program on the basis of a decision by the German Bundestag.

References

1. Hausmann, J., Hafemann, T.E., Rüdiger, F., Herzberg, M., Gottlöber, C.: Particle tracking velocimetry as a method for chip ejection studies during groove milling of particleboard. Eur. J. Wood Prod. 81, pp. 605–615, (2023). doi.org/10.1007/s00107-022-01917-0
2. Pałubicki, B., Rogoziński, T., Wilkowski, J., Godek, L.: Influence of feed per tooth on particle size of chips created in particleboard peripheral milling. Annals WULS - SGGW, Forestry and Wood Technology, vol. 97, pp. 144-149, (2017)
3. Wyeth, D.J., Goli G., Atkins, A.G.: Fracture toughness, chip types and the mechanics of cutting wood. A review. Holzforschung, vol. 63, pp. 168–180, (2009). doi.org/10.1515/HF.2009.017
4. Hausmann, J., Hafemann, T., Gottlöber, C., Rüdiger, F.: Analysis of the particle shape of wood chips using dynamic image analysis and particle classification for the numerical simulation of chip flight. Holztechnologie, vol. 2022, pp. 52-63. [In German] (2022)
5. Hausmann, J., Müller, F., Liu, Z., Rüdiger, F.: Development of a methodology for the investigation of particle-wall collisions similar to those in extraction hoods for woodworking. Tagungsband des 21. Holztechnologischen Kolloquiums, Dresden, 18.–19. April 2024. Schriftenreihe Holz- und Papiertechnik, Band 42, pp. 225 - 238. [In German] (2024)
6. Hausmann, J., Gottlöber, C.: Modelling chip ejection of wood cutting tools using the Discrete Element Method with bonded particles. Proceedings of the 25th International Wood Machining Seminar (IWMS-25), Nagoya, Japan, 04.– 07.10.2023 (2023)
7. Dosta, M., Skorych, V.: MUSEN: An open-source framework for GPU-accelerated DEM simulations. SoftwareX, vol. 12, (2020). https://doi.org/10.1016/j.softx.2020.100618
8. Curti, R.: Analysis, modelling and simulation of the orthogonal cutting of green wood for application to canter milling. doctoral thesis, Mechanical Engineering [physics.class-ph], Ecole Nationale Supérieure d'Arts et Métiers – ENSAM. [In French]. NNT: 2018ENAM0034. (2018)
9. Potyondy, D. O., Cundall, P. A.: A bonded-particle model for rock. International Journal of Rock Mechanics and Mining Sciences, vol. 41, no. 8, pp. 1329–1364. (2004). doi.org/10.1016/j.ijrmms.2004.09.011
10. Chen, X., Peng, D., Morrissey, J.P., Ooi, J.Y.: A comparative assessment and unification of bond models in DEM simulations. Granular Matter 24, 29 (2022). doi.org/10.1007/s10035-021-01187-2

Influence of pinewood moisture swelling and shrinkage on robotic montage susceptibility

Maciej Sydor[1[0000-0003-0076-3190]], Anna Jasińska[1[0000-0003-2291-2425]], Wojciech Turbański[2[0000-0002-1879-430X]]

[1] Departament of Woodworking and Fundamentals of Machine Design, Faculty of Forestry and Wood Technology, Poznań University of Life Sciences, Poznań, Poland
[2] Euroline sp. z o.o. Leszno, Poland

Abstract. Robotic assembly, while offering significant reductions in product defect rates compared to non-robotic methods, remains vulnerable to disruptions caused by excessive variability in component dimensions. In wooden furniture, these dimensional variations can arise from cyclic temperature and humidity fluctuations during storage, which induce wood swelling and shrinkage, leading to poor fit between furniture components. This study investigated the impact of variable environmental storage conditions on clearances and interferences in upholstered furniture frame components. Samples were stored for 30 days in three distinct environments: an industrial hall (control), a room with amplified temperature and humidity fluctuations, and an outdoor covered area. The influence of these storage conditions on assembly success was then analyzed. Critical clearances were identified between the mating parts intended for robotic assembly by comparing samples exhibiting the best and worst fit. Results indicate a greater probability of disrupting the robotic assembly process (due to changing from loose to press fit) under more unstable storage conditions. The study suggests that a thorough understanding of potential dimensional changes range and associated assembly challenges is crucial, particularly in robotic assembly systems, which are inherently more sensitive to unpredictable component variations.

Keywords: robotic assembly, storage conditions of wood elements, quality of joints, environmental conditions, dimensional tolerances, industrially manufactured wood products, shrinkage, swelling

1 Introduction

Assemblability refers to the ease with which components or elements can be combined into a larger structure or system. It measures the suitability of components for assembly and the ease of assembly itself. The term is commonly used in engineering to describe the ability of parts to be joined together to create a functional product. Assemblability considers factors such as the design and size of components, the method of assembly, and the materials used. A high degree of assemblability makes the manufacturing process more efficient and reduces the time and costs associated with an assembly process. The assembly technology that uses robots to assemble products is a robotic assembly line (RAL) [1]. This automation allows for productive, efficient, and precise production while reducing the need for human labor. Some specific issues with the use of robotic assembly lines in furniture production include: a) high upfront cost: Implementing a robotic assembly line can be expensive, [2], b) the Robotic Assembly Line Balancing Problem (RALBP) involves allocating tasks to autonomic workstations sequentially to optimize a predefined objective function while adhering to resource and technological constraints [3], c) integration with other processes: Robotic assembly lines may require integration with other production processes, d) maintenance requirements: Robots require regular maintenance and repair, [4], e) lack of flexibility: Robotic assembly lines are typically designed for specific tasks, making it difficult to switch between different product types or manufacturing processes quickly.[5], f) quality control: Although robots are capable of precise and consistent production, they may not be able to detect and correct quality issues in real-time, requiring additional human oversight [6], g) difficulty in handling delicate parts: Furniture includes delicate parts that may be damaged if handled by a robot, requiring additional human intervention. Sensitive to the unpredictable behavior of furniture elements, such as springs and wooden parts [7]. Due to the challenges posed by automated robotic assembly lines, various variants of human-robot collaboration exist. Depending on the type of line, robots can assist workers in performing simple, repetitive tasks (cobots), act as supervisors in automated production, or support transporting materials and components in large factories. Table 1. presents the main models of human-robot collaboration in assembly lines.

Table 1. The main models of human-robot collaboration in assembly lines (based on: [22,23,24].

Type of robotic assembly line	Line Features
Assembly Line with Collaborative Robots (Cobots) Assisting Humans	Robots collaborate with humans but do not perform all the work independently. Humans remain responsible for more complex tasks.
Assembly Line with Autonomous Robots (Full Automation) Involving Humans	Robots are used to perform monotonous, precise tasks, e.g., screwing, assembling parts.Humans act as supervisors and quality controllers.
Assembly Line with Mobile Robots (AGVs – Automated Guided Vehicles) and Humans	Autonomous robots transport components and optimize internal logistics. Humans perform assembly at individual stations while robots ensure a continuous supply.
Assembly Line with Collaborative Robots and Supervision (Joint Work of Humans and Robots)	Robots are used for precise, physically demanding, or dangerous tasks, while workers focus on tasks requiring flexibility and decision-making. Cobots or autonomous robots perform simpler tasks, while humans handle more complex stages.

The higher the degree of robotization of the line, the greater the sensitivity to the variability of the assembled components in relation to the standardized elements recognized by the robot. An example of this is wooden furniture parts, which naturally (depending on storage conditions) change their nominal dimensions and can be problematic for a fully automated line. The article presents the impact of storage conditions of wooden frame components on the specified dimensions of the joining elements and attempts to answer the question: How can the risk of failure during the assembly of components made of anisotropic materials such as wood be minimized?

2 The impact of dimensional changes in wooden components on collisions during assembly

Wood tends to change in size, which can make robotic assembly difficult. Below the fiber saturation point, pine wood absorbs or releases moisture, resulting in changes in its dimensions. The shrinkage and swelling depend on the relative humidity of the environment. The dimensional changes below the fiber saturation point are primarily due to the hygroscopic nature of the wood fibers [8]. These changes can affect the fit and function of wooden products, such as furniture, and it is essential to consider and account for these changes in the design and manufacture of wooden products [7]. Many scientific studies have reviewed the factors that affect wood shrinkage and swelling, including the impact of moisture content (MC) on the dimensional changes of wood. These studies aim to understand how wood's dimensional changes can be accurately measured and predicted. Wood shrinkage is known to be anisotropic, meaning that it depends on the grain pattern in the wooden element.

On average, shrinkage in the longitudinal (L) direction is less than 1%, which is of negligible practical importance. Due to changes in its MC, the dimensional changes in wood occur primarily in the tangential (T) and radial (R) directions. Shrinkage or swelling in the tangential direction can be up to three times greater than in the radial direction. There is anisotropy of T/R shrinkage and swelling. Each subsequent desorption and adsorption proceeds differently; the wood does not return to its original dimensions but tends to deform and even crack [9–13].It is worth mentioning that exposure to cyclic changes in humidity also deteriorates the strength properties of wood. Schniewind studied the time to failure of small Douglas-fir beams under constant loads while the beams were exposed to cyclic ambient relative humidity and temperature changes. The study found that exposing the loaded beams to cyclic variations in ambient conditions resulted in a marked decrease in the average time to failure. The extent of this decrease was directly linked to the intensity of change in the moisture content [14]. Changes in wood moisture also increase the tendency to propagate cracks in loaded elements. Chaplain et al. found that air-drying and air-wetting significantly increase the cracking rate [15]. The changes in the moisture content of wood products affect the clearance and interference of mating parts [16–19]. For this reason, research is being conducted to indicate the development direction for robotic assembly lines in terms of adapting to varying dimensional tolerances of components. The scientific literature reports examples of studies on Reinforcement Learning (RL) systems to control robot movements in contact-rich and tolerance-prone assembly tasks. Using RL, a robotic system can independently develop strategies to handle manipulation in environments with frequent contact, even without prior information about the environment or the dynamics model. Because these strategies can adapt to new situations and react to real-time data, RL has become a widely used method for developing control strategies in robotic assembly tasks. The introduction of real-time responsive sensors is a solution for controlling the assembly of components with varying tolerances, inaccuracies, and naturally occurring deformations [22]. Despite the development of RL methodology, the question remains of how to support robotic lines in minimizing errors and collisions. Considering the dimensional changes in timber components due to temperature and humidity fluctuations, it was decided to examine the degree of dimensional tolerance changes depending on the storage conditions of typical timber frames.The influence of relative air humidity (RH) changes on wooden element dimensions was widely studied [20]. The conclusions from these studies are implemented in the technical standard DIN 68100:2010 [21], which provides guidelines for establishing tolerances in wood processing, taking into account the natural variations and dimensional changes that occur in wood, including such factors as the type of wood, the intended use of the product, and the degree of precision required.

This study explores the impact of dimensional moisture changes in pine rails on clearances and interferences during the robotic assembly of upholstery frames. The upholstery frames are four rails assembled with box joints, thanks to designed assembly clearances. However, relative air humidity and temperature changes can result in dimensional moisture changes in the pine rails, leading to changes in the clearances. This can result in difficulties for the robotic assembly process, potentially leading to an unsuccessful assembly.

3 Materials and Methods

3.1 Materials

The research subject was a box joint in a pinewood frame used in upholstery furniture. Figure 1 shows two places where the mounted elements are adjusted: the C_{long}-C_{short} and BCD_{long}-BCD_{short} pairs of dimensions.

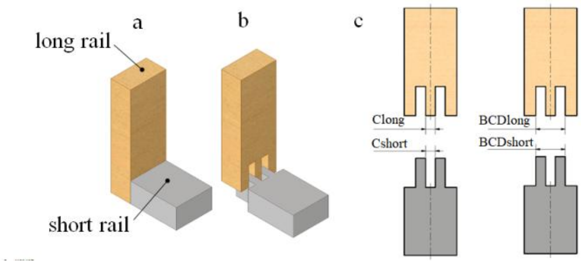

Fig. 1. The structure and nominal dimensions of the box joint: a, b – the box joint structure, c – the engineering fits

For trouble-free assembly, the dimensions shown in Figure 1 should be matched such that the external dimensions are consistently smaller than the internal dimensions (C_{long} must always be smaller than C_{short}, and BCD_{short} must always be smaller than BCD_{long}).

This ensures component assembly due to the resulting gaps. Converting these clearance-fits into press-fits would disrupt the assembly process

3.2 Methods

From a large batch of components of upholstery frames, 36 pairs of rails made of pine wood were randomly selected; each set contained a pair: a short rail and a long rail. The sets were divided into three series of 12 elements and marked as A, B, and C. Firstly, the assembly dimensions were measured (C_{long}, C_{short}, and BCD_{short}, BCD_{long}). Then, each series of samples was exposed to different environmental conditions: indoors in the industrial hall (air with RH in the range of 29-48% and temperature in the range of 16-24°C), marked as storage conditions X; indoor in the compressor room (air with RH in the range of 24-51%, and temperature in the range of 13-27°C), marked as storage conditions Y; outdoor in a covered shed (air with RH in the range of 20-50%, and temperature in th e range 3-23°C), marked as storage conditions Z. After 30 days of storage, the assembly dimensions were measured again.

4. Results

As mentioned, three sets of rails were stored for one month under three different conditions: X (indoor, stabilized conditions), Y (indoor, moderate unstabilized conditions, elevated temperature), and Z (outdoor, very unstable conditions). This resulted in a change in the moisture content of the components. A comparison of the moisture contents of test samples, initial and after storage, is shown in Table 2.

Table 2. Comparison of the moisture contents of test samples, before and after storage.

Storage condition	Initial moisture content		Moisture content after storage	
	Long rail	Short rail	Long rail	Short rail
X	15.34 (1.67)	13.14 (1.37)	10.70 (0.78)	10.17 (0.69)
Y	15.12 (1.33)	13.53 (0.52)	8.34 (1.02)	8.33 (0.61)
Z	15.42 (1.60)	12.60 (0.73)	12.55 (0.64)	11.45 (0.69)

Standard deviations is given in parentheses. *n* = 12

The results are changes in fitting between the mating elements. As a result of such storage, the clearances or interferences the component pairs changed. These changes occurred to varying degrees depending on the storage conditions. The samples initially had clearances in the range of 0.05-1.27 mm; after storage for 30 days, the clearances did not change significantly, amounting to in the range of −0.12-1.04 mm (minus sign means interference).

A one-way ANOVA was performed to compare the effect of storage in the industrial hall (case X), seasoning in the compressor room (case Y), and seasoning outside in a covered shed] (case Z) on clearances and interferences. The ANOVA revealed that there was not a statistically significant difference in clearances or interferences between compared groups in case X and there is a statistically significant difference in case Y and case Z.

The change in the range of dimension values and the number of recorded measurements for frames (in the problematic area C-short - C-long) stored under conditions Z are presented in histograms (Figs. 1-2). Figures 2 and 3 show one selected series out of the three examined, the one in which the greatest changes were noted. Both figures present a pair of histograms of external (C-long) and internal (C-short) dimensions. For a loose fit, C-long should always be smaller than C-short.

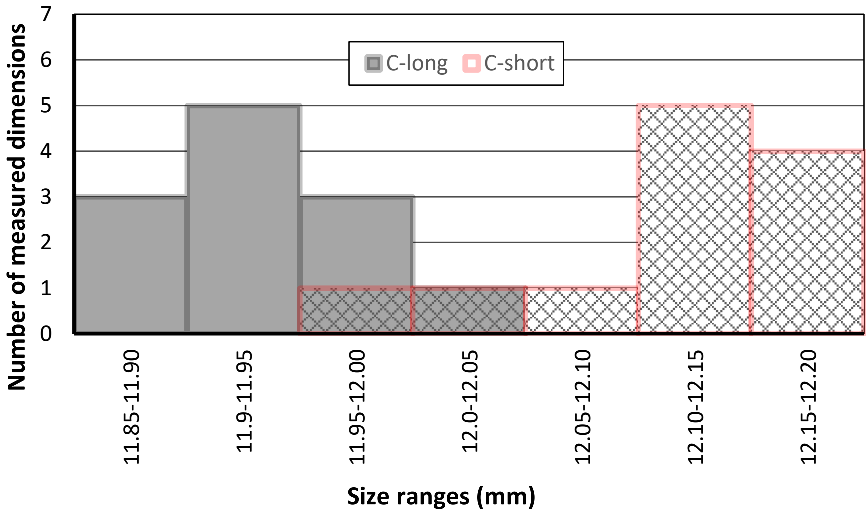

Fig. 2. C-long and C-short Dimension Distributions Before Storage

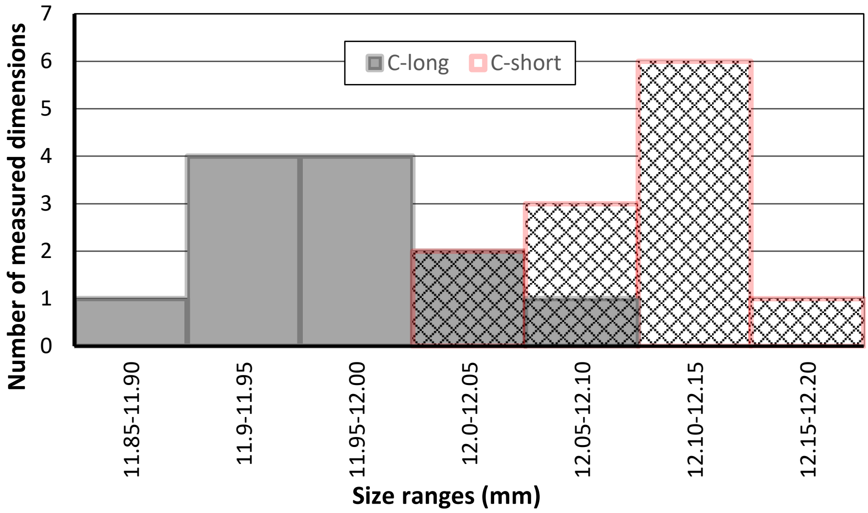

Fig. 3. C-long and C-short Dimension Distributions After Storage

The histogram overlap is particularly interesting, as it indicates the number of measurements where negative clearance (interference) occurs between C-long and C-short. Figure 1 shows two problematic C-short dimensions (sockets smaller than 12.10 mm). This number increased to five after storage (Fig. 2).

Measurements of samples stored under Z conditions show the largest dimensional changes. Despite the assumption of appropriately large tolerance ranges, the probability of collisions during assembly is high, as can be seen from the histograms presented above.

4 Discussion

Broad engineering tolerances for wooden components result from the inherent conditions of wood processing and storage (shrinkage and wood swelling due to moisture changes). Reducing the allowable dimensional variation of wood processing and stabilizing the storage conditions of components may increase assembly susceptibility, but it comes with higher production costs. This has been experimentally proven in earlier research [7]. Storing wooden components increases dimensional deviation values in all storage condition variants. Exposure to cyclic changes in moisture content and temperature, even without changing the final moisture content of the components, results in more significant dimensional changes than storage under more stable conditions that reduce the moisture content of the wood. The study confirmed that wood dimensional moisture changes are not fully reversible. Once a wooden component changes its dimensions, the new shape becomes the permanent shape of the wood.

Considering the frequency of occurrence of given dimensions before and after storage it is possible to calculate the elementary probability corresponding to a specific Δ error [25]. When the constant C is determined, assuming that the error is in the range of (-∞, +∞). The sum of partial error probabilities is certain, therefore expressed by the value 1. Assuming the constant h, the following equality can be determined:

$$C\int_{-\infty}^{+\infty} e^{-h^2\Delta^2 d\Delta} = 1$$

Assuming hΔ = t, the integral is transformed into:

$$\frac{C}{h}\int_{-\infty}^{+\infty} e^{-t^2} dt = 1$$

The integral on the left side is known and has a constant value, i.e.:

$$C = \frac{h}{\sqrt{\pi}}$$

Taking this into account, the elementary probability corresponding to a specific Δ error can be expressed as:

$$p = \frac{h}{\sqrt{\pi}} e^{-h^2\Delta^2} d\Delta$$

In summary, h can be considered a measure of the precision of the process [25].

5 Conclusions

A thorough understanding of the range of clearance and interference variations is essential, especially given the increased sensitivity of robotic assembly systems to unpredictable dimensional changes in furniture components. While advancements in Reinforcement Learning offer potential avenues for mitigation, the minimization of dimensional discrepancies from designed in assembled components remains critical.

This study explores how moisture-induced dimensional instability in pinewood rails affects clearances and interferences critical to the robotic assembly of upholstery frames. Results demonstrate that fluctuating humidity during storage can convert acceptable initial clearances into problematic interferences, preventing component assembly. These findings highlight the challenge of prolonged storage for wooden components intended for robotic assembly, particularly when environmental conditions fluctuate.

If immediate assembly is not feasible, stable temperature and humidity are recommended for wooden furniture component storage. Desorption and fluctuating environmental conditions, even without final moisture content change, are more detrimental to assembly success than air-wetting and storage under stable environmental conditions. Grouping components based on similar dimensional changes can further mitigate assembly risks. However, this complicates robotic assembly technology by introducing the need to sort components.

References

1. Chutima, P. A Comprehensive Review of Robotic Assembly Line Balancing Problem. J Intell Manuf 2020, doi:10.1007/s10845-020-01641-7.
2. Abu, F.; Gholami, H.; Mat Saman, M.Z.; Zakuan, N.; Streimikiene, D. The Implementation of Lean Manufacturing in the Furniture Industry: A Review and Analysis on the Motives, Barriers, Challenges, and the Applications. Journal of Cleaner Production 2019, 234, 660–680, doi:10.1016/j.jclepro.2019.06.279.
3. Rubinovitz, J.; Bukchin, J. Design and Balancing of Robotic Assembly Lines. In Proceedings of the Proceedings of the Fourth World Conference on Robotics Research; Robotics International of Society of Manufacturing Engineers (SME).: Dearborn, MI, USA, 1991; pp. MS91-335.
4. Martins, A.P.Q. Maintenance Management of a Production Line – a Case Study in a Furniture Industry. Masters Dissertation, University of Porto: Porto, Portugal, 2019.
5. Salonitis, K. Modular Design for Increasing Assembly Automation. CIRP Annals 2014, 63, 189–192, doi:10.1016/j.cirp.2014.03.100.
6. Turbański, W.; Matwiej, Ł.; Wiaderek, K.; Sydor, M. Comparative Analysis of the Manual and Robotic Upholstery Frame Assembly Processes. Study Based on Many Years of Research. In Proceedings of the MATEC Web of Conferences; Borowski, S., Ligaj, B., Strzelecki, P., Hujo, Ľ., Eds.; EDP Sciences: Bydgoszcz, June 25 2021; Vol. 338, p. 01028.
7. Turbański, W.; Sydor, M.; Matwiej, Ł.; Wiaderek, K. Moisture Swelling and Shrinkage of Pine Wood versus Susceptibility to Robotic Assembly of Furniture Elements. Ann. Wars. Univ. Life Sci., For. Wood Technol. 2021, 115, 63–71, doi:10.5604/01.3001.0015.5274.
8. Skaar, C. Wood-Water Relations; Springer Series in Wood Science; 1st ed.; Springer Berlin Heidelberg: Berlin, Heidelberg, 1988; ISBN 978-3-642-73683-4.
9. Kollmann, F.F.; Côté, W.A. Principles of Wood Science and Technology. I Solid Wood; Springer-Verlag: Berlin-Heidelberg, 1968; ISBN 978-3-642-87930-2.
10. Noack, D.; Schwab, E.; Bartz, A. Characteristics for a Judgment of the Sorption and Swelling Behavior of Wood. Wood Sci. Technol. 1973, 7, 218–236, doi:10.1007/BF00355552.
11. Skaar, C. Wood-Water Relations; Springer-Verlag: Berlin; New York, 1988; ISBN 0-387-19258-1.
12. Wagenführ, R. Holzatlas; 6th ed.; Fachbuchverlag Leipzig im Carl Hanser Verlag: München, 2006; ISBN 978-3-446-40649-0.
13. Kain, G.; Idam, F.; Federspiel, F.; Réh, R.; Krišťák, Ľ. Suitability of Wooden Shingles for Ventilated Roofs: An Evaluation of Ventilation Efficiency. Appl. Sci. 2020, 10, 6499, doi:10.3390/app10186499.
14. Schniewind, A.P. Creep-Rupture Life of Douglas-Fir under Cyclic Environmental Conditions. Wood Science and Technology 1967, 1, 278–288, doi:10.1007/BF00349759.
15. Chaplain, M.; Dethan, T.; Castera, P. Effects of Climatic Conditions Changes on Crack Growth. In Proceedings of the 9th World Conference on Timber Engineering 2006, WCTE 2006; Curran Associates, Inc.: Red Hook, NY, USA, 2006; Vol. 1, pp. 128–135.
16. Kien, W.; Kortylewski, B.; Miński, K.; Palka, Z.; Porankiewicz, B.; Staniszewska, A.; Staniszewski, J.; Szymański, W. Tolerancje i Pasowania Wymiarów Liniowych Drewna w Przemyśle Meblarskim / Geometric Dimensioning and Tolerancing of Linear Dimensions of Wood in the Furniture Industry; Instytut Podstaw Techniki, Wyższa Szkoła Rolnicza: Poznań, 1979; p. 23;.

17. Porankiewicz, B. Problemy Układu Tolerancji i Pasowań Dla Przemysłu Drzewnego / Issues of Geometric Dimensioning and Tolerancing for Wood Industry; Roczniki Akademii Rolniczej w Poznaniu. Rozprawy Naukowe; Wydawnictwo Akademii Rolniczej im. A. Cieszkowskiego w Poznaniu: Poznań, 1989; Vol. 183;.
18. Kruś, S. Metrologia Techniczna a Specyfika Drewna Na Przykładzie Układu Tolerancji i Pasowań / Metrology and Technical Specificity of Wood on the Example System of Geometric Dimensioning and Tolerancing. Zeszyty Naukowe Wyższej Szkoły Pedagogicznej w Bydgoszczy. Studia Techniczne 1997, 193–202.
19. Eckelman, C.A. The Shrinking and Swelling of Wood and Its Effect on Furniture; Forestry & Natural resources; Purdue University. Department of Forestry & Natural Resource: West Lafayette, 1998; p. 26;.
20. Praast, S. Einheitliches Toleranzsystem Für Die Längenmaße Bei Holz Und Holzwerkstoffen. Holz Roh- Werkst. 1982, 40, 101–104, doi:10.1007/BF02612569.
21. DIN 68100 Toleranzsystem Für Holzbe- Und -Verarbeitung - Begriffe, Toleranzreihen, Schwind- Und Quellmaße / Tolerance System for Wood Working and Wood Processing - Concepts, Series of Tolerances, Shrinkage and Swelling 2010.
22. Apolinarska, A.A.; Pacher, M.; Li, H.; Cote, N.; Pastrana, R.; Gramazio, F.; Kohler, M. Robotic Assembly of Timber Joints Using Reinforcement Learning. Automation in Construction 2021, 125, 103569, doi:10.1016/j.autcon.2021.103569.
23. Cote, N., Tish, D., Koehle, M. et al. Adaptive robotic construction of wood frames. Constr Robot 8, 8 (2024). https://doi.org/10.1007/s41693-024-00122-0
24. Mukund Nilakantan, J.; Huang, G.Q.; Ponnambalam, S.G. An Investigation on Minimizing Cycle Time and Total Energy Consumption in Robotic Assembly Line Systems. Journal of Cleaner Production 2015, 90, 311–325, doi:10.1016/j.jclepro.2014.11.041.
25. Mierzejewski, H. (1924). Metrologia techniczna. Książnica - Atlas.

Influence of pretreatments on the machining processes of softwood and hardwood and evaluation of surface roughness

Paola Cetera[1,2*], Jarno Bontadi[2], Mario Marra[2], Martino Negri[2]

[1] Department of Agricultural Sciences, University of Sassari. Viale Italia 39/a, 07100 Sassari, Sardinia, Italy (e-mail: pcetera@uniss.it)
[2] National Research Council (CNR) - Institute of BioEconomy (CNR-IBE), Via Biasi, 75, 38010 San Michele all'Adige (TN), Italy. E-mail: jarno.bontadi@ibe.cnr.it; mario.marra@ibe.cnr.it; martino.negri@ibe.cnr.it
*Corresponding author: Paola Cetera (pcetera@uniss.it)

Abstract. The rising demand for ultra-thin veneers in applications such as furniture and interior design is attributed to their aesthetic appeal and lightweight properties. This study explores the production of ultra-thin veneers from three wood alpine species: Norway spruce (*Picea abies* Karst), silver fir (*Abies alba* Mill.), and beech (*Fagus sylvatica* L.), utilizing the Marunaka SuperMeca super-finishing planer. Two different pretreatments, such as heat treatment with superheated steam at 105 ° and 120 °C, were employed to facilitate the processing of wooden boards. Key machining parameters, such as knife type, knife projection (veneer thickness), feed roller pressure, and horizontal blade angle, were systematically adjusted during veneer slicing operations. The roughness of the wood samples was measured using a Mitutoyo SurfTest SJ-301 instrument. Results indicated that wood surface hydration is crucial for achieving uniform veneer thickness. This research provides insights into the factors influencing ultra-thin veneer production, offering implications for optimizing wood processing techniques. By adopting improved pretreatment methods and machining parameters, manufacturers can enhance surface finishes and consistency in ultra-thin veneers, paving the way for broader applications in high end furniture design and sustainable materials.

Keywords: Softwood, Hardwood, Treatment, Wood Surface, Roughness.

1 Introduction

The production of ultra-thin wood veneers is gaining importance due to the increasing demand for lightweight and aesthetically appealing materials in furniture design and sustainable applications. This study addresses the optimization of ultra-thin veneer production from three alpine wood species: Norway spruce (*Picea abies* Karst), silver fir (*Abies alba* Mill.), and beech (*Fagus sylvatica* L.). Effective wood pretreatment is crucial for achieving uniform veneer thickness and quality.

Heat treatments, such as those using superheated steam, can influence the average veneer thickness, but may also compromise the final veneer quality. The Marunaka

SuperMeca superfine planer is utilized in this study to explore its potential for producing consistent, high-quality ultra-thin veneers, shifting its conventional use from waste generation to valuable composite material production. Key parameters such as knife type, knife projection, feed roller pressure, and horizontal blade angle are systematically adjusted to optimize veneer slicing operations. The research evaluates the impact of different pretreatments, including standard conditioning, treatment at 105 °C, and treatment at 120 °C on the qualitative parameters of the semi-finished products, such as colour, gloss, and surface roughness. This comprehensive evaluation aims to provide insights into optimizing wood processing techniques, enhancing surface finishes, and improving the consistency of ultra-thin veneers for broader applications in high end furniture design and sustainable building materials or packaging.

2 Materials and Methods

2.1 Samples wood species

Three wood species from the alpine region were used: red spruce (*Picea abies* Karst.), silver fir (*Abies alba* Mill.), and beech (*Fagus sylvatica* L.). The wood boards were selected based on quality and ring orientation. They were cut to size (length between 50 and 200 cm depending on the species). Where necessary, they were trimmed and brought to a constant thickness by planning, with typical thicknesses between 40 and 100 mm.

2.2 Pretreatments of wood boards

Three different pretreatments to optimize the cutting process of the wood boards were applied:

1. Standard conditioning: Boards processed at room temperature and normal humidity (11-12%).
2. Treatment at 105 °C: All wood species treated in an autoclave chamber with superheated steam at 105 °C for 1 hour.
3. Treatment at 120 °C: A treatment of 120 °C for 1 hour for all type of samples was done.

2.3 Superfinishing planing

Marunaka SuperMeca (Marunaka Tekkosho Inc., Japan) machine to produce ultra-thin veneers was used (Fig.1). The following process parameters were varied:

- Horizontal inclination angle of the blade: Varied between 10°, 15°, 20°, 25°, 30° and 45° with respect to the feed direction.
- Feed system pressure: Set to standard and "heavy" (maximum vertical pressure).
- Knife protrusion: Adjusted via the screw registers of the blade holder to maximize the veneer thickness.

All slicing operations of wood samples were performed with Kanefusa BCH 335 mm type K knives (Kanefusa Corp., Japan).

Fig. 1. Marunaka SuperMeca machine.

2.4 Colour and surface roughness measurements

- Colour: Measured with a Datacolour spectrophotometer in the L*a*b* (CIELAB) colour space.
- Gloss: Measured with a reflectometer to determine the wood surfaces gloss, expressed in Gloss Units (GU), with a range from 0 GU (very matt surface) to 100 GU (very shiny surface). Lower values indicate less gloss and more matt, while higher values correspond to shiny surfaces.
- Surface roughness: Measured with a Mitutoyo SurfTest SJ-301 portable roughness tester (Mitutoyo Italiana S.r.l., Milan - Italy), with a 2 µm diamond stylus tip. The parameters Ra, Rz, and Rq were evaluated according to ISO 4287:1997 “Surface texture: Profile method — Terms, definitions and surface texture parameters”

Results

The research project TAF/17 investigated the effects of different wood pretreatments and machine settings on the quality of ultra-thin veneers from red spruce, silver fir, and beech wood. The main goal was to optimize the production process for innovative ultra-thin veneers to propose in the packaging sector.

The application of water at room temperature on the surfaces of boards with normal humidity (11-12%) proved to be the best condition for producing the veneers needed for the project. Pretreatments with steam at high temperatures reduced the effort needed to advance the boards but caused collapses and detachments in the veneers and fraying of the board surfaces, making them inconvenient (Fig. 2).

Fig. 2. Effects of the pretreatment of wood board on the final quality of the veneers Inadequate (left) high quality (right).

The following Table 1 summarize the key findings related to the effectiveness of pre-treatments.

Table 1. Synthetic evaluation of the effectiveness of pretreatments as a function of ease of processing, percentage of waste and quality of the veneer sheet obtained. Values from 0 to 5, with 0: inadmissible and 5: most desirable value.

Treatment	Ease of processing	Waste amount	Veneer quality
Untreated	1	0	0
105° C	5	1	4
120° C	5	1	2

Regarding colour changes, in all three wood species showed a colour variation towards darker tones (Tab. 2), decreasing their luminosity and gloss after pretreatments at 105 °C and 120 °C. This is confirmed by the colorimetric coordinates L*a*b* and the total colour variation (ΔE), which ranged from 27 to 31% depending on the species.

Table 2. Colour coordinates in CIELab space of different wood samples

Wood species	L *	a*	b*
Beech untreated	77.7 *0.84*	6.0 0.19	16.5 0.70
Beech 105 °C	51.0 *3.46*	8.5 0.41	16.3 0.54
Beech 120 °C	46.1 *1.05*	9.4 0.20	16.8 0.29
Fir untreated	83.7 *0.21*	4.5 0.11	21.4 0.35
Fir 105 °C	61.2 *2.10*	12.0 0.36	23.2 0.83
Fir 120 °C	54.5 *2.07*	10.1 0.74	22.1 1.06
Spruce untreated	83.6 *0.29*	4.7 0.21	21.6 0.68

Spruce 105 °C	54.3 *1.34*	9.4 0.28	22.3 1.08
Spruce 120 °C	56.9 *1.64*	10.9 0.53	24.2 0.92

The summarized data reported in Table 3 gloss are referred to gloss measurements and standard deviations (SD) for untreated and treated beech, fir, and spruce wood species. Gloss is an important characteristic that influences the aesthetic appeal and perceived quality of wood surfaces.

Table 3. Gloss of each type of wood pre and post treament

Wood species	Gloss	SD
Beech untreated	4.2	*1.86*
Beech 105 °C	1.97	*0.23*
Beech 120 °C	2.40	*0.48*
Fir untreated	5.29	*1.17*
Fir 105 °C	3.54	*0.58*
Fir 120 °C	2.42	*0.64*
Spruce untreated	1.97	*0.23*
Spruce 105 °C	3.16	*0.47*
Spruce 120 °C	2.77	*0.84*

Overall, the data illustrates how pretreatments affect the gloss levels of different wood species. Untreated fir shows the highest gloss value, making it suitable for applications where a shiny finish is desired, while untreated beech and spruce have lower values, favouring a more natural look. In this study the pre-treatments generally reduce gloss levels across all species but can enhance consistency in measurements, particularly at lower temperatures (105 °C). These findings can guide manufacturers and designers in selecting appropriate wood finishes based on desired aesthetic qualities and performance characteristics. About the surface roughness, Table 4 shows the main results.

Table 4. Roughness values of the beech, fir and spruce wood, where Ra (Arithmetic Roughness Average): is the most common surface roughness parameter. It represents the arithmetic average of the absolute values of the profile heights over the evaluation length; Rz (Mean Roughness Depth): Rz is the average of the tallest peak to the depth of the lowest valley from each subsection of a surface measurement; Rq (Root Mean Square Roughness): Rq measures the root-mean-square deviation of a profile.

Wood species	Pretreatment conditions	Roughness parameters	Longitudinal direction radial section		Cross direction radial section	
			Average (µm)	c.v. (%)	Average (µm)	c.v. (%)
Beech	Ctrl *(untreated)*	Ra	4.71 0.29	6.17	5.93 0.65	10.97
		Rz	26.07 2.09	8.01	44.11 4.40	9.97
		Rq	5.81 0.32	5.55	7.92 0.71	9.03
	105° - 100%	Ra	4.29 0.63	14.66	6.36 0.36	5.60
		Rz	24.59 2.68	10.91	45.20 2.29	5.06
		Rq	5.32 0.69	12.92	8.21 0.35	4.26
	120° - 100%	Ra	4.58 0.80	17.38	6.86 0.36	5.22
		Rz	24.88 4.06	16.32	48.02 4.00	8.32
		Rq	5.59 0.93	16.71	8.88 0.48	5.42
Fir	Ctrl *(untreated)*	Ra	3.91 0.61	15.68	5.57 0.19	3.32
		Rz	21.95 3.27	14.90	38.98 1.85	4.75
		Rq	4.82 0.77	15.89	7.04 0.21	2.95
	105° - 100%	Ra	4.56 0.76	16.72	6.45 1.08	16.73
		Rz	26.38 8.34	31.63	43.16 9.73	22.54
		Rq	5.66 1.18	20.84	8.13 1.52	18.70
	120° - 100%	Ra	3.50 0.77	22.03	4.21 0.27	6.42
		Rz	20.57 5.16	25.09	30.95 0.68	2.20
		Rq	4.35 0.99	22.67	5.36 0.28	5.31
Spruce	Ctrl *(untreated)*	Ra	3.71 0.58	15.63	4.87 0.41	8.51
		Rz	22.11 3.84	17.37	35.72 2.20	6.17
		Rq	4.56 0.58	12.79	6.14 0.45	7.33
	105° - 100%	Ra	3.59 0.70	19.45	5.29 0.77	14.48
		Rz	19.94 3.10	15.54	38.31 6.98	18.22

		Rq	4.38 0.80	18.19	6.78 1.08	15.97
	120° - 100%	Ra	3.57 0.53	14.97	6.07 1.91	31.41
		Rz	20.32 2.95	14.52	42.01 8.79	20.91
		Rq	4.39 0.66	15.06	7.72 2.29	29.70

For beech, roughness parameters appear to increase with the pretreatment temperature. This suggests that higher temperatures may lead to a rougher surface finish. In fact, the c.v. values for beech also vary with pretreatment, indicating changes in the consistency of the surface roughness. Fir exhibits variations in surface roughness with different pretreatment conditions: at 120° - 100%, fir shows a decrease in Ra, Rz, and Rq compared to the room condition. This suggests that this specific pretreatment may result in a smoother surface for fir. The c.v. values for fir are generally higher than those for beech, indicating greater variability in surface roughness. Spruce also shows variations in surface roughness with different pretreatment conditions.
Generally, higher pretreatment temperatures (105 °C and 120 °C) tend to increase surface roughness parameters (Ra, Rz, Rq) for beech, while the impact varies for fir and Spruce. The response to pretreatment varies significantly among the wood species. Fir and spruce exhibit different trends compared to beech.

Conclusion

The study identified that using water at room temperature as a pretreatment is the most effective way to ensure wood workability and veneer quality. This avoids the problems of collapse and fraying found with more extreme heat treatments. Process of the pretreatments with steam at 105 °C and 120 °C cause the wood to change colour, becoming darker and losing brightness. Therefore, using ultra-thin veneers obtained with the optimized pretreatment can lead to composites with better mechanical properties and durability. Future research could focus on optimizing the Marunaka SuperMeca planer's process parameters, such as feed rate and roller pressure, to maximize productivity and veneer quality. In addition, is important to assess the environmental impact of different wood pretreatments to identify the most sustainable and energy efficient solutions and explore new markets for this type of the ultra-thin veneers, such as packaging, where their lightweight, strength, and sustainability can be beneficial.

Funding

This research was funded by the TALENTED Trentino Agriculture-Forestry “TAF/17” Project. Fondi Programma di Sviluppo Rurale per la Provincia Autonoma di Trento 2014-2020. Misura 16. sottomisura 16.1 “Sostegno per la costituzione e la gestione dei

gruppi operativi del Partenariato Europeo d'Innovazione in materia di produttività e sostenibilità dell'agricoltura.

Acknowledgments

All the Authors would like to thank the technicians A. Gianotti. M. Natale and A. Ottombrino for their support during this research at the Institute of BioEconomy of San Michele all'Adige (North Italy).

High Volume Semi Automatized on-site Production of Sustainable Refugee Shelters

Adrian Riegel[1]

[1] University of Applied Sciences Ostwestfalen Lippe, Campusallee 12, D-32657 Lemgo Germany

Abstract. In times of crisis and conflict, the importance of sustainable and efficiently producible emergency shelters, which enable a life in safety and dignity, increases. The construction of such accommodation must meet the requirements of various areas, including minimum standards of humanitarian organization, structural requirements and manufacturing restrictions. The shelter solution presented here, which results from these requirements, is intended to be a sustainable alternative to existing emergency accommodation, especially tents. In order to actually replace tents in some scenarios, the accommodation must be able to be manufactured industrially in large series. Various concept studies were carried out for this purpose. The principle was: “form follows function & follows production”

Keywords: Refugee Shelter, Emergency accommodation, sustainability, serial production, timber frame construction

1 Introduction

The increasing frequency of crisis and conflict situations of all kinds occurring worldwide requires the development of innovative solutions for the rapid, cost-efficient and sustainable provision of emergency shelters. The United Nations High Commissioner for Refugees publishes a ‘mid-year trend report’ every year, outlining the extent of the refugee problem. According to the report, 110 million people worldwide were considered to be forcibly displaced [1]. The increasing number of refugees poses challenges in terms of international protection and humanitarian aid. The overarching goal is to save lives, alleviate suffering, uphold human dignity and protect the rights of involved human beings [2]. An essential aspect can be the provision of shelters that meet the basic needs of the people concerned.

According to A. M. Maslow, human needs are subject to a hierarchical structure. Higher needs only become more important when the underlying ones are already satisfied [3]. People who have had to leave their homes because of an emergency situation face the immediate challenge of meeting basic needs such as food, sleep and safe living. Emergency shelters are intended to provide refugees with a first habitable and safe environment. The design of the accommodation can help to create a supportive environment for a good life together [4]. Overall, the provision of adequate accommodation is therefore not only a humanitarian necessity, but also a decisive step towards meeting far-reaching needs and the independent life of those seeking protection.

2 The Shelter

Important actors and contact persons for the conception of emergency shelters are the United Nations High Commissioner for Refugees (UNHCR) and the International Federation of the Red Cross and Red Crescent Society (IFRC). The Sphere Association also offers an orientation option. The constantly evolving Sphere Manual [5] sets minimum standards. The UNHCR provides both temporary and retrofit emergency shelters, most of which have plastic and steel as their main materials (e.g. the Refugee Housing Unit RHU developed by Better Shelter with 17.5 square meters of floor space). With an expected service life of one to three years, their sustainability is at least debatable.

2.1 Conception and Design

The accommodation concept of TH OWL should be as production-efficient, sustainable and yet cost-effective as possible. The main materials used are OSB boards and solid wood with minimal waste. In addition more or less unprocessed boards as large as possible have the advantage that these can be reused afterwards for various other purposes. The same applies to the profiled beams. Production costs are reduced by using as many identical parts as possible.

The primary structure of the shelter consists of six columns as well as cross-beams and rafters made of coniferous wood (see Fig. 1). The six main supports are tightly bolted to the four OSB walls. In order to protect the narrow surfaces of the OSB walls from weather influences, the corner supports and crossbeams of the accommodation are profiled. The OSB plates, which form the supporting secondary structure, are fastened by screws and screw nails to the corner columns. Structural bonding would make sense, but was discarded in favor of dismantling and upcycling. Only in the front wall are a window and a door as machined openings.

Fig. 1. Model of the shelter. Front view left, Sight in the interior right

Depending on the installation area of the shelter, insulation can optionally be fixed from the outside between the OSB panels and the leading edge of the columns. For example, styrodur, corrugated board or wood fibre insulation boards can be used as material. All beam layers are positioned forward by the same dimension, so that the insulation materials can be protected with a flame-retardant tensioning membrane (e.g. made of Tyvek®). Lockable sliding windows are located on the one hand on the front and on the other hand on the back as a skylight. The PC glasses are guided in aluminium profiles. The roof forms a trapezoidal sheet, which in the variant for hot applications is only supported by a cotton tarpaulin. In order to be able to use as long and reusable sheet metal sections as possible, the corrugated tins are mounted longitudinally. Due to a slight inclination of the pent roof, the rainwater drainage and, if necessary, a collection of water is guaranteed. Inside the shelter there are some fixed pieces of furniture that perform a co-stiffening function. Three bunk beds are used for sleeping, which are mounted on the 12mm thick OSB walls. On 17.5 square meters there is space for cooking, sitting, sleeping and storage.

The main material of the interior furniture is again OSB panels, which are provided with an edgebanding. In order to host further higher-level functions in a camp, further modules based on this type are planned. The co-stiffening function of the original fittings must be taken over by other fixed elements.

2.2 Calculation and Engineering

The Shelter is a timber frame housing that is intended to serve as a living space. The short service life of about 4 years and the location of the accommodation does not comply with the requirements for flying structures (DIN EN 13782:2015). Furthermore, the shelter does not represent a building in the classical sense, since according to DIN EN 1990:2002 the shortest period of use for the design already provides for a period of 10 years. The standards of the Eurocode program were used as an indication for the design and engineering. The load assumptions were taken from DIN EN 1991-1-1 to DIN EN 1991-1-7 and the calculation rule from DIN EN 1995-1-1.

The structural penetration of the shelter is a deviation from the norm due to the multiple functional use of various components, such as the use of a ladder to reach the upper bunk bed and to stiffen the outer wall. Nevertheless, in order to make a meaningful prediction about the failure of the accommodation, it was designed using the finite element method and manual calculations. This approach enables the solution of the boundary value problem with the help of finite elements [6]. The results optimized the use of materials and the co-stiffening effect of the furniture.

The clamping situation of the 12 mm OSB plates in the profiles of the corner supports was clarified by orienting experiments on a universal tensile testing machine. Constructively, the minimum margin distances of the fastening devices were initially exhausted. These were enlarged after the experiments, which resulted in larger cross-sections of the entire primary structure.

In addition to the calculations, the load-bearing behaviour and stability of the accommodation will be experimentally proven in the future. A prototype of the property has been freely weathered since July 2024 (see Fig. 2) and is to be tested for burglary, stability and fire behaviour in 2028.

Fig. 2. Prototype with slightly other dimensions

3 The Production Line

The project was planned from the beginning as a large-scale series. The shelter is to be produced and assembled automatically on site in or near the camp. Particular attention was paid to the following aspects:

- Use of fixtures and/or NC machines in manufacturing and assembly
- designated component areas in which they can be transported, gripped or manipulated
- Tolerance design of the essential components, in particular with regard to the dwelling and shrinkage of the components made of wood and wood-based materials and the thermal expansion of metallic devices
- Design of the joints with regard to the positioning accuracy of automated or semi automated handling devices
- Use of as many identical parts as possible or standardised machining methods

The entire mobile production plant consists of five modules, which can be set up more or less coherently within about a week, depending on the location on site. Moulded strips and beams are produced on moulding machines or four-side planers and a NC double cross cutting saw with drilling units. This part of the plant, also the workshop for windows and built-in parts, is housed in several containers that can be opened on the side. In a tightly linked transfer line with flow production aspects, the OSB boards are unstacked, formatted, CNC-milled or printed with assembly guides and then transferred to an assembly device (see Fig. 3). This last part of the plant is to be designed as a special trailer similar to the 'break-dancer' ride. A rotary indexing table with two turntables is used (see Fig. 4). Since two turntable devices are firmly mounted on the pivoting rotary indexing table, they can be equipped well with sensors and actuators. For safety reasons, all manipulators are designed as balancers or other hand-operated machines.

Fig. 3. Model of the production line without additional subplants

1. Unstacking
2. Formatting
3. CNC-routing and printing
4. Handling of the long and short walls
5. Pivoting rotary indexing table
6. Installing beds and seats
7. Roofing
8. Moulding, cut to length and drilling of strips and beams
9. Production of windows, doors and interior

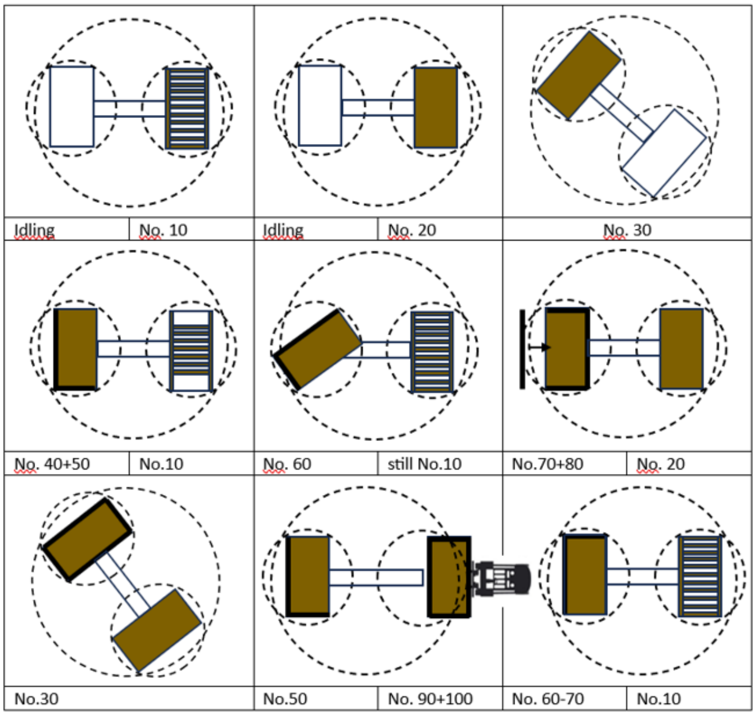

Fig. 4. Assembly steps for floor and walls on the rotary indexing table

The cycle time of 13 minutes in this first transfer line, housed in a large tent, could also be maintained for the transfer line of the final assembly. Here, the shelter is roofed and completed in seven stations. In the final assembly line, scaffoldings are built for roofing work from containers, which are also used for storage, which are then covered by special tent constructions. Special modules of the shelter are assembled in construction site production on their own places. After completion, each two shelters will be dropped off in the camp on the final position by truck, trailer and loader crane. The surface protection by means of layer-giving oils is to be completed by the residents themselves. In two shift shelters will be built on the line. Components are pre-produced in a third shift in batch production. The cycle times were calculated by hand. Armbrecht [7] does indeed propose a simulation-based methodology for the design of such production systems also in timber panel construction. However, factory planning only took place with regard to layout modeled and not simulated. The efforts would have been too high.

In addition to a specialized regular stuff, residents of the camp will also be trained and employed in the facility. It is hoped that the corresponding timber construction know-how will remain on crisis site. After the end of the crisis, the components of many shelters can then be upcycled to supplements or new buildings. The core components of the production plant are to be reused. Other components of the plant, such as forklifts, generator sets, office containers, etc., are likely to remain on site.

4 Outlook

After the establishment of an NGO, the concepts are to be professionally revised, in particular with regard to a wide variety of application scenarios and areas. Especially the necessary material logistics significantly limits the usability of the mobile production plant. 60 shelters are built every day (OEE 80%), which corresponds to about 50 tons of material. While solid wood can perhaps still be purchased on site, this is more difficult for panel material. A substitution of the OSB boards by plywood or suitable particle boards is possible, but only insignificantly simplifies the supply chain in case. In the future, the production plant will be first in North America to be used for homeless accommodation in order to gain relatively secure technical and organizational experience.

References

1. UNHCR (Ed.): Mid-year-trends-2023. https://www.unhcr.org/sites/default/files/2023-10/Mid-year-trends-2023.pdf, last accessed 2024/03/13.
2. Hack, S.: Humanitäre Hilfe: Was ist Humanitäre Hilfe? https://www.unicef.de/informieren/aktuelles/blog/-/humanitaere-hilfe/311274, last accessed 2024/03/13.
3. Hering, E.: Personalmanagement für Ingenieure. Wiesbaden: Springer Vieweg (2014).
4. UNHCR (Ed.): Shelter. https://www.unhcr.org/what-we-do/respond-emergencies/shelter, last accessed 2024/03/13.
5. Sphere Association (Ed.): Das Sphere-Handbuch. Humanitäre Charta und Mindeststandards in der humanitären Hilfe. Bonn: Köllen Druck- und Verlagsgesellschaft mbH (2019). Online https://spherestandards.org/wp-content/uploads/Sphere-Handbook-2018-German.pdf, last accessed 2024/03/13
6. Barth, C., Rustler, W. (2013): Finite Elemente in der Baustatik-Praxis. Berlin: Beuth Verlag (2013)
7. Armbrecht, C.: Simulationsbasierte Auslegung flexibler Fertigungssysteme der Holz- und Möbelindustrie. Diss. TU Braunschweig (2009).

DIN EN 1990, 01.10.2021: Eurocode: Grundlagen der Tragwerksplanung; Deutsche Fassung EN 1990:2002 + A1:2005 + A1:2005/AC:2010

DIN EN 1991-1-1, 01.12.2010: DE: Eurocode 1: Einwirkungen auf Tragwerke - Teil 1-1: Allgemeine Einwirkungen auf Tragwerke - Wichten, Eigengewicht und Nutzlasten im Hochbau; Deutsche Fassung EN 1991-1-1:2002 + AC:2009

DIN EN 1995-1-1, 01.12.2010: Eurocode 5: Bemessung und Konstruktion von Holzbauten – Teil 1-1: Allgemeines – Allgemeine Regeln und Regeln für den Hochbau; Deutsche Fassung EN 1995-1-1:2004 + AC:2006 + A1:2008

DIN EN 13782, 01.06.2015: Fliegende Bauten - Zelte - Sicherheit; Deutsche Fassung EN 13782:2015

Friction Forces Between Cutting Edge Flanks and Machined Wood Due to the Moisture Content of Scots Pine

Daniel Chuchala[1][0000-0001-6368-6810], Yunbo Huang[2][0000-0002-3286-2292], Kazimierz A. Orlowski[1][0000-0003-1998-521X], Mikael Svensson[2, 3], Magnus Fredriksson[2][0000-0003-4530-0536], Olof Broman[2][0000-0002-3444-9194]

[1] Gdańsk University of Technology, Faculty of Mechanical Engineering and Ship Technology, Institute of Manufacturing and Materials Technology, Gdańsk, Poland
daniel.chuchala@pg.edu.pl, kazimierz.orlowski@pg.edu.pl
[2] Luleå University of Technology, Wood Science and Engineering, Skelleftea, Sweden
yunbo.huang@ltu.se, magnus.1.fredriksson@ltu.se, olof.broman@ltu.se
[3] LSAB, Research and Development, Svinöhed 415, Långshyttan, 77673, Sweden
mikael.svensson@lsab.se

Abstract. During the wood cutting process, various interactions occur, such as material dislocations in the shear zone, chip displacement along the cutting tool face, and friction on the flanks. These interactions generate forces that serve as components of the total cutting force. The components of the cutting force contribute not only to chip formation and the creation of a new surface (machined surface) but also exert pressure on the workpiece in the feed and lateral directions. The material under pressure undergoes elastic deformation, pushing against the tool as it attempts to return to its original position. This reaction can increase friction forces at the flanks of the cutting edge. To accurately design the cutting process, understanding these aspects and their effects on cutting forces is essential. This research is focused on determining the spring-back friction forces measured for Scots pine (*Pinus sylvestris* L.) from Sweden under wet and dry conditions. Friction forces at the major and minor flanks of a single cutting edge of a band saw were measured immediately after a quasi-linear cutting process with three different feed per tooth values. Noticeable differences in friction force values were observed between wet and dry wood, notable across all three feed per tooth settings. These results provide a new understanding of the effect of elasticity properties of pine wood, which can generate friction forces and increase the total cutting force during wood cutting processes in both wet and dry conditions.

Keywords: Flank, Cutting process, Friction force, Moisture content, Pine, Sawing,

1 Introduction

Modelling wood sawing processes is challenging because wood is a natural material with heterogeneous structure, anisotropic and hydroscopic properties. These properties affect the conditions of the cutting process and must be taken into account when attempting to forecast cutting forces and cutting power. A number of studies have shown that as the moisture content (MC) of wood decreases, cutting forces and cutting power increase. These phenomena were observed by Moradpour et al [1], where the effect of moisture content and cutting direction was analysed for beech and oak wood. All three basic components of cutting force (main F_c, feed F_f and lateral F_p) had significantly lower values for green wood with respect to dry wood. An interesting observation was made in the work of Hanincová et al [2], where the main and feed cutting forces were analysed for spruce and oak wood. Namely, the values of the cutting forces increased with decreasing moisture content, however, only until the wood reached a moisture content of about 30%, i.e. around the fibre saturation point (FSP) and then began to decrease. The observed phenomena are explained by the fact that in wood with a moisture content above FSP, there is free intercellular water, which produces a friction-reducing film between the cutting edge and the generated chip on the rake surface and between the cutting edge and the machined surface on the flank surface. Very similar relationships can be observed in studies analysing the effect of moisture content in wood on its strength and elastic properties. In the study presented by Fu et al. [3], a rapid increase in compressive strength and elastic modulus occurs when the moisture content drops below the FSP (MC ≈ 30%). In this case, however, no decrease in material strength and elastic properties was observed when the wood is very dry (MC ≈ 5%).

In contrast, Fu et al [4] presented in their study that frictional forces decrease as the moisture content of the wood decreases. A similar relationship was observed for both static and dynamic friction coefficients. In this case, there was also a rapid decrease in the values of friction coefficients at the FSP limit, with decreasing moisture content.

Cutting forces are significantly influenced by tribological conditions [5, 6]. It is the friction in the cutting process that significantly influences the wear of the cutting edge on both the rake and the flank surfaces. The aim of the study was to analyse the forces generated by the friction of the cutting edge against the machined surface of pine wood as a function of the change in wood moisture content. These forces are generated as a result of the elastic deformation of the workpiece caused by the pressure of the cutting edge during the cutting process, and the subsequent attempt to return the deformed material to its original position and induce pressure on the cutting blade. Such an analysis may allow a better understanding of the friction phenomenon in the wood sawing process and its contribution to the cutting forces.

2 Theoretical background

Cutting forces are generated by the interaction of the cutting edge and the workpiece. The values of these forces are determined by a number of parameters and properties. The resultant (total) cutting force F_T consists of three basic components: main cutting force F_c, feed force F_f, lateral (side) force F_p (Equation 1).

$$\bar{F}_T = \bar{F}_c + \bar{F}_f + \bar{F}_p \tag{1}$$

Assuming that the cutting resistance and friction conditions are the same on both sides of the tooth, the cutting force F_c acting on one tooth can be represented as the sum of the forces acting on the workpiece material (Fig. 1) can be presented as follows [7]:

$$F_c = F_{cS} + F_{c\mu} + 2 \cdot F'_{cS} + 2 \cdot F'_{c\mu} \qquad (2)$$

where: F_{cS} – the cutting force component exerted on the major cutting edge; $F_{c\mu}$ – friction force between the major flank of the cutting edge and the machined material; F'_{cS} – the cutting force component exerted on the minor cutting edge; $F'_{c\mu}$ – friction force between the minor flank of the cutting edge and the machined material.

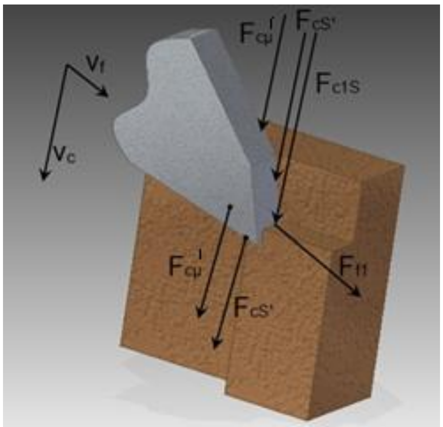

Fig. 1. Cutting forces related to the direction of the main movement per one saw tooth [7], where: v_c - cutting speed, v_f - feed speed, F_{f1} – feed force acting on one saw tooth.

3 Material and Methods

3.1 Materials

The study was carried out on four beams of Scots pine (*Pinus sylvestris* L.) prepared from one log harvested from northern Sweden in early winter. The log was stored under snow cover to spring, when beams were prepared. Two sections, each approximately 400 mm in length, were extracted from the log. These sections were selected to ensure that any knots were at least 20 cm away from one side of the section. From each section, four samples were extracted, resulting in a total of eight samples (Fig. 2). After trimming into square shapes, the samples measured 80 x 80 mm^2 in cross-section and approximately 350 mm in length. The samples were analyzed on seven steps of MC (MC0 - MC6). The samples at MC0 were in green condition directly after cut out from log. Next levels of MC (MC1 to MC5) were obtained by conditioning in a climate chamber at 20°C and 65% relative humidity (RH). Finally, MC6 was achieved by oven-drying at 103°C. The individual wood moisture contents for the tests below, divided into sapwood and heartwood, are presented in Table 1.

a) b)

Fig. 2. Preparation of research samples from a log: rough sawing of samples from a log using a chainsaw a), distribution of the collected samples in the log cross-section b).

Table 5. The moisture content of the analyzed pine wood for the individual machinability tests

Cutting test number	Moisture content, %							
	Sapwood				Heartwood			
	S1	S2	S3	S4	S1	S2	S3	S4
MC0	84	94	104	85	29	31	30	30
MC1	53	58	105	58	25	23	25	22
MC2	52	72	84	80	20	23	23	21
MC3	24	24	32	35	24	25	26	24
MC4	24	23	31	27	23	23	27	24
MC5	17	15	17	16	16	18	17	16
MC6	2	1	1	1	1	5	2	2

Machine tools, cutting tools and cutting procedure

The experimental cuts were performed on a special cutting station with a rotating arm with a radius of 610 mm, including the clamped workpiece. The arm was rotated clockwise at a revolution speed n = 40.4 min^{-1}, resulting in a cutting speed of v_c = 3 $m \cdot s^{-1}$. A detailed description of the station is presented in Huang et al [8].

The cutting tooth in sharp condition used in this study was tipped with Stellite 12 (Deloro Wear Solutions GmbH, Koblenz, Germany). The side clearance angle was α_f = 12°, and the side rake angle was γ_f = 27°. The theoretical kerf (overall set), was

S_t = 2.87 mm, while the saw blade thickness was s = 1.47 mm. The cutting tooth was mounted at the tooth holder (Fig 3). The holder was securely attached to a measuring plate (Type 9122AA, Kistler Instrumente AG). The measuring plate measures cutting forces in three orthogonal directions: the main cutting direction, the feeding direction, and the lateral (side) direction.

Fig. 3. The single-tooth mounted on the measuring plate.

Analog signals from the measuring plate were amplified and low-pass filtered with a cutoff frequency of 10 kHz using charge amplifiers (Type 5080A, Kistler Instrumente AG). The signals were then digitized using an analog-to-digital converter (USB-6009, National Instruments) at a sampling frequency of 15 kHz.

Each cross-section of analyzed four samples contained ten grooves (Fig. 3). These grooves were generated during the cutting process with use three uncut chip thicknesses per groove: h_1 = 0.3 mm, h_2 = 0.5 mm, and h_3 = 0.7 mm. Between the respective steps of cutting test, several revolutions of empty cuts, where h_0 = 0 mm, were carried out. During these empty cuts the friction force analyzed in this study was recorded. The cutting sequence for each groove followed this pattern: $h_1 \times 15 + h_0 \times 2 + h_2 \times 10 + h_0 \times 2 + h_3 \times 6$.

4 Results and Discussion

The recorded values of the friction forces between the cutting edge flank surfaces and the workpiece for the four analyzed samples and the subsequent cutting tests are shown in Fig. 4. The first half of the curves, approximately, concerns the heartwood, while the second half shows the sapwood, which had different moisture contents compared to heartwoods in the first three tests (Tab. 1). It can be observed that frictional forces decrease with decreasing moisture content below the FSP (Fig. 4g and 4h). Moreover, when testing a sample for which the moisture content of the heartwood and sapwood is significantly different, this can also be seen in the difference in friction forces (Fig. 4d and Tab. 1).

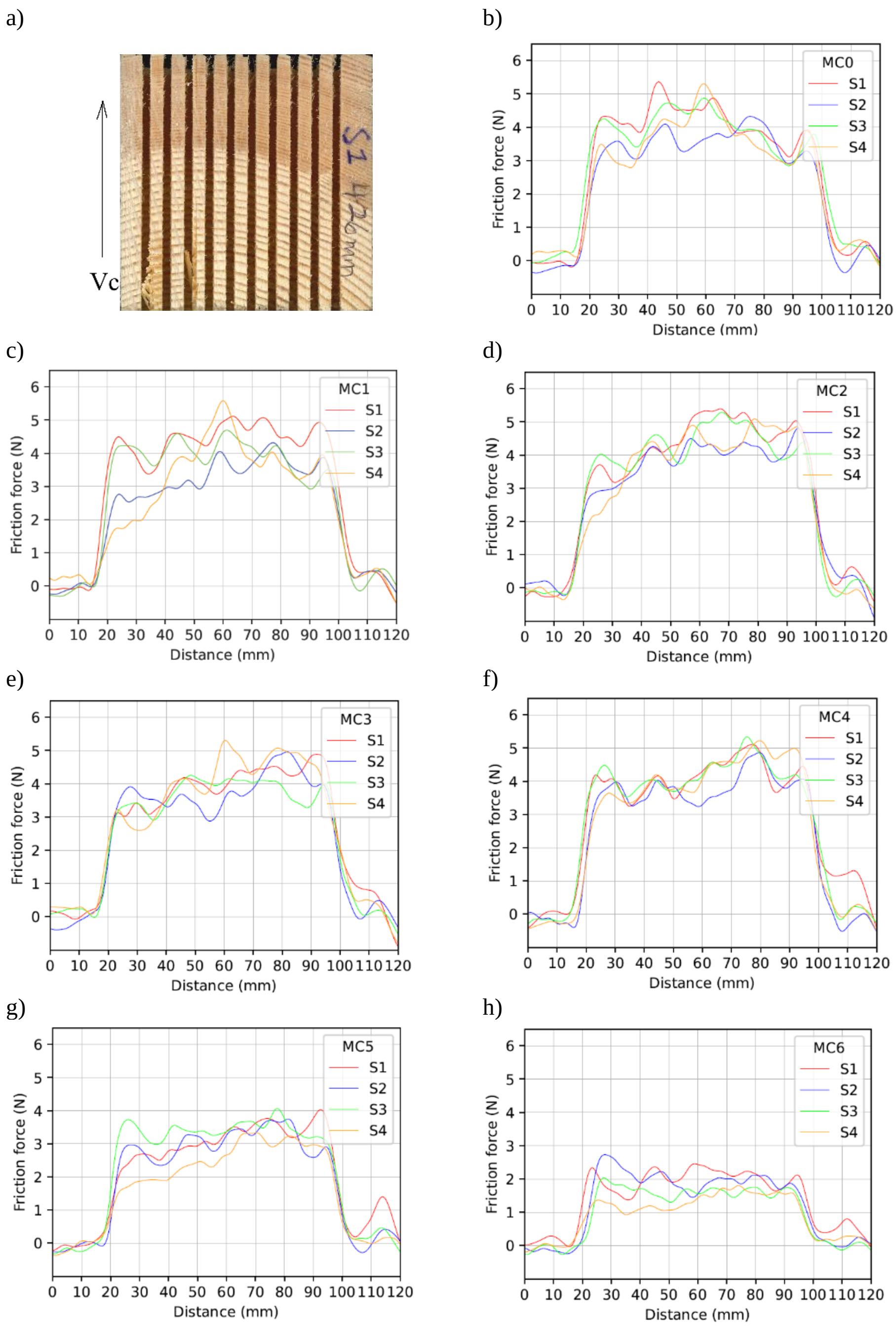

Fig. 4. The friction forces between the cutting edge flank surfaces and the pine wood.

Figure 5 shows the relationship between the friction forces of the cutting edge flanks and the moisture content of the machined pine wood.

a)

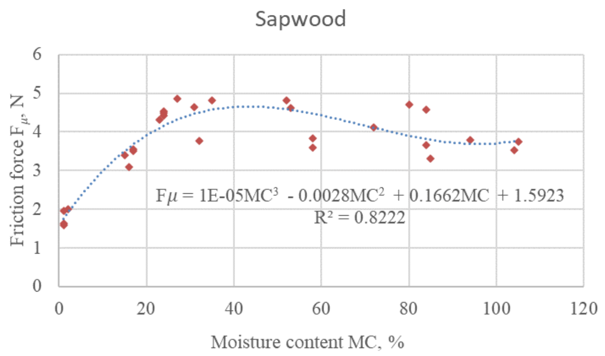

b)

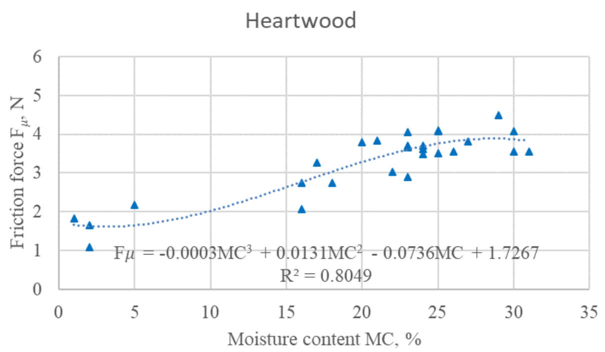

c)

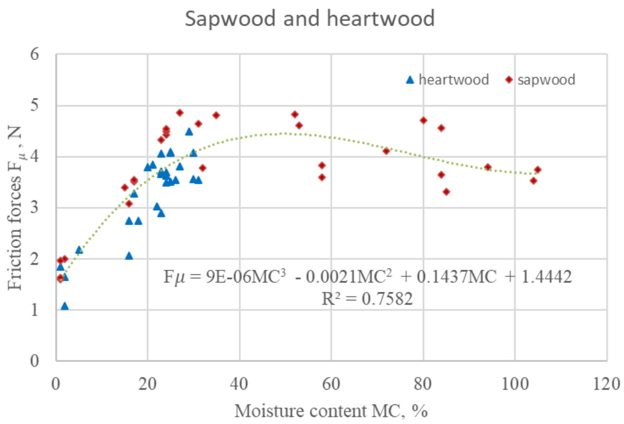

Fig. 5. Relationship between the friction force and moisture content.

For both sapwood and heartwood, a rapid decrease in frictional forces can be observed with a decrease in the moisture content of the wood, which can be directly related to an increase in the stiffness and strength of the material [3, 9], i.e. less elastic deformation of the wood during the implementation of cutting. Similar relationships were observed by Fu et al. [4] in a study of the friction process. Furthermore, very similar relationships between the cutting forces and the moisture content of the sawed wood were observed by Hanincová et al [2] in their study. In this study [2], a rapid decrease in cutting force values was also observed when the moisture content fell below FSP. Hanincová et al [2] explained this phenomenon by the lack of free water contained in the wood and its lubricating properties during the cutting process. However, this may be related to a significant extent to the change in the elastic properties of the material, which depend precisely on the moisture content of the wood [3, 4, 9]. Additionally noteworthy is the observation that no significant difference in frictional forces was observed for sapwood and heartwood, which have the same moisture content (Fig. 5c).

5 Conclusions

Based on the research carried out, the following conclusions can be drawn:

- Moisture content of pine wood affects the friction forces between the flanks of cutting edge and the machined material.
- The friction forces between the flanks of cutting edge and the machined pine wood decrease rapidly when the moisture content falls below FSP.
- No difference in frictional forces was observed for sapwood and heartwood with the same moisture content.

Acknowledgements. The authors gratefully acknowledge the financial support received from the Gdańsk University of Technology through the 11/2023/IDUB/II.1/AMERICIUM grant under the Americium International Career Development through “The Excellence Initiative − Research University” program. The authors express their sincere gratitude for the substantial support provided by CT WOOD, a center of excellence at Luleå University of Technology, in the advancement of X-ray computed tomography applications for the forest products industry.

References

1. Moradpour P., Doosthoseini K., Scholz F., Tarmian A.: Cutting forces in bandsaw processing of oak and beech wood as affected by wood moisture content and cutting directions. European Journal of Wood and Wood Products 71, 747–754 (2013). https://doi.org/10.1007/s00107-013-0734-z
2. Hanincová L., Procházka J., Novák V., Kopecký Z.: Influence of moisture content on cutting parameters and fracture characteristics of spruce and oak wood. Drvna industrija 73(3), 341-349 (2022). https://doi.org/10.5552/drvind.2022.0026
3. Fu W.-L., Guan H.-Y., Kei S.: Effects of moisture content and grain direction on the elastic properties of beech wood based on experiment and finite element method. Forests 12, 610 (2021). https://doi.org/10.3390/f12050610

4. Fu W., Guan H., Chen B.: Investigation on the influence of moisture content and wood section on the frictional properties of beech wood surface. Tribology Transactions, 64(5), 830-840 (2021). https://doi.org/10.1080/10402004.2021.1926029
5. Merchant M.E.: Basics mechanics of metal cutting process. Trans. ASME Journal of Applied mechanics Phys. 16, 267–318 (1945).
6. Atkins A.: Toughness and cutting: a new way of simultaneously determining ductile fracture toughness and strength, Engineering Fracture Mechanics 72(6), 849 – 860 (2005).
7. Orłowski K. : Materiałooszczędne i dokładne przecinanie drewna piłami (In Polish: *Narrow-kerf and accurate sawing of wood*). Monografia 40, Gdańsk. Wydawnictwo Politechniki Gdańskiej (2003).
8. Huang Y., Chuchala D., Buck D., Orlowski K.A., Fredriksson M., Svensson M.: Analysis of the relationship between cutting forces and local structural properties of Scots pine wood aided by computed tomography. Int J Adv Manuf Technol 135, 4975–4987 (2024). https://doi.org/10.1007/s00170-024-14797-w
9. Yilmaz Aydin T., Ozveren A.: Effects of moisture content on elastic constants of fir wood. European Journal of Wood and Wood Products 77, 63–70 (2019). https://doi.org/10.1007/s00107-018-1363-3

Effect of wood properties on warp of lumber sawn from large-diameter sugi (*Cryptomeria japonica*) logs

Kana Yamashita[1], Yukari Matsumura[1], Yosuke Matsuda[1], Miyuki Matsuo-Ueda[2], Masato Yoshida[3], Hiroyuki Yamamoto[3]

[1] Forestry and Forest Products Research Institute, 1 Matsunosato, Tsukuba, Ibaraki, Japan
[2] Graduate School of Agriculture, Kyoto University, Sakyo-ku, Kyoto, Japan
[3] Graduate School of Bio-agricultural Sciences, Nagoya University, Chikusa, Nagoya, Japan
zaikana@ffpri.affrc.go.jp

Abstract. Growth stress accumulated in the stem during tree growth is released when logs are sawn, which causes warp on the sawn lumber. If the wood properties related with the residual stress and warp are better understood, it would be possible to predict the warp degree before sawing. However, the degrees of residual stress and warp vary even within the same species and the same diameter class. In this study, flitches were ripped into inner and outer lumber, and the relationship between wood properties and warp was studied using sugi (*Cryptomeria japonica*). Warp was significantly correlated with the moduli of log elasticity of the lumber taken from the inner part, but not with that taken from the outer part. The modulus of elasticity of the core wood, which varies among trees within sugi, may predict warp due to the release of growth stress. Furthermore, the warp increased by air-drying, and the increase was larger in the inner lumber. This might have been caused by a very slight long-term relaxation of internal residual stress.

Keywords: Sawing, Lumber warp, Residual stress, Growth stress

Introduction

The increase in the supply of large diameter logs in Japan allows for sawing logs into various types of lumber. However, significant residual stress accumulated during tree growth is released at the sawing stage, causing lumber to warp. The degree of residual stress and warp vary a lot even within the same species and the same diameter class. If the wood properties affecting residual stress and warp are understood, it would be possible to predict warp degree before sawing.

Sugi (*Cryptomeria japonica*) is one of the main plantation tree species and its wood properties vary within and among trees. In this study, the warp due to ripping was compared between the lumber taken from the inner part and outer part of logs. The relationship between warp and the modulus of elasticity (MOE), which can be measured non-destructively, was examined. Furthermore, the warp change by air-drying was compared between lumber taken from the inner and outer part of logs.

2 Materials and methods

2.1 Materials

Twenty-four straight green logs of sugi with a top diameter from 34 cm to 39 cm and a length of 4 m were used. The logs were harvested from plantation forests in Ibaraki, Japan. Prior to processing, the modulus of elasticity of logs (MOE_log) were measured by the longitudinal vibration method. Fifteen logs (Group A) were cut into end-matched pairs of 2 m-long logs. The bottom half logs were used for the measurement of the released strain in the longitudinal direction. The top half logs were used for the measurement of warp due to ripping and drying. Nine logs (Group B) were also cut into pairs of 2 m-long logs. Both bottom and top logs were used for the measurement of warp due to ripping and drying.

2.2 Measurement of release of residual stress

The distribution of the released strain in the longitudinal direction across the diameter was measured for fifteen boards. The method using strain gauges is described in detail by Matsuo-Ueda et al. [1]. From each log with a length of 2 m, a quartersawn board including the pith with a thickness of 5 cm was sawn. The unedged green boards were surfaced into 4 cm thickness using a single surface planer. The measuring points were set at the middle of the length. The strain gauges (KFGS-10-120-C1-11 L3M3R, Kyowa Electronic Instruments Co., Ltd., Tokyo, Japan) were glued onto the boards along the longitudinal direction at 2 cm intervals in the radial direction from the pith to bark. Their lead wires were connected to a data logger (UCAM-550A, Kyowa Electronic Instruments Co., Ltd.) to monitor the strains. After the initial strains were measured, the board was cut at 1 cm from each end of the strain gauges using a handsaw, and the strains after cutting were measured. The released strain was calculated as the difference between before and after cutting.

2.3 Warp due to ripping and drying

Fifteen logs from Group A and 18 logs from Group B were used for studying the warp due to ripping and drying. From each log with a length of 2 m, a flitch including the pith with a thickness of 12.4 cm was sawn and both edges were ripped off as far outside as possible to prepare a four-sided cant. The flitch widths ranged from 28.6 cm to 37.3 cm. The four-sided flitches were surfaced into 12 cm thickness using a single surface planer.

In order to evaluate the warp due to ripping, the flitches were ripped into four segments (two inner lumber and two outer lumber) using a bandsaw. The ripping process is described by Yamamoto et al. [2, 3]. The ripped lines were along the pith and the middle of the pith and the edges. The height of the concavity was measured in 1 mm increments using a thread and ruler.

In order to evaluate the change of warp due to air-drying, the lumber segments were stacked with the straight grain side facing up and down, and air-dried for over four years. The warp was measured for the air-dried lumber. At the same time of each warp measurement, the weight, dimension (width, height and length) and the MOE of lumber (MOE_lumber) were measured. The basic density (BD) (oven-dry weight / green volume) was obtained for each lumber segment. The moisture content of the air-dried lumber was 13.8±0.5% for Group A and 15.2±1.0% for Group B.

Fig. 1. An example of a flitch ripped into four lumber segments

3 Results and discussions

3.1 Warp due to ripping

Fig. 2 shows the distribution of the released strain across the diameter obtained from the fifteen quartersawn boards including the pith. The released strain exhibited the maximum elongation at the pith, decreased towards the bark side. It turned into contraction at more than one-third of the distance from the pith.

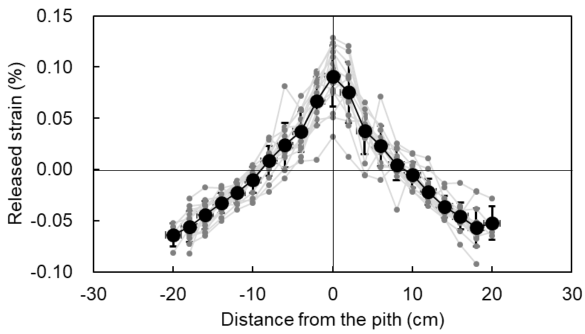

Fig. 2. Radial distribution of the released strain of the residual stress. A black circle shows the average of fifteen boards.

The lumber ripped from flitches exhibited warp, which was caused by the elongation at the pith side and contraction at the bark side. The warps due to ripping ranged from 1 to 7 mm. The inner lumber exhibited more warp than the outer lumber in both Groups

A and B (Table 1). The difference between the inner and outer lumber was significant (P < 0.001) in Group A, but not significant at 5% level in Group B.

Table 1. Warp of the lumber just after ripping and air-drying

	Group A			Group B		
	N	Ripping	Air-drying	N	Ripping	Air-drying
Inner lumber	30	4.2±1.5 mm	5.6±2.3 mm	36	3.9±1.2 mm	5.3±2.1 mm
Outer lumber	30	3.0±1.0 mm	3.3±1.2 mm	36	3.7±1.5 mm	4.2±1.5 mm

*Mean±STD is shown.

The relationship between the wood properties (MOE, BD and MOE/BD) and warp was examined. The MOE_log ranged from 6.1 to 9.9 GPa. The MOE_lumber was lower for the inner lumber than for the outer lumber. The mean of MOE_lumber was 7.3 GPa and 8.5 GPa for the inner and outer lumber in Group A, and 6.1 GPa and 9.9 GPa in Group B. The BD was a little higher for the inner lumber than for the outer lumber. The BD of the inner and outer lumber was 310 kg/m^3 and 302 kg/m^3 in Group A, and 327 kg/m^3 and 307 kg/m^3 in Group B. There were significant correlations with MOE and MOE/BD of log and the inner lumber, but not with any properties of the outer lumber in both Groups A and B (Table 2). There was no significant correlation with BD. Those results suggest that any factor related to the MOE at the core part can predict warp occurring due to the release of growth stress.

Table 2. Correlation coefficients between warp and wood properties for Group A.

	Properties of log			Properties of lumber		
	MOE	BD	MOE/BD	MOE	BD	MOE/BD
Group A						
Inner lumber	0.443 *	n.s.	0.597 ***	0.501 **	n.s	0.602 ***
Outer lumber	n.s	n.s	n.s.	n.s	n.s	n.s
Group B						
Inner lumber	0.443 *	n.s.	0.597 ***	0.501 **	n.s	0.602 ***
Outer lumber	n.s	n.s	n.s.	n.s	n.s	n.s

***: P<0.001, **: P<0.01, *: P<0.05

3.2 Warp due to air-drying

The warps of air-dried lumber ranged from 1 to 11 mm. The inner lumber exhibited larger warp than the outer lumber, which was the same trend observed in green lumber (Table 1). The difference between inner and outer lumber were significant both in Groups A (P < 0.001) and B (P<0.05). Warps of air-dried lumber increased compared to those of green lumber. There is a possibility that a very slight long-term relaxation of internal residual stress might have caused the increase of warp.

The length of lumber decreased vary slightly by air-drying; length shrinkage was a little larger for the outer lumber. Length shrinkage was 0.012% and 0.035% for the inner and outer lumber, respectively, in Group A, and 0.010% and 0.020% in Group B. The longitudinal shrinkage measured with small clear specimens after oven-drying is reported to be larger at the core wood in some Sugi cultivars [4], but that trend was not clear for the air-dried lumber used in this study. This might be because of the sample dimensions, sample properties and/or the hydrothermal history.

Acknowledgements

This paper consists of a part of the published references (1, 2 and 3). This research was supported by grants from the Project of the Bio-oriented Technology Research Advancement Institution, NARO (the special scheme project on advanced research and development for next-generation technology) and MAFF-commissioned project study on “Development of a stable supply system for domestic lumber by utilizing large-diameter logs”, Grant Number JPJ012040.

References

1. Matsuo-Ueda M., Tsunezumi T., Jiang Z., Yoshida M., Yamashita K., Matsuda Y., Matsumura Y., Ikami Y., Yamamoto H.: Comprehensive study of distributions of residual stress and Young’s modulus in large-diameter sugi (*Cryptomeria japonica*) log. Wood Sci. Technol. 56, 573-588 (2022).
2. Yamamoto H., Matsuo-Ueda M., Tsunezumi T., Yoshida M., Yamashita K., Matsumura Y., Matsuda Y., Ikami Y.: Effect of residual stress distribution in a log on lumber warp due to sawing: a numerical simulation based on beam theory. Wood Sci. Technol. 55: 125-153 (2021)
3. Yamamoto H., Matsuo-Ueda M., Tsunezumi T., Jiang Z., Yoshida M., Yamashita K., Matsumura Y., Matsuda Y., Ikami Y.: A computational approach to predict warp of sawn lumber due to residual growth stress in a log. 14th World Congress in Computational Mechanics (WCCM), ECCOMAS Congress 2020, https://www.scipedia.com/public/Yamamoto_et_al_2021a (2021).
4. Yamashita K., Hirakawa Y., Nakatani H., Ikeda M.: Longitudinal shrinkage variations within trees of sugi (*Cryptomeria japoni*ca) cultivars. J Wood Sci: 55 1-7 (2009).

Effect of tool wear and wood species on surface quality and finger-jointing performance

Julie Cool[1[0000-0002-9508-589X]], Shiqing Li[1] and William Nguegang Nkeuwa[2,3]

[1] Department of Wood Science, Faculty of Forestry, 2424 Main Mall, Vancouver BC, V6T 1Z4, Canada
[2] Henkel Corportation, 2515 Meadowpine Boulevard, Mississauga ON, L5N 6C3, Canada
[3] Department of Sustainable Biomatrials, College of Natural Resources and Environment, Virginia Tech,1650 Research Center Drive, Blacksburg VA, 24060, USA
julie.cool@ubc.ca

Abstract. In British Columbia (Canada), the need for high-performance structural finger-jointed lamellas is increasing. However, the effect of tool wear and coastal wood species on surface quality of finger-joints (FJ) and the performance of the corresponding FJ is not well known. The main objective of this study was to evaluate the effect of tool wear on the surface quality and bonding performance of finger-jointed (FJ) lamellas for three Coastal wood species. Two tool wear levels (freshly sharpened, worn) and three wood species (Coastal Douglas-fir (*Pseudotsuga menziesii* (Mirb.) Franco), western redcedar (*Thuja plicata* Donn ex D. Don) and Hem-Fir corresponding to a sawmill mix of western hemlock (*Tsuga heterophylla* (Raf.) Sarg.) and amabilis fir (*Abies amabilis* (Dougl.) Forbes) were used as independent variables. A full factorial experimental design was devised and yielded 6 finger-jointing conditions. Experiments were conducted in an industrial context. Surface quality measurements (i.e., surface roughness and wettability) were done on freshly FJ surfaces, while delamination and ultimate tensile strength tests were made with the FJ boards. Results highlight the effect of tool wear on surface quality and, consequently, on the mechanical properties of FJ boards. Species-specific characteristics also had an impact on surface quality and FJ properties, which provides valuable information on potential maintenance schedules.

Keywords: surface roughness, microscopy, wettability, ultimate tensile strength glueline delamination.

1 Introduction

The utilization of mass timber products, such as cross-laminated timber (CLT) and glue-laminated timber (glulam), in tall wood buildings is growing fast in North America. In British Columbia (BC), the Mass Timber Action Plan [1] aims to maximize opportunities for the mass timber construction sector, which should lead to the construction of 10 new mid-sized factories by 2035 [1]. This should be associated with a significant increase in sales of mass timber product in both Canada and the USA [2]. The need for manufactured long and high-performance structural finger-jointed (FJ) lamellas is therefore expected to increase.

The finger-joint (FJ) is one of the most common end-grain joints used when manufacturing CLT and glulam. Tool wear leads to surface quality defects and cell damage, which can affect the strength of FJ wood. For instance, studies have shown that increased tool wear leads to more cellular damage and a reduction in tensile and bending strengths of FJ silver fir [3] and ponderosa pine [4] wood. However, this effect can differ depending on wood anatomy. For example, diffuse-porous woods like sugar maple tend to show a reduction in shear gluing strength with increased tool wear [5], while ring-porous woods like northern red oak did not exhibit the same response [6]. Gradual wear of cutting edges not only reduces the quality of machining, but also increases the risk of sudden catastrophic tool failure, which can lead to unplanned downtime [7] and contribute to an increase in power consumption [8]. Therefore, assessing and monitoring tool condition and changing tools regularly is essential to maintain consistent tool performance throughout the production process [9].

In the Pacific Northwest Region, there is growing interest in using coastal wood species for structural finger-jointing (FJ) applications due to their geographical availability and cultural relevance. However, the effect of tool wear on the surface quality and gluing performance of these species is not well-documented. Douglas-fir (DF), Hem-Fir (HF), and western redcedar (WRC) differ significantly in density, chemical properties, and strength [10]. These natural variations could lead to different responses to tool wear, impacting the quality and durability of glued joints. To our knowledge, there are limited studies investigating the impacts of cutting tool wear and polyurethane (PUR) adhesive chemistry on the bonding performance of FJ for DF, HF, and WRC. Only few studies focused on FJ using PUR adhesive with DF [11-13], eastern Hemlock [14] and WRC [15] were conducted. While some studies have evaluated the effect of tool wear on surface quality and gluing performance for different wood species, very few have focused specifically on FJ using these particular species.

One of the key challenges in meeting the increasing demand of sustainable engineered wood products is the effective management of tool wear to ensure a consistent gluing performance. The general objective of this study was to evaluate the impact tool wear levels on surface quality and bonding performance of FJ lamellas made of Coastal DF, HF, and WRC to improve the manufacturability and quality of FJ lamellas. Specifically, this study aimed to 1) assess the effect of tool wear on surface topography and wettability, 2) quantify the influence of surface quality on the ultimate tensile strength and 3) correlate tool wear levels with bonding performance.

2 Materials and Methods

2.1 Testing Materials

Three hundred and thirty kiln-dried flat-sawn 3-m long No. 2&B [16] DF (*Pseudotsuga menziesii* (Mirb.) Franco), HF – representing a sawmill mix of western hemlock (*Tsuga heterophylla* (Raf.) Sarg) and amabilis fir (*Abies amabilis* (Dougl.) Forbes) – and WRC (*Thuja plicata* Donn ex D. Don) lumbers pieces were purchased from distributors local to Vancouver (Canada). Each piece had a nominal 2x4 cross-section corresponding to a 34-mm (radial (R)) thickness and 139-mm (tangential (T)) width. Each piece was crosscut with a PS50-F manual pendulum saw to a 91.4-cm (longitudinal (L)) length that was defect-free over a 5.1-cm L length from both ends. This resulted in 360 specimens per wood species that were randomly assigned to 6 different samples with each containing 40 replicates or specimens. The mean basic density ($M_{0\%}/V_{GREEN}$) for DF, HF and WRC was 414.1 ± 59.3kg/m^3, 356.0 ± 23.7 kg/m^3 and 290.9 ± 27.3 kg/m^3, respectively. All specimens were stored in a conditioning room at 20°C and 65% relative humidity until they reached an equilibrium moisture content of 12.6%.

A full factorial experimental design was devised with two independent variables (wood species and tool wear) and three dependent ones (surface roughness, surface wettability, and ultimate tensile strength), and each sample was assigned a specific FJ condition. Following finger-jointing, twenty specimens per sample were then glued according to the specifications of the manufacturer and sawn to a length of 1813.8 mm (with the FJ in the center) to test for their ultimate tensile strength according to ASTM D 4688 [17]. The remaining 20 specimens (finger-jointed but not glued) per sample were used to assess surface quality of the fingers.

2.2 Finger-Jointing Process

A Weinig Profitjoint machine was used within its industrial context. One defect-free end of each specimen was machined to obtain vertical FJ with a feather profile. The geometry of the fingers was 15 mm length, 3.8 mm pitch, 0.86 mm tip and 4.8° slope and the cutterhead had a diameter of 170 mm. The FJ were machined at a rotation speed of 4200 rpm and a feed speed of 15 m/min. Two tool wear levels were used during the tests: freshly sharpened and worn (Fig. 1).

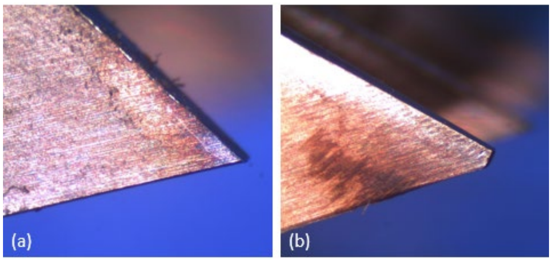

Fig. 1. Tool condition measurement for a freshly sharpened tool (a) and a worn tool obtained after finger-jointing green western redcedar wood within its industrial context (b).

Twenty FJ specimens per sample were glued with a PUR structural adhesive HB X102 (Henkel) applied using a comb. The quality of the glue application process was assessed by experienced operators to ensure an even glueline. The adhesive was applied according to the technical recommendations supplied by the glue manufacturer. An end pressure of 10 MPa was applied for a duration of 10 seconds.

2.3 Surface Quality Evaluation

The 3D surface roughness was measured on defect-free areas with an Olympus LEXT OLS 4000 Confocal Laser Microscope. An area of 50 mm^2 located at the center of a finger was scanned. Three fingers per specimen were scanned. The arithmetical mean deviation of the profile (S_A), the maximum profile peak height (S_P) and the minimum profile valley depth (S_V), were calculated according to ISO 21920 [18].

The wettability was quantified by measuring the contact angle (θ) of a 5-µl drop of PUR adhesive on a defect-free areas of a finger within 24 hours following the machining treatments. The contact angles were measured with Theta Flex 300-Pulsating Drop 200 Tensiometer at 20°C and calculated as a mean of both sides of the drop to compensate for any longitudinal variations. A frame grabber recorded the changes in droplet profile every second during the first 60 s of wetting. Measurements were carried out in the longitudinal direction. Wetting rate was calculated as $\Delta\theta/\Delta t$ to assess the spreading and penetration rate of the adhesive.

2.4 Mechanical Properties Tests

After FJ, all glued specimens were stored in a conditioning room at 20°C and 65% relative humidity until tested. Tensile tests were performed according to ASTM D4688 [18] and SPS-1 2014 [19] using an Metriguard 403 Tension Proof Tester. The ultimate tensile stress (UTS) was determined along with the failure mode, which was determined by carefully examining the area of failure and classifying the type failure in accordance with ASTM D4688 [17].

3 Results and Discussion

3.1 Surface Topography

The results of the ANOVA showed that the single effects of tool condition and wood species were significant for all surface roughness parameters, and the interaction of tool condition and wood species was only significant for S_P.

It is known that tool wear level impacts cutting forces [20] and modifies chip formation [21] due to the change in cutting edge geometry. The use of worn cutting tools is associated with greater friction forces [22] that corresponded to higher cutting power values (30.4 kW vs. 15.9 kW for worn and freshly sharpened knives, respectively). FJ HF wood with freshly sharpened knives resulted in the lowest mean surface roughness (R_A) (Table 1). The use of worn cutting tools resulted in an 8.9% increase in R_A for DF and HF wood surfaces. In contrast, the R_A of WRC remained statistically unchanged (Table 1); thus, suggesting WRC could be more resilient to tool wear in terms of its surface topography. This could be due to its lower wood density and mechanical properties that made WRC easier to machine. This was confirmed by the lower cutting power recorded when processing this wood species and the little difference observed between tool wear levels, which resulted in a more uniform surface quality (Fig. 1).

Table 1. Mean 3D surface roughness parameters (standard error in parenthesis) of three wood species finger-jointed with either freshly sharpened or worn cutting tools. Mean within a column followed by a same letter are not significantly different at the 95% confidence level.

Tool wear level	Wood species	Surface roughness parameters (µm)					
		S_A		S_P		S_V	
Freshly sharpened	Douglas-fir	14.5 (1.2)	b	232.8 (15.5)	a	176.0 (19.9)	a
	Hem-Fir	12.9 (1.8)	a	238.6 (21.1)	a	170.2 (17.7)	a
	Western redcedar	16.4 (2.2)	c	268.5 (28.2)	b	185.3 (19.3)	abc
Worn	Douglas-fir	15.8 (1.2)	c	324.4 (32.5)	d	197.3 (30.6)	a
	Hem-Fir	14.0 (1.5)	b	296.3 (25.9)	c	181.6 (33.3)	ab
	Western redcedar	16.8 (2.0)	c	321.2 (45.5)	d	194.9 (25.4)	bc

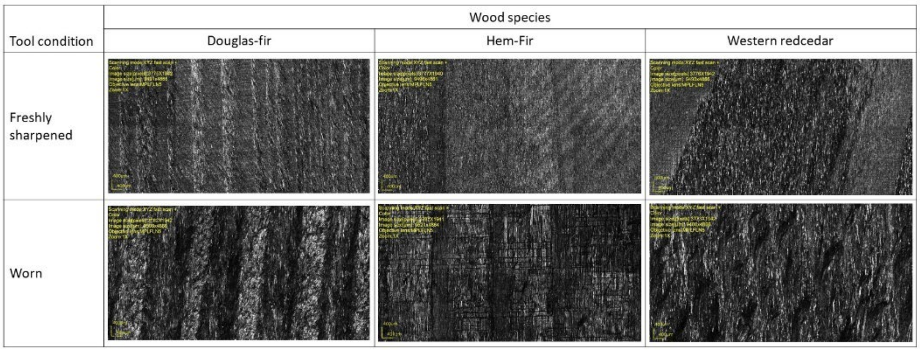

Fig. 2. Topography of Douglas-fir, Hem-Fir and western redcedar finger-jointed surfaces machined with freshly sharpened and worn cutting tools. The images were acquired by the optical profilometer.

The maximum profile peak height (S_P) clearly showed the effect of tool wear (Table 1). As the surfaces showed more irregularities with tool wear (Fig. 1), the S_P values increased significantly. The more aggressive tool action involved when using worn knives likely removed the earlywood tracheid cells, which generated the wave-like appearance on the fingers. This effect was amplified for DF wood surfaces because of the stark difference in wood density between early- and latewood [23]. This resulted in a 38.0% increase in S_P for DF compared with 24.2% and 19.6% for HF and WRC, respectively. The minimum profile valley depth (S_V) followed a similar trend to that of S_P (Table 1).

3.2 Wettability

The surface topography influenced the PUR wettability. Specifically, the initial contact angle was significantly greater for surfaces prepared with freshly sharpened FJ knives (77.7° vs. 73.5° for worn cutting tools). However, the wetting rate over the first 60 seconds was greater for the FJ surfaces prepared with freshly sharpened knives (Fig. 2). Based on the surface topography, it was expected that the wetting rate would be greater for surfaces prepared with worn cutting tools. While spreading in the longitudinal direction was likely favored by a higher overall surface roughness, it is hypothesized that cellular damage hindered the penetration of the PUR adhesive within the specimen prepared with worn cutting tools. In other words, PUR spreading was likely facilitated on fingers prepared with worn cutting tools, whereas PUR was able to penetrate in surfaces FJ with freshly sharpened knives characterized by less cellular damage.

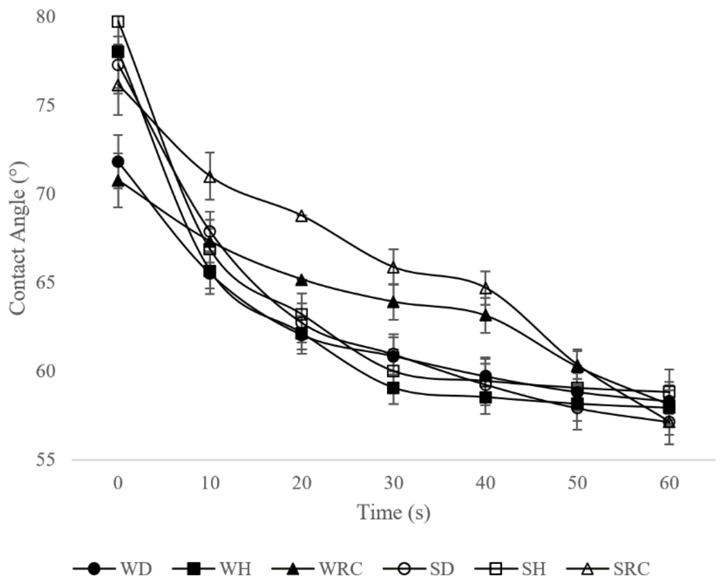

Fig. 3. Contact angle evolution with wetting time for Douglas-fir (D), Hem-Fir (H) and western redcedar (WRC) when finger-jointing with worn (W) or freshly sharpened (S) cutting tools.

The wood species also had an effect on the wettability of the PUR adhesive. When using freshly sharpened or worn tools, the initial contact angle was greater for HF finger-jointed surfaces than that of DF or WRC suggesting the latter may facilitate the application of PUR (Fig. 2). The apparent smoother surface topography of HF could be a contributing factor to slow the initial wetting process. However, there were no significant differences between wood species after 60 seconds of wetting regardless of tool wear level (Fig. 2). The results suggest the time between glue and pressure application may be an important factor to consider based on each species. Similarly, tool maintenance could have a significant effect on adhesive performance.

3.3 Mechanical Properties

According to the ANOVA, the interaction of tool condition and wood species was significant for the UTS. When using freshly sharpened tools, there were no significant difference between wood species (Table 2). However, when using worn cutting tools, finger-jointed DF wood resulted in significantly stronger UTS (20.5% increase) – suggesting that tool sharpness may not have a consistent impact on bonding performance. As reported previously [24-25], a certain level of surface roughness and/or cellular damage could be favorable to mechanical adhesion. DF also had a greater wood density and is generally known to have stronger mechanical properties [10]. It is hypothesized that the greater surface roughness and level of cellular damage contributed to mechanical adhesion. The UTS of HF and WRC FJ wood did not improve with tool wear. Although the UTS was 10.7% and 11.3% lower for HF and WRC when using worn knives, it was not statistically significant.

Table 2. Mean ultimate tensile strength values (UTS) and proportion of delamination of three wood species finger-jointed with either freshly sharpened or worn cutting tools. Mean within a column followed by a same letter are not significantly different at the 95% confidence level.

Tool wear level	Wood species	UTS (MPa)	
Freshly sharpened	Douglas-fir	129.6 (37.5)	b
	Hem-Fir	130.9 (31.3)	b
	Western redcedar	133.7 (35.7)	b
Worn	Douglas-fir	156.2 (45.8)	a
	Hem-Fir	116.9 (30.7)	b
	Western redcedar	118.6 (19.8)	b

The assessment of the failure modes associated with the UTS tests showed that only 6% were Type 1 wood failures (i.e., less than 70% wood failure) whether the cutting tools were sharp or worn. This confirms the gluing process was well-done. When using sharp FJ knives, the Type 6 (i.e., failure occurred away from the joint) failure mode was most common (35%) followed by failure Type 2 (i.e., more than 70% wood failure) (23%). As expected, the distribution of the failure modes changed when FJ with worn tools to Type 3 (i.e., good overall shear failure along joint profile) (30%) and Type 6 (25%). Amongst the wood species under study, WRC generated twice as many Type 1failures than the other two wood species. While the surface topography of WRC appeared more resilient to tool wear, it is possible its cellular structure was more impacted by the machining process due to its lower density and mechanical properties. Thus, weakening the FJ strength.

4 Conclusions

The results of this study showed that tool condition and wood species had a significant impact on the surface topography, wettability, and mechanical properties of FJ. The worn cutting tools had a negative impact on the mean surface roughness and cutting power, but WRC showed strong adaptability due to its lower density. When FJ with worn cutting tools, the S_P and S_V surface roughness parameters increased significantly, especially for DF, due to the significant difference in density between early- and latewood.

Surface topography seemed to have influenced the PUR wettability. The use of freshly sharpened FJ knives resulted in surface having a greater wetting rate. This was likely due to the lower cellular damage generated when using sharp cutting tools that favored PUR penetration in the fingers. In contrast, cell damage caused by the worn tools may have hindered the penetration of PUR, indicating that optimal surface preparation is necessary to achieve effective adhesive performance.

The interaction between tool wear and wood species also affected the UTS. DF showed a significant increase in UTS after tool wear due to a potential level of cell damage promoting mechanical adhesion. In contrast, HF and WRC showed a reduction in UTS. Failure mode analysis confirmed an effective bonding process, but WRC was found to be more susceptible to structural failure under worn tool conditions.

References

1. Government of BC: B.C.'s Mass Timber Action Plan. 24 pp. (2022). Available: https://www2.gov.bc.ca/assets/gov/business/construction-industry/bc_masstimber_action_plan_2022.pdf (accessed January 24, 2023).
2. Sorensen, J.: Building taller: BC mass timber suppliers see surging sales in Canada, US. Canadian Forest Industries (2019). Available: https://www.woodbusiness.ca/building-taller-bc-mass-timber-suppliers-see-surging-sales-in-canada-us/ (accessed January 23, 2023).
3. Vassileiou, V.: Effect of knife wear on finger-joint strength of silver fir (Abis alba) wood. Wood Material Science & Engineering, 6(3), 128–131 (2011).
4. Reeb, J. E., Karchesy, J. J., Foster, J. R., Krahmer, R. L.: Finger-joint quality after 4, 6, and 32 hours of knife wear: preliminary results. Forest Products Journal, 45(7/8), 33–36 (1998).
5. Hernández, R. E., Rojas, G.: Effects of knife jointing and wear on the planed surface quality of sugar maple wood. Wood and Fiber Science, 34(2), 293–305 (2001).
6. Hernández, R. E., de Moura, L. F.: Effects of knife jointing and wear on the planed surface quality of northern red oak wood. Wood and Fiber Science, 34(4), 540–552 (2001).
7. Wei, W., Li, Y., Xue, T., Tao, S., Mei, C., Zhou, W., Wang, J., Wang, T.: The research progress of machining mechanisms in milling wood-based materials. BioResources, 13(1), 2139–2149 (2018). DOI: 10.15376/biores.13.1.2139-2149
8. Itaya, S., Tsuchiya, A.: Development of CrN coated tool to create smooth surface of solid wood aiming to omit sanding process in furniture production. In: Proceeding of the 16th International Wood Machining Seminar, Matsue, Japan, pp. 74–81 (2003).
9. Iskra, P., Hernández, R. E.: Toward a process monitoring of CNC wood router. Sensor selection and surface roughness prediction. Wood Science and Technology, 46(1–3), 115–128 (2012). DOI: 10.1007/s00226-010-0378-7

10. Senalik, C. A., Farber, B.: Mechanical properties of wood. In: FPL-GTR-282, Chapter 5, pp. 5–1 (2021).
11. Rammer, D. R., Zelinka, S. L., Hasburgh, L. E., Craft, S. T.: Ability of finger-jointed lumber to maintain load at elevated temperatures. Wood and Fiber Science, 50(1), 44–54 (2018).
12. Yue, K., Wang, F., Lu, W., Tang, Z., Chen, Z., Liu, W.: Tensile properties of finger-jointed lumber under high-temperature and oxygen-free conditions. Holzforschung, 75(9), 838–846 (2021).
13. Lehringer, C., Gabriel, J.: Review of recent research activities on one-component PUR-adhesives for engineered wood products. Materials and Joints in Timber Structures: Recent Developments of Technology, 405–420 (2014).
14. Sterley, M.: Green gluing of wood (Doctoral dissertation). Byggvetenskap (2004).
15. González-Prieto, O., Casas Mirás, J. M., Torres, L. O.: Finger-jointing of green Eucalyptus globulus L. wood with one-component polyurethane adhesives. European Journal of Wood and Wood Products, 1–9 (2021).
16. (National Lumber Grading Authority, 2014) Para 114 – Boards sheathing and form lumber – Rough or surfaced shiplapped or tongued & grooved under nominal 2" in thickness and 2" & wider. *In Standard grading rules for Canadian lumber*. 238 pp Retrieved from: https://nlga.org/wp-content/uploads/2023/01/NLGA-GR-2022-version-__Website-Pages-1-238.pdf
17. American Society for Testing and Materials (ASTM): Standard test method for evaluating structural adhesives for finger jointing lumber. ASTM D4688. ASTM International, West Conshohocken, PA, 8 pp. (2021).
18. International Organization for Standardization (ISO): Geometrical product specifications (GPS) – Surface texture: Profile – Part 1: Indication of surface texture (ISO 21920-1:2021). Geneva, Switzerland: ISO (2021).
19. National Lumber Grades Authority: SPS 1 special products standard for fingerjoined structural lumber. Vancouver, BC: National Lumber Grades Authority (2014). Retrieved from: http://www.nlga.org
20. Pérez-Salinas, C., de Lacalle, L., del Olmo, A., Kumar, C. S.: The relationship between the cutting-edge, tool wear, and chip formation during Inconel 718 dry cutting. The International Journal of Advanced Manufacturing Technology, 132(11), 6001–6017 (2024).
21. Cui, X., Zhao, B., Jiao, F., Zheng, J.: Chip formation and its effects on cutting force, tool temperature, tool stress, and cutting edge wear in high- and ultra-high-speed milling. The International Journal of Advanced Manufacturing Technology, 83, 55–65 (2016).
22. Rao, A. S.: Effect of nose radius on the chip morphology, cutting force, and tool wear during dry turning of Inconel 718. Tribology-Materials, Surfaces & Interfaces, 17(1), 62–71 (2023).
23. Abdel-Gadir, A. Y., Krahmer, R. L., McKimmy, M. D.: Intra-ring variations in mature Douglas-fir trees from provenance plantations. Wood and Fiber Science, 170–181 (1993).
24. Moanda, D. B., Volkmer, T., Niemz P., Schinle, F., Stapf, G., Canoine, B., Josset, S., Campos, C., Hazir, E., Sandak, J., Lehman, M. Effect of wood machining conditions on the delamination of bond lines. In: Proceeding of the 25th International Wood Machining Seminar, Nagoya, Japan (2023).
25. Cool, J., Hernández, R. E.: Improving the sanding process of black spruce wood for surface quality and water-based coating adhesion. Forest Products Journal, 61(5), 372–380 (2011).

How Digital Printing Technology Can Optimize The Wood-Based Element Finishing Process

Silver Santandrea[1] and Lorenzo Melloni[1]

[1] Cefla Finishing, Imola (BO) 40026, Italy
silver.santandrea@cefla.it

Abstract. Optimising a production process inevitably involves the adoption of innovative technologies that allow manufacturers to respond to growing market demand for flexibility, sustainability and cost reduction. In the specific case of wood-based floor plank colouring, using a digital printing machine to apply ink offers significant advantages compared to the traditional analogue technique with roller machines. At present, the use of roller machines requires producers to keep extensive stocks of dyes in order to create the variety of shades needed to match the different wood substrates. This application method has significant inefficiencies, especially as regards little-used shades: while the latter represent only about 25% of the total, they still need to be kept in stock to ensure they're readily available to the customer. Vice versa, the remaining 75% of shades consist of frequently-used colours in large quantities. Introducing digital printing would drastically reduce stocks of lesser-used dyes, streamlining warehouse efficiency and limiting the costs associated with low-demand products. Furthermore, the flexibility of digital technology would permit rapid adaptation to the customer's customisation needs, reducing set-up and dye changeover times. The transition from an analogue to a digital system also meets sustainability needs as it reduces waste and optimises use of resources. Investing in a digital printing machine would, therefore, not only improve the company's market competitiveness: it would also provide a practical response to warehouse management problems, enhance sustainability and speed up adaptation to demand. Such a change would bring tangible benefits in both economic and operational terms, favouring leaner production in alignment with Industry 4.0 / 5.0 principles.

Keywords: Digital printing, Sustainability, Flexibility.

1 Framing of the topic of this article

1.1 Overview - Base terminology

FINISHING (VARNISHING): application of a uniform [mainly protective, but aesthetic as well] layer on an article

DECORATION: application of an image on an artifact [embellishment]

PRINTING: a way to decorate a product

Wood-based elements printing is a segment of the DÉCOR printing sector which in turn is part of the wider INDUSTRIAL digital printing market, as depict-ed in the picture.Subsequent paragraphs, however, are indented.

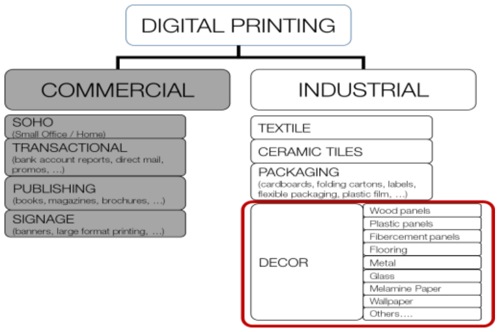

1.2 Introduction to Digital Printing Decoration

Digital printing has emerged as a leading technology in the wood industry, allowing for high-quality decoration and customization. Inkjet printing, in particular, is prominent in this transformation.

Inkjet technology is indeed a “short description” that encompasses a wide range of specific technologies. Piezo-electric drop-on-demand (DOD) technology is the decidedly dominant one in the color printing and decoration sector.

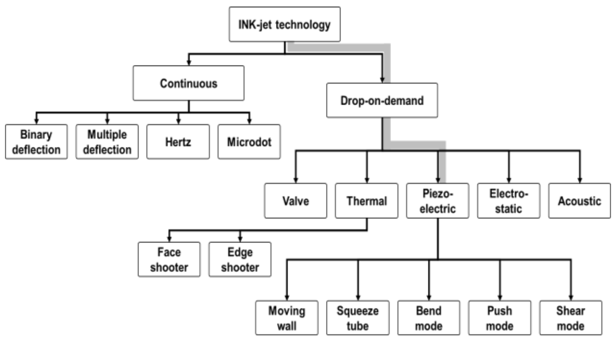

2 General Pros and Cons of Digital Printing Decoration

2.1 Pros of Digital Inkjet Printing on Wood Derivatives

- High Customization and Flexibility: Digital inkjet printing enables intricate designs and color patterns on wood, and mainly wood derivatives, products without the need for costly rolls, screens, molds or stencils.
- Shorter Setup Times: Compared to traditional printing techniques, inkjet printing has minimal setup requirements, making it suitable for short-run or on-demand production.
- Cost-Effective for Small Runs: The ability to print designs directly onto substrates, without the need of design-specific tools and/or consumables, eliminates the need for inventory management, making it cost-efficient for small and medium-sized runs.
- Environmental Benefits: Digital printing reduces the need for chemicals like cleaning solvents and enables waste reduction, with fewer materials being used compared to traditional methods.
- Fine Detail and Precision: The high resolution of inkjet printing allows for detailed and vibrant designs, improving the aesthetic appeal of wood derivatives.

2.2 Cons of Digital Inkjet Printing on Wood Derivatives

- Higher Initial Investment: The upfront cost of inkjet printers is generally higher compared to “conventional”, comparable, decoration systems and can appear “scaring”, if not prohibitive, for some manufacturers, especially small companies.
- Durability and Surface Wear: Printed designs may not be as durable as those created with traditional techniques like laminating or veneering, particularly when exposed to wear and tear. However, a proper surface resistance can be achieved with adequate top-coating.
- Sensitive to proper Maintenance: Inkjet printers require regular maintenance to ensure consistent output quality, and issues such as nozzle clogging can oc-cur.
- Need of Material Preparation: Wood derivatives such as MDF and plywood require pre-treatment to ensure optimal ink adhesion and image quality. In-deed, this point is true also on “conventional” decoration systems, although with some differences in the substrate preparation.

3 Applications

3.1 Digital Color décor

Digital printing machines configurations

The digital printing machines, more specifically the inkjet ones, can be divided in two big categories: multi-pass and single-pass.

In the multi-pass machines, the group of heads is moved along an axis perpendicular to the “conveyor” direction. There are two possible general configurations of the multi-pass printers: gantry and reciprocator/belt configuration. In the gantry configuration the pieces to be decorated are delivered in the printing position and then an X-Y axis group take over to completely decorate the pieces before they are moved away again. In the reciprocator/belt configuration the pieces are delivered step-by-step under the reciprocating group of heads (X axis).

The benefit of the multi-pass configuration is the possibility of defining the printing “quality” in a software manner by modifying the number, pitch and speed of the print head's strokes, making the most of its physical characteristics ("firing" frequency).

In the single-pass configuration the head assemblies are static. It is the movement of the pieces on the conveyor system that allows the decoration. The width of the print heads assembly must correspond to the maximum width of the pieces to be decorated.

The maximum speed of the conveyor system corresponds to the speed allowed by the "firing" frequency of the print heads at the desired resolution in the direction of motion of the pieces and with the defined ink (and related firing "waveform").

The resolution in the direction perpendicular to the direction of motion of the pieces is defined by the pitch between the nozzles of the individual heads and the number of heads installed in parallel.

The benefit of the single-pass configuration is the enormous productivity.

Substrate preparation

An image of good quality and resolution is just a good starting point for printing a nice product on a good machine.

The type of substrate and its color (generally "white") are fundamental in color rendering. The goal is to have a prepared substrate in order to achieve the most defined print possible

To achieve this objective, the drops of ink must remain in the deposited position without slight movements (or "dodging") and possibly with a slight "enlargement" of the drop itself (named dot gain; i.e. a slight increase in the diameter of the printed dot).

The optimal result described above is influenced by the surface state of the sub-strate (roughness, presence of small defects, etc...), as well as by the print base product that is applied to it and by the state of drying of the same (and possibly by the number of "coat layers" with which it is made). Any surface roughness of the substrate not sufficiently levelled by the print base or any roughness intro-duced during the application phase of the print base itself, tends to be "copied" by the printed ink and show an increased graininess of the print.

Finally, the surface tension of the print base is crucial in order to achieve the objectives mentioned above. Surface tension which must generally be higher than 45-50 mN/m.

To summarize, a well-polished (smooth) substrate, a print primer product capable of leveling as best as possible and a final surface of the primer itself with high surface tension are the keys to a quality print; maintaining these parameters over time is instead the key to the stability of the process.

Process workflow

It is for the reasons set out above that for each new support (or print background) it is necessary to proceed with the generation of the relevant "color profile", which, in short, is the "map" that best matches each desired color with the color to be sent to the printer to best obtain said desired color on the finished product.

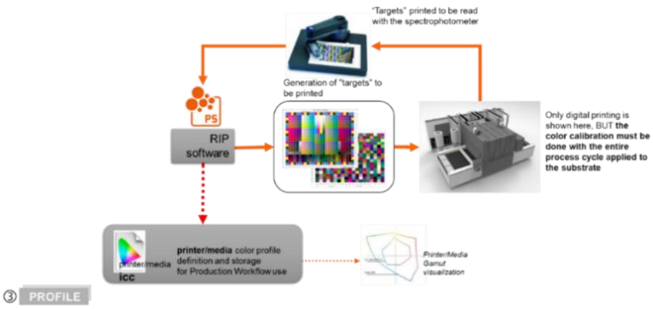

A depiction of the base process workflow is shown in the picture below where (from left to right) are represented the phases of the image acquisition and preparation, of the soft- and hard-proofing of the said image (and retouching, if needed) and the final printing on real substrate to obtain the desired product.

It is important to underline that, for the general decoration market, the most common way to best match the desired image with the printed one on the real product is to have, or prepare, a white substrate and create a color profile for the set of inks available in the printer and the specific prepared substrate, following the scheme shown at the beginning of this paragraph.

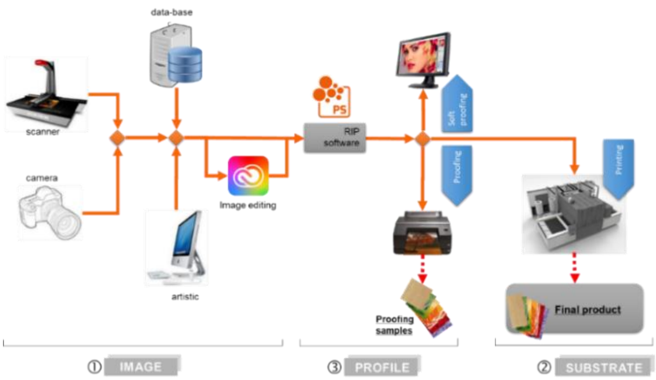

The described procedure is not the only one used in the market but it's definitely the most common one. We will see in the Digital Staining description that, for that specific market niche, a different approach is followed.

3.2 Digital Staining

Introduction to Digital Staining Technology

Digital Staining is the process of coloring wood-based materials, such as flooring planks, veneered panels or other substrates with at least the top layer made out of real rough wood. The process is carried out using inkjet digital printer, both single-pass and multi-pass, with the advantage to drastically reduce stocks of low-rotating dyes, thus improving warehouse efficiency and limiting costs related to low-demand products. Furthermore, the flexibility of digital technology would allow rapid adaptation to the customer's customization needs, reducing set-up and color change times. The transition from an analogue to a digital system also responds to sustainability needs, thanks to the reduction of waste and the possibility of optimizing the use of resources.

Key details of Digital Staining Technology

Because of its specific characteristics, this market niche requires an approach to colour-matching different to the one described in the previous chapter. The rough wood substrate with differences in color shades from lot to lot as well as inside the single lot makes it difficult, if not impossible, to use the technique of color profiling.

Arise the need of create “color atlas” for any of the species of rough wood to be processed, from where to select the desired “digital stain” (that is to say the de-sired combination of CMYK colors or L*a*b* values) together with a proper digital white amount underneath the digital stain (if needed).

Once the right area in the atlas is found, fine adjustments can be carried out both printing more specific and detailed atlases in the neighborhood of the found match or comparing the spectrophotometer readings of the desired original and the “corresponding” position on the printed atlases.

The examples depicted above are the most common expected in the wood market, but the technology opens to more “daring” color options like the following ones.

The digital printing technology, gives as well the possibility to more general color decorations, but still keeping the natural wood feeling (both “texture” and “warm feeling”).

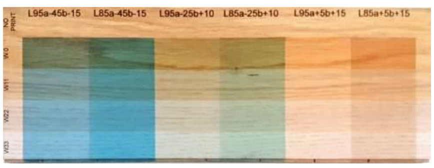

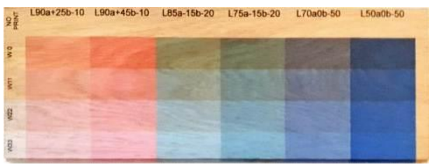

The digital printing technology, gives as well the possibility to more general color decorations, but still keeping the natural wood feeling (both “texture” and “warm feeling”).

3.3 Digital Texturing

Introduction to 3D Digital Texturing Technologies
One of the most exciting advancements in the inkjet printing sector is the ability to print textures, creating 3D effects on wood-based materials. These technologies not only enhance the visual appeal but also add a tactile dimension, giving the surface a realistic feel—such as the natural texture of wood grain or stone-like finishes.

Benefits of 3D Digital Texturing.
Enhanced Aesthetics: 3D digital texturing allows for the replication of natural patterns, adding depth to designs.
Increased Value: Textured finishes are often perceived as higher quality and more premium, making them suitable for luxury products.
Customization Opportunities: These technologies allow for a wide range of customizable textures, which is ideal for creating unique, one-of-a-kind products.
Innovation and Differentiation: Manufacturers can distinguish their products in a crowded market by offering innovative textures that are not easily replicated with traditional methods.

Challenges.
Cost of Implementation: 3D digital texturing requires sophisticated equipment and comes with higher capital investment costs, although not operational ones.
Complexity of Design: Creating textures "in register" with the color decoration (EIR) needs scan of real samples and specific image processing as well as requires precise calibration of the machines and expertise in running the production line.
Maintenance carefulness: any digital printing equipment requires more careful maintenance compared to conventional decoration systems being the printing-heads very sensitive devices; digital texturing, mainly subtractive digital texturing, may add some more carefulness requirements to the maintenance due to the specific process to achieve the final textured products

Subtractive texturing

Key Technologies for 3D subtractive Texturing in Wood Printing.

Digilogico®:
The Digilogico® process is based on the "shielding" that the texturizing fluid operates on the curing intensity of the coating varnish. The latter must have good compatibility with the texturizing fluid, but above all it must guarantee high resistance and an "elasticity" such as to limit the tendency of "curling" the substrate once dried, mainly if deep textures are needed, that corresponds to a high amount of the mentioned coating varnish. To reveal the texture the last step of this process is the brushing of the surface with "strong" iron/metal brushes that removes the less cured part of coating varnish.

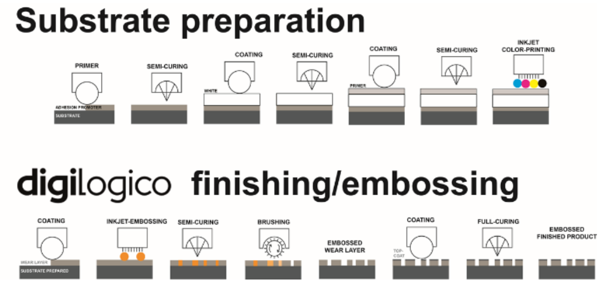

Deep-Blue:
The Deep Blue technology differs from the previous technology for the texturing fluid and the corresponding process to reveal the texture. The texturing fluid is a jettable sublimatable mixture/dispersion. The process to reveal the texture is a sublimation station where the texturing fluid sublimates, weakening the close surrounding area of the coating varnish, followed by a brushing station to remove the weakened areas and unveiling the texture pattern.

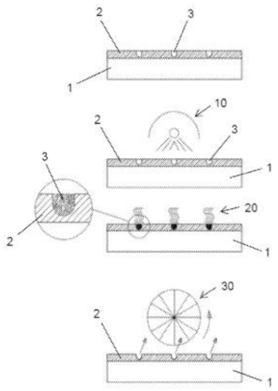

DLE-Plus:
DLE Plus process is pretty much similar the Digilogico® one, differing in formulation details about the texturing fluid and the coating varnish, but very similar from the general workflow.

Additive texturing.

Key features of 3D additive Texturing in Wood Printing.
Additive texturing is a process in which an ink is used to print "texture patterns" to create tactile relief on a wood-based substrate. This process can be achieved by printing a white textured pattern underneath the colored decoration or by printing a clear ink varnish over it.

This technology is mainly feasible with multi-pass printers (but also feasible with single-pass printers with some limitations/constraints).

The technology has high process cost and limited surface resistance compared to the subtractive texturing technology but offers the possibility of very detailed and deep textures with the possibility of "grayscales" levels of depth.

The same base technology can also be dedicated to the creation of molds (both for very deep surface texturing of fiber cement and ceramics still in "wet" stage, and for texturing of impregnated papers).

4 Inks

4.1 Inks classification

There could be many ways to classify inks. We show below a couple of classifications, one based on the curing speed and the other based on the processing peak temperature.

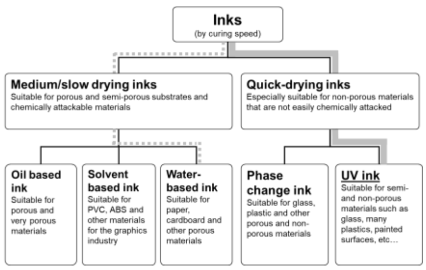

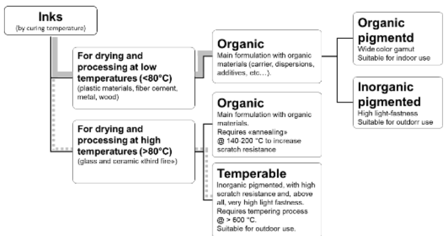

It worth to underline the availability of inorganic-pigmented "organic inks" (curable at "low temperatures"), that show a very high light-fastness giving the possibility for outdoor use of the decorated products up to 10-15 years without a significant fading of the colors.

5 Conclusion

In summary, inkjet printing on wood derivatives is a transformative technology that offers numerous benefits, from customization to cost savings, but also presents challenges related to durability and setup costs. The economic impact of this technology continues to grow globally, with specific countries driving market adoption. As the technology evolves, it holds great promise for the future of the wood industry, balancing cost, aesthetics, and functionality.

Impact of Sandpaper and Machining Settings on Triboelectric Charges in Wood Sanding

Lena M Leiter[1][0000-0002-7790-0854], Roman Myna[1], Julie Cool[2][0000-0002-9508-589X], and Rupert Wimmer[1][0000-0002-7023-6209]

[1] University of Natural Resources and Life Sciences, Vienna, Austria
[2] The University of British Columbia, Vancouver, BC, Canada
lena.leiter@boku.ac.at

Abstract. Triboelectricity, a largely overlooked phenomenon in woodworking, holds significant potential to transform sanding processes by improving efficiency and reducing health hazards. This study investigates the triboelectrification phenomena occurring during wood sanding, with a focus on the charges of freshly sanded surfaces and dust particles. Our findings reveal that grit size was the most influential factor, with larger grit sizes reducing surface charges, followed by feed speed and sandpaper speed. Higher feed speeds increased surface charges but also correlated with greater material removal rates. By optimizing these parameters, it is possible to control triboelectric charges, improving the safety and efficiency of the sanding process. Additionally, we found that wood dust produced during sanding carries either positive or negative charges depending on the type of sandpaper used. This discovery suggests opportunities to enhance wood dust management and reduce fine dust generation by exploiting triboelectric effects. This research underscores the potential of harnessing triboelectric effects to advance industrial woodworking practices. Future studies could focus on developing practical applications to minimize fine dust and enhance dust collection systems, contributing to safer and more sustainable woodworking environments.

Keywords: Triboelectrification, contact electrification, wood dust, wood dust

1 Introduction

Sanding is a fundamental operation in the wood industry, essential for producing smooth surfaces, achieving precise dimensions, and enhancing finish quality. However, it generates wood particles as by-products, ranging from sawdust to fine dust. Efficient dust collection is critical for workplace safety, machining efficiency, and surface quality. Ineffective dust management poses significant challenges: (1) Fine particles generated during sanding interfere with cutting edges, causing double cutting, increased tool wear, and diminished surface quality [1]. (2) Accumulated dust contributes to higher cleaning and maintenance costs [1]. (3) Fine dust exacerbates respiratory and environmental hazards, particularly with modern machining speeds and finer surface requirements. Traditional dust management strategies rely on suction systems and filters, but these often fail to address the unique behavior of fine, airborne particles.

One overlooked factor influencing wood dust behavior is triboelectricity – the phenomenon of material surfaces acquiring charge through frictional contact and separation [2] [3]. Insulating materials, such as wood, are particularly prone to triboelectric charging during machining, where friction between sandpaper and wood generates electric charges on both the particles and the machined surface [4] [5]. These charges create repulsive or adhesive forces, which lead to the formation of dust clouds and hinder effective dust collection [6]. Research in other fields has demonstrated the utility of triboelectric effects for applications such as material separation [7], [8] and energy generation [9], [10], but their implications for woodworking processes remain largely unexplored.

Triboelectricity plays a significant role in fine dust generation, adhesion, and dispersion. Studies reveal that smaller particles tend to acquire negative charges due to the trapping of electrons in high-energy states [11]. Additionally, triboelectrification in granular systems shows that charge transfer occurs from larger to smaller particles [12], further influencing dust behavior. By understanding these mechanisms, it may be possible to optimize sanding processes, reduce fine dust generation, and enhance dust collection efficiency.

1.1 Knowledge Gap and Study Objectives

While other industries have leveraged triboelectric phenomena, the woodworking sector has yet to explore its implications. Key questions remain unanswered: How do machining parameters such as sandpaper grit size, feed speed, and sanding speed influence triboelectric charges? How do different abrasive materials and binding agents affect the polarity and magnitude of these charges?

Addressing these questions could lead to advancements in sanding optimization, fine dust reduction, and innovative dust management solutions. This study aims to bridge this gap by:

1. Investigating the triboelectric charges of wood dust and freshly sanded surfaces under various machining conditions.
2. Analyzing the impact of key machining parameters, including sandpaper grit size, feed speed, and sanding speed, on triboelectric charges.
3. Evaluating the effects of different binding agents on the polarity and magnitude of triboelectric charges.

2 Materials and Methods

2.1 Materials

Rough flat-sawn boards of European beech (*Fagus sylvatica L.*) were used as the primary material in this study. On one hand, five samples were prepared, each with a radial thickness of 5.5 cm, a tangential width of 9 cm, and a length of 60 cm for surface charging experiments. On the other hand, ten samples with a radial width of 12 cm and a length of 12, having a tangential thickness of 2.5 cm were prepared for dust charging experiments. All samples were knot-free to ensure uniformity and consistency in the experimental results. Before testing, the samples were stored in a conditioning room at a controlled temperature of 20°C and 65% relative humidity until they reached equilibrium moisture content. This conditioning process ensured the stability and comparability of the material properties across all experiments.

Abrasive materials used in this study included aluminum oxide sandpaper (CS 311 Y ACT abrasive belt, Klingspor, Stoney Creek, Canada) in grit sizes P180, P120, and P80. These grits were selected to represent a range of surface finishes, from fine to coarse, commonly used in woodworking applications. The first five samples were processed using this sandpaper, while the next ten samples were sanded using sandpapers with varying binding agents to evaluate their impact on triboelectric charges, including corundum, zircon, garnet, brilliant, and ruby (STF D150 P120 sanding disc, Festool, Wendlingen a. N., Germany). These materials were chosen as producers claim them to be antistatic and have better performances in at least one of the following categories: binding strength, durability, flexibility, heat resistance, clogging and stress resistance.

2.2 Experimental Setup

The triboelectric charges generated during the sanding process were measured using a setup designed to measure electric field strength in kV/m, based on the well-established Faraday cup principle [13]. The system incorporates a Faraday cage to isolate and measure the charges with high precision. An electrostatic fieldmeter (EFM 115, Kleinwächter®, Germany) was attached to a detection device to measure the electric field strength generated during the sanding process.

For surface charge measurements, the ConSurChaD device, introduced by Leiter et al. [14], was used. This device is specifically designed to quantify triboelectric surface charges on materials and provides accurate readings during the sanding process. To measure the dust charges generated during sanding, a device introduced by Myna et al. [4] was used to collect and quantify the charges on the fine wood dust particles.

Surface charge measurements were conducted on surfaces immediately following their surfacing with an edge sander (LZK 3-NCV, Langzauner, Lambrechten, Austria) equipped with a flat pressure shoe, which created a 30 mm wide contact zone. Dust charging measurements involved the use of a handheld random orbital sander (ETS 150/3 EQ, Festool, Wendlingen a. N., Germany) where sanding conditions (pressure and moving speed) were kept as constant as possible for a duration of 3 minutes.

2.3 Experimental Design and Data Analysis

To assess the effect of sanding conditions on the triboelectric surface charges, the following parameters were investigated: (1) three distinct sanding speed levels – 4.4 m/s, 8.8 m/s, and 13.2 m/s. (2) three feed speeds – 3.4 m/min, 6.8 m/min, and 10.2 m/min. And (3) three sandpaper grit sizes: P180, P120, and P80. A full factorial design was used resulting in 27 sanding conditions, which were investigated on five wood samples with 10 repetitions each.

The effect of different binding agents was investigated using five different agents: corundum, zircon, garnet, brilliant, and ruby. Each 10 samples were investigated with four repetitions.

Descriptive statistics were calculated for all conditions and the results were visualised using box plots. Levene's test was used to test for equality of variance prior to analysis of variance (ANOVA). Multiple comparisons of means were performed using Tukey's HSD post hoc test.

3 Results and Discussion

This study confirmed that sanding generates significant triboelectric charges on both wood dust particles and freshly sanded surfaces. Across all tested conditions, the polarity of particles remained consistent, while charge magnitude varied with particle size and machining parameters. Smaller particles exhibited stronger negative charges, likely due to electron trapping in high-energy states, a phenomenon supported by previous research [11]. The positive charges observed on freshly sanded surfaces suggest electron transfer predominantly occurs from the wood to the sandpaper.

These results align with triboelectric behavior in other granular systems, where larger particles tend to donate electrons to smaller particles [12]. The polarity and magnitude of triboelectric charges are critical factors influencing dust dispersion, as the repulsive forces between similarly charged particles contribute to airborne dust formation, complicating collection efforts [6].

3.1 Effects of Machining Parameters

The effects of machining parameters – including grit size, feed speed, and sanding belt speed – on triboelectric field strength is presented in Fig. 1. Grit size emerged as a primary determinant of triboelectric output, with finer grits generating stronger fields.

Finer grits (e.g., P180, cutting depth: 0.033 mm) produced significantly higher triboelectric field strengths compared to coarser grits (e.g., P80, cutting depth: 0.12 mm). For example, P180-grit produced a field strength of 5.06 ± 0.96 kV/m at a feed speed of 3.4 m/min and sanding belt speed of 4.4 m/s, while P80-grit generated 1.36 ± 0.29 kV/m under the same conditions. This trend likely arises from increased surface contact and finer abrasion dynamics associated with finer grits [15]. However, stronger triboelectric fields exacerbate dust dispersion, complicating dust collection [16].

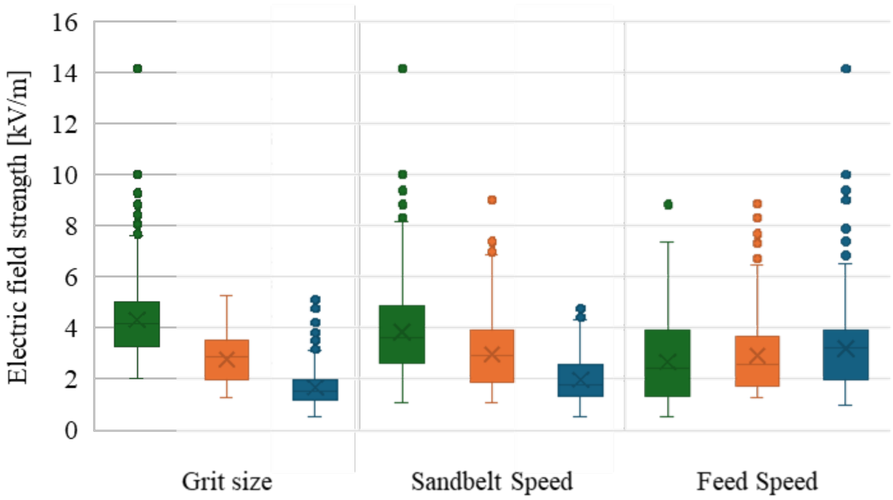

Fig. 1: Influence of machining parameters, including grit size (P180, P120, P80), sanding belt speed (4.4 m/s, 8.8 m/s, 13.2 m/s), and feed speed (3.4 m/min, 6.8 m/min, 10.2 m/min) on triboelectric field strength (n=50).

Higher sanding belt speeds diminished triboelectric field strength for finer grits. For instance, P180-grit at a feed speed of 3.4 m/min showed a decline in field strength from 5.56 ± 0.98 kV/m at 4.4 m/s to 2.62 ± 0.54 kV/m at 13.2 m/s. In contrast, coarser grits like P80 exhibited smaller variations with belt speed, suggesting that grit size modulates the relationship between belt speed and charge generation. High-speed sanding is therefore on one hand improving machining efficiency [17] but on the other hand worsening dust dispersion due to stronger repulsive forces between charged particles.

Lower feed speeds consistently resulted in higher triboelectric field strengths across all grit sizes. For example, with P180-grit at a sanding belt speed of 4.4 m/s, the field strength declined from 5.56 ± 0.98 kV/m at 3.4 m/min to 3.62 ± 0.48 kV/m at 10.2 m/min. This effect was most pronounced for finer grits, while coarser grits produced lower field strengths across all feed speeds. This may mitigate dust dispersion but could compromise surface quality.

Statistical analysis (Table 1) confirmed significant differences ($p < 0.05$) across parameter combinations. These findings highlight the interplay between machining parameters, suggesting that optimizing grit size and feed speed can minimize triboelectric charges to improve dust management.

Table 1. Statistical analysis of triboelectric field strength [kV/m] as a function of feed speed, sanding belt speed, and grit size. Results indicate significant differences ($p < 0.05$) across parameter combinations, expressed as homogenous subsets.

Feed speed	Sand belt speed	Sanding progam P180-grit 0.033 mm		Sanding progam P120-grit 0.067 mm		Sanding progam P80-grit 0.12 mm	
3.4 m/min	4.4 m/s	5.56 (0.96)	z	3.71 (0.39)	tuv	1.36 (0.29)	cdef
	8.8 m/s	4.27 (0.36)	wx	2.75 (0.49)	lmn	1.28 (0.2)	bcde
	13.2 m/s	2.62 (0.54)	jklm	1.79 (0.55)	fgh	0.66 (0.13)	a
6.8 m/min	4.4 m/s	6.07 (1.26)	z	3.36 (0.37)	prst	2.09 (0.64)	ghij
	8.8 m/s	4.08 (0.52)	vw	2.46 (0.33)	jkl	1.66 (0.32)	defg
	13.2 m/s	3.11 (0.6)	nopqrs	1. 71 (0.31)	efg	1.72 (0.56)	efg
10.2 m/min	4.4 m/s	5.65 (1.79)	z	3.86 (0.52)	uvw	3.05 (0.7)	mnopqr s
	8.8 m/s	4.59 (1.38)	xy	3.47 (0.25)	stu	2.06 (0.58)	ghij
	13.2 m/s	3.06 (0.68)	nopqrs	1.82 (0.44)	ghi	1.22 (0.25)	bc

3.2 Influence of Bonding Agent

The bonding agent significantly influenced both polarity and magnitude of triboelectric field strength, as shown in Fig. 2. Resin-based bonding agents produced stronger negative charges, particularly on smaller particles, compared to synthetic adhesives. Corundum displayed the lowest mean field strength (-14.53 ± 2.56 kV/m), while Ruby generated the only positive charges, with a mean field strength of +8.95 ± 4.92 kV/m. Other agents, such as Zircon and Brilliant, exhibited intermediate negative charges (-2.12 ± 1.22 kV/m and -4.53 ± 1.78 kV/m, respectively).

Ruby's distinct positive polarity was accompanied by high variability, as evidenced by larger error bars and a standard deviation of 4.92 kV/m, compared to other agents like Corundum (2.56 kV/m) and Garnet (2.51 kV/m). This variability likely stems from inconsistencies in material surface properties or bonding quality.

Statistical analysis revealed significant differences ($F = 40.712$, $p < 0.001$), with material type explaining 91.6% of the variability ($R^2 = 0.916$). Distinct groupings were observed: Corundum and Garnet formed one subset, while Zircon and Brilliant formed another. Ruby remained statistically distinct, emphasizing its unique behavior.

Selecting bonding agents tailored to specific triboelectric properties can influence dust management strategies [18]. For instance, using Ruby may enhance electrostatic dust collection due to its positive polarity, while Corundum's consistent negative charges may promote dust adhesion. These findings could guide the design of electrostatic dust collection systems or inform the selection of sandpapers for specific applications.

Fig. 2: Influence of bonding agents on triboelectric field strength for Corundum, Zircon, Garnet, Brilliant, and Ruby (n=40).

3.3 Conclusion

This study provides an investigation into the triboelectric charging behavior of wood dust and freshly sanded surfaces, revealing how machining parameters such as sandpaper grit size, feed speed, and sanding speed influence charge magnitudes and polarity. We found that finer sandpaper grits generate smaller, highly charged particles due to enhanced electron trapping on smaller surface areas, with feed speed and sanding speed enhancing the variability of these charges. Furthermore, the role of bonding agents, including Corundum, Ruby, and Zircon, was analyzed, demonstrating their contributions to triboelectric interactions. These findings address a critical gap in the literature, offering new insights into the fundamental mechanisms behind triboelectric charging during sanding operations.

References

1. U. Heisel, “Auslegung von Absaughauben bezüglich der Späneerfassung durch Simulationsrechnung,” Stuttgart, Abschlussbericht, 2002. [Online]. Available: https://elib.uni-stuttgart.de/bitstream/11682/4024/1/Abschlussbericht_Dressler.pdf
2. Y. Murata, T. Hodoshima, and S. Kittaka, “Evidence for Electron Transfer as the Mechanism of Contact Charging of Polyethylene with Metals,” Japanese Journal of Applied Physics, vol. 18, no. 12, p. 2215, Dec. 1979, doi: 10.1143/JJAP.18.2215.

3. W. R. Harper, “The Volta effect as a cause of static electrification,” Proceedings of the Royal Society of London. Series A. Mathematical and Physical Sciences, vol. 205, no. 1080, pp. 83–103, Jan. 1951, doi: 10.1098/rspa.1951.0019.
4. R. Myna, R. Wimmer, F. Liebner, L. M. Leiter, and S. Frömel-Frybort, “Triboelectric charging of dust particles during hand-held circular sawing of wood and wood-based materials,” WOOD MATERIAL SCIENCE & ENGINEERING, vol. 16, no. 1, pp. 64–73, Jan. 2021, doi: 10.1080/17480272.2020.1830850.
5. L. M. Leiter, R. Myna, S. Frömel-Frybort, F. Liebner, and R. Wimmer, “Triboelectric surface field strength of wood after brushing,” Wood Science and Technology, vol. 56, pp. 1401–1417, 2022, doi: 10.1007/s00226-022-01411-z.
6. K. Lauer, “Untersuchung des Einflusses der elektrostatischen Aufladung von Stäuben auf die Neigung dieser Stäube zur Staubwolkenbildung,” Fachhochschule Mannheim, 2003.
7. J. He et al., “Recent advances in the intensification of triboelectric separation and its application in resource recovery: A review,” Chemical Engineering and Processing - Process Intensification, vol. 185, p. 109308, Mar. 2023, doi: 10.1016/j.cep.2023.109308.
8. J. Li and L. Dascalescu, “Newly-patented technical solutions for improving the triboelectrostatic Separation of mixed granulär solids,” Recent Pat. Eng., vol. 6, no. 2, pp. 104–115.
9. J. Bang, I. K. Moon, Y. P. Jeon, B. Ki, and J. Oh, “Fully wood-based green triboelectric nanogenerators,” Applied Surface Science, vol. 567, p. 150806, Nov. 2021, doi: 10.1016/j.apsusc.2021.150806.
10. D. W. Kim, J. H. Lee, J. K. Kim, and U. Jeong, “Material aspects of triboelectric energy generation and sensors,” NPG Asia Materials, vol. 12, no. 1, p. 6, Jan. 2020, doi: 10.1038/s41427-019-0176-0.
11. D. J. Lacks and A. Levandovsky, “Effect of particle size distribution on the polarity of triboelectric charging in granular insulator systems,” Journal of Electrostatics, vol. 65, no. 2, pp. 107–112, Feb. 2007, doi: 10.1016/j.elstat.2006.07.010.
12. N. Duff and D. J. Lacks, “Particle dynamics simulations of triboelectric charging in granular insulator systems,” Journal of Electrostatics, vol. 66, no. 1, pp. 51–57, Jan. 2008, doi: 10.1016/j.elstat.2007.08.005.
13. Q. Chen, B. Cheng, T. Wang, H. Shang, and T. Shao, “Method for the measurement of triboelectric charge transfer at solid–liquid interface,” Friction, vol. 11, no. 8, pp. 1544–1556, Aug. 2023, doi: 10.1007/s40544-022-0740-z.
14. L. M. Leiter, R. Myna, J. Dömény, and R. Wimmer, “Development of a Continuous Wood Surface Charge Detection Device,” Wood Fiber Sci., vol. 56, pp. 173–180, 2024.
15. B. S. Linke, “A review on properties of abrasive grits and grit selection,” International Journal of Abrasive Technology, vol. 7, no. 1, pp. 46–58, Jan. 2015, doi: 10.1504/IJAT.2015.070582.
16. J. Hou, G. Hu, J. R. Grace, and X. Bi, “Experimental study of electrostatic charging related to prevention of fire and dust explosions in wood processing facilities,” Journal of Electrostatics, vol. 132, p. 103983, Dec. 2024, doi: 10.1016/j.elstat.2024.103983.
17. M. Sydor, R. Mirski, K. Stuper-Szablewska, and T. Rogoziński, “Efficiency of Machine Sanding of Wood,” Applied Sciences, vol. 11, no. 6, 2021, doi: 10.3390/app11062860.
18. R. Myna, et al., “Werkzeug zur spanenden Bearbeitung von Werkstoffen (Tool for machining of materials)” EP 3 881 958 A1, 2021

Embedded sensors in wood cutting tools State of Art and future developments

S. Meddour[1], B. Garnier[2], P. Beer[3] and M.A. Djouadi[1]

[1] Institut des Matériaux Jean Rouxel IMN UMR 6502, Université de Nantes, 2 rue de La Houssinière
BP 32229, CEDEX, 44322 Nantes, France.
[2] Laboratoire de Thermique et Energie de Nantes (LTN – UMR 6607) La Chantrerie, rue Christian Pauc, 44306 Nantes.
[3] Warsaw Agricultural University (SGGW), Rakowiecka 26/30, 02 528 Warszawa, Poland.

Abstract. There is a real need for extending the service life of tools, increase their surface quality, lower the energy consumption and decrease the cutting time in several wood cutting industry as it has been done in metal cutting one. One of the method taking over the market, for tools metals processing, is to cover the cutting edges with hard anti-abrasive coatings such as TiN, Ti(C,N), ZrN, (Ti,Zr)N, TiAlN, CrN, CrAlN and of course diamond films.
Since twenty or even thirty years one has tried to apply pretreatments, post treatment and thin films on tools for wood cutting industry. The first example was study that had examined whether the peeling process can be improved by modifying the surface of the cutting tools. The modi®cation of the clearance and rake surfaces of the tools consisted of covering them with TiN, (Ti,Zr)N or CrN anti-abrasive coatings. Such study have shown that the well-adherent anti-abrasive CrN coatings increase the service life of the cutting tools. Morover, Such CrN coatings were also deposited onto carbide tools and tested in wood machining. Machining tests were performed up to 5 and 10 km of cutting distance with industrial routers on Oriented Strand Board. Tool wear and service life were compared between the uncoated and coated tools. First, it has been observed that the edge wear is very high, just at the beginning of the routing process. The best result was shown by a carbide tool CrN coated on both faces; the service life of this tool is four times higher than the one of an uncoated tool. Nevertheless, testing all treatments and coatings emerging nowadays and mainly at an industrial scale appears complicated or even impossible. Moreover, the cutting conditions are not stable and reproducible from one trial to another. So, the rising idea is to embedded some temperature, thermal flux, wear sensors in wood cutting tools in order to accelerate such trials and made them more reproducible. The aim of our presentation is to give a State of Art on such embedded sensors for both metal and wood cutting application and highlight some trials and attempts.

Keywords: metal and wood cutting applications, cutting edge protection, hard coatings, thin films, embedded sensors, toward adaptive cutting process, …

Analysis of Tool-Workpiece Interaction in Peripheral Planing of Douglas Fir Using Jointed Hydro-Clamped Tools

Christian Kortüm

Technische Hochschule Rosenheim, Hochschulstraße 1, 83024 Rosenheim, Germany
christian.kortuem@th-rosenheim.de

Abstract. The interaction between tool and workpiece plays a pivotal role in determining cutting performance and surface quality in woodworking processes. This study investigates the peripheral planing of Douglas fir with a focus on constant chip removal conditions. Hydro-clamped tools were utilized to assess the impact of joint land geometry on cutting performance. Key performance metrics, including cutting force, tool wear, and tool life, were evaluated under varying cutting conditions. The research involved wear and durability tests, providing insights into tool longevity when planing a softwood species known for its heterogeneity. Additionally, surface quality was systematically analyzed to determine the influence of cutting parameters on the resulting finish. Special attention was given to the role of the joint land in maintaining consistent cutting forces and minimizing vibrations, which are critical for achieving high surface quality and extended tool life. The experimental results reveal that hydro-clamping contributes significantly to the stability of the cutting process, ensuring optimal alignment and consistent performance. The wear patterns observed highlight the importance of maintaining a sharp cutting edge, with clear correlations between tool wear, cutting power, and surface smoothness. These findings provide valuable guidelines for industrial applications, where maximizing tool life and maintaining product quality are essential. This study contributes to a deeper understanding of tool-workpiece dynamics in woodworking, offering practical recommendations for improving efficiency in peripheral planing operations.

Keywords: cutting performance, surface quality, jointed hydro-clamped tools

1 Introduction

In peripheral planing of high quality surfaces - or in high-speed planing at high feed rates - it is essential that each cutting edge of the tool leaves its mark on the workpiece. This requirement ensures that the entire cutting interface actively contributes to the final surface quality. Consequently, the accuracy of the tool runout is critical, as it is directly influenced by tool mark depth (t).

For example, to achieve a high quality surface finish according to VDI 3414 Part 3, with a feed per tooth (f_z) of 0.2 mm, the tool mark depth (t) must be as low as 0.06 µm when using a 160 mm diameter tool (see Equation 1) [1]. This stringent parameter underlines the importance of maintaining precise rotational accuracy to ensure that all cutting edges work effectively together.

$$t = \frac{{f_z}^2}{4D} = \frac{(0{,}2\ mm)^2}{4*160\ mm} = 6{,}25 * 10^{-5} mm = 0{,}0625\ \mu m \quad (1)$$

However, achieving this level of runout accuracy is not possible solely due to the manufacturing tolerances of the tool and the inherent play required during tool assembly. To overcome these limitations, hydro-clamped tools are used to compensate for assembly play. In addition, a joint mechanism is incorporated to grind the tool at operating speed within the machine, ensuring that the joint land - as well as the other cutting edges - remains effective and accurately aligned during the cutting process (see Figure 1) [2].

Fig. 1. Jointing mechanism and resulting joint land geometry of Weinig planers and tools [3]

Although jointed hydro-clamped tools are a standard feature in planing operations, there is a notable lack of scientific investigation into its role and interaction with the workpiece. This papers aims to fill this gap by investigating the behaviour of the joint land during peripheral planing of Douglas fir. By examining how the joint land interacts with the workpiece, the study aims to provide a deeper insight into its influence on cutting performance, tool wear and surface quality. Ultimately, this research will contribute to a better understanding of the complex dynamics involved in tool-workpiece interactions and support the optimisation of machining processes in the wood industry.

2 Materials and Methods

For the experiments, milling tests were carried out on Douglas fir under constant and realistic cutting conditions achieved by pre-milling the workpiece with a special pre-milling tool. The tests were carried out on a planing machine (Weinig Powermat 3000) equipped with seven milling spindles, including two upper milling spindles. The process investigated in this study was carried out on the second upper milling spindle using a hydro-clamped tool with HSS cutting knifes. Details of the process parameters and the resulting parameters are shown in Table 1.

Prior to milling, the tool was ground and its concentricity measured on a grinding machine (Weinig Rondamt 960) and, once mounted on the planer, with a dial gauge (Mahr Millimess 2001W). The tool, in particular the cutting edges, was examined with a microscope (Alicona G4) after grinding and both before and after the jointing process. During milling, the cutting performance was monitored using a power meter (Zimmer LGM 450). Finally, the resulting surface quality was evaluated according to VDI 3414 [1, 4, 5].

Table 1. Process parameters and resulting parameters

Parameter	Equation	Value
n_{tool}		6000 1/min
D_{tool}		162.36 mm
z_{tool}		6
α		28 °
β		37 °
γ		25 °
v_f		14.4 m/min
a_e		1 mm
f_z	$f_z = \frac{v_f}{z * n}$ (2)	0.4 mm
t	$t = \frac{f_z^2}{4D}$ (1)	0.246 µm
φ_e	$\varphi_e = \cos^{-1}\left(1 - \frac{2a_e}{D}\right)$ (3)	9.0 °
h_m	$h_m = f_z * \sin\frac{\varphi_e}{2}$ (4)	31.39 µm
l_c	$l_c = D * \pi * \frac{\varphi_e}{360°}$ (5)	12.75 mm

3 Results

3.1 Sharpening and Setting Up the Tool

At the start of the investigations, the tool was manually ground on a Weinig Rondamat 960 grinding machine. The concentricity was measured with the tool clamped on the spindle of the grinder (see Figure 2, left). The results show a run-out accuracy of 0.029 mm. However, measuring with the high precision dial gauge, which has a repeatability of 0.1 µm, is challenging because of the elastic behaviour of all elements that has to be taken into account.

The tool diameter D was then measured using the Weinig OptiControl tool measuring system, which confirmed that the run-out inaccuracy was in this range. After mounting the tool on the milling spindle, the concentricity was measured again and showed a deviation of approximately 0.021 mm. After sharpening the tool, the cutting edges were precisely measured using a microscope (Alicona G4), and then measured again after the initial jointing with 2 passes. The infeed of the joint stone is 16 µm per operation (see Figure 2, right).

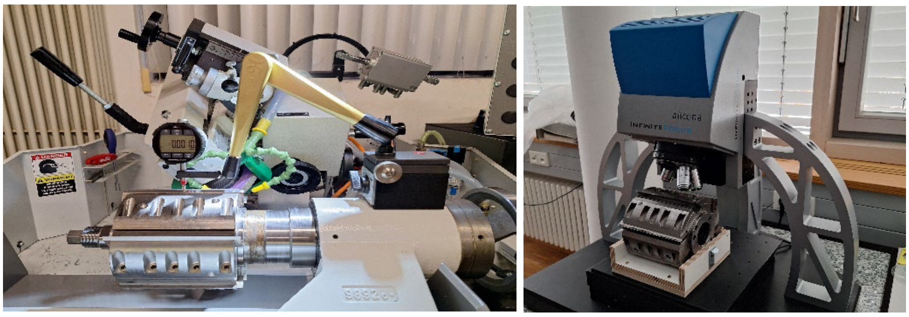

Fig. 2. Measurement of concentricity (left) and cutting edge geometry (right)

The results of the cutting edge measurements are presented in Figure 3. In addition to the geometric contouring, the mean cutting edge radius r and the joint land were evaluated using the defined parameter supporting chamfers length bα [6].

Edge 1	Edge 2	Edge 3	Edge 4	Edge 5	Edge 6
Cutting edges after grinding of the cutter head					
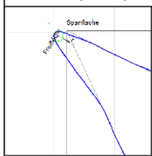	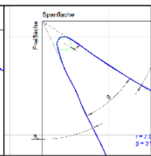	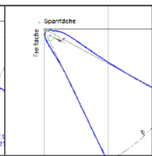	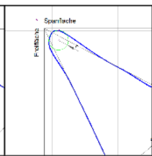	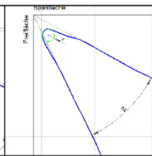	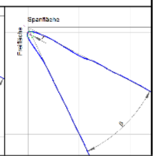
r = 4.0 µm	r = 7.0 µm	r = 4.2 µm	r = 7.5 µm	r = 5,8 µm	r = 3,3 µm
Cutting edges after 1. jointing (2 passes) of the cutter head in the planing machine					
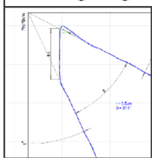	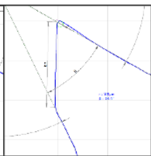	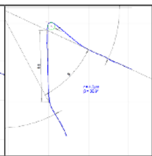	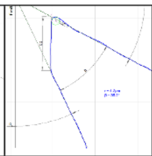		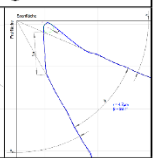
r = 3.5 µm	r = 3.0 µm	r = 4.6 *µm*	r = 4.7 µm	r = 3.3 µm	r = 4.7 µm
bα = 53.1 µm	bα = 87.2 µm	bα = 90.3 µm	bα = 64.3 µm	bα = 97.5 µm	bα = 45.8 µm

Fig. 3. Results of the measurements of the Cutting edges after grinding and initial jointing

The results in Figure 3 show on the one hand that jointing results in a more uniform cutting edge radius across all edges and a smaller average radius. This results in extremely sharp cutting edges. On the other hand, the significant difference in the width of the joint land indicates that run-out inaccuracies are effectively compensated for. It is also understandable that the width of the joint land is relatively larger for cutting edges 2, 3 and 5, as these edges are the furthest from the center according to the run-out measurements. Looking at the joint land on an ideal cutting edge with the parameters in Table 1, the distance between the narrowest and widest joint land is 0.037 mm and is therefore greater than the measured concentricity (Figure 4).

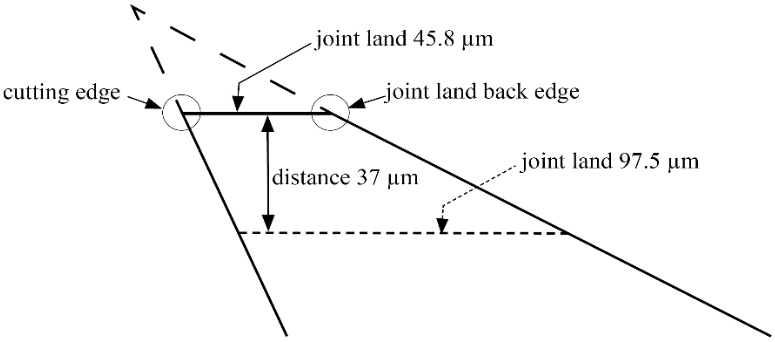

Fig. 4. Joint lands on an ideal cutting edge

3.2 Milling tests and tool wear

At the start of the milling tests on Douglas fir, it was observed that all the cutting edges were marking the surface, resulting in a visible feed per tooth of f_z = 0.4 mm. The surface quality was still very good after the first cut and a tactile inspection revealed no detectable marks - the surface felt exceptionally smooth. However, as the feed distance increased, so did the surface roughness.

Edge 1	Edge 2	Edge 3	Edge 4	Edge 5	Edge 6
Cutting edges after 377 m feed path before 2. jointing					
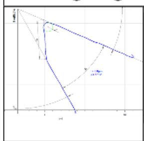	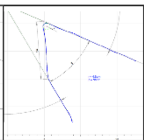		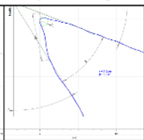	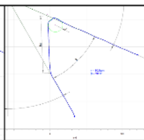	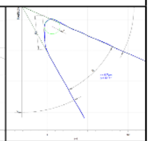
r = 5.8 µm	r = 4.8 µm	r = 7.8 µm	r = 5.5 µm	r = 10 µm	r = 9.7 µm
bα = 57.7 µm	bα = 83.7 µm	bα = 88.3 µm	bα = 66 µm	bα = 84 µm	bα = 44.1 µm
Cutting edges after 2. jointing (2 passes) of the cutter head in the planing machine					
	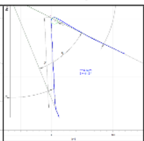	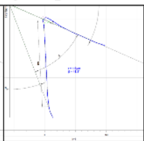	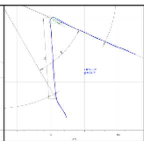	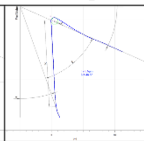	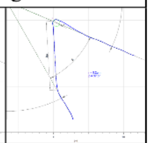
r = 5.6 µm	r = 5.6 µm	r = 4.6 *µm*	r = 5 µm	r = 5 µm	r = 5.2 µm
bα = 120 µm	bα = 154 µm	bα = 149 µm	bα = 127 µm	bα = 144 µm	bα = 104 µm

Fig. 5. Results of the measurements of the Cutting edges after 377 m feed path

This increase in roughness was due to two main factors: firstly, markings in the feed direction, which appeared as notches on the cutting edges, and secondly, the inherent roughness resulting from the differences between earlywood and latewood. This effect is well known, particularly when there is an increase in edge rounding combined with the variable density and modulus of elasticity also found in Douglas fir [7, 8].

After a feed path of 377 m, giving a total cutting distance of 2002.8 m per cutting edge, the surface quality required sharpening, so the tool was measured, jointed for the second time - again with 2 passes with a 16 µm infeed of the regrinding stone - and measured again (Figure 5). After a feed path of 700 m the surface quality required the 3 jointing auf the cutter head (with 2 passes). The results of this measurement are presented in Figure 6.

Edge 1	Edge 2	Edge 3	Edge 4	Edge 5	Edge 6
Cutting edges after 377 m feed path before 2. jointing					
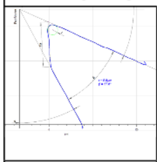		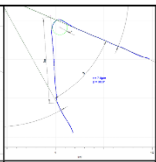	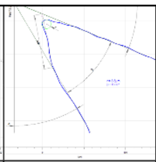		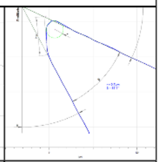
r = 5.8 µm	r = 4.8 µm	r = 7.8 µm	r = 5.5 µm	r = 10 µm	r = 9.7 µm
bα = 57.7 µm	bα = 83.7 µm	bα = 88.3 µm	bα = 66 µm	bα = 84 µm	bα = 44.1 µm
Cutting edges after 2. jointing (2 passes) of the cutter head in the planing machine					
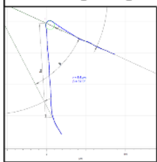	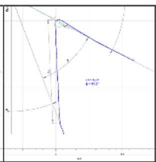	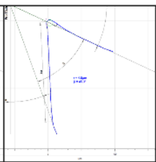	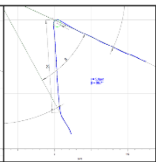	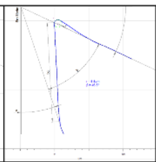	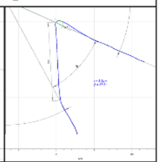
r = 5.6 µm	r = 5.6 µm	r = 4.6 *µm*	r = 5 µm	r = 5 µm	r = 5.2 µm
bα = 120 µm	bα = 154 µm	bα = 149 µm	bα = 127 µm	bα = 144 µm	bα = 104 µm

Fig. 6. Results of the measurements of the Cutting edges after 700 m feed path

Finally, the tests were continued until a total feed path of 1000 m was reached. During this time, the tool was joined several more times, giving a total of 20 jointing operations, each with a jointing stone infeed of 16 µm. In theory, this should have reduced the tool radius by 0.32 mm. However, the tool measurements showed a tool diameter of 161.74 mm, which means that the measured difference from the initial value in terms of radius is 0.31 mm.

4 Discussion

Starting with the final aspect of the results regarding the theoretical and actual diameter differences, it was demonstrated that, given the process parameters and the interaction between HSS as the cutting material and Douglas fir as the workpiece, there is virtually no difference between the calculated and measured diameters. However, this correlation cannot be generalized and must be further investigated for other cutting materials and workpiece types. Regarding the tool wear behavior, the measurement results indicate that even slight increases in the cutting edge radius lead to a significant deterioration in surface quality. Figures 5 and 6 show that once the maximum rounding reaches 10 to 12 µm, tool life is effectively exhausted – this is particularly critical given the high demands on surface quality.

Considering the cutting edge rounding as an isolated parameter is not meaningful, especially for jointed tools. Instead, the interaction between edge rounding and the joint land must always be taken into account, starting with the influence of the joint land itself. Literature on jointing consistently emphasizes that the joint land must not be too wide, as excessive width can lead to excessive compressive forces [2]. This effect can be analyzed geometrically by interpreting the trailing edge of the joint land as an additional cutting edge and calculating the corresponding chip thickness. This calculated chip thickness represents the extent to which the material is compressed since this edge does not contribute to actual chip formation: Equation 6 (based on Equation 2) calculates the feed per tooth between the cutting edge and the back edge for a joint land (see Figure 4) width of 400 µm, which was reached at the end of the experiments:

$$f_{z\,back\,edge} = \frac{vf}{\frac{D*\pi}{w_{joint\,land}}*n} = \frac{14400\frac{m}{min}*1000\frac{\mu m}{mm}}{\frac{161.74\,mm*\pi}{0.4\,mm}*6000\frac{1}{min}} = 1.89\,\mu m \tag{6}$$

With the calculated feed per tooth for the back edge, the average chip thickness is - according to Equation 4: $h_{m\,back\,edge} = 0.148$ µm. This represents the way in which the back edge of the joint land is pressed into the workpiece in average. This is a very small value which, in combination with a cutting edge radius of 5 µm, has still resulted in a very good surface quality in recent tests.

Nevertheless, a low cutting edge rounding in combination with a joint land leads more quickly to a deterioration in the surface quality, which only occurs with higher cutting edge rounding without a joint land from other tests (for example in [7,8]). Further and comprehensive investigations must also be carried out in this regard.

5 Outlook

The investigations presented show that the geometric analysis of the cutting edges using the chosen methodology works very well and gives accurate results. However, the power measurement in these experiments did not provide conclusive results. To overcome this limitation, future studies will include an extension of the measurement technology. In particular, the interaction between the cutting edge radius and the joint face requires further investigation. In addition to milling experiments, a simulation model should be developed to analyse this interaction in more detail. Further series of experiments will contribute to a deeper understanding of the jointing process for woodworking tools.

References

1. VDI 3414-3:2019-08: Quality evaluation of wood and wood-based surfaces – Milled, sawn, planed, drilled, and turned surfaces.
2. Englert, H., Dawidziak, A.: Verfahren zum Jointen der Schneide wenigstens eines Schneidmessers eines rotierenden Werkzeuges, European Patent, EP1231021A2 (2002).
3. MICHAEL WEINIG AG: Alles über Werkzeuge, https://m.weinig.com/fileadmin/assets/migrated_zu_verschieben/pdfs_docs/Alles_ueber_Werkzeug_Screen_05.pdf, last accessed 2025/02/13.
4. VDI 3414-1:2019-02: Quality evaluation of wood and wood-based surfaces – Surface characteristics.
5. VDI 3414-2:2019-02: Quality evaluation of wood and wood-based surfaces – Testing and measuring methods.
6. DIN 6581:1985-10: Begriffe der Zerspantechnik; Bezugssysteme und Winkel am Schneidteil des Werkzeuges.
7. Riegel, A., Westkämper, E., Kisselbach, A.: Gefügeschädigungen als Standzeitkriterium? Teil 1, Holzbau-Magazin Architektur & Holz 32(10):47-49 (1997)
8. Riegel, A., Westkämper, E., Kisselbach, A., Schadoffsky, O.: Gefügeschädigungen als Standzeitkriterium. Beschichten nach dem Fräsen und Schleifen (Teil 3), HK 32(11):80-82 (1997).

Thermally Modified Wood (TMW) with TermoVuoto Method

Alessio Lucarelli [1] and Umberto Pagnozzi [1]

[1] WDE Maspell Srl, Italy

alessio.lucarelli@wde-maspell.it

Abstract. Thermal modification of wood is a well-established process aimed at enhancing its dimensional stability, biological durability, and resistance to environmental factors without the use of chemical preservatives. Among various thermal modification technologies, the vacuum-based TermoVuoto method has gained prominence due to its high energy efficiency and controlled process conditions, which minimize oxidative degradation.
The TermoVuoto process is conducted in a system under vacuum, which significantly reduces energy dispersion, lowers the thermal stress on the wood structure, and results in a homogeneous modification of its chemical composition. Unlike conventional thermal treatments, this method ensures the safe collection and disposal of process emissions as non-hazardous industrial waste. Furthermore, the volatile organic compound (VOC) emissions of TermoVuoto-modified wood are comparable to those of untreated wood, making it particularly suitable for indoor applications.
This paper presents a comprehensive analysis of the TermoVuoto process, its impact on wood properties, and its diverse applications, highlighting its role in sustainable material engineering and the potential for expanding its industrial adoption.

Keywords: Thermal Modification, Vacuum Technology, Hygroscopicity, Wood Stability, Sustainability, Indoor Air Quality.

1 Introduction

Wood is an essential material in various industrial applications, but its inherent hygroscopicity and susceptibility to biodegradation limit its long-term performance. Thermal modification is a well-established technique to enhance wood’s dimensional stability and biological durability without the use of chemical treatments. Traditional thermal modification processes operate under atmospheric pressure and require prolonged high-temperature exposure, which can lead to uneven heating, excessive mass loss, and the degradation of mechanical properties.

The TermoVuoto process, a vacuum-assisted thermal modification technology, addresses these limitations by modifying wood under reduced pressure, which lowers the boiling point of water and enhances heat penetration while minimizing oxidation. This controlled environment allows for precise process tuning, resulting in superior material properties with reduced energy consumption. This study examines the underlying mechanisms of the TermoVuoto process, its impact on wood properties, and its broad industrial applications. Moreover, the TermoVuoto system can also work as a simple vacuum dryer, if needed, retaining all the advantages that come with it in terms of very high quality and speed of drying.

2 The TermoVuoto Process

The TermoVuoto process is performed in a sealed chamber under controlled vacuum conditions, typically at pressures between 300 and 400 mBar. The process consists of three key stages:

- Pre-heating: The wood is gradually heated to approximately 100-120°C to remove free water while avoiding the risk of cracks.
- Thermal modification: The temperature is increased to a range of 160-220°C, inducing chemical transformations in hemicellulose and lignin that reduce hygroscopicity and enhance durability. The absence of oxygen minimizes oxidative degradation.
- Cooling and stabilization: The material is slowly cooled under vacuum to avoid internal stress and ensure uniform modification.

By conducting the process under vacuum, the TermoVuoto method significantly reduces the formation of degradation by-products, allowing for improved control over the final material properties.

3 Effects on Material Properties

Thermal modification via the TermoVuoto method leads to significant changes in the physical and chemical properties of wood:

Hygroscopicity Reduction: The decreased availability of hydroxyl groups results in reduced water absorption and swelling behavior.

- Biological Resistance: The degradation of hemicellulose eliminates key nutrients, making the material less susceptible to fungal decay and insect attack.
- Color Modification: The process causes a uniform darkening of the wood, which is desirable for aesthetic applications.
- Mechanical Performance: While minor reductions in mechanical strength occur due to hemicellulose degradation, the vacuum process minimizes this effect.
- VOC Emissions: The emissions remain close to those of untreated wood, ensuring compliance with indoor air quality standards.

4 Applications of TMW in Different Industries

Due to its enhanced properties, TermoVuoto-modified wood is widely used in various industrial sectors:

- Construction Industry: Used for exterior and interior applications, including cladding, decking, and flooring, where improved stability and durability are essential.
- Furniture & Design: Preferred in both indoor and outdoor furniture due to its enhanced weathering resistance and refined aesthetic appearance.
- Urban Infrastructure: Utilized in public furniture, boardwalks, and architectural installations that require prolonged exposure to environmental conditions.
- Nautical & Marine Applications: Applied in marine decking and structural elements where moisture resistance is critical.
- Specialized Applications: Employed in high-performance sectors such as musical instrument manufacturing and vehicle interiors.

5 Sustainability and Future Perspectives

The TermoVuoto method significantly contributes to sustainability in wood processing. The reduction in energy consumption and the elimination of chemical preservatives align with principles of circular economy and environmental responsibility.

Future research will focus on optimizing the process parameters to further improve material performance and expand the range of treatable wood species. Additionally, advances in lifecycle assessment (LCA) methodologies will provide a more comprehensive evaluation of the environmental benefits associated with this technology.

6 Conclusion

The vacuum-assisted TermoVuoto process represents a significant advancement in wood thermal modification. By improving dimensional stability, reducing hygroscopicity, and maintaining low VOC emissions, this method provides a sustainable alternative to traditional chemical treatments. Its diverse applications across construction, marine, and high-performance design sectors underline its industrial relevance and potential for future development.

References

5. Eng. Dr. Ernesto Pagnozzi, European Patent Specification nr. EP 2 535 156 B1 (2014).

Assessing the Impact of Machining Processes on Industrial Wood Packaging: An LCA-Based Approach

Giulia Cortina[1], Giacomo Goli[2], Viola Arena[1], Lisa Bernacchi[1], Riccardo Barbieri[1], Massimo Delogu[1]

[1] Department of Industrial Engineering, University of Florence, Florence 50139, Italy
[2] Department of Agriculture, Food, Environment and Forestry (DAGRI), University of Florence, Florence 50144, Italy

Abstract. This study evaluated the environmental impact of industrial wood packaging production. This study, developed with the collaboration of the institutional partner ASSOIMBALLAGGI, is part of a scientific context characterized by a scarcity of Life Cycle Assessment scientific literature applied to industrial wood packaging. Although some scientific papers focus on individual components of packaging, the sources addressing the entire life cycle of a complete packaging box are pretty limited.
The analysis was conducted by ISO 14040:2021 and ISO 14044:2021 standards and following the PCR Packaging 2019:13 by basing a cradle-to-grave approach. Primary data were directly collected from the two companies, and secondary data was supplemented by databases and scientific literature. The environmental impact assessment used all the categories from the Environmental Footprint (EF) 3.1 methodology.
The results indicate that the production phase has a marginal effect on the overall environmental impact compared to stages such as raw material procurement, use, and end-of-life. This suggests that the production processes for industrial wood packaging are energy efficient. However, the Life Cycle Assessment allowed identifying hot spots stages of processing and machinery that generate the highest consumption and environmental impacts, providing valuable insights for optimizing the most critical operations along the production chain.

Keywords: Life Cycle Assessment, machining process, wood packaging.

1 Introduction

In recent years, the transition towards a Circular Economy (CE) has increasingly captured the interest of businesses, consumers, and their associations [1]. Within this context, wooden packaging, a key sector in the Italian industry, is a sustainable solution that can significantly reduce environmental impact. According to the Rilegno report of 2023, the volume of packaging placed on the Italian market has risen by approximately 60% since 2010. This shows a growing market and an increasing societal interest in more sustainable packaging solutions [2].

According to the PCR Packaging 2019:13 [3], industrial wooden packaging is defined as a "product to be used for the containment, protection, handling, delivery, storage, transport and presentation of goods, from raw materials to processed goods, from the producer to the user or consumer, including processor, assembler or other intermediary". This definition encompasses both the components of the packaging: the box used to transport the product, and the pallet used to handle the box.

A literature review shows that numerous studies have examined wooden packaging; however, they have primarily focused on the environmental impacts of individual components rather than analyzing an entire industrial packaging.

For example, Gasol et al. (2008) said that the most environmentally impactful steps are those related to raw material procurement, transportation, and the supply chain [4]. Many articles published subsequently confirmed these results. These studies say that the initial phase of raw material supply and the subsequent production phase show the highest environmental impact [5,6]. Approximately 90% of pallets' producers purchase the four main components (boards, crossbars, blocks, nails) from external suppliers, significantly increasing the product's overall environmental impact. Only a few producers have an in-house sawmill that allows them to produce pallets directly from logs [7]. The studies on the other components of industrial packaging revealed a notable scarcity of literature on the subject. The available information remains incomplete and insufficiently explored.

To fully exploit the potential of wooden packaging, it's essential to assess its entirety (box + pallet), considering the entire life cycle of the supply chain, from raw material procurement to the final disposal phase. Although Italy holds an essential position in the wood and wood-based products market, the sector is severely constrained by the limited availability of domestic forest resources. This shortage forces the country to rely heavily on international markets for raw wood supplies, primarily imported from timber-rich regions such as the Nordic and former Soviet countries [7].

For this study, the Life Cycle Assessment (LCA) methodology was applied to evaluate the environmental impact of two case studies representing different types of industrial wooden packaging. Considering what has emerged from the literature, this article does not focus on the raw material procurement phase, as it is beyond direct control. Instead, attention is directed towards the following production phase; in fact, it's here that companies have the opportunity to enhance environmental performance through targeted measures and best practices.

2 Materials and Methods

The Life Cycle Assessment (LCA) methodology was applied to conduct this study, following the guidelines set out in the ISO 14040-44:2021 standards [8].

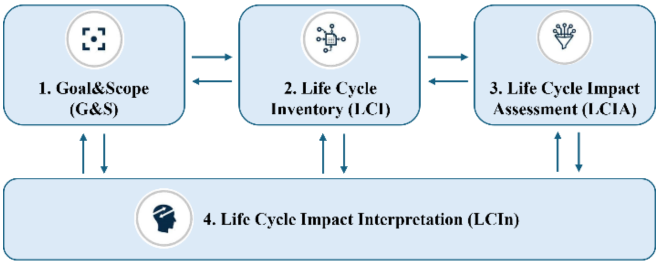

Fig.1. The LCA phases diagram.

The flow diagram shown in Figure 1illustrates the general structure of an LCA analysis for a product, process, or service. This systematic and step-by-step approach is divided, according to the standards, into four main phases:

1. Goal&Scope
2. Life Cycle Inventory (LCI)
3. Life Cycle Impact Assessment (LCIA)
4. Life Cycle Interpretation (LCIn)

The first phase of G&S is of fundamental importance as it clearly and unequivocally defines the objective and purpose of the LCA study [9].

At this stage, the key aspects to be determined include:
Functional/declared unit (FU), which represents the reference point for the study and enables comparisons between alternatives.
System boundaries, which specify the processes included in the analysis.
Environmental indicators identify the impact categories relevant to the system under examination.
Cut-off criteria are the rules used to determine which material, energy, or emission flows to include or exclude from the LCI phase. These criteria simplify the inventory by focusing on data or contributions that significantly impact the overall result, avoiding minimal influences.

The LCI represents another critical phase of the study. Environmental and energy flows entering and exiting the process units of the analyzed system are identified and quantified. The data collected can be classified as either primary or secondary. Primary data refers to original information collected specifically for the research being conducted. Secondary data, on the other hand, is information collected in databases or literature used for similar research purposes. The collection of adequate and comprehensive data is essential to obtain a detailed overview and ensure accurate and reliable results [10].

In the LCIA phase, the data collected during the inventory analysis are correlated with the various environmental impact categories considered in the study. This step allows the environmental flows to be translated into impact indicators that can be compared and interpreted.

The final phase of LCIn involves interpreting the results, where the influence of initial choices (inputs) on the study's outputs is analyzed. Additionally, it is assessed whether the quality of the data used is sufficiently robust to ensure the validity of the conclusions [11]. This method can be used iteratively, and the phases that constitute it are interdependent; therefore, none can be considered complete until the entire process is finished.

The products analyzed in this study are industrial wooden packaging for transporting industrial goods. Below, two different types of industrial packaging (packaging-1 and packaging-2), produced by two different Italian companies in the sector, will be presented and examined.

The first type of industrial packaging is the “E-box,” entirely made in Italy by *Emiliana Imballaggi S.p.A*. The E-box is a foldable box made of timber spruce and plywood and produced using a standardized production line.

The different components of packaging-1 were made from the following materials:

- Batch of timber spruce measuring 4000x23x80 mm, from Austria.
- Batch of birch plywood panels measuring 1525x1525x6 mm, from Russia.
- Blocks made in Italy from recycled particleboard, measuring 75x75x75 mm.
- A roll of laminate, steel nails, and hooks produced in Germany.

The second type of industrial packaging is the box “Pichler n°305”, which was entirely made in Italy by *Spigolon Imballaggi Srl*. The box is made of fir wood and OSB (Oriented Strand Board), with a customized production line. So, this type of packaging is made to order based on the customer's specific requirements.

The different components of packaging-2 were made from the following materials:

- Batch of timber spruce beams measuring 8000x110x95 mm, from Austria.
- Batch of timber spruce boards measuring 3200x100x23 mm, from Austria.
- Blocks of OSB panels measuring 1250x2500x9 mm from Hungary.
- Steel nails produced in Germany.

A representative diagram of the two types of boxes is shown in Fig. 1 and Fig. 2.

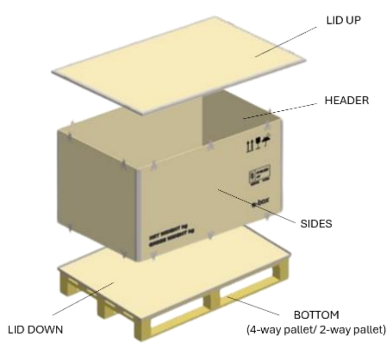

Fig. 1. Components of packaging-1.

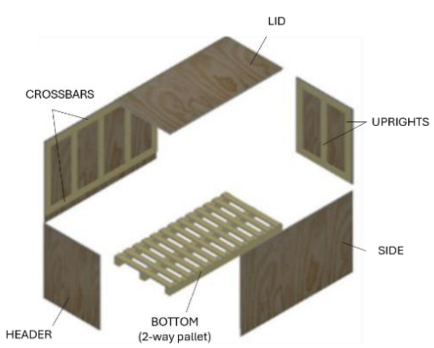

Fig. 2. Components of the packaging-2.

The FU chosen in both analyses is: 1 (one) wooden industrial packaging.

The system boundaries included in the LCA analysis are from cradle to grave. Specifically, with reference to the PCR Packaging 2019:13 [3].

The cut-off rules in this study included the impact of machinery for packaging and for raw material production, infrastructure-related effects such as construction, demolition, and facility management, and the impact of personnel, including transportation and services for employees and visitors.

The LCI phase was mainly conducted by collecting primary data related to material and energy flows into and out of the system. All other data necessary for the modeling is secondary data that refers to literature or scientific databases.

In Figure 4**Errore. L'origine riferimento non è stata trovata.** the typical production process of industrial wooden packaging is shown, from the raw material supply to the end-of-life phase. The figure also shows the main flows to be considered as inputs and outputs of the individual processes.

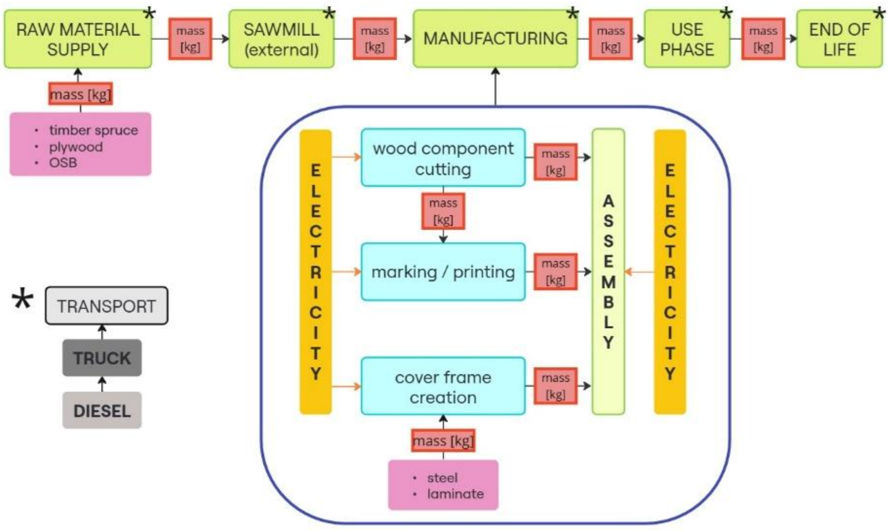

Fig. 4. The typical production process of industrial wooden packaging.

Specifically, the data related to the energy consumption of the machinery used during the production of the two types of packaging were directly recorded using an ammeter clamp with a data logger (HT GSC60 model for packaging-1 and HT GSC57 model for packaging-2). This device allows data to be collected at preset intervals, which are then stored in internal memory and can be subsequently downloaded. The energy consumption related to the production of the Spigolon Imballaggi Srl packaging is shown in Table 1

Table . These represent an example of possible energy consumption for industrial packaging production.

Table 1. Energy consumption values of machinery used for producing the Pichler case n°305 by Spigolon Imballaggi Srl.

SPIGOLON Srl			
Industrial Machinery	**Element**	**Unit**	**Energy Grid Mix [kWh]**
Automatic Panel Sizing Machine SIGMA 65 SMC	1/2 Side - 1188x1200x9mm	4	0,184
	1/3 Lid - 800x1200x9mm	3	0,084
	Header - 1194x1376x9mm	2	0,256
CNC Pantograph	Slots (200x70x95mm) on 1/2 side	16	0,016
	Slots (200x70x95mm) on bottom beams	12	0,418
Automatic Wood Pack Cutter	Beams 95x1100x2400mm	10	0,344
	Boards 23x100x2380 mm	6	0,219
	Boards 23x100x570 mm	by-product	
	Boards 23x100x1130 mm	25	0,231
	Boards 23x100x965 mm	by-product	
	Boards 23x100x730 mm	by-product	

Finally, the LCIn phase was carried out using the Environmental Footprint 3.1 methodology (EF 3.1). The complete packaging (pallet + box) was evaluated by considering all the impact categories related to EF 3.1. To assess only the production phase of the packaging and to identify the hotspots, it was decided to evaluate only the Global Warming Potential (GWP) because it was considered the most relevant.

3 Results and Discussion

As said before, in the current state of the art, the most impacting phase is the upstream (i.e., procurement of raw materials). This is also evident from the graph shown in Fig. 3, which illustrates the percentage distribution of the average environmental impact of generic packaging throughout its entire life cycle. However, because it is impossible to reduce the effect in this phase due to our country's scarcity of raw materials, this study focuses on the second most impactful phase, the production phase.

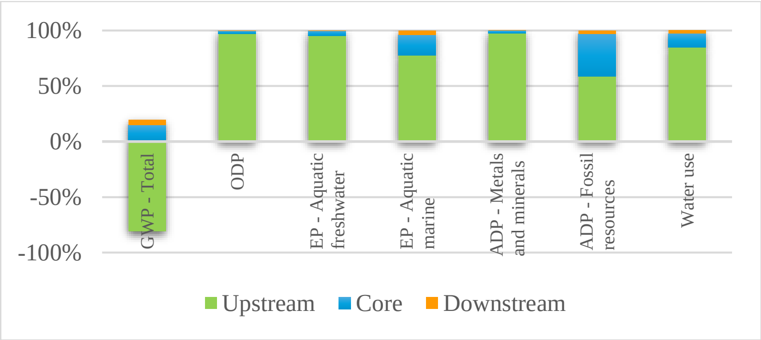

Fig. 3. Percentage distribution of the average environmental impact of generic packaging.

The production of wooden packaging, limited to cutting, assembly, and in-house processing operations, takes to high energy consumption and significant environmental impacts. Electricity is primarily used to power the machinery involved in the cutting and assembly stages. The impacts associated with the different subcategories of GWP related to the industrial production of the two analyzed packaging types are presented in Table 2 for Spigolon Imballaggi Srl and Table 3 for Emiliana Imballaggi S.p.A.

Table 2. Environmental impacts related to the production of box Pichler n°305.

Spigolon Imballaggi Srl. | Global Warming Potential (GWP) [kg CO_2 eq.]			
	Automatic Panel Sizing Machine	*CNC Pantograph*	*Automatic Wood Pack Cutter*
Total	1,92E-01	1,60E-01	2,92E-01
Fossil	1,90E-01	1,57E-01	2,88E-01
Biogenic	2,62E-03	2,17E-03	3,97E-03
LULUC	2,79E-05	2,32E-05	4,24E-05

Table 3. Environmental impacts related to the production of E-box.

Emiliana Imballaggi S.p.A. | Global Warming Potential (GWP) [kg CO_2 eq.]						
	Tecnomat panel saw	*Wood Pack Cutter Delta*	*Roll Printing*	*Nailing Robot*	*Baykal Corner Press*	*Edge forming line*
Total	1,52E-01	7,35E-04	1,10E-03	3,68E-04	8,60E-02	2,21E-02
Fossil	1,50E-01	7,25E-04	1,09E-03	3,62E-04	8,48E-02	2,17E-02
Bioge-nic	2,07E-03	1,00E-05	1,50E-05	5,01E-06	1,17E-03	3,00E-04
LULUC	2,20E-05	1,07E-07	1,60E-07	5,34E-08	1,25E-05	3,20E-06

The processing of the various components has been categorized according to the machinery used. As evidenced by the tabulated values, the most impactful machinery is the automatic panel sizing machine for Spigolon Imballaggi Srl and Tecnomat Panel

Saw for Emiliana Imballaggi S.p.A. This is likely due to the quantity of material processed or inefficiencies arising from outdated technologies and the use of fossil fuels.

The associated impact is strongly influenced by the energy source employed, with higher CO_2 emissions in the case of fossil fuels or electricity generated from non-renewable sources. For this reason, an analysis was conducted to assess how impacts would vary by replacing the fossil-based energy mix with renewable sources such as photovoltaic, biogas, and wind power.

The following graph illustrates the differences in total GWP. Considering this single impact category, which is nonetheless representative of all the others, it is evident that opting for more sustainable energy sources reduces impacts. Indeed, as shown in Figure 6, both companies exhibit a reduction in environmental impacts compared to the grid mix of approximately 32% when using energy from biogas, around 93% when utilizing energy from photovoltaic sources, and roughly 95% when employing energy derived from wind power.

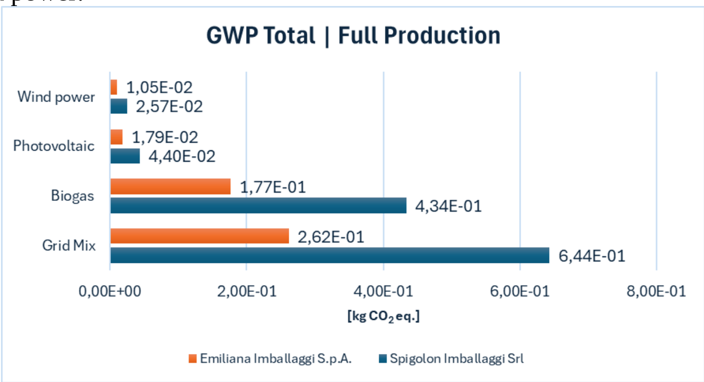

Fig. 6. Comparison of environmental impacts of different types of energy sources.

To further reduce environmental impact, improving the machinery by investing in more modern, energy-efficient equipment is essential. This must go hand in hand with optimizing production processes. Adopting digital tools for monitoring energy consumption enables the identification of inefficiencies and waste reduction, while automation enhances processing precision, minimizing waste generation. In this regard, mass production is undoubtedly preferable to custom manufacturing.

The implementation of these strategies, combined with continuous investment in innovative technologies, is a fundamental step towards reducing the environmental footprint of production and promoting a more sustainable use of resources.

4 Conclusion

In recent years, the transition towards a circular economy has aroused increasing interest, particularly in the wooden packaging sector, which is regarded as a sustainable solution for reducing environmental impact.

This study applied the Life Cycle Assessment (LCA) methodology to evaluate the environmental impact of two types of industrial wooden packaging, with a particular focus on the production phase, as this is where companies can directly implement improvements to enhance sustainability. During the LCI phase, primary data were collected through an experimental campaign based on direct measurements of the energy consumption of the machinery used in the production process. Where direct measurements were not feasible, secondary data from scientific literature and industry databases were utilized.

The analysis has confirmed what emerged from the literature: the most impactful phase is raw materials supply. However, since it is impossible to intervene directly in this phase, as the material is imported from abroad, the possibility of acting on the second most impactful phase, i.e., processing and assembly, has been evaluated. The emissions associated with these stages, presented in this work only by GWP but extendable to all other impact categories, are strongly influenced by the energy mix employed: the use of electricity from fossil fuels significantly increases the carbon footprint, whereas relying on renewable sources such as solar, wind, or biogas could substantially reduce overall environmental impact. Furthermore, investing in more efficient machinery, optimizing production processes, and implementing digital tools for energy consumption monitoring are fundamental strategies for minimizing environmental impact and fostering a more efficient circular economy model.

Wood, a biogenic material, offers an additional advantage in terms of sustainability, as it helps to reduce environmental impacts compared to other packaging materials. In Italy, a well-established wood recycling chain extends the material's lifecycle and reduces the demand for new virgin resources. This approach minimizes waste and emissions from producing new materials and promotes a more circular and resource-efficient production model.

Acknowledgment

The author(s) sincerely thank Assoimballaggi and Federlegno Arredo for their support. Emiliana Imballaggi S.p.A. and Spigolon Imballaggi Srl for their collaboration and for providing the essential data for this work. Views and opinions expressed are those of the author(s) only and do not necessarily reflect those of the companies or associations mentioned, who cannot be held responsible for them.

References

1. Elia V, Gnoni MG, Tornese F (2017) Measuring circular economy strategies through index methods: A critical analysis. Journal of Cleaner Production 142:2741–2751. https://doi.org/10.1016/j.jclepro.2016.10.196
2. Rapporto Rilegno 2024
3. PCR 2019:13 Packaging (Version 1.1.2)
4. Gasol CM, Farreny R, Gabarrell X, Rieradevall J (2008) Life cycle assessment comparison among different reuse intensities for industrial wooden containers. Int J Life Cycle Assess 13(5):421–431. https://doi.org/10.1007/s11367-008-0005-0
5. García-Durañona L, Farreny R, Navarro P, Boschmonart-Rives J (2016) Life Cycle Assessment of a coniferous wood supply chain for pallet production in Catalonia, Spain. Journal of Cleaner Production 137:178–188. https://doi.org/10.1016/j.jclepro.2016.07.032

6. Alanya-Rosenbaum S, Bergman RD, Gething B (2021) Assessing the life-cycle environmental impacts of the wood pallet sector in the United States. Journal of Cleaner Production 320:128726. https://doi.org/10.1016/j.jclepro.2021.128726
7. Dallari, Fabrizio, Marchet, Gino Il ruolo dei pallet nei moderni sistemi distributivi. Da strumento di lavoro a moneta di scambio.
8. International Organization for Standardization (ISO). UNI EN ISO 14040:2006 – Environmental management – Life cycle assessment – Principles and framework. Geneva: ISO; 2006.
9. International Standard Organization. UNI EN ISO 14044:2006 Environmental management. Life cycle assessment. Requirements and guidelines. Geneva: ISO; 2006.
10. Nuss P (2015) Life Cycle Assessment Handbook: A Guide for Environmentally Sustainable Products, edited by MaryAnn Curran. Hoboken, NJ, USA: John Wiley & Sons, Inc., and Salem, MA, USA: Scrivener Publishing LLC, 2012, 611 pp., ISBN 9781118099728, $199.00 (paper), $159.99 (e-book). J of Industrial Ecology 19(1):167–168. https://doi.org/10.1111/jiec.12217
11. Aviso KB (2024) Overview of LCA—History, Concept, and Methodology. In: Encyclopedia of Sustainable Technologies. Elsevier, pp 107–114

Influence of wood chip moisture content on the environmental impact of a biomass boiler of a sawmill drying plant in Veneto (Italy)

Annalisa Magnabosco,[1] Martina Boschiero,[1] Michela Zanetti[1]

[1] University of Padova, Dip. TESAF, 35020 Legnaro (PD), Italy

Abstract. The forest-wood supply chain in Veneto (Italy) is experiencing a deep crisis due to a lack of coordination among its phases, increased competition from foreign markets, and the economic advantages of imported timber. One of the most critical points is the initial processing stage, which struggles to compete due to outdated technology. This study analyzes a case study of a sawmill equipped with a biomass-fueled drying system, aiming at technological improvement and circular economy principles. An environmental impact analysis was conducted using the Life Cycle Assessment (LCA) methodology. The focus was on evaluating how the moisture content of wood chips used to fuel the boiler affects the drying process in terms of emissions. The analysis revealed that the sawmill's wood chips had a high moisture content (45%). A sensitivity analysis was conducted with three different moisture contents (25%, 30%, and 45%) to evaluate variations in thermal efficiency and emissions. The results indicate that the combustion process of wet wood chips has the highest environmental impact across multiple impact categories. Additionally, recommendations for optimizing drying efficiency and reducing emissions through improved biomass management are discussed.

Keywords: Life Cycle Assessment, drying process, wood chips, moisture content.

1 Introduction

However, the Veneto forest-wood sector has been declining due to competition from foreign timber markets, where technological advancements have led to higher efficiency and lower costs. The research aims to evaluate the environmental impact of a sawmill's drying process powered by a biomass boiler, specifically analysing the effect of wood chip moisture content on efficiency and emissions. The study employs LCA methodology to assess different scenarios of wood chip moisture content and discusses potential solutions for optimizing the drying process.

Wood has historically been a fundamental resource for human societies, particularly in mountainous regions, for both material production and energy supply. Various professions developed around forestry and wood processing, including loggers, rafters, sawyers, carpenters, and charcoal makers [1-3]. In different civilizations, wood and forests have played central roles in economic development, urban growth, and energy production [2].

The wood industry has experienced alternating periods of growth and decline over the centuries, leading to the closure of many sawmills and reliance on imported wood [1, 4]. A major expansion occurred in the 1700s during the Venetian Republic with the introduction of hydraulic sawmills in Veneto and the Alpine region, which significantly improved efficiency compared to manual cutting [3]. In Italy, the first references on wood drying and seasoning appear in the works of De Buffon and Francesco Milizia, who described natural and artificial drying techniques [5].

During the 20th century, the Venetian wood market declined due to resource depletion and competition from Austrian timber, which was of higher quality and more cost-effective [3]. Many sawmills closed, and wood usage in construction decreased. Although modernization efforts in the 1950s temporarily revived the sector, the number of sawmills has steadily declined since the 1980s [6]. Today, Italy remains one of the largest wood importers, despite its growing forested areas, due to low domestic logging rates and economic challenges in the primary wood processing sector [7].

The underutilization of Italian forests has environmental and economic consequences, including illegal logging abroad, increased CO_2 emissions from transportation, and biodiversity loss. To address these issues, better forest management and modernization of sawmills are essential. European policies emphasize sustainable forest utilization, promoting efficient wood processing and the cascading use of timber [8].

In this context, a case study was conducted on a sawmill in Veneto, Northern Italy, equipped with a biomass-powered drying system, using wood chips derived from its own processing waste. The study evaluates the impact of different wood chip moisture contents (25%, 30%, and 45%) on drying efficiency and emissions [9-15] using Life Cycle Assessment methodology. LCA enables the evaluation of a product or service's environmental impact based on resource and energy use, as well as emissions. The impact assessment using LCA can contribute to a sustainability perspective when related to environmental carrying capacities [16-18]. Nevertheless, LCA is internationally recognized as a methodology that helps identify the most environmentally favorable product [17].

The findings highlight the importance of using dry wood chips to improve boiler efficiency, reduce emissions, and enhance the sustainability of sawmill operations.

2 Material and Methods

2.1 LCA

Life Cycle Assessment (LCA) is a standardized method for evaluating the environmental impact of a product throughout its life cycle. Originating in the 1960s, it has evolved into an internationally recognized methodology, guided by ISO 14040:2021 [19] and ISO 14044:2021 [20].

Goal and Scope definition

In this study, the LCA analysis was applied to evaluate the environmental impact of producing dried boards in a medium-sized sawmill located in the Veneto region, Northern Italy. The sawmill uses a drying kiln powered by a biomass boiler. The biomass used is wood chips produced from the sawmill's own processing waste. The boiler used for burning the wood chips is an Almar Collalto 301 kW.

During data collection, it was found that the burned wood chips had a higher moisture content (MC) than the optimal 25% for boiler efficiency. Since combustion affects both efficiency and emissions, a sensitivity analysis was conducted to assess variations in wood chip consumption, electricity use, and emissions when drying 1 m^3 of boards. Three MC levels were considered: 45%, 30%, and 25%.

The functional unit considered is 1 m^3 of dried Norway spruce (Picea abies (L.) H. Karst.) board. The analysis focused solely on sawmill production using a "gate-to-gate" approach, specifically examining the following unitary processes: (1) log handling in the yard, (2) log cutting, (3) board handling, (4) chipping of offcuts from log cutting, (5) combustion of wood chips in the boiler, and (6) the drying process. The study excluded forest operations, log transportation to the sawmill, and the final stages of product use and disposal.

The log-cutting process was divided into three subprocesses: one for sawn timber and two for co-products (wood chips and sawdust). The energy and material inputs for the cutting process were allocated among these three subprocesses. The input and output analysis considered mass and energy values (diesel, lubricating oil, and electricity), but other resource consumption, such as water, was excluded.

The data collected in the sawmill for the LCA analysis cover the period from October 2019 to June 2020. Primary data were directly obtained from the sawmill, while secondary data were sourced from the Ecoinvent database and literature. The software used for the analysis was GaBi (Sphera), and the impact indicators, assessed using the CML2001 - Aug. 2016 method, include: Global Warming Potential (GWP, kg CO_{2eq}), Ozone Depletion Potential (ODP, mg $R11_{eq}$), Photochemical Ozone Creation Potential (POCP, g $Ethene_{eq}$), and Human Toxicity Potential (HTP, kg DCB_{eq}).

Life Cycle Inventory (LCI)

The analysis considers the sawmill production processes, from log handling in the yard to board drying (gate-to-gate) (Table 1).

Table 1. LCI data

Logs handling, sawmill yard	Unit	Quantity
Inputs		
Debarked logs	m^3	2.067
Energy (Diesel)	MJ	54.53
Lubricant oil	kg	0.025
Outputs		
Debarked logs	m^3	2.067

Logs cutting – sawn timber production		
Inputs		
Debarked logs (MC 50%)	m^3	2.07
Energy (Diesel)	MJ	25.95
Energy (Electricity)	MJ	62.5
Lubricant oil	kg	0.09
Outputs		
Sawn timbers (MC 50%)	m^3	1.45
– co-products. shavings		
Inputs		
Debarked logs (MC 50%)	m^3	2.07
Energy (Diesel)	MJ	2.06
Energy (Electricity)	MJ	4.96
Lubricant oil	kg	0.03
Outputs		
Shavings	kg_{dry}	156.66
Sawn timbers handling yard		
Inputs		
Sawn timbers	m^3	1.45
Energy (Diesel)	kg	24.39
Lubricant oil	kg	0.032
Outputs		
Sawn timbers	m^3	1.45
Movimentazione tavole per carico essiccatoio		
Inputs		
Tavole (MC 45%)	m^3	1.04
Energia (Diesel)	MJ	4.71
Olio lubrificante	kg	0.0061
Outputs		
Tavole (MC 45%)	m^3	1.04
Handling of dried boards/unloading dryer		
Inputs		
Boards (MC 20%)	m^3	1
Energy (Diesel)	MJ	4.71
Lubricating oil	kg	0.0058
Outputs		
Boards (MC 20%)	m^3	1
Chipping of the shavings		
Inputs		
Shavings	kg_{dry}	156.66
Energy (Electricity)	MJ	17.02
Lubricating oil	kg	0.0005
Outputs		
Wood chips (MC 45%)	m^3	156.66

Log Handling

During the time period considered for the LCA analysis. the sawmill processed logs from forests affected by Vaia Hurricane, which had already been debarked, in the sawmill yard, the logs are handled using a self-propelled wheel loader (Solmec. 120 HP). Subsequently, the logs are transported to the log saw. This analysis considers Norway spruce logs, assuming a bulk density of 758 kg/m³ with a moisture content of 50% [21].

Log Cutting

The log is cut using a band saw with a nominal power of 75 kW, powered by electricity. Once the timber is cut, it is transported via a series of rollers and conveyor belts to a three-blade trim saw with an adjustable step (75 kW), which trims the sawn material. If necessary, the material is further processed by a reciprocating saw (55 kW).

The cutting yield of a Norway spruce log in this sawmill is 70%. Cutting residues account for 30% of the log, divided into slabs (20-22%) and sawdust (8-10%). All slabs are chipped.

Board Handling

The produced boards are manually picked up and stacked into piles. These piles are then moved using dedicated self-propelled forklifts and stored in the sawmill yard for several weeks to reduce their moisture content. The forklifts used, powered by diesel, have a load capacity of 7 tons and 4 tons.

The board piles are then loaded into the drying kiln, where the boards are manually arranged to form a stack. Once the drying cycle is complete, the dried boards are retrieved using a self-propelled forklift and stored in the yard until they are sold.

Chipping

Processing residues are conveyed via a series of conveyor belts to a drum chipper with a nominal power of 55 kW. The produced wood chips are transported outside the sawmill by a screw conveyor and stacked in an open area.

A portion of the wood chips is later transported into a structure located above the boiler before being burned to power the drying kiln. This structure does not include any drying systems for the wood chips.

Combustion of wood chips in the boiler

The produced and stored wood chips have a moisture content of over 45% [22] and during the winter season or periods of heavy rainfall, this value can exceed 50%, reaching up to 60%. According to the technical datasheet, the boiler operates at a maximum efficiency of 92.4% when using wood chips with a moisture content of 25%. In particular, the focus was on determining how boiler efficiency varies with moisture content, as air emissions and the biofuel consumption for drying depend on combustion quality, which improves when the boiler operates at maximum efficiency.

The technical datasheet of the combustion process selected from the Ecoinvent database provides some equations used for process modeling but does not include a specific relationship between biomass moisture content and boiler thermal efficiency. Based on the data presented in the study by Celen and Erdem [23], the following relationship was developed:

$$y = -5{,}072X^2 + 2{,}527x + 0{,}604 \quad (1)$$

where y represents thermal efficiency and x is the biomass moisture content.

Applying equation (1) to moisture contents of 25%, 30%, and 45%, the thermal efficiency values of 91.88%, 90.56%, and 71%, respectively, were obtained.

To adjust the mass of wood chips required for combustion according to the thermal efficiency of the boiler, an equation was found in the Ecoinvent process datasheet. The required quantity of dry mass of wood chip (*Wch*) is given by multiplying a parameter (*a = 0.05291*) by a scaling factor (*fc*), which is the inverse of the boiler's thermal efficiency (*ET*):

$$Wch = a * fc = a * \frac{1}{ET} \quad (2)$$

Using equation (1), the formula becomes:

$$Wch = \frac{a}{y} = \frac{a}{-5{,}072X^2 + 2{,}527x + 0{,}604} \quad (3)$$

The calculated quantity represents the fuel needed to generate thermal energy for drying 1 m³ of boards, which, in this case study, was determined to be 580.10 MJ/m³ of dried boards.

Based on these relationships, three different scenarios were developed for the three moisture contents (25%, 30%, 45%) (Table 2).

Table 2. LCI results for wood chip combustion at three different moisture contents for the production of 1 m³ of dried boards.

Wood Chip Combustion in Boiler	Unit	MC 25%	MC 30%	MC 45%
Inputs				
Wood Chips (a)	kg_{dry}	33.41	33.89	42.98
Energy (Electricity) (b)	MJ	9.48	9.62	12.19
Output				
Thermal Energy	MJ	580.10	580.10	580.10

Drying Process

The sawmill is equipped with a Big on Dry drying kiln (Model: LEM 96.58.41), powered by a biomass boiler. The drying process requires both thermal energy generated from wood chip combustion and electrical energy.

For this LCA analysis, the energy consumption for a single drying cycle was considered. The results showed that 580.10 MJ/m³ of thermal energy and 172.17 MJ/m³ of electricity are needed to dry 1 m³ of lumber (MC 20%).

3 Results and Discussion

3.1 Life Cycle Impact Assessment (LCIA)

The production of 1 m³ of dried spruce (Picea abies (L.) H. Karst.) board using wood chips with a 45% moisture content, in terms of global warming potential (GWP), generates the highest air emissions value of 143.98 kg CO_2eq, which is 14% higher than the emissions produced with wood chips at 25% moisture content (Table 5). The largest contribution comes from combustion for heat production required for drying (62%) and the drying process itself (23%).

For all impact categories considered, emissions generated by the combustion process vary depending on the moisture content of the wood chips (Table 5), with the highest contribution coming from chips with 45% moisture content, emitting 89.36 kg CO_2eq. The combustion of wood chips with a 30% moisture content emits 70.46 kg CO_2eq, while those with 25% moisture content emit 69.45 kg CO_2eq. In all cases, emissions from chip combustion account for more than 50% of total emissions (62% for wood chips with 45% moisture content and 56% for the other two).

When considering only the input of electrical energy—which remains unchanged across the analyzed LCA systems—the drying process generates emissions of 32.63 kg CO_2eq in all three cases.

The gas contributing the most to GWP is CO_2 (139.07 kg for chips with 45% MC), specifically biogenic CO_2 (88.96 kg), 98% (87.13 kg) of which is emitted during the combustion process. Methane (CH_4) is the second most significant contributor to GWP (3.62 kg CO_2eq for wood chips with 45% MC), with the most impactful emission process being drying.

Regarding human toxicity potential (HTP), the highest emissions occur in the scenario with the highest wood chip moisture content, reaching 10.88 kg DCBeq. The combustion process contributes 41%, while drying accounts for 33%. In this case, the emissions that contribute the most to the HTP indicator are heavy metals (3.02 kg DCBeq) and volatile organic compounds (VOC, 3.81 kg DCBeq). Heavy metal emissions are mainly due to the drying process, representing 60.3% (1.82 kg DCBeq). As for VOCs, these primarily originate from wood chip combustion (1.84 kg DCBeq) and the board drying process (1.11 kg DCBeq).

Using wood chips with a 45% moisture content also results in higher emissions in the photochemical ozone creation potential (POCP) impact indicator, with a total of 31.65 g Etheneeq. The processes with the highest incidence are again combustion (46%) and drying (30%). In this impact indicator, the most significant emissions come from inorganic substances (17.12 g for chips with 45% moisture content) and VOCs (7.49 g for chips with 45% moisture content).

The ozone depletion potential (ODP) indicator does not show variability among the three different moisture content levels.

Table 3. Total air emissions for the three different wood chip moisture contents for the impact indicators: Global Warming Potential (GWP), Human Toxicity Potential (HTP), Ozone Depletion Potential (ODP), and Photochemical Ozone Creation Potential (POCP) (MC= Moisture Content).

Global Warning Potential (GWP) kg CO_2eq	**MC 45 %**	**MC 30%**	**MC 25%**
Emissions to air	143.98	125.08	124.08
Ecoinvent long-term to air	0.000041	4.08E-05	4.08E-05
Inorganic emissions to air	140.06	121.21	120.2
Carbon dioxide	50.11	49.86	49.79
Carbon dioxide (biotic)	88.96	70.53	69.54
Nitrous oxide (laughing gas)	0.98	0.87	0.86
Sulphur hexafluoride	0.011	0.011	0.011
Organic emissions to air (group VOC)	3.92	3.88	3.87
Halogenated organic emissions to air	0.012	0.012	0.012
Methane	3.62	3.59	3.59
Methane (biotic)	0.29	0.27	0.26
Human Toxicity Potential (HTP) kg DCB eq	**MC 45%**	**MC 30%**	**MC 25%**
Emissions to air	10.88	9.95	9.89
Ecoinvent long-term to air	0.06	0.06	0.06
Heavy metals to air	3.02	2.95	2.95
Inorganic emissions to air	1.03	1.02	1.02
Non-urban air or from high stacks	0.61	0.59	0.59
Particulates. < 2.5 um	0.0016	0.0016	0.0016
Particulates. > 10 um	0.0043	0.0042	0.0042
Particulates. > 2.5 um. and < 10um	0.0005	0.0005	0.0005
Organic emissions to air (group VOC)	3.91	3.52	3.5
Particles to air (Dust > PM10, PM2.5, silicon dust)	0.02	0.02	0.02
Urban air close to ground	2.24	1.78	1.75
Ozone Depletion Potential (ODP) mg R11eq	**MC 45%**	**MC 30%**	**MC 25%**
Emissions to air	7.54	7.49	7.49
Ecoinvent long-term to air	0.0003	0.0003	0.0003
Non-urban air or from high stacks	0.0002	0.0002	0.0002

Halogenated organic emissions to air	7.54	7.49	7.49
Photochemical Ozone Creation Potential (POCP) g Etheneeq	**MC 45%**	**MC 30%**	**MC 25%**
Emissions to air	31.65	28.58	28.42
Ecoinvent long-term to air	0.001	0.001	0.001
Inorganic emissions to air	17.12	15.37	15.28
Carbon monoxide	1.1	1.08	1.08
Carbon monoxide. non-fossil	8.27	6.54	6.44
Nitrogen oxides	2.92	2.92	2.92
Sulphur dioxide	4.83	4.83	4.83
Non-urban air or from high stacks	1.79	1.74	1.74
Organic emissions to air (group VOC)	7.49	7.23	7.21
Group NMVOC to air	6.65	6.4	6.38
Hydrocarbons (unspecified)	0.0000135	0.000013	0.000013
Methane	0.78	0.77	0.77
Methane (biotic)	0.062	0.057	0.057
VOC (unspecified)	0.00074	0.00074	0.00074
Urban air close to ground	5.25	4.23	4.18

These results have been compared with studies made by Sahoo and coauthors and Milota and coworkers [24,25,26]. In the LCA study by Sahoo et al. [24, 25], the analysis examined the entire life cycle of redwood boards (*Sequoia sempervirens*) produced in sawmills in Northern California (US). The study followed a cradle-to-grave approach and compared the production and end-of-life stages of rough and planed boards, considering both wet and kiln-dried boards. The functional unit of the study is 1 m^3 of redwood board. Another relevant LCA study is by Milota and Puettman [26], which reviews prior studies by the same authors [27-29] on board production in the Pacific Northwest and Southeastern United States. The functional unit was 1 m^3 of dried and planed lumber. The studied species included Douglas fir (Pseudotsuga menziesii (Mirb.) Franco), western hemlock (Tsuga heterophylla (Raf.) Sarg), white fir (Abies alba Mill), and pine (Pinus spp.).

In the LCA analysis conducted in this study, total energy consumption for the entire production cycle was 968.65 MJ m^{-3}, with drying contributing 77% (752.27 MJ m^{-3}), of which 77% came from biomass and 23% from electricity. Energy consumption was distributed as follows: 60% from wood chips, 28% from electricity, and 12% from diesel. Unlike previous studies, fossil fuel-derived energy accounted for 40% of total energy use, a higher proportion than reported in Sahoo et al. [25] and Milota and Puettman [26], whereas biomass-derived energy was comparatively lower.

Regarding air emissions and global warming potential (GWP), values were significantly higher (143.98 – 124.08 kg CO2eq) than those reported in prior studies. However, as confirmed by Sahoo et al. [25] and Milota and Puettman [26], biomass combustion in boilers was the main contributor (62%). High moisture content in wood chips was identified as a key factor increasing emissions and reducing drying efficiency.

4 Conclusions

The LCA models of this study revealed, as expected, that increasing the moisture content of the wood chips decreases boiler efficiency, requiring a greater amount of chips to be burned and consequently increasing air emissions, particularly those related to global warming potential. In the LCA analysis, the electricity used for the drying phase was kept constant across the three cases due to time and data availability constraints. However, for greater accuracy, it would be useful to assess how the energy consumption in the drying phase varies with changes in the moisture content of the biomass burned in the boiler, considering wood chips combustion and board drying as a single process.

Thermal energy produced from biomass combustion accounts for 60% of total energy consumption, and the biomass combustion process in the boiler is the most emissive. The emissions obtained from the LCA study conducted on the sawmill in the Veneto Region were significantly higher than those reported by other authors. Several factors may explain this difference, including how the LCA study was conducted, the model construction, the amount of data analyzed, the technological and geographical context, the efficiency of sawmill's production systems.

Considering the case study sawmill, it is evident that improving the combustion process by enhancing wood chips quality is crucial to reducing air emissions and minimizing environmental impact. To achieve this, installing a wood chip drying system capable of reaching a moisture content of 25% would be necessary. This would ensure maximum boiler efficiency, reduce emissions, and improve the board drying process.

References

1. Viola F., (2017). Le antiche foreste del Veneto e le politiche forestali della Serenissima. Il risveglio della Foresta, le politiche forestali dalla Serenissima a oggi. Quaderno della collana di Europe Direct Veneto, n.19. Agenzia Veneto Agricoltura, Legnaro (PD)
2. Zannini A., (2011). I mercanti di legname delle Alpi orientali (secc. XV-XVIII). Note da alcuni studi recenti, in Andrea Csillaghy, Antonella Riem Natale, Milena Romero Allué, Roberta De Giorgi, Andrea Del Ben e Lisa Gasparotto (a cura di), Un tremore di foglie. Scritti e studi in ricordo di Anna Panicali, Udine, Forum,, pp. 471-478
3. Celetti D. (2008). Il bosco nelle provincie venete dall'Unità ad oggi. Strutture e dinamiche economiche in età contemporanea. Padova: Cleup - Coop. Libraria Editrice Università di Padova
4. Vanni E., (2014). Sistemi agro-silvo-pastorali in un contesto dell'Etruria costiera. Aspetti conservativi del paesaggio in una prospettiva di lunga durata. Relatore Cambi F. Dipartimento di studi umanistici. Scuola di Dottorato Le culture dell'ambiente, del territorio e dei paesaggi. Università di Foggia
5. Ruggeri, N., (2011). Il legno nel '700: aspetti meccanici e d'anatomia. bollettino ingegneri n.6. pp. 3-16. ISSN 2035-2417

6. Resente G. A., Carraro F., Cavalli R., Zanetti M., (2020). Le segherie in Veneto. Stato dell'arte e prospettive future. Sherwood. Foreste e alberi oggi, n. 248, vol.26(5):21-25
7. Marchetti M, Motta R, Pettenella D, Sallustio L,Vacchiano G., (2018). Le foreste e il sistema foresta-legno in Italia: verso una nuova strategia per rispondere alle sfide interne e globali. Forest@ 15: 41-50. – doi: 10.3832/efor2796-015 [online 2018-05-03]
8. Ciccarese L., Pellegrino P., Pettenella D., (2014) – A new principle of the European Union forest policy: the cascading use of wood products. L'Italia Forestale e Montana, 69 (5): 285-290. http://dx.doi.org/10.4129/ifm.2014.5.01
9. Gebreegziabher T., Oyedun A. O.,Hui C.W., (2013). Optimum biomass drying for combustion e A modeling approach. Energy53, 67-73
10. Dzurenda L., Banski A. (2015). Dependence of the boiler flue gas losses on humidity of wood biomass. Archives of thermodynamics. Vol. 36 (2015), No. 4, 77–86 DOI: 10.1515/aoter-2015-0034
11. Dzurenda, L., & Banski, A. (2017). Influence of moisture content of combusted wood on the thermal efficiency of a boiler. Archives of Thermodynamics, 63-74
12. Orang, N., & Tran, H., (2015). Effect of feedstock moisture content on biomass boiler operation. Tappi J, 14(10), 629-637
13. Price-Allison, A., Lea-Langton, A. R., Mitchell, E. J. S., Gudka, B., Jones, J. M., Mason, P. E., Williams, A., (2019). Emissions performance of high moisture wood fuels burned in a residential stove. Fuel, 239, 1038-1045
14. Schön, C., Kuptz, D., Mack, R., Zelinski, V., Loewen, A., Hartmann, H., (2019). Influence of wood chip quality on emission behaviour in small-scale wood chip boilers. Biomass Conversion and Biorefinery, 9(1), 71-82
15. Bošnjaković M.; Veljić N.; Soldan C. (2020). Influence of moisture content in wood chips on the boiler operation. 7th International Conference "VALLIS AURE" 2020 pp. 0091-0101
16. Bjørn, A., Diamond, M., Owsianiak, M., Verzat, B., Hauschild, M. Z. (2015). Strengthening the link between life cycle assessment and indicators for absolute sustainability to support development within planetary boundaries. Environmental Science & Technology, 49 (11), 6370−6371
17. Hauschild, M. Z., Rosenbaum, R. K., Olsen, S. I., (2018). Life cycle assessment. Springer International Publishing, Cham. https://doi. org/10.1007/978-3-319-56475-3 Book
18. Ryberg, M. W., Owsianiak, M., Richardson, K., Hauschild, M. Z., (2018). Development of a life-cycle impact assessment methodology linked to the Planetary Boundaries framework. *EcologicalIndicators*, *88*, 250-262
19. International Standard Organization (ISO). Environmental management. Life cycle assessment. Principles and framework. ISO 14040. Geneva: International Organization for Standardization; 2021
20. International Organization for Standardization (ISO). Environmental management. Life cycle assessment. Requirements and guidelines. ISO 14044. Geneva: International Organization for Standardization; 2021
21. Francescato, V., Antonini E., (2009). Legna e cippato. Manuale pratico. Ed. AIEL, pg. 9-16. Legnaro (PD)
22. International Organization for Standardization (ISO). Solid biofuels — Determination of moisture content — Oven dry method Part 1: Total moisture — Reference method. ISO 18134-1. Geneva: International Organization for Standardization; 2015
23. Celen, P., Erdem, H. H. (2017). A case study for calculation of boiler efficiency by using indirect method. 3rd Conference on advances in mechanical engineering, Istanbul 2017 – ICAME2017 19-21 December 2017, Yildiz Technical University, Istanbul, Turkey

24. Sahoo, K., Bergman, R., Runge, T., (2021). Life-cycle assessment of redwood lumber products in the US. The International Journal of Life Cycle Assessment, 26(8), 1702-1720
25. Sahoo, K., Bergman, R., Alanya-Rosenbaum, S., Gu, H., Liang, S., (2019). Life cycle assessment of forest-based products: A review. Sustainability, 11(17), 4722
26. Milota, M., Puettmann, M. E., (2017). Life-cycle assessment for the cradle-to-gate production of softwood lumber in the pacific northwest and southeast regions. Forest Products Journal, 67(5-6), 331-342
27. Milota, M. R., West, C. D., & Hartley, I. D., (2005). Gate-to-gate life-cycle inventory of softwood lumber production. Wood and fiber science, 37, 47-57
28. Milota, M., (2015). Life cycle assessment for the production of Pacific Northwest softwood lumber. CORRIM Final Report, Module B. December, 15, 56
29. Puettmann, M., (2013), Oneil E., Bergman R. Cradle to Gate Life Cycle Assessment of Softwood Lumber Production from the Northeast- North Central (source: ResearchGate, https://www.researchgate.net/profile/Maureen-Puettmann)

Exclusive finishing with DMC laser technology

Marco Venturini[1]

1 SCM Group, Rimini (Italy)

Abstract. To meet a market where customization is the most important requirement, the process has evolved over the years with new features that allow the creation of innovative aesthetic finishes. The evolution of the process has led to a parallel development of machines and, as a result, sanders have been transformed from simple machines with flexible abrasives to machining centers capable of producing 3D finishes on the panel. To this end, as highest expression of the concept of customization, SCM introduced a new CO2 laser module on the DMC System sander, which allows any image to be transferred onto the workpiece. Unlike traditional laser marking systems, where the workpiece remains static while the laser head moves, the SCM system operates in a continuous flow. This configuration significantly increases productivity, making the processing time independent of the complexity of the image to be created. Another advantage of continuous flow processing is the ability to handle workpieces of any length, making it ideal for various production needs. The system integrates seamlessly into the modular structure of SCM's DMC System sanders, allowing for the combination of laser processing with other finishing units.

Keywords: Customization, Innovation, Productivity, Modularity

Optimization of knots assessment using laser scattering for predicting beech mechanical properties

Michela Nocetti[1[0000-0003-0906-0483]], Giovanni Aminti[1[0000-0003-2262-4095]], Martin Bacher[2[0000-0002-2870-5884]], Nicola Conforto[2], Michele Brunetti[1[0000-0001-7105-0716]]

[1] CNR IBE, Institute of Bioeconomy, 50019 Sesto Fiorentino (FI), Italy
[2] MiCROTEC, 39042 Bressanone, Italy
michela.nocetti@cnr.it

Abstract. Hardwood is becoming an increasingly important resource for the construction sector due to its high mechanical performance and its growing availability linked to ongoing climate changes. However, the use of wood in structures requires that it be classified according to its strength, and for hardwood, the parameters used in production lines, which are typically designed for softwoods, do not have the same predictive efficiency.
This study aims to explore the possibility of optimizing the measurement of local grain direction (GD) using laser scattering technology to predict the mechanical properties of beech wood within automated machine grading lines. For the purposes of this study, the extent of knots in approximately 100 beech boards was assessed visually by an expert operator and with the laser scattering technique. The data obtained were compared with one another and subsequently used to predict the bending strength and elastic modulus of the elasticity, as determined by four-point destructive bending tests.
Among the predictive parameters considered, localized GD provided the best results, showing medium-to-high correlations with the mechanical properties. This highlights that this technology is very promising for machine strength grading of beech and likely for other hardwood species as well.

Keywords: Slope of grain, structural timber, hardwood, strength grading.

1 Introduction

Hardwoods are increasingly used in the construction sector due to rising demand and climate change, which make them more suitable for the evolving environment [1].

Improvements in strength grading of hardwoods are therefore crucial for better utilization of this resource. On one hand, strength grading is mandatory for timber used as a structural product; on the other hand, hardwoods are more difficult to grade compared to softwoods. This is mainly due to the lower correlation between the non-destructive parameters typically used in strength grading and the mechanical properties of hardwoods [2].

The dynamic modulus of elasticity and the presence of knots remain the most common parameters used as predictors [3]. However, in the case of knots, strength grading machines struggle to detect them in hardwoods, as the differences in color (used by RGB cameras) or density (used by X-ray) are less pronounced than in softwoods.

Laser scattering is a well-known technique used to measure local grain direction in wood [4–6]. Grain disturbances are mostly associated with the presence of knots and can therefore be easily detected. In particular, for beech wood, this technique has been effectively tested for predicting tensile strength [7]. In this study, an optimized algorithm is implemented to calculate a grain direction parameter from laser scattering in beech wood. This parameter is then used as a predictor of bending strength and stiffness and compared to other parameters measured by machines (dynamic modulus of elasticity) or visually assessed by an operator (knots).

2 Material and Methods

2.1 Material

The experimental activities were conducted on 100 beech boards sourced from northeastern Italy. The cross-sections, lengths, and number of specimens are provided in Table 1.

Table 1. Nominal dimensions and number of specimens (N).

Cross section (b x h) (mm^2)	Length (mm)	N
20 x 100	4100	33
45 x 120	4300	42
50 x 140	4400	25

2.2 Measurements by machine sensors

Machine measurements were done by the MiCROTEC machine Goldeneye 706. The natural frequency of vibration of each board was determined by a laser interferometer, with the excitation necessary to induce a vibration provided by a steel ball mounted on a spring retracted piston rod.

Density was determined by X-ray radiation (Figure 1b), and the dynamic modulus of elasticity was calculated as follow:

$$E_{dyn} = 4f^2L^2\rho \tag{7}$$

where f is the natural frequency of vibration, L the length of the timber piece and ρ is the density.

Wood fibre orientation was measured as follow: the machine projects a pattern of circular laser dots onto each surface of the board while a set of cameras, positioned perpendicular to the measured area, captures the shape of the scattered dots on the surface. Since the light scatters more along the wood cells than across them, the direction of the wood cells is determined as the angle of the larger semi-axis of the scattered laser ellipse. As the board advances through the scanner, its entire surfaces are measured. On the wide faces (width) of the board the cameras measure the horizontal component of the fibre orientation angle, while on the narrow faces (thickness) they measure its vertical component. On each specimen, the board volume was divided into regions along all X-Y-Z directions. For each region, the horizontal and vertical components of the inner fibre angle were calculated by linear interpolation of the grain direction measured on the corresponding surfaces. A 3D-spatial fibre orientation was then calculated for each volumetric region, by combining the horizontal and vertical components with the formula [7]:

$$3DAngle = \arccos\left(\cos(HorizontalAngle) \cdot \cos(VerticalAngle)\right) \quad (2)$$

This provides, for each volumetric region, the expected grain angle relative to the boards' main axis. A Grain Direction (GD) profile was then produced by computing, for each centimetre along the board length, the average of all 3D-spatial angles within a 150 mm window (Figure 1d). For each board, the highest value of GD profile in the middle third of the bending test span (described below) was selected for further analysis.

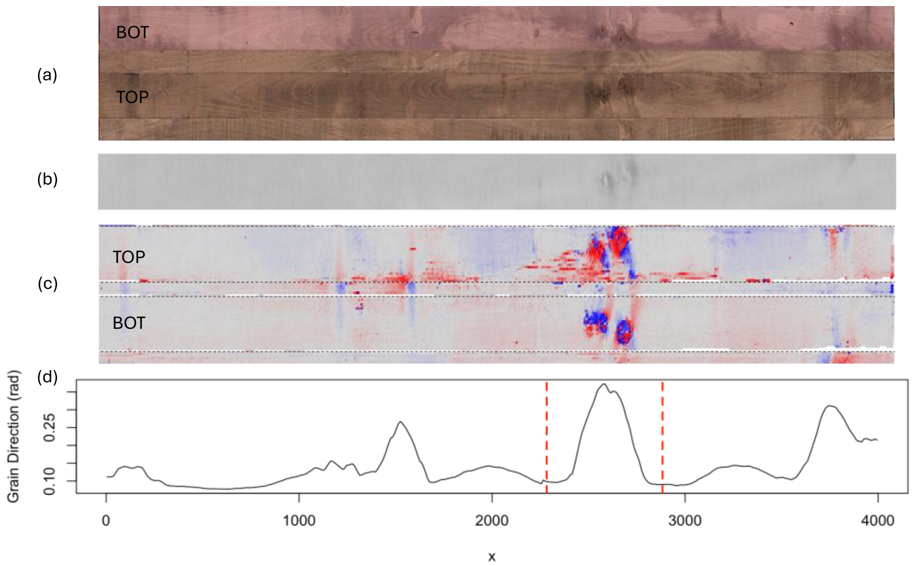

Fig. 1. Example of scan: (a) the four sides of the board by a RGB camera; (b) X-ray; (c) reconstruction of the fiber angles in the four sides (blue and red color indicated opposite grain direction; (d) profile of the average fiber direction.

2.3 Visual assessment

The knots were visually detected by an operator. The minimum diameter and its projection on the side of the board were recorded, and knot parameters were calculated as follows: (1) the ratio of the knot diameter to the dimension of the side (KN_D), and (2) the ratio of the sum of the knot projections on the sides to twice the width (KN_P) [8]. For each board, the highest value of each knot parameter within the middle third of the bending test span (described below) was selected for further analysis.

2.4 Destructive tests

Four-point edgewise bending tests were performed in accordance with the European standard EN 408 [9], to measure the local static modulus of elasticity and the bending strength. The total span was 18 times the nominal depth, with the load applied at two symmetrical points.

3 Results and discussion

Table 2 presents the descriptive statistics of mechanical properties and non-destructive evaluations for each cross-section. Among the various properties, only density differed significantly across cross-sections, with the smallest sections being the least dense. However, this had no effect on mechanical properties, as bending strength and stiffness did not vary with element size. Similarly, the dynamic modulus of elasticity, grain direction and knot parameters showed no significant differences.

Table 2. Mean values and standard deviation (in brackets) physical and mechanical properties and knot parameters by cross section.

Property	Symbol	Cross-section (mm^2)		
		20 x 100	45 x 120	50 x 140
Bending strength (MPa)	f_m	50.4 (± 19.6)	52.1 (± 20.6)	54.8 (± 18.7)
Modulus of elasticity (GPa)	$E_{m,l}$	11.6 (± 2.8)	11.9 (± 3.5)	12.2 (± 3.0)
Density (kg / m^3)	ρ	663 (± 22)	742 (± 26)	724 (± 34)
Dynamic MoE (GPa)	E_{dyn}	13.2 (± 1.7)	13.8 (± 2.3)	12.5 (± 2.1)
Grain direction (rad)	GD	0.41 (± 0.15)	0.38 (± 0.15)	0.37 (± 0.14)
Knot D_{min} / S (-)	KN_D	0.43 (± 0.38)	0.45 (± 0.32)	0.38 (± 0.29)
Knot sPr / 2w (-)	KN_P	0.22 (± 0.19)	0.30 (± 0.25)	0.24 (± 0.21)

The lack of influence of density on the mechanical properties of beech is confirmed by the coefficients of determination presented in Table 2, which were consistently close to zero for density. The same has been reported in previous studies for beech [8,10,11] and chestnut [2,12].

Among the other parameters, grain direction exhibited the highest predictive power for both strength and stiffness, with coefficients of determination of 0.61 and 0.67, respectively. This was higher than that of the dynamic modulus of elasticity, which is widely recognized as the single non-destructive property that best predicts the mechanical performance of timber. Predicting tensile strength by grain direction in beech, Rais et al [7] obtained a coefficient of determination ranging from 0.46 to 0.60 depending on the regression used for modelling.

Knot parameters showed moderate predictive power, similar to the dynamic modulus of elasticity. This is higher than what has been observed for other hardwoods [3] but has already been documented for beech. Indeed, a previous study comparing visual grading (based on knots) and machine grading (based on the dynamic modulus) found that both methods were equally effective for beech [8].

Of the two visually determined knot parameters, the one based on knot projection correlated better with strength, stiffness, and grain direction than the parameter calculated using knot diameter. This finding also aligns with previous observations [8].

Table 3. Coefficients of determination (R^2) of linear regression between variables. Symbols are explained in Table .

	f_m	$E_{m,l}$	ρ	E_{dyn}	GD	KN_D
$E_{m,l}$	0.74					
ρ	0.00	0.00				
E_{dyn}	0.42	0.49	0.01			
GD	0.61	0.67	0.00	0.35		
KN_D	0.40	0.45	0.01	0.19	0.38	
KN_P	0.48	0.60	0.02	0.37	0.50	0.59

The measurement of grain direction using laser scattering successfully detected the presence of knots in beech, as well as other localized grain disturbances that may influence its mechanical performance [13]. This resulted in a high level of predictive accuracy.

The grain direction parameter was plotted against strength and elastic modulus for each cross-section (Figure 2), demonstrating that the predictive ability was not affected by timber size. Indeed, the coefficients of determination remained very similar across cross-sections.

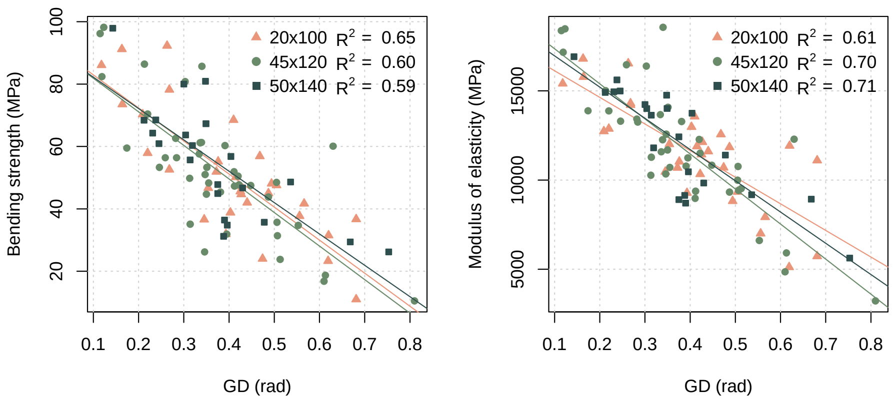

Fig. 2. Regression between bending strength (left) and modulus of elasticity (right) and grain direction for the three cross sections.

4 Conclusions

Grain direction, as detected locally by laser scattering, proved to be the best single predictor of bending strength and stiffness in beech, better than both the dynamic modulus of elasticity and visually determined knot parameters.

This technique effectively identified the presence of knots as well as other localized grain disturbances, which are common strength-reducing factors in beech.

Acknowledgments. This study was supported by the Agritech National Research Center and received funding from the European Union Next-GenerationEU (PIANO NAZIONALE DI RIPRESA E RESILIENZA (PNRR) –MISSIONE 4 COMPONENTE 2, INVESTIMENTO 1.4 – D.D. 1032 17/06/2022, CN00000022).

References

1. Schlotzhauer, P., Kovryga, A., Emmerich, L., Bollmus, S., Van De Kuilen, J.-W. Militz, H.: Analysis of economic feasibility of ash and maple lamella production for glued laminated timber. Forests, 10, 529 (2019).
2. Nocetti, M., Bacher, M., Brunetti, M., Crivellaro, A., van de Kuilen, J.W.G.: Machine grading of Italian structural timber: Preliminary results on different wood species. In: Proceedings of the World Conference on Timber Engineering, WCTE, Riva del Garda, Italy, 2010, pp. 285–292.
3. Vega, A., Dieste, A., Guaita, M., Majada, J., Baño, V.: Modelling of the mechanical properties of *Castanea sativa* Mill. structural timber by a combination of non-destructive variables and visual grading parameters. European Journal of Wood and Wood Products 70, 839–844, (2012).

4. Olsson, A., Oscarsson, J., Serrano, E., Källsner, B., Johansson, M., Enquist, B.: Prediction of timber bending strength and in-member cross-sectional stiffness variation on the basis of local wood fibre orientation. European Journal of Wood and Wood Products 71, 319–333, (2013).
5. Olsson, A., Pot, G., Viguier, J., Faydi, Y., Oscarsson, J.: Performance of strength grading methods based on fibre orientation and axial resonance frequency applied to Norway spruce (*Picea abies* L.), Douglas fir (*Pseudotsuga menziesii* (Mirb.) Franco) and European oak (*Quercus petraea* (Matt.) Liebl./*Quercus robur* L.). Annals of Forest Science, 75, 102, (2018).
6. Besseau, B., Pot, G., Collet, R., Viguier, J.: Influence of wood anatomy on fiber orientation measurement obtained by laser scanning on five European species. Journal of Wood Science, 66, 74, (2020).
7. Rais, A., Bacher, M., Khaloian-Sarnaghi, A., Zeilhofer, M., Kovryga, A., Fontanini, F., Hilmers, T., Westermayr, M., Jacobs, M., Pretzsch, H., et al.: Local 3D fibre orientation for tensile strength prediction of European beech timber. Construction and Building Materials, 279, 122527, (2021).
8. Brunetti, M., Nocetti, M., Pizzo, B., Aminti, G., Cremonini, C., Negro, F., Zanuttini, R., Romagnoli, M., Scarascia Mugnozza, G.: Structural products made of beech wood: quality assessment of the raw material. European Journal of Wood and Wood Products, 78, 961–970, (2020).
9. EN 408 Timber Structures. Structural Timber and Glued Laminated Timber. Determination of Some Physical and Mechanical Properties, CEN - European Committee for Standardization: Brussels, 2012,
10. Cibecchini, D., Cavalli, A., Goli, G., Togni, M.: Beech sawn timber for structural use: a case study for mechanical characterization and optimization of the italian visual strength grading rule. Journal of Forest Science, 62, 521–528, (2016).
11. Ehrhart, T., Fink, G., Steiger, R., Frangi, A.: Experimental investigation of tensile strength and stiffness indicators regarding European beech timber. In Proceedings of the World Conference on Timber Engineering, WCTE, Vienna, Austria, Vienna University of Technology: Vienna, 2016, pp. 600–607.
12. Nocetti, M., Brunetti, M., Bacher, M.: Efficiency of the machine grading of chestnut structural timber: prediction of strength classes by dry and wet measurements. Materials and Structures, 49, 4439–4450, (2016).
13. Ehrhart, T., Palma, P., Schubert, M., Steiger, R.; Frangi, A.: Predicting the strength of european beech (*Fagus sylvatica* L.) boards using image-based local fibre direction data. Wood Science and Technology, 56, 123–146, (2022).

EDGE-o-SCOPE System for real-time assessment of laminated particleboard edge quality

Palubicki Bartosz[1][0000-0003-3915-1781], Kowaluk Grzegorz[2][0000-0003-1463-0540], Negri Martino[3][0000-0002-0351-4723], Sandak Jakub[4, 5][0000-0001-9190-677X]

[1] Poznan University of Life Sciences, Wojska Polskiego 28, 60-637 Poznan, Poland
[2] Warsaw University of Life Sciences, Nowoursynowska 166, 02-787 Warszawa, Poland
[3] National Research Council, via Biasi, 75 - 38010 San Michele all'Adige (TN), Italy
[4] InnoRenew CoE, Livade 6a, 6310 Izola, Slovenia
[5] University of Primorska, Muzejski trg 2; SI-6000 Koper, Slovenia

Abstract. The quality of laminated particleboard edges plays a crucial role in the furniture industry, as defects can lead to significant financial losses and damage to a company's reputation. The typical cabinet production process dividing laminated panels is performed in sawing or nesting operations. Both can generate cracks and spalls on the top and bottom laminates. Early detection of these defects minimizes costs associated with repairs and replacements. This paper introduces the Edge-o-Scope, a real-time edge quality control system designed to meet industrial requirements, including integration into existing production lines and operation at feed rates up to 100 m/min. Based on a simplified triangulation method, the system uses a laser line and camera setup to detect edge defects by measuring deviations in edge profiles. The system might be controlled by a standard PC or by a very reliable Real-Time Compact Vision System controller. It calculates three quality indicators - maximum crack width, weighted crack area, and cumulative weighted crack area - to classify the panel quality. When installed in-line, e.g., by the feeder to the edge-bander, it can be a decision maker, accepting or declining the element for further production. The Edge-o-Scope prototype demonstrates reliability despite melamine coating color changes.

Keywords: laminated panels, laminated particleboard, melamine coating, edge quality

1 Introduction

The quality of the edge of panels made out of laminated particleboard is a very important issue in the furniture industry. The problem of this quality is the occurrence of spalls (see Fig.) being the effect of machining (sawing, routing, etc.). Low quality of the edges may be a source of significant costs, which strongly depend on the stage when the defect is detected. In the worst case, when the element of poor edge quality is noticed by the customer who has bought the furniture, the costs of a complaint (new cabinet, transportation, montage, etc.) have to be covered by the cabinet producer. The image of a company loses its value, which brings extra loss of possible income. On the other side, in the best case the defected edge of the panel is detected just after milling or final sawing. The minimal cost of the element reproduction is generated. In between these two cases, the costs augment with the stage of detection because more technological operations have to be redone. The Sooner the defective edge is recognized, the lower the costs provoked. If the quality limit is not satisfied, it should be detected before cabinet assemblage, reproduced, and then replaced in the material flow.

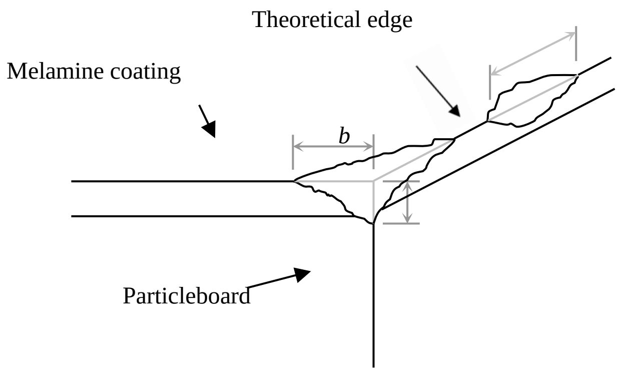

Fig. 1. Cracks on the edge of laminated particleboard

Advancements in woodworking and machining technologies have enabled the development of sophisticated methods for quality evaluation. Manual inspections, once the norm, are increasingly being replaced by automated systems that offer greater precision and consistency. Optical techniques, including image analysis and triangulation-based methods, have shown significant promise. Salje and Drueckhammer (1984) explored in-line methods for measuring edge roughness, while Coelho et al. (2005) investigated the influence of machining conditions on the finished wood surface quality, demonstrating the potential of optical methods in production environments.

Edge quality evaluation systems have evolved to include highly specialized setups, such as the EQUAM PC4 system described by Hesselbach (n.d.), which provides a framework for assessing the edges of coated wood materials. Hoffmeister and Gruebler (2004) highlighted the growing integration of quality control into machining centers, further emphasizing the industry's shift toward automation. However, challenges persist in adapting these systems to high-speed industrial environments, where feed rates often exceed 20–60 m/min (Porankiewicz & Tanaka, 2001).

One of the key developments in this domain is the application of triangulation methods for defect detection. Mammel (1998) and Salje and Stuehmeier (1988) demonstrated the effectiveness of such techniques in capturing geometric deviations in edge profiles. These methods have been further refined to accommodate variations in panel coatings and machining conditions, as seen in studies of Garrido et al. (2006) and Salje et al. (1985). Despite these advancements, achieving real-time, high-speed edge quality assessment with minimal system complexity remains a challenge.

Therefore, it might be stated that there is a need for a high-yield method of 100% control of the panels' edges as soon as the final edges are created. The detector must

work with the normal feed rates used in the industry and should not require any extra operation (implementation in the existing production lines).
The goal of the present work is to propose a system fulfilling the above demands for in-line control of laminated particleboard edge quality after machining. The output of such a system would be a simple signal informing the operator at once if the quality of the panel is below the acceptable limit.

2 Methods

The edge quality assessment chosen to fulfill the goal integrates insights from studies by Porankiewicz (1993), Salje, and Drueckhammer (1985) to propose a novel approach. The edge quality controlling system called Edge-o-Scope is based on a simplified triangulation method. Laser line light is directed to the edge of the panel at some angle to its wide surface (see Figure 2). Watching this line with a camera set on the other angle allows observing the height of all illuminated points by the positioning of the line, appearing segmented and curved (see Figure 3).

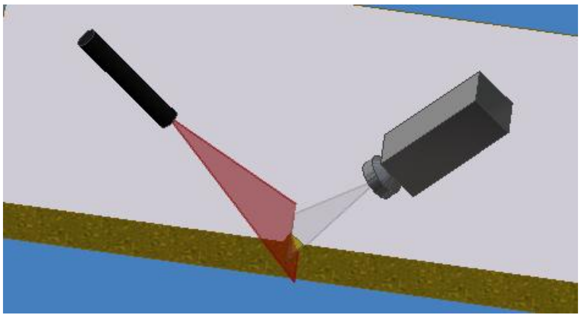

Fig. 2. Simplified triangulation method scheme

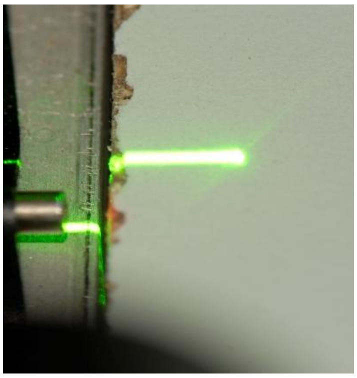

Fig. 3. Camera view of fragmented and curved laser line

The base height is determined by the panel's wide surface position (in fact, panel thickness), and all points of the structure located out of this plane (like cracks on the edge) are considered to be defects.

Usually, area-scan cameras are necessary for the triangulation method; in the current set-up, a line-scan camera might be used since no crack depth information is necessary. In such a case one cannot obtain the information on the depth of spall or crack in a current spot. By sequential measurements of panel passing with a feed speed, it is possible to integrate the single results into the complete measurement of separate spalls' area on the surface of the panel.

It is assumed that the low quality of the edge might be caused by a poor edge on its whole length or acceptable most of the edge and one or more local cracks so big that they disqualify the panel. Therefore three quality indicators are proposed:

- Maximum width of local defect bmax (mm2) – is the maximal width of a spall (or spalls along the whole edge). The width value is measured on the wide surface of the panel, counting from the theoretical edge (see Fig.). The value is calculated as a maximum of the edge profile function (Eq. 1).

$$b_{\max} = Max\big(b(x)\big) \tag{8}$$

- Weighted area of a single crack Wi (mm2) – is also dedicated to pointing out the local defects. The weighted area is calculated for each i crack, as shown by Eq 2. The weighting function (Eq. 3) is applied to decrease the importance of narrow cracks (narrower than the critical width bg) and highlight wider cracks.

$$W_i = \int b(x) w(x) dx \tag{9}$$

$$w(x) = \left(\frac{b(x)}{b_g} \right)^2 \tag{10}$$

  The bg (mm) is the critical width of the spall.

- Specific weighted area of cracks Qm (mm2/m) – indicates the global edge quality by means of the cumulative weighted area of all cracks referred to the edge length (eq. 4).

$$Q_m = \frac{1}{l_e} \sum_i W_i \tag{11}$$

Where le (m) is the length of the assessed panel's edge.

Each of these parameters, compared to preset values, may cause an alert to occur during the measurement. The most rigorous option regarding edge quality is to classify the panel as good only when all three alerts indicate a PASSED value. Some of the alerts may be switched off if needed. The block diagram of the proposed algorithm is presented in Fig. .

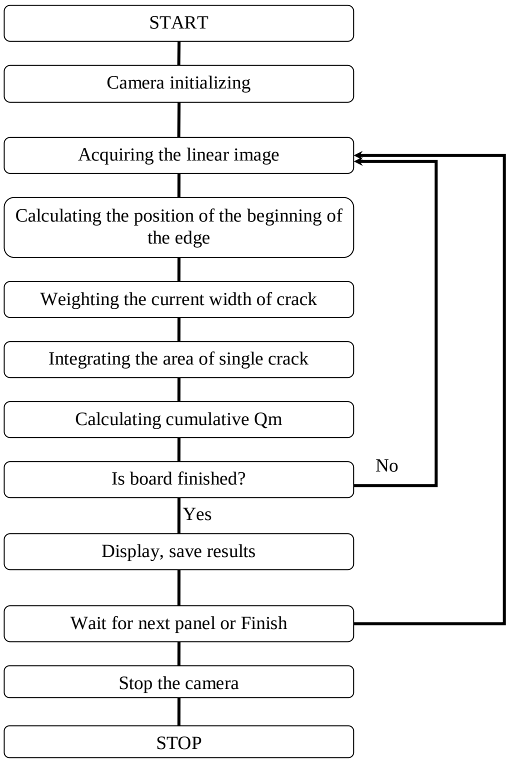

Fig. 4. Block diagram of Edge-o-Scope software

3 Results

3.1 Hardware

The panel's edge classifying system was invented in IVALSA / CNR. Edge-o-Scope device was first a prototype built with the use of adjustable supports (see Fig. 5). Next, a non-adjustable version was created (see Fig. 6), but for later use in existing production lines, it might have an even more compact shape and size. It is possible to apply Edge-o-Scope in the existing manufacturing lines (e.g. on edge banding machine).
An area-scan CCD camera, working as a single line-scan one, was used working at a maximum of 8 kHz, which is enough to scan edges with efficient resolution (each 0,2 mm) with feed rates reaching almost 100 m/min. The beam of light necessary for the triangulation is provided by the green laser line projector of power 5 mW.
For detecting if the board has arrived at (or has left) the measuring unit, one or two (optional) proximity sensors are installed.

The hardware of the system was very easy to maintain. All components of the device are fixed and there is no need for adjustment. The only thing to be regulated is the height position of the main support, which depends on the panel thickness. Motorization of this adjustment is possible.

The system might be controlled by a standard PC or by a more reliable Real-Time Compact Vision System controller.

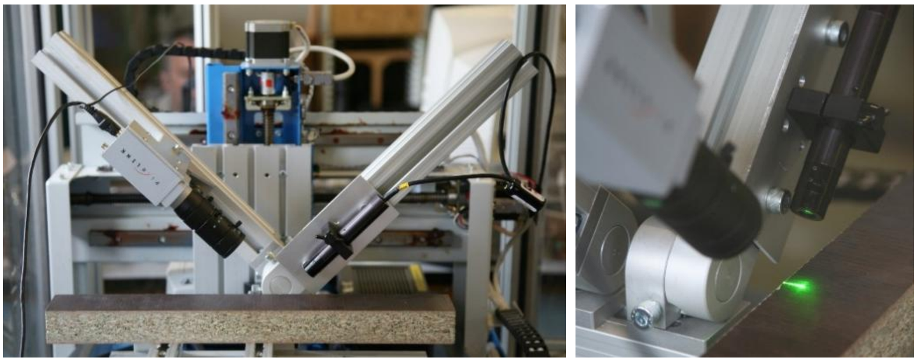

Fig.5. Adjustable Edge-o-Scope prototype

Fig.6 . Non-adjustable version of Edge-o-Scope prototype

3.2 Software

For performing measurements and maintaining the hardware, two software versions have been created in the LabView environment: one for the PC / Windows system and another for the Compact Vision System / Real-Time system. The software is simplified as far as possible to ensure high efficiency and compliance with the industrial feed rates of panels. The basic version of the software includes only alert limits to be set up (depending on producers' requirements for the edge quality) and the PASSED / FAILED indicator, showing if the panel under inspection fulfills the mentioned requirements or not. More advanced analysis of edges, including visualizing the edge profile and its filtering was also possible (see Fig. 7).

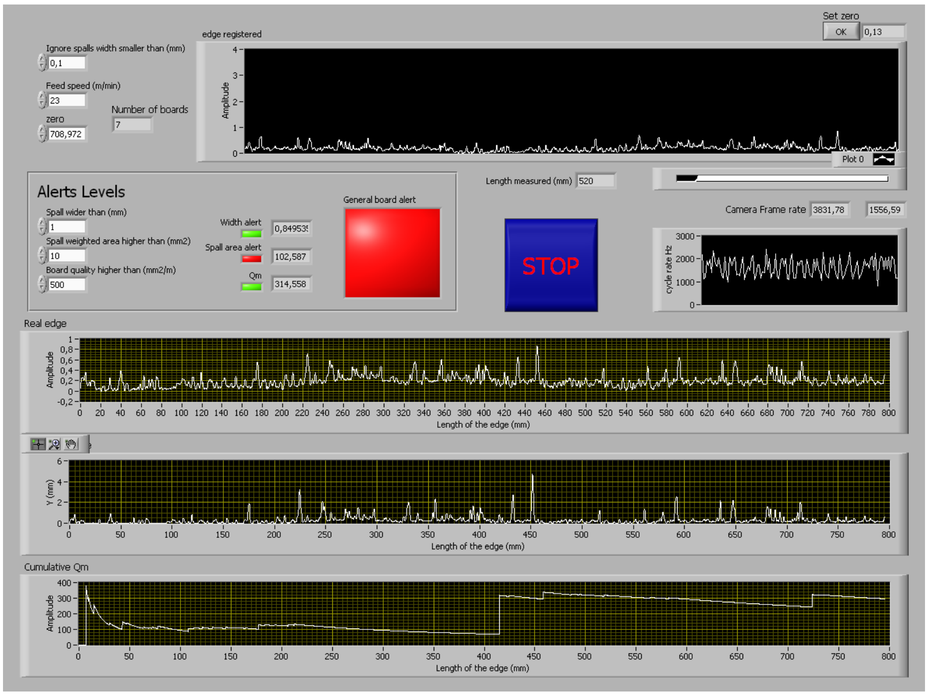

Fig.7. Interface of advanced edge analyzer

In Fig. 8, the photo of the panel’s edge is shown against its resulting profile determined with the use of the Edge-o-Scope system. Besides the 3 parameters calculated directly as the panel passes, the edge profile is available for further, more advanced analysis.

Fig. 8. Comparison of edge photo and its profile

3.3 Validation of the method

The presented method, prototype, and software as a whole system were provisionally validated by recognizing different edge defects and by testing panels with different melamine coating colors. In Table 1, three artificially made spalls are shown together with their obtained profiles and results of measurements. They represent different shapes, and widths from less than 2 mm to over 3 mm. A wider but shorter crack (case b), even if it has a smaller area, is qualified as worse (in terms of weighted area) compared to a longer but narrower crack (case c). And in fact, these kinds of cracks are more unwanted on the edge of the panel. Spalls a) and b) have similar lengths (c.a. 5mm) and slightly different areas, but the weighted area parameter of a) spall is twice as big as that of b), because of its bigger width. This stays in accordance with the subjective feelings of the authors about the “weight” of the problem.

Table 1. Different spalls, their profile reconstruction, and analyzed quality indicators

a)	b)	c)
		
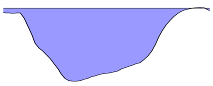	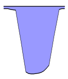	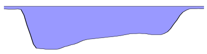
Width *b* (mm) = 2,93 Area (mm^2) = 10,55 Weighted area *W* (mm^2) = 151,7	Width *b* (mm) = 3,09 Area (mm^2) = 5,18 Weighted area (mm^2) = 82,8	Width *b* (mm) = 1,88 Area (mm^2) = 8,95 Weighted area (mm^2) = 76,8

Fig. 9 presents the spall on the left-hand side and two fake cracks drawn with a permanent marker. The edge profile detected by the Edge-o-scope is shown below and is not influenced by the fake cracks. It means that the system is resistant to coating color changes (e.g., multi-color printouts on decorative paper or artificial dirt). It measures the geometry of the edge and is not influenced by the color pattern, which is the big issue in commonly used image analysis based quality control systems.

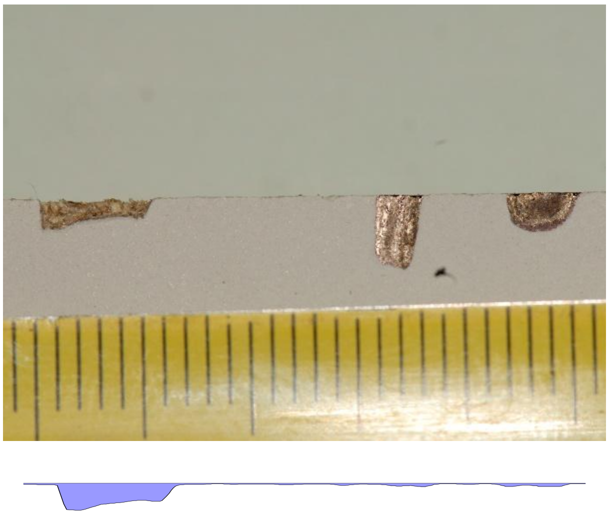

Fig. 9. Negligible influence of color change on the resulting profile

4 Summary

The presented Edge-o-scope prototype system is a high-performance and high-resolution scanner for the edges of melamine-coated panels compatible with existing manufacturing setups (feed rates of up to 100 m/min). It uses a simplified yet effective triangulation-based solution for detecting and quantifying edge defects. Calculating three key indicators—maximum crack width, weighted crack area, and cumulative weighted crack area, ensures a comprehensive evaluation of panel edges. Its advantages are:

- Simple construction and software and operation
- Possibility of applying in high-speed panel processing lines
- Elasticity of setting acceptability limits for the quality
- Short qualification time (may be even before finishing of panel scanning)
- Certainty of detecting low quality panels' edges for different panel colors

References

1. Salje E., Drueckhammer J. (1984): Qualitaetskontrolle bei der Kantenbearbeitung. Holz als Roh- Werkstoff 42: 187-192
2. Coelho C., Martins J., Carvalho L., Massan D., Meausoone P. (2005): A novel method for evaluating the influence of wood machining conditions on the quality of a finished surface. Materiały konferencyjne: 17th Inter. Wood Machining Seminar, Resenheim, Germany
3. Hesselbach J. ( ): Kantenschartigkeitmesssystem fuer beschichtete Holzwerkstoffplatten EQUAM PC4. *Commercial materials*
4. Hoffmeister H.W., Gruebler T. (2004): Qualitaetskontrolheim Bearbeitungszentrum. HOB 6 52

5. Porankiewicz B., Tanaka Ch. (2001): Workpiece Edge Quality after Milling Melamine-Coated Particleboard. Mem. Fac. Sci. Eng. Shimane Univ. Series A (35): 139-147
6. Mammel R. (1998): Maschinell sehen. Holz- und Kunststoffverarbeitung 2/1998
7. Salje E., Stuehmeier W. (1988): Milling Laminated Chipboard with Tungsten Carbide and PCD. Industrial Diamond Review (4): 171-178
8. Garrido N., Martins J., Carvalho L., Mendes J., Costa C. (2006): A novel method for evaluating the influence of wood machining conditions on the particleboard edges. Proceedings of International Conference on Integrated Approach to Wood Structure, Behaviour and Applications, 15 – 17 may, Florence, Italy, p. 291 – 296
9. Salje E., Drueckhammer J., Keuchel K. (1985): On-line Measuring the Edge Roughness of Wooden Materials at Machining. Proceedings of the 8th International Wood Machining Seminar, October 1985, University of California Forest Products Laboratory, USA, p. 342 – 349
10. Porankiewicz B. (1993): The Relation Between Some Mechanical Properties and the Edge Quality When Milling Melamine Coated Particle Board. Proceedings of 11th IWMS, May 25-27 Oslo: 515-519
11. Salje E., Drueckhammer J. (1985): Kantenschartigkeitsmessung an beschichteten Spanplatten, Holz-Zentralblatt, 122

Use of millimeter waves for non-destructive quality analysis during the production stages of fiber-based panels

Massimo Bergonzini[1], Riccardo Centi[2], Giuseppe Amico[3]

1 IMAL srl, Modena, Italy, Manager, Electronic Production Dept.

2 IMAL srl, Modena, Italy, R&D Developing Engineer

3 IMAL srl, Modena, Italy, R&D Project Engineer

massimo.bergonzini@imal.com

Abstract. Millimeter waves (mmW) represent a new frontier in the field of non-destructive testing (NDT) of materials, particularly for plant-based composite products. Positioned between visible light and radio frequencies, mmW offer excellent penetration capabilities comparable to X-rays, but without the associated health risks. Unlike conventional X-ray sources commonly used in industrial settings—which require expensive cooling systems and have a limited operational lifespan—millimeter-wave technologies provide a safe and sustainable alternative.

However, the widespread adoption of this technology is currently hindered by the high cost of the required hardware and equipment. To date, mmW have been primarily employed in military applications, satellite synthetic aperture radar (SAR) systems, airport security scanners (body scanners), experimental dielectric measurements, and next-generation communication networks (5G and 6G), although the millimeter spectrum has yet to be fully implemented in the latter.

Since 2016, Imal has established a dedicated research group focused on developing mmW-based solutions aimed at progressively replacing X-ray sources in quality control systems. The first results have already led to operational solutions, which are now being implemented in industrial plants equipped with advanced technologies.

Keywords: millimeter waves, non-destructive testing (ndt), industrial quality control

1 Introduction

Imal Srl, headquartered in Modena, is a leading company in the design and production of plants and machinery for the wood industry and other industrial sectors. Founded with a strong commitment to innovation, the company has established itself on the international stage thanks to its continuous pursuit of advanced technological solutions, ensuring quality, reliability, and sustainability in its products. With solid experience

and consolidated know-how, Imal stands out for its focus on quality and sustainability, significantly contributing to the development of the Italian industrial sector.
Thanks to a highly qualified team and constant investment in research and development, the company has secured a prominent role on an international level. Its ability to offer cutting-edge, customized solutions has allowed Imal to effectively respond to the needs of an ever-evolving market.
Recently, the company has introduced new technologies aimed at optimizing production and reducing environmental impact, reaffirming its commitment to the transition toward an increasingly green and sustainable industry.
With its combination of tradition, innovation, and sustainability, Imal Srl establishes itself as a reference point in the sector, showcasing the excellence of Made in Italy worldwide.

2 Materials and Methods

2.1 Millimeter Waves: Innovation for Non-Destructive Testing in the Wood Industry

In the industrial production sector, material quality control is crucial to ensuring safety, efficiency, and waste reduction. Traditionally, X-ray technology has been widely used for non-destructive testing (NDT); however, it presents several challenges, including the hazards of ionizing radiation, high maintenance costs, and strict regulations. Today, an emerging alternative is gaining traction: millimeter waves (mm-wave), a technology that promises to revolutionize the sector with its numerous advantages.

2.2 The Limitations of X-Ray Technology

The use of X-rays in production processes involves several operational and regulatory constraints. First, as ionizing radiation, they require strict safety measures, such as lead shielding and mandatory operator training. Additionally, maintaining a stable temperature in X-ray tubes and using different energy levels to obtain spectrographic images necessitate expensive cooling systems and frequent maintenance to replace components.

From a legal perspective, the use of X-rays is subject to strict international regulations and specific customs declarations for the transportation and installation of devices. Lastly, environmental impacts related to the regulated disposal of hazardous materials cannot be overlooked.

2.3 The Millimeter Wave Alternative

Millimeter waves, positioned between visible light and radio frequency, offer a highly innovative solution for non-destructive testing. Unlike X-rays, mm-waves do not emit ionizing radiation, eliminating health risks and reducing the need for shielding and specialized training. Additionally, this technology requires less energy, lowering operational costs.

From an application standpoint, millimeter waves provide high penetration capability into materials and can be used across various industrial sectors. Key applications include the military sector (SAR radar and precision-guided munitions), airport security (body scanners), 5G and 6G communications, and dielectric measurements for material analysis.

3 Results and discussion

3.1 Challenges in the Adoption of Millimeter Waves

Despite their many advantages, mm-wave technology still faces challenges in achieving widespread adoption. One major obstacle is the high cost of hardware, driven by the need for advanced sensors, high-frequency antennas, and specialized semiconductor materials such as GaAs and GaN. Furthermore, limited production currently prevents economies of scale.

From an operational standpoint, millimeter waves have a limited range and are sensitive to target orientation, necessitating the use of multiple devices or repeaters to enhance measurement accuracy. Additionally, as an emerging technology, global regulatory standardization is still lacking, complicating industrial adoption.

3.2 Imal's Role in Millimeter Wave Research

Since 2016, Imal has initiated a research and development program focused on applying millimeter waves in the wood industry, aiming to replace X-ray-based systems. The results of this effort are already evident:

- In 2018, the company began initial experiments, demonstrating the correlation between wood density and moisture content with its dielectric properties.
- In 2019, the first reflectometer prototype was presented at the Hannover exhibition.
- In 2020, a millimeter-wave system was installed at an Italian customer's facility, achieving an accuracy of 3% compared to laboratory measurements.
- Between 2021 and 2025, Imal has been developing Synthetic Aperture Radar (SAR) for detecting foreign objects in industrial materials.

3.3 Innovation and Accessibility: The Breakthrough in Reflectometry Systems

Laboratory measurements conducted using Waveguide technology have confirmed that mm-wave technology is highly effective in analyzing the dielectric properties of wood. The millimeter-wave reflectometry method allows for the measurement of the complex dielectric constant in free space, applicable to both single and multilayer materials.

Imal has developed an innovative industrial reflectometer capable of offering accuracy comparable to laboratory instruments but at a significantly lower cost. This technology enables real-time, low-cost measurements, making it accessible to production sectors characterized by mass production and low technological investment margins, such as the wood industry.

3.4 The Future: Synthetic Aperture Radar (SAR) for the Industrial Sector

Looking ahead, Imal is working on applying Synthetic Aperture Radar (SAR) to the wood sector. This technology, already employed in airport security and satellite detection, enables data acquisition from multiple angles and positions to reconstruct highly precise three-dimensional models. The goal is to identify and classify contaminants in recycled wood, allowing for their selective removal.

Imal's objective is to develop an optimized version for the industrial sector, reducing implementation costs and overcoming the limitations of X-ray technologies.

4 Conclusions

Millimeter waves represent a revolutionary technology for non-destructive material analysis, with the potential to surpass X-ray limitations in terms of safety, cost, and sustainability. Although challenges related to hardware costs and commercial adoption still exist, research advancements and the development of accessible solutions are accelerating industrial adoption.

Thanks to the commitment of companies like Imal, the wood industry is approaching a new era of innovation, where millimeter waves will become an essential tool for material quality control and safety.

Early wood quality assessment for a better use of the forest resource. The DigiMedFor project

Michela Nocetti[1][0000-0003-0906-0483], Giovanni Aminti[1][0000-0003-2262-4095], Michele Brunetti[1][0000-0001-7105-0716], Giovanni Fontani[1], Simo Kivimaki[2], Timo Rouvinen[2] and Luigi Saulino[3][0000-0003-4939-0583]

[1] CNR IBE, Institute of Bioeconomy, 50019 Sesto Fiorentino (FI), Italy
[2] Trestima Oy, Solkimäenkatu 29, 33710 Tampere, Finland
[3] University of Naples Federico II, Via Università 100, 80055 Portici, Italy
michela.nocetti@cnr.it

Abstract. The in-situ wood evaluation aims to advance timber quality assessment by addressing it earlier in the supply chain, directly in the forest on standing trees and shortly after harvest on felled logs. This perspective provides forest owners with valuable insights into the quality of their properties, offering a clear understanding of the potential value of their trees. Unlike traditional methods, our approach is designed to provide quick and easy-to-use evaluations, saving time and effort while delivering enhanced value information.
An inventory app is being trained to assess the stems of standing trees, generating a quality index that will be included in the inventory report for each forest parcel. Both forest owners and users will benefit from this enhanced understanding of forest compartment quality, enabling more efficient buying and selling decisions.

Keywords: stem quality, mobile app, forest inventory.

1 Introduction

Along the forest-wood value chain, wood quality is often assessed on the semi-finished or finished product stage, when both marketing strategies or compliance with the legislation (i.e. in the construction sector) make it either profitable or necessary. However, anticipating the quality evaluation to forests stands or roundwood soon after logging could provide additional advantages from both a forest management and resource exploitation perspective [1]. On the one hand, having information about quality besides quantity could support decision-makers in silvicultural choices to cultivate value. On the other hand, a better understanding of the wood resource would optimize selling and purchasing decisions, finding the best destination for the material according to its qualitative characteristics.

In this context, the DigiMedFor project aims to modernise the technological landscape of the Mediterranean forest-wood supply chain (https://digimedfor.eu/). The project focuses on simultaneously enhancing competitiveness and promoting sustainable management by, among other initiatives, implementing quick and easy-to-use tools for assessing the quality of standing trees and logs. Here, the activities done to evaluate standing trees are presented.

2 Material and methods

The quality assessment is using an inventory mobile application, Trestima, to assign to each forest unit a quality index related to the quality of the trees inside it.
Trestima is a mobile application working on pictures taken from the mobile camera while walking across the forest [2]. Thanks to image analysis techniques, tree stems are segmented, the wooden species are identified and their stem diameters are measured (Figure 1). Reports about the basal area, diameter distribution, tree height and volume are produced.

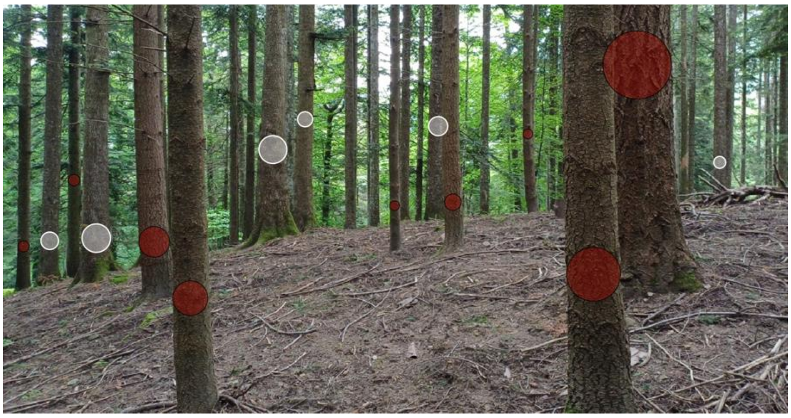

Fig. 1. Image analyzed by Trestima app for tree recognition and diameter measurement. Pictures were taken in Douglas fir (*Pseudotsuga menziesii*) stand of the Vallombrosa Forest (Tuscany, Italy)

In the territory of the Model Forest of Montagne Fiorentine, Italy, a survey was done to evaluate the quality of Douglas fir tree stems in 31 forest units. A quality index was elaborated so to divide the plot into three classes: being the class 1 the best and the three the worst. The index was based mainly on the first 5-6 m stem form and branchiness. A quality index was assigned to each surveyed plot.
Pictures were taken with the mobile app in all the plots, and a training was carried out to improve stem segmentation and branch recognition, and subsequently predict the quality index of the plot.

3 Results

The smart application was effective in segmenting stems and defining them accordingly. However, further refinement is required for branchiness, as the segmentation was not sufficiently accurate for longer branches (see Figure 2). Nonetheless, the correlation between the Human-made quality index and the Trestima QI prediction was moderately significant (r = 0.58). Efforts are currently underway to enhance the detection of protruding branches, which is expected to significantly improve the picture-based quality predictions.

Fig. 2. Stem and branches segmentation.

Acknowledgments. This study was supported by DIGIMEDFOR project, European Commission's HORIZON-CL6- 2022-CIRCBIO-02-two-stage (Project No. 101081928).

References

1. Nocetti, M.; Brunetti, M.: Advancements in wood quality assessment: standing tree visual evaluation—a review. Forests, 15, 943, (2024).
2. Ficko, A. Bayesian evaluation of smartphone applications for forest inventories in small forest holdings. Forests, 11, 1148, (2020).

Critical Speed Design of Circular Saws

Gary S. Schajer

University of British Columbia - Vancouver, Canada
schajer@mech.ubc.ca

Abstract. The critical speed concept is introduced as a basis for circular saw design. The cutting behavior of a circular saw is shown to be a vibrational response to the applied cutting forces. Resonant vibration occurs when the saw rotates at a speed close to a "critical speed," causing large lateral motions and "snaking" sawcuts. Saw tensioning is effective in increasing critical speeds by 20-30%. For a traditional collared saw, stable operation can be achieved up to 85% of the lowest critical speed. Guided saws are generally more stable and can operate super critically between the first and second critical speeds. This allows guided saws to have thinner kerf than equivalent collared saws.

Keywords: Circular saws, Critical Speed, Cutting Stability.

1 Introduction

Circular saws are a very common and popular type of tool for cutting many different materials, including wood, plastics and metals [1,2]. They have the advantage of being straightforward to use and to be available in many different types and designs at economical cost. They are particularly popular in sawmills because a group of several saws can be combined onto a single shaft so that they can cut many lumber pieces simultaneously within one machine.

There are many details to consider when designing a circular saw. For example, the size, shape and number of the teeth must be designed to work effectively for the particular application. This is an area of much research and innovation, discussed in detail elsewhere [1,2]. In terms of overall geometry, the diameter of the saw must be sufficient to accommodate the desired depth of cut and the thickness sufficient to handle the loads during the cutting process. Rotation speed also plays a key role, with higher speeds allowing faster cutting rates. However, these latter design quantities are interconnected and need to be considered together to make an effective design.

Sawblade stiffness is a fundamental concern in circular saw design [3,4]. An operating saw must be sufficiently stiff to withstand the cutting forces, both in- and out-of-plane. A larger outside diameter reduces stiffness, which can be compensated by increasing the tool thickness. However, a greater thickness increases the kerf width and the amount of sawdust waste that is produced. Thus, there is a practical pressure to minimize saw thickness. However, thickness reduction cannot be taken too far else the saw will have insufficient stiffness to withstand the cutting forces. In that case the saw will not cut in a straight line and will produce inaccurate lumber.

Saw rotation speed also strongly affects saw stiffness [4]. Since the saw is a moving object, it is the dynamic stiffness of the saw at its operating speed that is the controlling factor rather than the static stiffness when at rest. In general, the dynamic stiffness of a saw decreases with rotation speed, although in some circumstances there may be an initial increase. This is a vibration phenomenon, where if the saw rotation speed increases to reach a critical speed, the dynamic stiffness falls to zero and a vibrational resonance occurs, causing large lateral oscillations called "snaking" [5,6,7].
This paper describes the vibration characteristics of a circular saw and how they are affected by saw rotation speed, reaching a resonance with zero dynamic stiffness at the critical speed. The consequent large lateral motions of the saw at or near critical speed cause curving sawcuts and rejected lumber. A method of increasing sawblade critical speed is discussed, also alternative circular machine designs that can allow super-critical speed operation.

2 Circular Saw Standing Wave Vibration

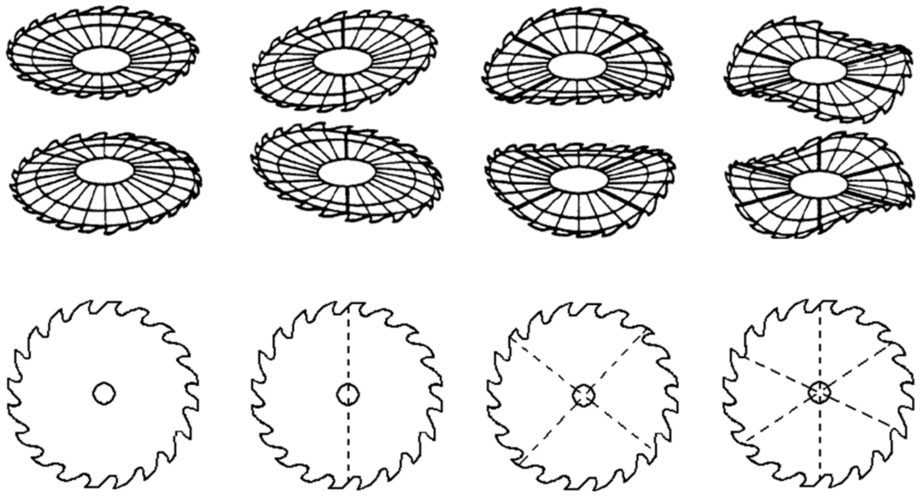

Fig. 1. Vibration mode shapes of a circular saw. (a) 0 nodal diameters, (b) 1 nodal diameter, (c) 2 nodal diameters, (d) 3 nodal diameters.

Fig.1 illustrates the first four vibration modes of a circular saw [7,8]. The first two rows of diagrams show the deformed shape of the saw at the extremes of the vibration. During the vibration the saw oscillates between one extreme and the other. Typically, vibrations are very small and the deformations shown in the figure are greatly exaggerated to show the shapes more clearly. The third row of diagrams shows the face-on views of the sawblades, where the dashed nodal lines indicate the positions of zero vibrational motion. These lines form the boundaries between the areas where the saw is vibrating to one side and where the saw is vibrating to the other side (upward and downward in the first two rows). The nodal lines take the form of evenly spaced diameters called nodal diameters. Fig.1 shows the first four vibration modes corresponding to 0 to 3 nodal diameters. Similar vibration modes with higher numbers of nodal diameters exist, theoretically up to infinity. Each vibration mode has its own natural (resonant) frequency, in general increasing with numbers of nodal diameters. Fig.2 illustrates the displacements around the rim of a circular saw over one vibration cycle of a 2-nodal diameter vibration mode. Fig.2(a) shows the mode shape whose nodal diameters form an × shape corresponding to Fig.1(c), while Fig.2(b) shows the similar vibration mode whose diameters form a + shape, similar to Fig.1(c) but rotated 45°. Because of the circular symmetry of the saw, the two vibration modes are the same, with the same natural frequencies; they just vary in their angular positions. They are called standing waves because the node positions indicated by the dashed lines stand in fixed places on the sawblade.

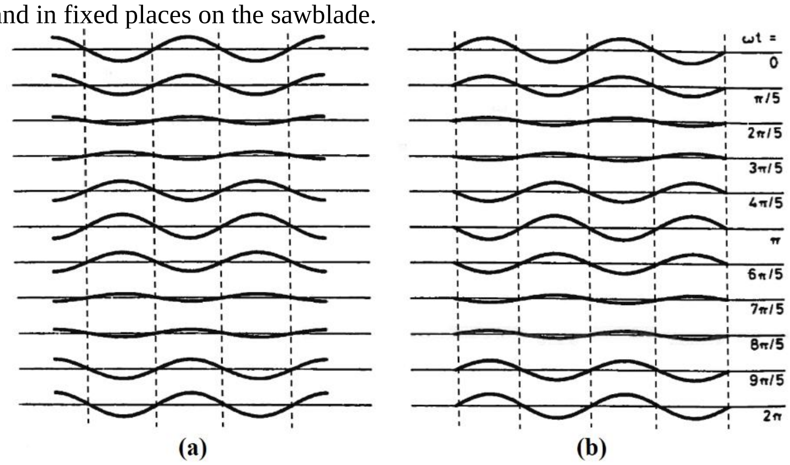

Fig. 2. Standing wave displacements around the rim of a circular saw over one vibration cycle of a 2 nodal diameter vibration mode. (a) × shaped mode, (b) + shaped mode.

3 Circular Saw Traveling Wave Vibration

In Fig.2, the two vibration modes are shown as having the same phase, such that they reach their extreme values at the same time. If the two vibration modes were present at the same time, they would combine to form a similar 2-nodal diameter standing wave vibration mode at some intermediate angle depending on the relative magnitudes of their vibrations. Alternatively, if the vibration in one mode occurred one quarter cycle out of phase, then the two vibrations would combine to form a traveling wave, as shown in Fig.3. Depending on whether the vibration modes are separated by plus or minus a quarter cycle, either a backward or forward traveling wave will be created. These traveling waves rotate at the same speed and have the same natural frequencies as the component standing waves in Fig.2.

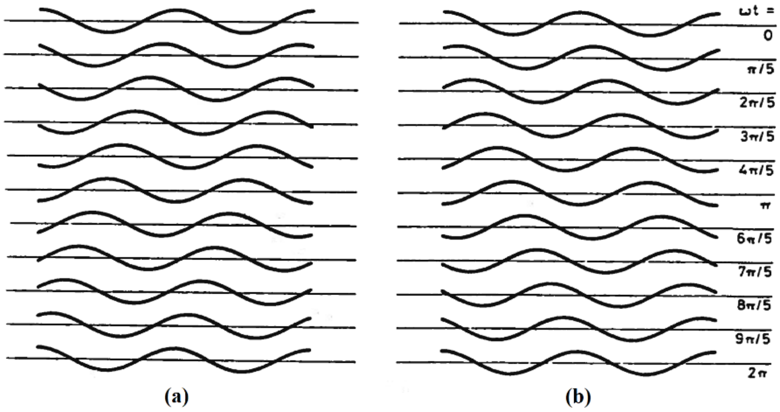

Fig. 3. 2-nodal diameter traveling wave displacements around the rim of a circular saw over one vibration cycle. (a) backward traveling wave, (b) forward traveling wave.

The discussions so far have been for a stationary circular saw. When the saw rotates it carries the vibrations with it. The saw rotation adds to the speed of the forward traveling wave and subtracts from the speed of the backward traveling wave. This causes the speeds of the two waves and their apparent frequencies to differ. Fig.4 shows a graph of the variation of the natural frequencies of a circular saw with rotation speed. The various starting points on the left are the natural frequencies of the saw when stationary, with the nodal diameter numbers as indicated. As the saw rotation speed increases, the stationary frequencies split into two parts, with the forward traveling wave frequencies increasing and the backward traveling wave frequencies decreasing. Exceptionally, the zero nodal diameter mode does not divide into two parts because it is circularly symmetric.

The backward traveling wave frequencies reduce with rotation speed and eventually decrease to zero. At this speed the saw rotation exactly counteracts the backward traveling wave such that it appears stationary in space. An analogy to this behavior could be a moving walkway at an airport with a person walking on it in the opposite direction. If they were walking oppositely at the same speed as the walkway their position would remain stationary in space. The apparent zero speed of the sawblade traveling wave corresponds to a zero natural frequency. This means that resonant vibrations can be created by a zero-frequency (constant) sideways force. Such small forces are always present in a practical circular saw machine due either to wood non-uniformities or to wood infeed imperfections. Thus, a large resonant vibration response readily occurs. In practice, the critical speed is not reached exactly, but at a nearby speed at which the backward traveling wave frequency has some low value. Thus, the response has the same low frequency, at which the sawblade “snakes” from side to side with substantial amplitude. Fig.5 shows a photo of a piece of lumber cut by a saw snaking near critical speed; the effect is quite dramatic.

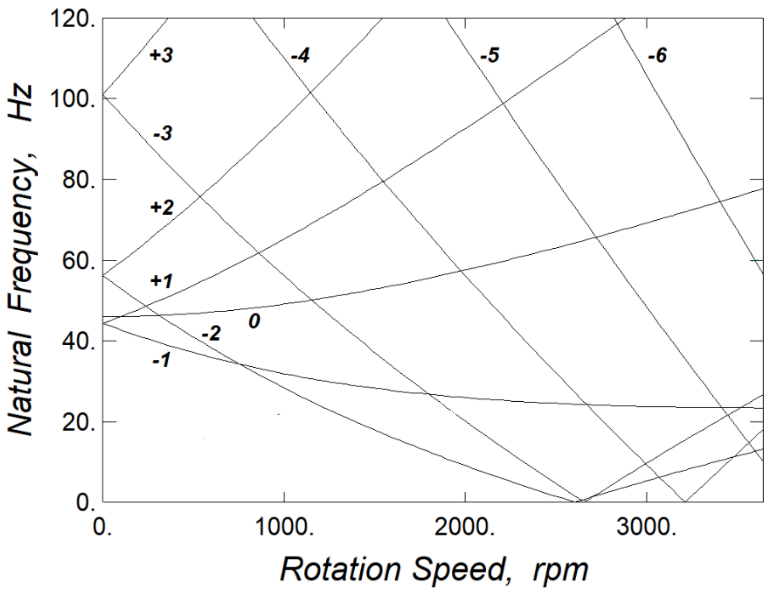

Fig. 4. Natural frequencies vs. rotation speed for a circular saw.

Fig. 5. A piece of lumber cut by a circular saw operating near critical speed.

4 Saw Tensioning

"Tensioning" is a common process used in industry to increase sawblade dynamic stiffness, hence natural frequencies and critical speeds [9]. It involves hammering or rolling the sawblade surface to deform the material locally and produce in-plane tensile circumferential stresses around the outer rim of saw [10]. Fig.6 illustrates the roll tensioning process. It stiffens the tooth area in a similar way as is done by tightening a hacksaw. Correspondingly, the natural frequencies increase in the same way as the notes of a stringed musical instrument increase as the strings are tightened. However, the tensioning process also induces compressive radial stresses, so excessive tensioning can cause the saw to lose stiffness and buckle into a bowl shape in a process called "dishing." The optimal tensioning is chosen to balance these two tendencies and can achieve a critical speed increase of 20-30%.

Fig. 6. Circular saw roll tensioning.

5 Guided Saws

The traditional and most common circular saw machine type has a fixed central collar to hold the saw. Although mechanically straightforward, it has a geometric drawback, which is that the saw support is at the center, while the teeth are on the outside edge, literally the furthest distance away. To address this issue, saw guides have been introduced in many sawmills to support the sawblade near the wood cutting zone [11,12,13]. The guides are made large enough to provide sufficient support to replace that of the center clamp. The drive to the saw is then provided by a splined shaft, as schematically illustrated in Fig.7. This guide arrangement not only stiffens the leading edge of the saw, where more support is needed, but also gives more flexibility at the trailing edge, where more freedom is needed, so as to allow that area of the saw to follow the sawcut smoothly and avoid backcutting (scratching of the cut wood surface by the teeth passing through the trailing side of the saw).

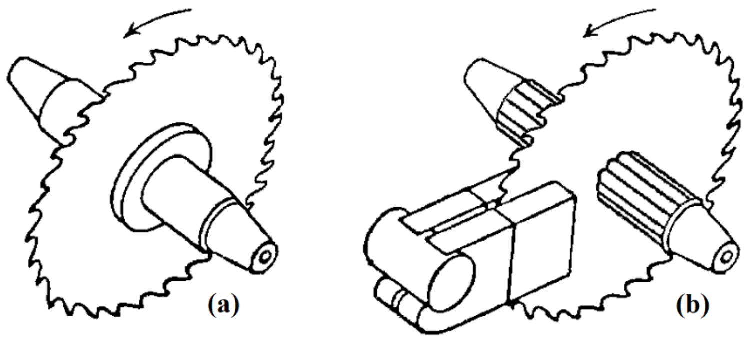

Fig. 7. Circular saw machine designs. (a) conventional saw, (b) guided saw.

The vibration of a conventional (unguided) saw, illustrated in Fig.7(a), may be divided into the two types exemplified in Figs.2 and 3. With a stationary saw, standing waves are favored because both the saw and the vibration modes are fixed in space (Fig.2). With a rotating saw, traveling waves are favored because both the saw and the vibration modes are rotating (Fig.3). Exceptionally, because of the axi-symmetry of a circular saw, either standing wave or traveling wave vibration can occur with a stationary circular saw.

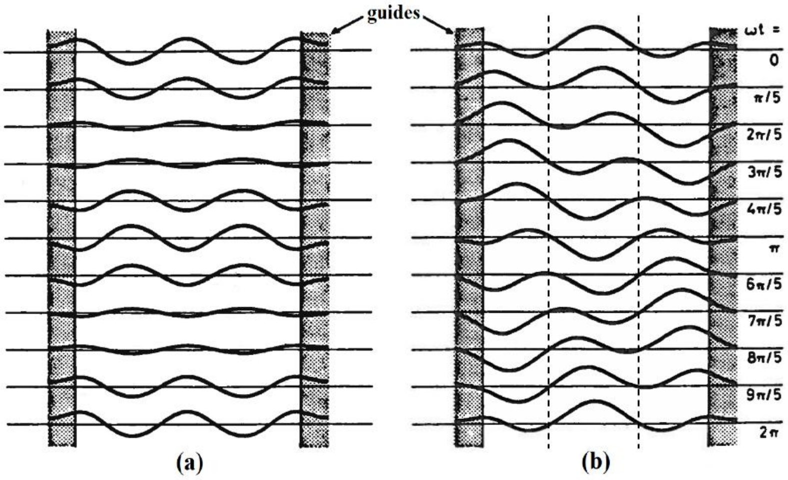

Fig. 8. Displacements around the rim of a guided circular saw over one vibration cycle. (a) stationary saw, (b) rotating saw.

The addition of the saw guides illustrated in Fig.7(b) influences the division of the two vibration mode types. The presence of the guides disturbs the axi-symmetry of the saw and creates a constraint fixed in space. Thus, only standing wave vibration is favored in a stationary saw. Fig.8(a) shows how the stiffness of the guides locally reduces the vibration amplitude and alters the vibration mode shapes away from the simple sinusoidal form illustrated in Fig.2(a). When the saw is rotating, there is a conflict between the trend for a standing wave vibration to fit the fixed-in-space constraint provided by the guides, and the trend for a traveling wave vibration to fit the saw rotation. The vibration pattern illustrated in Fig.8(b) resolves this apparent conflict by creating an interesting mixture of standing wave and traveling wave vibration. It can be seen that nodal points occur at the positions of the dashed lines, showing a standing wave vibration analogous to that seen in Fig.2(b). At the same time, a traveling wave motion analogous to that seen in Fig.3(b) also occurs.

6 Critical Speed Instability

As previously described, a circular saw becomes unstable when its rotation speed approaches its critical speed. In that case, the lowest natural frequency of the saw falls to zero and large amplitude resonant vibrations can occur due to constant (= zero frequency) lateral forces. Small constant lateral forces are inevitably present in practical sawing machines due to minor alignment imperfections and to grain deviations within the wood being cut. “Snaking” sawcuts of the type shown in Fig.5 occur as a result. In the case of a conventional unguided circular saw of the type shown in Fig.7(a), critical speed instability starts to occur when the saw rotation speed exceeds 85% of the lowest critical speed [6]. As can be seen in Fig.4, each nodal diameter vibration mode has its own critical speed, thus there may exist the possibility of operating a saw between successive critical speeds. This would be attractive for the increased cutting rate that could be achieved, however, supercritical speed operation of conventional collared saws is not practical in industrial operation.

The natural frequency vs. rotation speed characteristic of a guided saw is different in detail from that of an unguided saw, but the reduction in natural frequency of the backward traveling wave modes with increase in saw rotation speed occurs in a similar way, reaching zero frequency at each critical speed. The loss of the support from the collar of a conventional circular saw as in Fig.7(a) reduces the critical speed of a similar size guided saws such as in Fig.7(b) by about 10%, but this is more than made up by the much greater stability of guided saws. An important practical feature of guided saws is that they retain their stability near their first critical speed and only become unstable when approaching their second critical speed [13,14,15]. Thus, much higher speed operation is possible.

The critical speed of a circular saw is proportional to the plate thickness and inversely proportional to the square of the outside diameter. These geometrical features allow the ability of a guided saw to remain stable at speeds approaching its second critical speed to be exploited to achieve different production objectives:

- Keep sawblade dimensions and use a high rotation speed to achieve high lineal cutting rate,
- Keep saw rotation speed and use a thinner saw to reduce sawdust production,
- Keep saw rotation speed and use a larger saw to cut larger workpieces.

While the discussion here has focused on the saw, it is essential to note that the surrounding machinery is also important. To achieve superior saw performance both the sawing machine and the wood transport systems must be secure and well aligned, any external shortcomings will negate any benefits of having a high-quality, well-designed saw.

Circular saw critical speeds can be evaluated from published data [16]. Skillful tensioning can increase critical speeds by 20-30% beyond those of an untensioned saw.

Care should be taken when seeking to operate a saw at a significantly higher speed or significantly reduced thickness from previous experience. In that case, the change towards the target should be made incrementally, with careful observation of actual performance made at each step. In addition, maintenance and alignment of the sawing machine and wood transport systems should be enhanced to meet the more stringent needs of a high-performance saw.

7 Conclusion

The cutting stability of a circular saw is a vibrational characteristic controlled by its critical speed(s). Large resonant oscillations called "snaking" can occur when a circular saw operates near a critical speed. Saw critical speeds can be increased 20-30% by skillful tensioning. For a traditional collared saw, stable operation can be achieved at speeds up to 85% of its lowest critical speed. Guided saws are much less sensitive to the first critical speed and can operate successfully between the first and second critical speeds. However, care must be taken to ensure that the sawing machine and wood transport system are well maintained and aligned.

Acknowledgements. This work was financially supported by the Natural Sciences and Engineering Research Council of Canada (NSERC). Dr. Ahmad Mohammadpanah kindly reviewed the manuscript and made several helpful suggestions.

References

1. Williston, E.M.: Saws: Design, Selection, Operation, Maintenance. Miller Freeman Publications, San Francisco, California (1989).
2. Stephenson, E.: Circular Saws: Their Manufacture, Maintenance and Application in the Woodworking Industries, 2nd ed. Stobart Davies Ltd, Ammanford, Wales (2002).
3. Szymani, R. Mote, C.D., Jr.: Circular Saw Stiffness as a Measure of Tension. Forest Products Journal 27(3), 28-32 (1977).
4. Schajer, G.S.: Why Are Guided Circular Saws More Stable than Unguided Saws? Holz als Roh-und Werkstoff, 44(12), 465-469, (1986).
5. Mote, C.D. Jr., Nieh L.T.: On the foundation of circular saw stability theory. Wood and Fiber 5(2), 160-169 (1973).
6. Stakhiev, Y.M.: Research on Circular Saw Disc Problems: Several of Results. Holz als Roh- und Werkstoff 61(1), 13-22 (2003).
7. Szymani, R.: Dynamic Design of Saws: From Theory to Practice. World Wood 28(2), 40-42 (1987).
8. Schajer, G.S.: Guided Circular Saw Critical Speed Theory. In: Proc. SawTech'89, Wood Machining Institute, Oakland, California 7.1-7.14 (1989).
9. Szymani, R., Mote, C.D. Jr.: Theoretical and Experimental Analysis of Circular Saw Tensioning. Wood Science and Technology 13(3):211-237 (1978).
10. Schajer, G.S.: North American Techniques for Circular Saw Tensioning and Leveling: Practical Adjustment Methods. Holz als Roh- und Werkstoff, 50(4),153-157 (1992)

11. Thrasher, E.W.: Method and Apparatus for Operating a Rotary Saw. US Patent 3,645,304, USPTO, Washington, USA (1972).
12. Hutton, S.G., Chonan, S. and Lehmann, B.F.: Dynamic Response of a Guided Circular Saw. Journal of Sound and Vibration, 112(3), 527-539 (1987).
13. Ahmad Mohammadpanah and Hutton S.G.: Theoretical and Experimental Verification of Dynamic Behavior of a Guided Spline Arbor Circular Saw. Journal of Shock and Vibration, Article ID 6213791 (2017).
14. D'Angelo, C., Mote, C.D., Jr.: A look at Supercritical Saw Phenomena. Proceedings of 9th International Wood Machining Seminar, 10-12 (1988).
15. Mohammadpanah, A., Hutton, S.G.: Maximum Operation Speed of Splined Saws. Wood Material Science and Engineering 11(3), 142–146 (2015).
16. Schajer, G.S.: Simple Formulas for Natural Frequencies and Critical Speeds of Circular Saws. Forest Products Journal, 36(2), 37-43 (1986).

Digital transformation in the context of the manufacturing industry in Italy: the SCM GROUP case

Alessandra Benedetti[1]

[1] SCM GROUP, Rimini (Italy)

Abstract. This document explores the strategic transformation of SCM Group from traditional manufacturing towards servitization enabled by digital technologies, focusing on enhancing after-sales service and deepening customer relationships. The study investigates SCM Group's journey from a transactional business model to one centered around customer lifecycle management, utilizing digital platforms, outcome-based agreements, and AI-driven solutions. It highlights the critical roles played by people management, cultural adaptation, and digital competencies in successfully driving this transformation. By examining SCM Group's case, the research illustrates how integrating digitalization, fostering organizational evolution, and leveraging core human competencies generate substantial competitive advantages. Ultimately, the findings underline the significance of organizational agility, continuous experimentation, and people-driven innovation in facilitating a comprehensive transition from machine manufacturer to trusted business partner.

Keywords: Digital Servitization, Change Management, Digital Transformation, Ambidexterity.

Tracking and learning: AI cross training between scanners in sawmills

Enrico Ursella[1]

[1] MICROTEC, Bressanone (Italy)
enrico.ursella@microtec.eu

Abstract. This paper explores the potential for improving AI-based training methods for product analysis in wood processing. Establishing an accurate ground truth is increasingly critical for training neural networks across various applications. The ability to use automatically collected information from one scanner to train different types of scanners is of great interest, as it eliminates the cost of manual labeling and allows for the correct classification of features that are difficult for an operator to verify. Microtec's range of scanners for sawmills and the ability to automatically link data from various scanners during normal production enable the creation of an effective training pipeline. The general framework will be presented, along with a specific application for detecting the three-dimensional position of the pith relative to a board based on color images of the surfaces.

Keywords: CNN training, wood traceability, sawmill optimization, AI automatic labelling.

Wood Traceability Along the Whole Value Chain: Exaggeration or Obligation

Gianni Picchi[1,2], Antonio Ruano[2], Simon Stegel[3], Jana Hmeljak[3], Bengt Sörvik[4], Mari Selkimäki[5], Heli Kymäläinen[5], Blas Mola[5], Enrico Ursella[6], Gennaro Azzollini[6], Johan Ekenstedt[7], Garret Mullooly[8], Alejandro Poveda[8], Silvia Melegari[9], Ryszard Sandak[10], Cuauhtli Campos Mijangos[10], Jakub Sandak[10,11]

[1] CNR-IBE, Via Madonna del Piano 10, 50019 Sesto Fiorentino, Italy
[2] CTFC, Crta. de St. Llorenç de Morunys, 25280 Solsona, Spain
[3] Simtrona d.o.o, PE Vipavska cesta 64, 5000 Nova Gorica, Slovenija
[4] Otmetka Log Marking AB, Västerberga 114 741 78, Uppsala, Sweden
[5] University of Eastern Finland, P.O. Box 111, FI-80101 Joensuu, Finland
[6] MiCROTEC Venice, Via Miranese 56 30171 Venice, Italy
[7] Arboreal, Kaserngatan 3 4 tr, 903 47, Umeå, Sweden
[8] Treemetrics Ltd., Munster Technological University, Bishopstown, Cork, T12 Y275, Ireland
[9] EOS, Rue Montoyer 40, BE-1000 Brussels, Belgium
[10] InnoRenew CoE, Livade 6a, 6310 Izola, Slovenia
[11] University of Primorska, Titov trg 4, 6000 Koper, Slovenia
jakub.sandak@innorenew.eu

Abstract. Determining the provenance and use history of timber products has traditionally been a niche application, requiring complex analytical procedures and significant human and economic resources. However, recent regulatory requirements and consumer demand for transparency are pushing industries to adopt innovative approaches to certify the proper procurement and transformation of resources. Notably, the EU Deforestation Regulation (Regulation (EU) 2023/1115) aims to ensure that products consumed within the European Union do not contribute to deforestation or forest degradation worldwide. Similarly, digital product passports (DPS) are recognized as necessary complements to sustainable product declarations.

Recent advancements in technology have made wood traceability along the value chain possible. Key methods include digital systems that create digital records and transactions (such as Distributed Ledger Technology, Internet of Things, and blockchain), biometric systems, and certification schemes (FSC, PEFC). Other solutions for authenticating timber provenance include spectroscopic fraud detection, DNA fingerprinting, and isotopic analysis. The most desired approach is single-item identification, which can be implemented by combining RFID, punching codes, QR/bar codes, and digital fingerprinting of logs and boards using CT and vision systems.

This scenario is integrated within the framework of the SINTETIC project, financed by the EU Horizon Europe research and innovation program. The core objective is to set up and demonstrate a traceability system for trees, logs, and boards based on Information and Communications Technology (ICT) innovations. The ambition is to define, prototype, and demonstrate a comprehensive digital platform for forest value chain data management. This process involves monitoring the entire supply chain, from the forest of origin to the final product on the market. The research presented here focuses on the sawmill solution and the practical integration of diverse data recorded along the supply chain operations. It is shown that a reliable system for full traceability of resources in sawmills is very challenging but feasible. It is expected that this technology will be broadly adopted by industries not only in the European Union but worldwide.

Keywords: wood traceability, RFID, punching code, wood fingerprint.

1 Introduction

The worldwide timber industry is currently at a crucial moment, driven by increasing regulatory demands and consumer expectations for sustainable and transparent supply chains. The SINTETIC project, funded by the EU Horizon Europe research and innovation program, addresses these challenges by pioneering advanced traceability systems for timber products. This initiative aims to revolutionize the way timber is tracked from forest to final product, ensuring compliance with the EU Deforestation Regulation (Regulation (EU) 2023/1115) and enhancing the credibility of sustainable product declarations through digital product passports (DPS).

The SINTETIC project harnesses digital technologies to create a comprehensive traceability system for trees, logs, and boards. The core ambition is to define, prototype, and demonstrate a complete digital platform dedicated to forest value chain data management. This platform will enhance the protection and production of European forests through innovative ICT solutions. A general concept for integrating several state-of-the-art solutions that can support this challenge is presented in Figure 1.

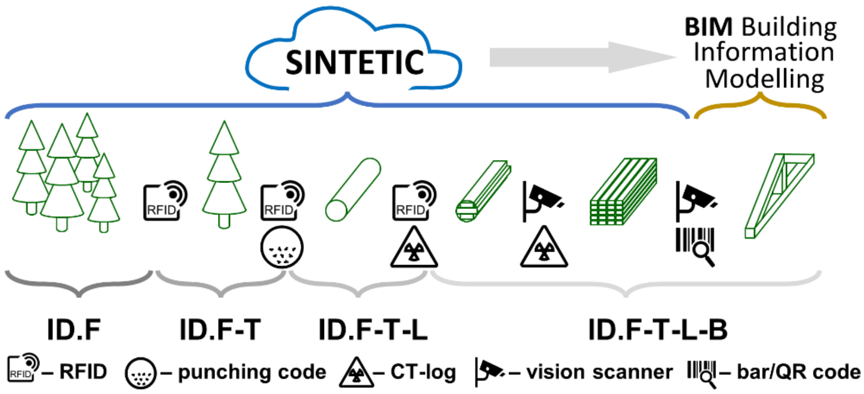

Fig. 1. ID detection systems integrated within frame of SINTETIC project and a concept of the traceability of wood from the forest till the final product installed in the timber structure.

2 Full traceability solution for timber production

As a key outcome, the SINTETIC project will develop a reliable, highly precise, and cost-effective traceability system. This system will generate unique IDs physically attached to each item and digitally transmitted to a central geodatabase. The geodatabase will relate each ID to data produced along the supply chain, spanning from forest inventory to final timber products. This integration will allow for detailed tracking of yield and quality output, historical climatic data, silvicultural treatments, and forest stand descriptors at all stages of the value chain. Such a solution is unique and has never been integrated to such an extent.

The project will leverage various technologies, including single-item identification and early-stage quality assessment. The traceability solution is based on implementing RFID, punching codes, QR/bar codes, and digital fingerprinting of logs and boards with computed tomography (CT) and vision systems (Figure 2).

Fig. 2. ID detection systems integrated within the framework of the SINTETIC project and a concept of the traceability of wood from the forest to the final product installed in the timber structure.

Several other technologies are integrated with the SINTETIC project solution, including a LiDAR scanning system installed on-board the forest harvester for value recovery optimization and post-harvesting forest inventory. Moreover, a smartphone app is proposed for forest inventory and accurate timber measurement with a standard mobile phone. An illegal logging detection system for early warning solutions for detecting forest cover changes associated with harvesting operations is developed based on routine satellite data analysis. In addition, a tool for forest ownership aggregation is provided by creating an integrated platform to enhance and facilitate fragmented forest inventories, planning, and management. All these innovative solutions improve the use of natural resources and promote higher mobilization of the available timber, which is desperately needed for the future development of the sustainable construction sector.

To make all this possible, SINTETIC develops a geodatabase with a set of data providers interconnected by the traceability system. The system includes multi-platform data acquisition for the whole supply chain, data transmission with secured digital tools and physical IDs on timber products, and optimized data storage, analysis, and distribution for the generation of further services. In addition, several technologies enabling the description of quality at all stages of the value chain are fully integrated with manual and automatic operations/processes generating unique IDs.

This talk presents how all the aforementioned SINTETIC project components innovate the future forest product industry by integrating diverse data sources within sawmill operations, demonstrating the feasibility and potential for widespread adoption of reliable traceability solutions.

Simulation of Internal Defect Detection in Logs Scanned with a Tilted X-ray Imager

Jakub Sandak[1,2], Piotr Taube[3], Daniel Chuchala[4] and Kazimierz Orlowski[4]

[1] InnoRenew CoE, Livade 6a, 6310 Izola, Slovenia
[2] University of Primorska, Titov trg 4, 6000 Koper, Slovenia
[3] SYLVA Sp. z o.o., Koscierska 2, 83-441 Wiele, Poland
[4] Gdańsk University of Technology, Gabriela Narutowicza 11/12, 80-222 Gdansk, Poland
jakub.sandak@innorenew.eu

Abstract. The increased demand for timber as a sustainable alternative to other construction materials has resulted in a shortage of natural resources available for sawmill conversion. This pushes industries to employ more rational and efficient technologies to increase production yields and minimize residuals. Several scanning technologies are integrated with state-of-the-art production facilities, although the majority determine log suitability based on dimensions and/or surface defect detection. It has always been the ultimate desire of sawmillers to see the interior of a log before the first cut to optimally determine the sawing pattern and estimate product quality/value early. Such technology, industrial CT, is now available but only to large companies that can afford the very high investment costs. A more affordable alternative is to use classical X-ray radiometry to scan logs in one or more cross-sections perpendicular to the feed direction. An alternative configuration is to tilt the direction of the X-ray beam away from perpendicular. The radiogram of a log generated with such a setup is not as intuitive for interpretation but can be a highly advantageous addition to an automated image analysis system. Assuming some simplifications and implementing appropriate machine learning algorithms, it may be possible to offer a scanning solution similar to CT at a fraction of the cost. The goal of the research presented was to build a digital simulator of the X-ray radiometer to test the feasibility of different configurations and to identify all limitations of the simplified tomography solution.

Keywords: wood scanning, x-ray radiography of logs, CT scanner.

1 Introduction

The growing demand for timber as a sustainable alternative to conventional construction materials stimulates the need for improved resource management and optimization in sawmill operations. This increase of demand has resulted in a scarcity of natural resources suitable for sawmill conversion, driving industries to adopt more rational and efficient technologies that enhance production yields and minimize residual waste. Among these advancements, the integration of advanced scanning technologies into state-of-the-art production facilities has marked a significant step forward. However, most of these systems assess log suitability based solely on dimensions or surface defect detection, leaving a critical gap in the ability to evaluate internal log characteristics before sawing.

For decades, sawmill operators desired to unlock the ability to visualize the interior structure of logs prior to the first cut, aiming to optimize sawing patterns and predict product quality and value. This desire has led to the development of industrial CT scanning technology, a powerful tool capable of providing detailed insights into the internal composition of logs. Yet, its widespread adoption remains limited due to prohibitively high investment costs, accessible only to large-scale enterprises.

Classical X-ray radiometry presents a promising alternative solution, offering the capability to scan logs at one or more cross-sections perpendicular to the feed direction. Figure 1 illustrates an example of such a scanner, which is employed for both log sorting and optimizing the crosscutting of stems into logs. The standard dataset derived from these scans encompasses radiograms (Figure 2), average density and its approximate distribution, log geometry and critical dimensions, detection of metal inclusions, and identification of various wood defects.

A particularly critical function of this X-ray system is its ability to detect, measure, and characterize knots, which significantly influence the value and usability of the sawmill's end products. The integration of this scanner, specifically the Logeye 302D produced by Microtec (Italy), formed a key component of the doctoral research and resulted in several technological advancements. Among these innovations was the novel approach of tilting the X-ray beam away from the perpendicular axis. This configuration generated radiograms that, although less intuitive for manual interpretation, proved to be highly advantageous when integrated with automated image analysis systems. By leveraging strategic simplifications and advanced machine learning algorithms, this approach presents the potential to deliver a scanning solution comparable to industrial CT, but at a substantially reduced cost.

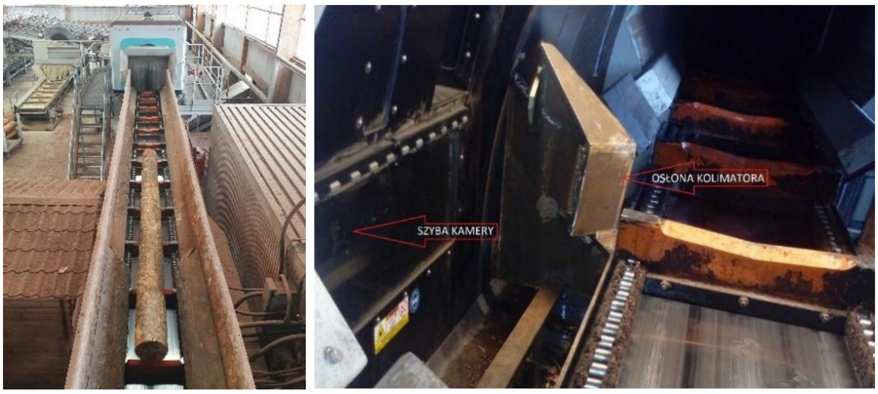

Fig. 1. Industrial scanner Logeye 302D (Microtec) used for sorting and cross-cut optimization of logs in the sawmill, equipped with experimental x-ray module with tilted scanning direction.

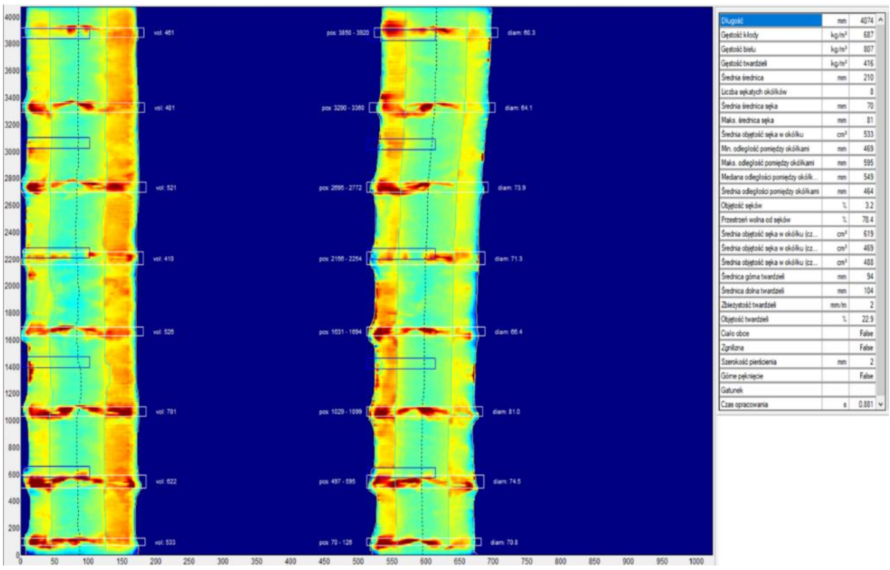

Fig. 2. Example of radiograms and derived log quality characteristics acquired after scanning logs with industrial scanner utilizing two x-ray modules installed perpendicularly to the log feed direction.

The goal of this research was to explore this possibility through the development of a digital simulator for the X-ray radiometer. The simulator enables comprehensive testing of various configurations and provides critical insights into the limitations and feasibility of simplified tomography solutions. This investigation aims to bridge the gap between high-cost industrial CT technologies and accessible, cost-effective alternatives, contributing to the advancement of sustainable and efficient sawmill practices.

2 Digital representation of log

The key to any digital simulation lies in the accurate representation of the analyzed objects, ensuring compatibility with the numerical algorithms being applied. In the case of an X-ray scanner simulation, this includes the representation of the log (comprising different zones such as sapwood and heartwood), wood defects that influence radiation attenuation (such as knots), as well as the scanning system's geometry.

For the purposes of this research, the log was represented as a truncated cone with a specified length, bottom diameter, and top diameter (Figure 3). Additionally, the sapwood zone was modeled as a constant offset from the external diameter toward the center of the log. The X-ray attenuation coefficients for the materials in the sapwood and heartwood were distinct, reflecting differences in moisture content during the scanning process.

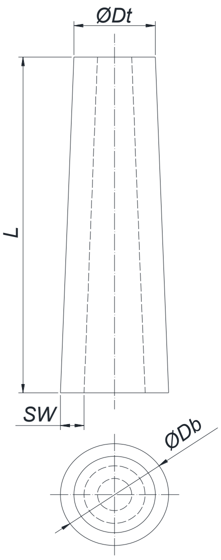

Fig. 3. A set of parameters required for defining geometry of the key features of wooden log: Dt – top diameter, Db – bottom diameter, L – length of the log, SW – width of sapwood.

Knots were represented as conical structures positioned at specific locations within the log volume. Their positions were defined using two angles (one denoting the rotation around the log's vertical axis and the other describing the knot's orientation relative to the cardinal directions of the log), as well as their height along the log (Figure 4). The size of each knot (cone) was defined by the external diameter of the branch and its length. To simplify the simulation, a single attenuation coefficient was assigned to knots, assuming a high wood density and consequently higher attenuation. Distinctions between dead and healthy knots or the presence of holes were not included in the model.

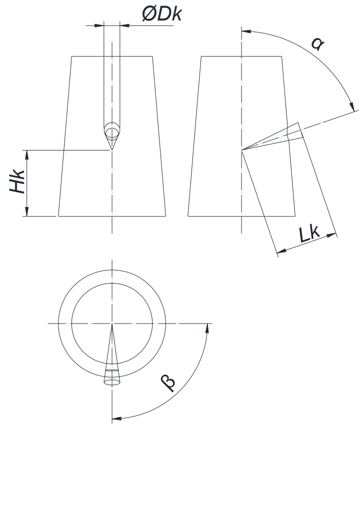

Fig. 4. A set of parameters required for defining geometry of the single knot in the wooden log: Dk – external diameter of the knot, Lk – length of knot, Hk – height of the knot placement along the log length, SW – width of sapwood zone.

The X-ray scanner was represented as a single point source paired with a linear detector comprising a specified number of pixels (Figure 5). The source and detector were separated by a fixed distance that remained constant, irrespective of changes to the tilting angle of the scanning plane. The distance of the x-ray source and the log was constant in vertical direction but varied in horizontal course to imitate the feed of log inside the scanner.

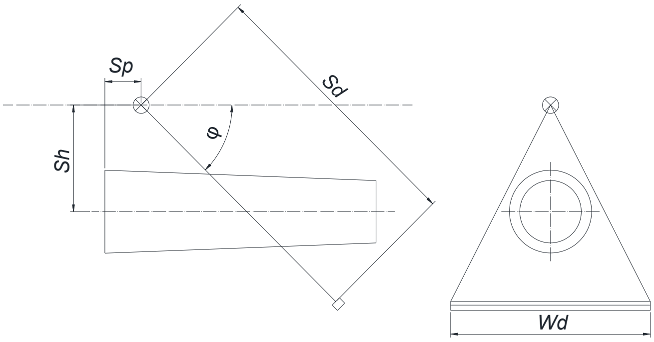

Fig. 5. A set of parameters required for defining geometry of the tilted x-ray scanning system for log: Sd – distance between source and x-ray detector, Wd – width of x-ray detector, Sp – position of the scanner regarding the log length, Sh – distance of the detector from the log central axis, φ – tilting angle of the X-ray scanning plane.

3 Simulation of log radiograms

Each key element of the simulation system can be represented as geometric primitives, as shown in Figure 6. The X-ray source and detector form a 3D plane that is described by a single mathematical equation. More complex structures, such as the cones representing logs and knots, were modelled as a series of lines rather than continuous mathematical functions. While this approach simplified the algorithm's structure, it also resulted in a slower computation process. To define the cone, a series of points was placed on the top and bottom circles. A pair of these points (one from the top circle and one from the bottom) was represented by the mathematical equation of a 3D line. In the case of knot simulation, the top circle was reduced to a single point.

Next, each constitutive line of the primitives was evaluated to compute its intersection with the plane. If the intersection point lay between the top and bottom circles, it was considered relevant for X-ray attenuation. Otherwise, it was excluded from further computations at the given scanner plane position. The resulting set of points formed the contour of the intersection between the cone and the scanner plane. This contour was then converted into an area representing a material with a specific attenuation coefficient. The same procedure was applied to identify all interaction contours, which were tested separately for each geometric primitive defining the log. Finally, these individual contours were combined to form a mathematical set representing the tomogram.

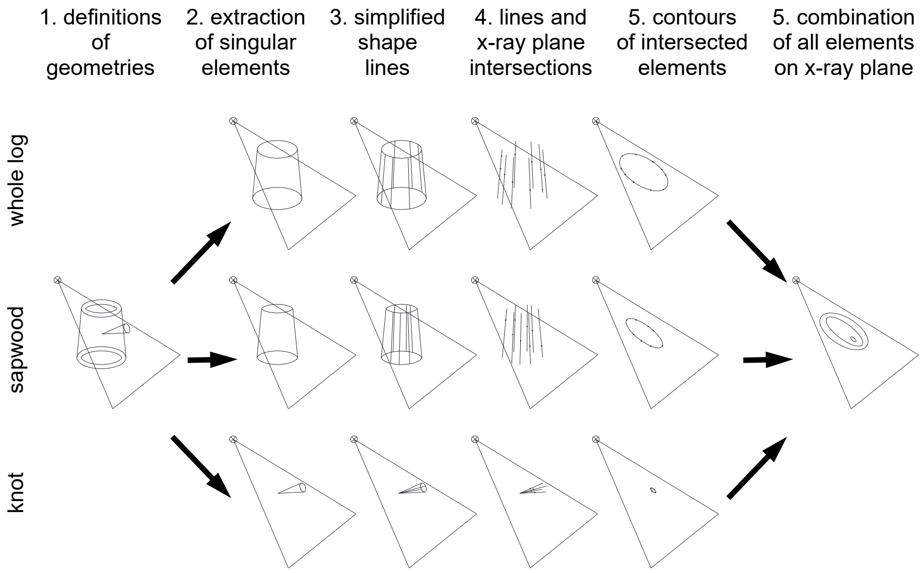

Fig. 6. Protocol for mapping the virtual log's material distribution on the X-ray scanning plane, including heartwood, sapwood, knots, and their combinations.

To simulate the X-ray scanner response, the following procedure was implemented: A line linking the X-ray source to a single pixel on the detector was defined as a mathematical equation. The length of the line passing through the previously derived intersection contours was calculated separately for heartwood, sapwood, and knots. The attenuation of X-rays was then computed using the Lambert-Beer law, which considers a linear combination of specific intersection lengths and pre-defined attenuation coefficients. As a result, the attenuation recorded for a single pixel was determined. This procedure was repeated for every pixel on the detector, generating a simulated attenuation profile corresponding to a single log section. A graphical representation of this procedure is shown in Figure 7.

By varying the position of the X-ray source and detector along the log, it was possible to simulate a radiogram for the log, including its parameterized wood defects (e.g., knots). This algorithm was implemented as a custom software tool developed in LabVIEW. Figure 8 presents the user interface, which includes parameters for defining the simulated log's characteristics. The source code, in the form of a virtual instrument, is shown in Figure 9. The execution time for simulating a 1 meter long log with eight knots was approximately 30 seconds, assuming a radiogram composed of 1,550 sections (scanner positions). In this case, each cone was represented by 360 lines connecting the top and bottom circles, with a rotational spacing of 1°.

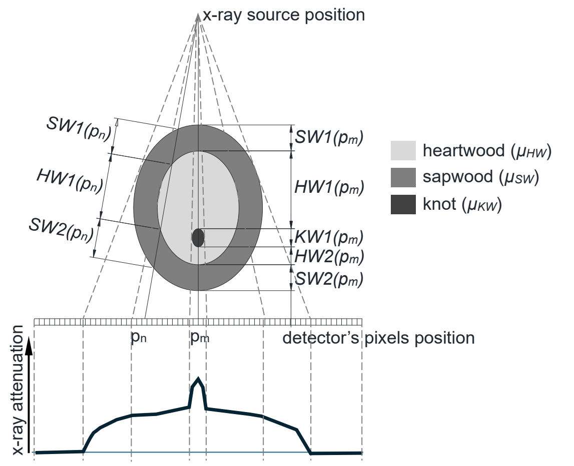

Fig. 7. Determination of the x-ray attenuation profile across the log section: *SWi(p$_j$)* – length of the x-ray path through sapwood zone of attenuation μ_{SW} detected at pixel *p* of the detector, *HWi(p$_j$)* – length of the x-ray path through heartwood zone of attenuation μ_{HW}, *KWi(p$_j$)* – length of the x-ray path through zone of knot with attenuation μ_{KW}.

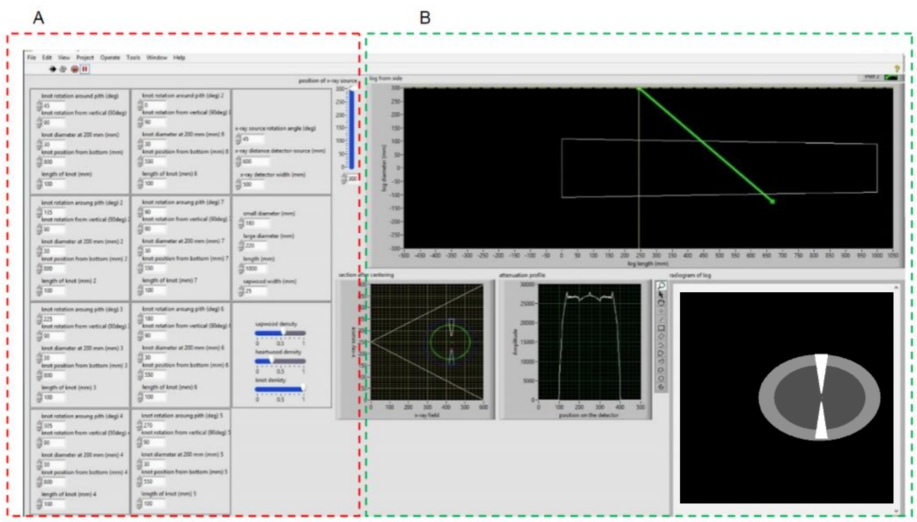

Fig. 8. Software developed for the simulation of radiograms at various tilting angles of the X-ray scanning plane. A: Parameter definitions for describing log, knot, and scanner geometries. B: Visualization of the simulation results.

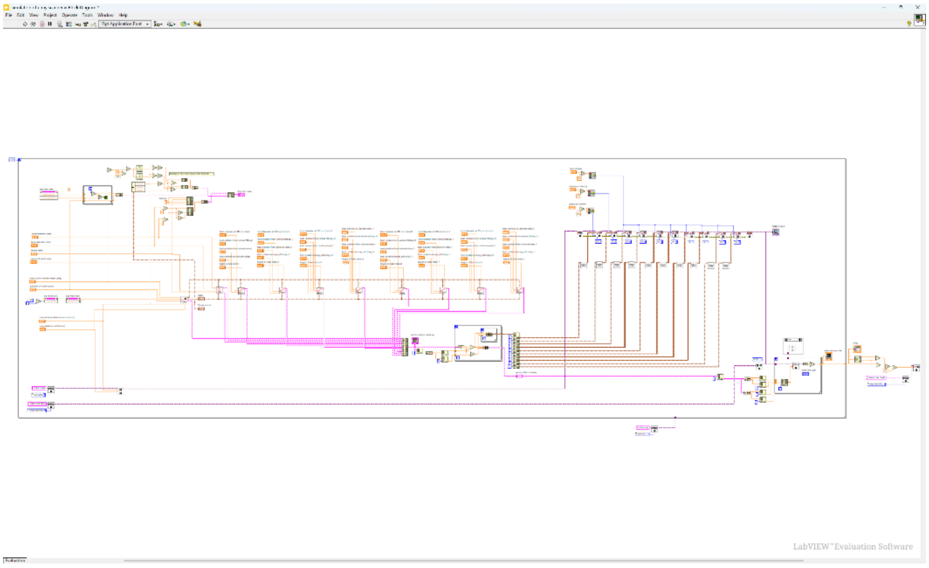

Fig. 9. Source code of the LabVIEW software developed for the simulation of radiograms at various tilting angles of the X-ray scanning plane.

An example of the simulation results is presented in Figure 10. It is evident that the visibility of knots changes significantly with varying tilting angles of the scanning plane. When the tilting angle is 0°, the number of knots, along with their size and spatial distribution, is difficult to recognize. However, the representation of knot formations becomes much more prominent as the tilting angle increases, with the optimal visualization observed at 35°.

It should be noted that increasing the tilting angle, while advantageous for improved knot detection, introduces certain challenges. First, higher X-ray energy levels may be required due to the extended path length of X-ray photons through the material as the scanning plane is tilted. Second, in real logs, clearly separated knots in the radiograms may appear overlapping if the distance between branch whorls is small. This effect is illustrated in Figure 11, which presents radiograms obtained using the industrial Logeye 302D scanner (Microtec) for different tilting angles. Additionally, the tomogram of a single whorl is included to emphasize the superior interior representation provided by CT scanners.

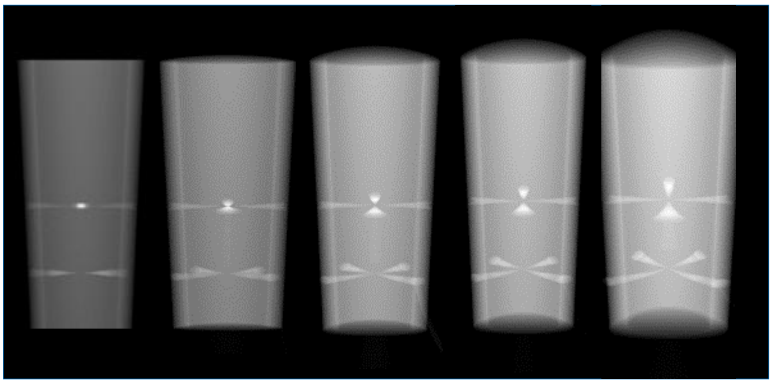

0° 10° 20° 25° 35°

Fig. 10. Radiograms generated by simulating a virtual log containing eight knots scanned with the X-ray system at different tilting angles.

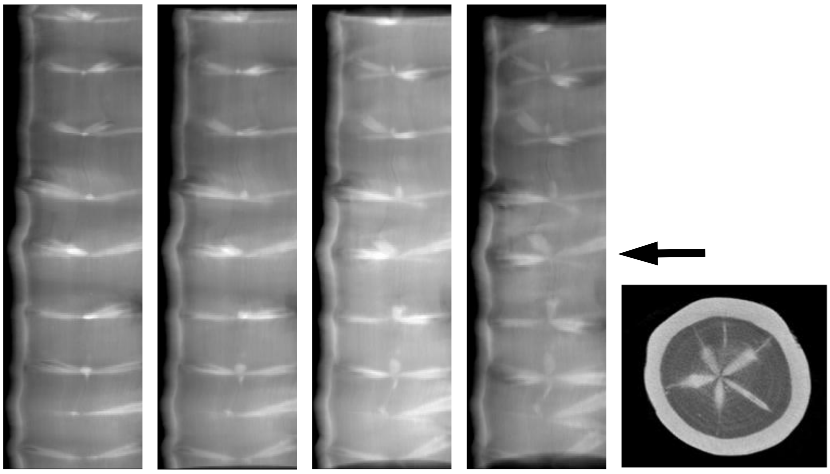

0° 15° 30° 45°

Fig. 11. Radiograms of a real Scotch pine log (*Pinus sylvestris*) acquired using the industrial Logeye 302D scanner (Microtec) at different tilting angles of the X-ray scanning plane. The tomogram of the knot whorl indicated by the arrow.

Effect of Wood Surface Brushing on Delamination Resistance of Glue-Laminated Timber

Drago Pregl[1], Tomaž Petrun[1], Ambrož Ahec[1], Edit Földvári-Nagy[2], Ryszard Sandak[3], Andreja Kutnar[2,3] and Jakub Sandak[2,3]

[1] Ledinek Engineering d.o.o. SI-2311 Hoče, Slovenia
[2] University of Primorska, Titov trg 4, 6000 Koper, Slovenia
[2] InnoRenew CoE, Livade 6a, 6310 Izola, Slovenia
jakub.sandak@innorenew.eu

Abstract. Engineered wooden materials are increasingly used in modern construction as sustainable alternatives to concrete and steel. Timber offers optimal mechanical properties, lightweight, and appealing aesthetics. Glue-laminated timber (GLT) and cross-laminated timber (CLT) are frequently employed as structural elements in contemporary timber buildings. Over the years, the manufacturing technology of engineered wood has advanced through experience and scientific research. Additionally, various building codes and certification schemes ensure proper performance and structural safety throughout the service life of these materials. A critical aspect of manufacturing engineered wood elements is ensuring the proper bonding of glued components. Several factors influence adhesive bond strength and delamination resistance, including the intrinsic properties of the wood, glue chemistry, application process, and pressing and curing conditions. Proper wood surface preparation before adhesive application is also essential for superior product quality. This research aimed to investigate the effect of wood machining conditions on surface characteristics and the delamination resistance of glued wood samples. The experiment was conducted using sharp tools with varying feed per tooth. Additionally, the effect of surface brushing after planing was examined to assess the impact of increased roughness on adhesive bond formation.

Keywords: gluing of wood, surface roughness, adhesive penetration, delamination, surface brushing.

1 Introduction

Engineered wooden materials are increasingly used in modern construction as sustainable alternatives to concrete and steel. Timber offers optimal mechanical properties, lightweight, and appealing aesthetics, making it a preferred choice for architects and builders. Among the various engineered wood products, glue-laminated timber (GLT) and cross-laminated timber (CLT) stand out for their versatility and strength, frequently employed as structural elements in contemporary timber buildings.

Over the years, the manufacturing technology of engineered wood has advanced significantly through both practical experience and scientific research. These advancements have led to improved performance, durability, and safety of timber structures.

Additionally, various building codes and certification schemes have been established to ensure proper performance and structural safety throughout the service life of these materials. These regulations play a crucial role in maintaining the integrity and reliability of timber constructions.

A critical aspect of manufacturing engineered wood elements is ensuring the proper bonding of glued components. The adhesive bond strength and delamination resistance are influenced by several factors, including the intrinsic properties of the wood, glue chemistry, application process, and pressing and curing conditions. Proper wood surface preparation before adhesive application is also essential for superior product quality. Ensuring optimal bonding not only enhances the mechanical properties of the timber but also contributes to the longevity and safety of the structure.

In conclusion, the use of engineered wooden materials in construction represents a significant step towards sustainable building practices. The continuous improvement in manufacturing technologies and adherence to stringent building codes ensure that timber remains a viable and reliable option for modern construction projects.

The goal of the experiment was to assess the effect of various wood machining solutions on the performance of glue connections in engineered timber products. Four surface variations were investigated to identify optimal production conditions.

2 Materials and methods

The timber used for testing was Yellow Southern Pine (*Pinus echinata*). The wood was sorted to have a density of 580–660 kg/m³, which is higher than the typical density of pine in the market. The moisture content was measured using three different moisture meters and was found to meet the requirements for gluing, with a moisture content (MC) ranging from 8% to 15%.

Four methods of surface preparation were defined for the following sample batches:

- *Sample S*: Planing with low feed speed (200 m/min)
- *Sample F*: Planing with high feed speed (300 m/min)
- *Sample B*: Planing with high feed speed (300 m/min) and surface brushing
- *Sample R*: Planing with RotoLes planer

The machining of wood samples S, F, and B was performed on a STRATO PLAN 400 4V400 machine produced by Ledinek (Figure 1). This was conducted on a new machine with very sharp knives. Wood samples B were processed using a moulder equipped with an additional brushing module. Sample R was machined on a RotoLes machine produced by Ledinek (Figure 2) at a feed speed of 30 m/min. The tool used was new and sharp.

Fig. 1. Surface planer STRATO PLAN 400 4V400 used for machining of samples.

Fig. 2. RotoLes machine used for the surface preparation of samples R.

The glue used in the experiments was a one-component polyurethane (1CPUR) adhesive (Henkel HPX1022). The open time of the adhesive was 10 minutes, and it was applied by hand using a special dispenser with a glue coverage rate of 150 g/m².

A primer was applied to the wood surface before adhesive application using a spray method at a conveyor feed speed of 180 m/min and a spray rate of 20 g/m². The airing time was 10 minutes. Samples were pressed immediately after glue application for 45 minutes at a pressure of 0.8 MPa, corresponding to a force of 54 kN. At least four replica sample blocks were produced for each surface machining scenario. The glued blocks were stored in a climatic chamber at 20°C and 55% RH for one week. After this storage period, it was assumed that the glue bond had reached its optimal strength, allowing further tests to be performed without risking weakening of the composite. All samples were surfaced and thickness planed to unify their size and prepare them for delamination tests according to standard EN14080. The delamination test was performed on samples 75 mm high, cut from each block using a circular saw. Three slices were extracted each time, including two samples for the delamination test and one for microscopic analysis (10 mm high).

Surface Roughness

Surface roughness of the wood surfaces generated during board machining was assessed in the laboratory to identify differences in topography and surface structure. A confocal microscope, Leica DCM8 was used for scanning the surfaces. Five independent samples from each machining option were randomly selected and measured independently at the early and late wood zones. The overall scan was performed as a stitching to cover an area of 4.5 x 3.5 mm², which was considered representative for the needs of this experiment. Leica Map software was used for 3D scan processing and determination of surface roughness parameters. The surface was first flattened by removing the plane error of form. All data outliers were filtered out and missing points were interpolated. On this prepared data, 2D surface indicators were computed, including *Sq*, *Ssk*, *Sku*, *SP*, *Sv*, *Sz*, and *Sa*. Additionally, the Abbott-Firestone curve was generated and expressed as *Sk*, *Spk*, and *Svk*.

Four profile sections were extracted from the 3D surface maps, including two horizontal and two vertical lines. These profiles were then filtered with a Gaussian filter (cut-off = 0.8 mm), and the following surface roughness indicators were calculated: *RP*, *Rv*, *Rz*, *Ra*, *Rq*, and *Rku*.

Glue Line Thickness

The hypothesis of different mechanisms of glue penetration related to the surface machining scenario was evaluated using fluorescence microscopy imaging. An EVOS M7000 microscope was used to host specially prepared glued wood samples. For this, one 10 mm thick slice cut out together with the delamination samples was identified, and its surface was sanded with gradually changing abrasives: P150, P250, P400, P800, P1500. As a result, a very smooth surface was generated, suitable for microscopic observations. Consequently, 30 fluorescence images were acquired for each slice, corresponding to specific surface machining scenarios.

Special software was developed in LabView for post-processing images and quantifying glue distribution patterns. A screenshot of the user interface showing the source and processed images is presented in Figure 3. The software was able to calculate glue line thickness, anisotropy of penetration (up/down), and histogram glue distribution referencing the center of the apparent glue line. It was possible to manually select the apparent glue line position and adjust the threshold value discriminating glue from other wood polymers.

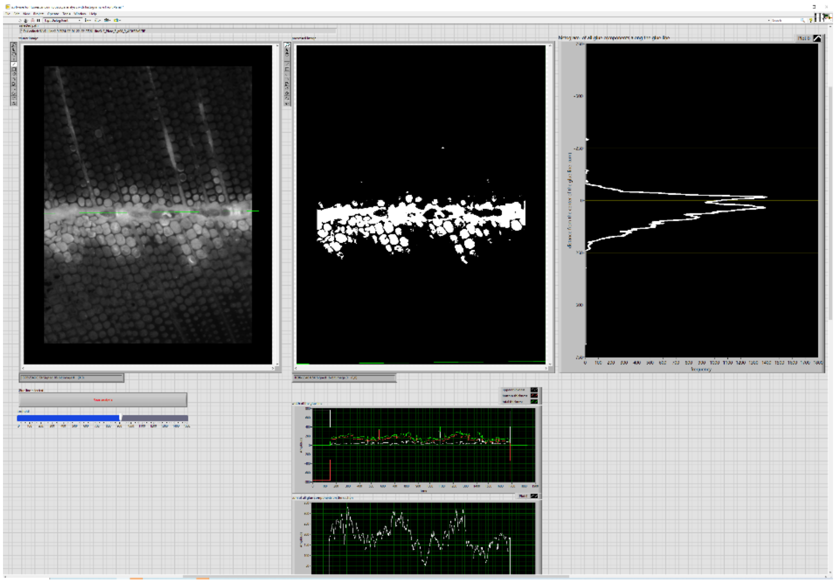

Fig. 3. Screenshot of the software developed for post-processing images representing glue distribution within the wood pores.

3 Results

Surface Roughness

The summarized results of the surface roughness indicators analysis are presented in a series of graphs below. Figures 4 shows the trends observed when assessing surface profiles *Ra* and *Rz*. Additionally, Figures 5 and 6 present results for the same surfaces, but assessed as 2D parameters, including *Sq* and *Sz*, as well as *Spk* and *Svk*, respectively.

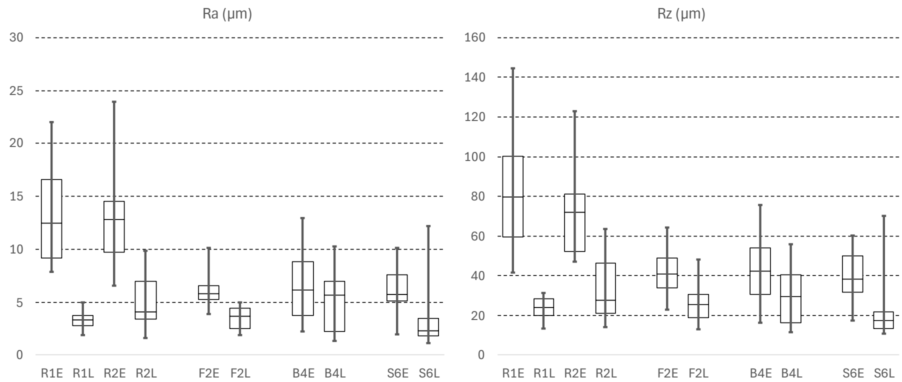

Fig. 4. Surface roughness *Ra* and *Rz* of wood after machining with different techniques: R- RotoLes, F – planing with 300 m/min, B – brushing after planing with 300 m/min, S - planing with 200 m/min. The number corresponds to the sample board ID, E – early wood, L – late wood zone.

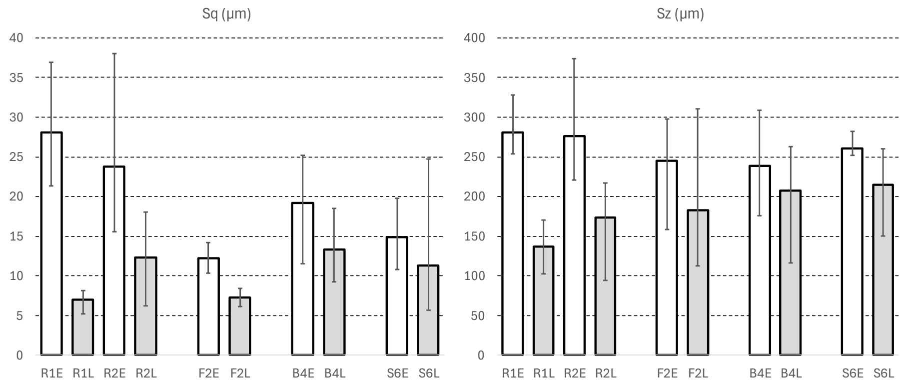

Fig. 5. Surface roughness *Sq* and *Sz* of wood after machining with different techniques: R- RotoLes, F – planing with 300 m/min, B – brushing after planing with 300 m/min, S - planing with 200 m/min. The number corresponds to the sample board ID, E – early wood, L – late wood zone

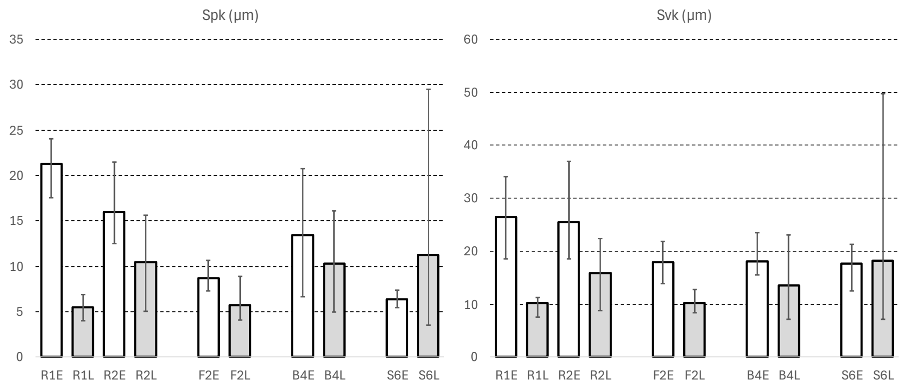

Fig. 6. Surface roughness *Spk* and *Svk* of wood after machining with different techniques: R-RotoLes, F – planing with 300 m/min, B – brushing after planing with 300 m/min, S - planing with 200 m/min. The number corresponds to the sample board ID, E – early wood, L – late wood zone.

It is evident that the majority of surface roughness parameters acquired from the early wood zone are higher than those from the late wood zone. Regarding the ranking of roughness, sample R (RotoLes) generated the highest roughness, especially in the early wood zone. Conversely, the late wood zone processed with RotoLes seemed smoother than other machining approaches. In some cases, the roughness of surfaces B generated by brushing was higher than that of samples S and F.

Delamination

Detailed results from the delamination test following the above protocol are shown in Figure 7.

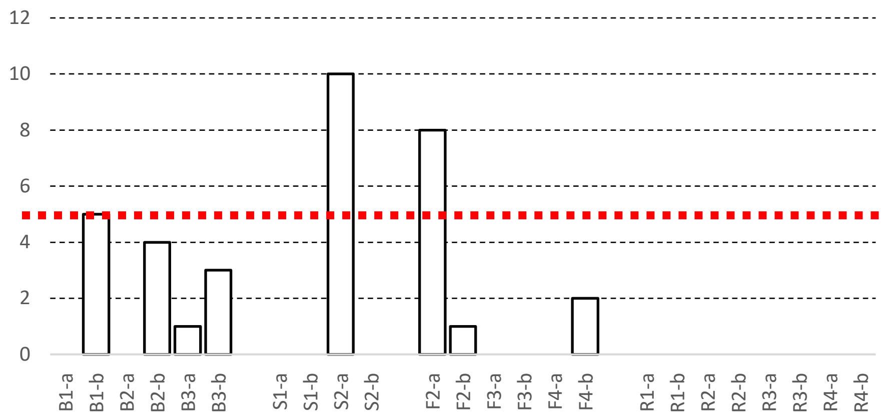

Fig. 7. Results of the delamination test for samples of wood after machining with different techniques: R- RotoLes, F – planing with 300 m/min, B – brushing after planing with 300 m/min, S - planing with 200 m/min. The number corresponds to the glued block ID, a – replica #1, b – replica #2. The red line corresponds to the allowed delamination rate.

Three of the measured specimens exceeded the allowed 5% delamination rate, prompting further inspection by splitting the bond line open and examining it under UV light. Sample F4-b, while under 5%, was also inspected. In the R group, there was almost no delamination present, while samples B, S, and F had delamination exceeding the allowed 5%.

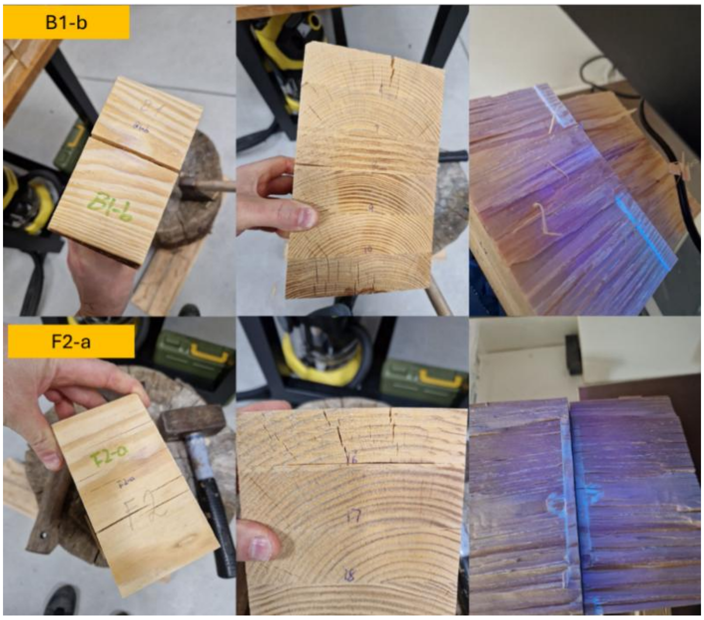

Fig. 8. Samples B1-b and F2 not conforming to standard requirements. These glue bonds were split for inspection using UV light.

Example images of the glue line observed on the fluorescence microscope are presented in Figures 9 to 12 for all surface machining scenarios studied.

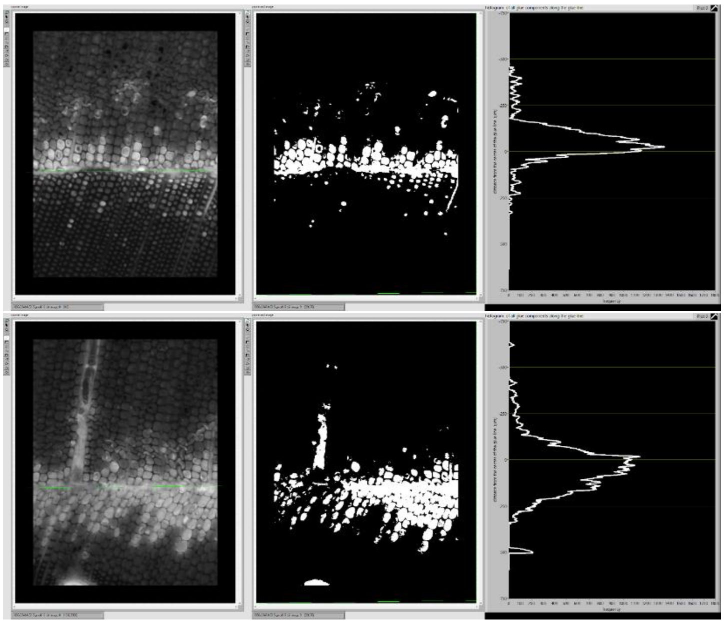

Fig. 9. Image of the glue line in sample B3 – brushed surface after planning with 300m/min.

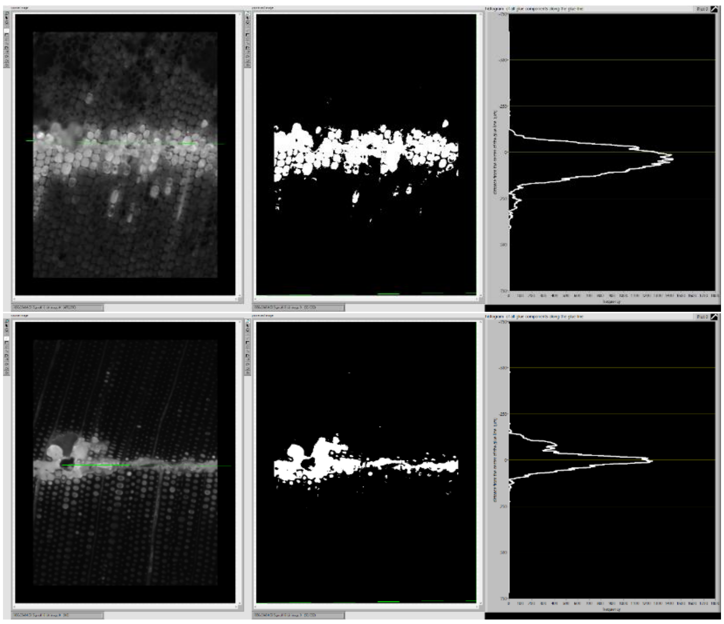

Fig. 10. Image of the glue line in sample F3 –after planning with 300m/min.

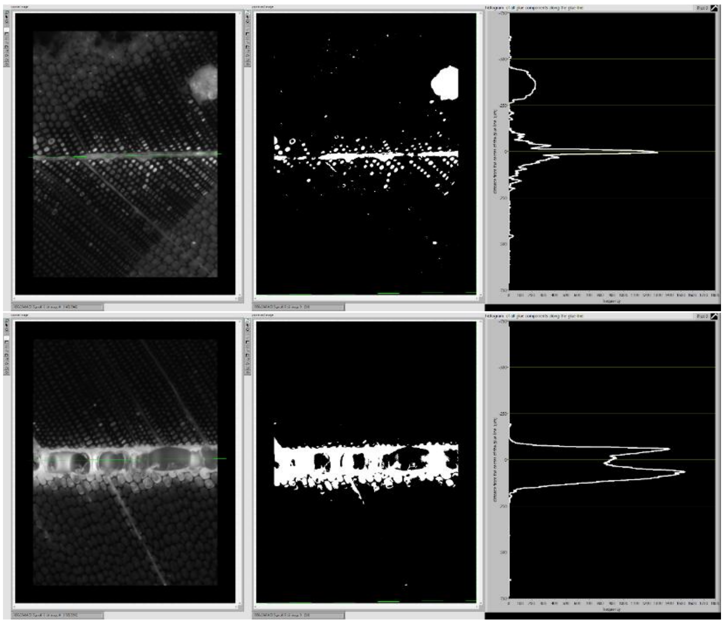

Fig. 11. Image of the glue line in sample S1 –after planning with 200m/min.

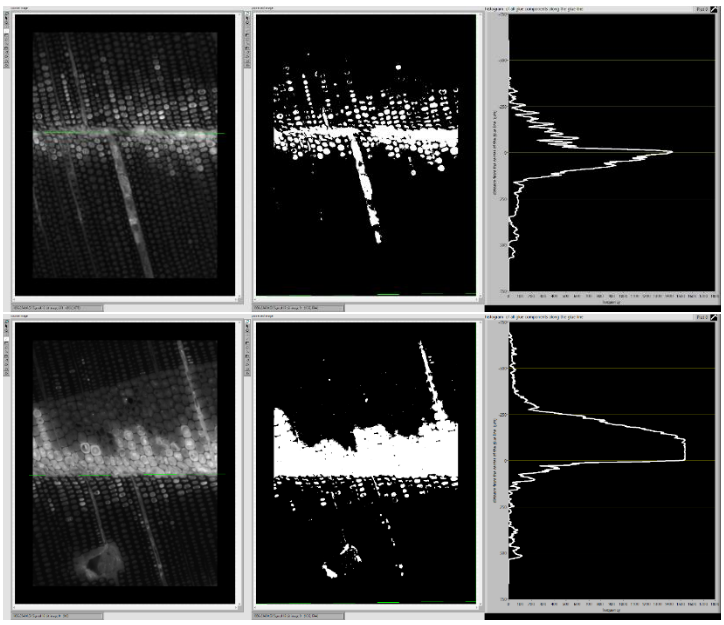

Fig. 12. Image the glue line in sample R4 –after planning with RotoLes machine.

Scaramuzzi Team
YOUR BEST PARTNER IN ORGANIZING MEETINGS AND EVENTS

Tel: 055 494949
scaramuzzi@scaramuzziteam.com

www.scaramuzziteam.com